Performance of Engineered Cementitious Composites for Concrete Repairs

Cover: Penguins on an iceberg, by David Fierstein 2002.

Performance of Engineered Cementitious Composites for Concrete Repairs

Proefschrift

ter verkrijging van de graad van doctor
aan de Technische Universiteit Delft,
op gezag van de Rector Magnificus prof. ir. K.C.A.M. Luyben,
voorzitter van het College voor Promoties,
in het openbaar te verdedigen op dinsdag 11 januari 2011 om 10.00 uur

door Jian ZHOU
civiel ingenieur
geboren te Shandong, China.

Dit proefschrift is goedgekeurd door de promotor:
Prof. dr. ir. K. van Breugel

Copromotor: Dr. G. Ye

Samenstelling promotiecommissie:

Rector Magnificus,	voorzitter
Prof. dr. ir. K. van Breugel,	Technische Universiteit Delft, promotor
Dr. G. Ye,	Technische Universiteit Delft, copromotor
Prof. dr. X. Gu,	Tongji University, China
Prof. dr. ir. G. De Schutter,	Universiteit Gent, België
Prof. dr. ir. L. Courard,	The University of Liège, België
Prof. ir. R.P.J. van Hees,	Technische Universiteit Delft
Prof. dr. ir. R.B. Polder,	Technische Universiteit Delft, reservelid

Printed in the Netherlands.

ACKNOWLEDGEMENT

I would like to thank my promotor Prof. Klaas van Breugel, who gave me the opportunity to work on this project in Microlab. His valuable guidance, inspiring discussions and great patience helped me to complete my PhD study. He also encouraged and supported me to collaborate with other universities and research institutes.

I would like to acknowledge my co-promotor Dr. Ye Guang for his guidance and help during both my master and PhD studies. He guided me to the world of Concrete Technology. His enthusiasm in research has greatly influenced me. I benefitted a lot from the many insightful discussions with him, and enjoyed working on topics stimulated by these discussions.

I also would like to thank Prof. Victor C. Li for hosting me at the Department of Civil and Environmental Engineering of the University of Michigan, USA. The conversation and discussion with Prof. Victor C. Li on ECC and self-healing topics are unforgettable. I enjoyed very much working at ACE-MRL and the collaboration with ACR-MRL.

I would like to thank Dr. Erik Schlangen for his valuable discussion on using FEMMASSE and Lattice models. I appreciate Dr. Rene Braam's effort in arranging the experiments for me. I would like to thank Zhiwei and Zhang Qi for their kind help on numerical study. I am grateful to Mr. Gerrit Nagtegaal and Mr. Arjan Thijssen, Mr. Gerard Timmers and Mr. Edwin Scharp for their assistance in experiments. I enjoyed the collaboration with Prof. Shunzhi Qian, Dr. Dessi Koleva and Dr. Oguzhan Copuroglu.

I enjoyed my PhD life in the Section of Materials and Environment, and I would like to thank the MEers for their presence. Many thanks go to Iris, Claudia and Nynke for their help in all kinds of documents and procedures.

Finally, I would like to thank my parents for their love and support. The last thanks are for my lovely wife. She helped me a lot with my writing and gave me endless support in every aspect.

Jian Zhou
Delft, Dec. 2010

Table of Contents

List of Symbols

Roman lower case letters

a [-]   Pore size distribution constant in HYMOSTRUC

$d_{0,x}$ [μm]   Initial diameter of cement particle x in HYMOSTRUC

f_m [MPa]   Tensile strength of ECC matrix

f_0 [MPa]   Maximum fiber bridging strength in ECC

f_b [MPa]   Bond strength between the repair material and the concrete substrate

f_{fc} [MPa]   First cracking strength of ECC

f_t [MPa]   Ultimate tensile strength

f_c [MPa]   Ultimate compressive strength

g [N/g]   The acceleration of gravity

h_r [mm]   Thickness of the repair material

h_s [mm]   Thickness of the concrete substrate

l_m [mm]   Evaluation length of the surface profile

k [-]   A correction factor

n [-]   An aging coefficient, which is 0.85 in this thesis

n_{pore} [-]   Number of pixels of the pores in BSE image

n_{total} [-]   Number of total pixels in BSE image

n_{hc} [-]   Number of pixels of the hydrated cement in BSE image

n_{hp} [-]   Number of pixels of the hydration products in BSE image

n_{uc} [-]   Number of pixels of the unhydrated cement in BSE image

p [N/mm^2]   Capillary pressure

q [1/(cm^2×s)]   Volumetric flux of water in HYMOSTRUC

r [μm]   Pore radius in HYMOSTRUC

r_0 [μm]   Radius of the minimum capillary pore in HYMOSTRUC

$r_{por}(\alpha)$ [μm]   Radius of the largest pore in HYMOSTRUC

$r_{wat}(\alpha)$ [μm]   Radius of the largest water-filled pore in HYMOSTRUC

r_c [μm]   The Kelvin equilibrium radius in HYMOSTRUC

r_s [μm]   The maximum water-filled pore radius when the adsorbed water is not considered

t [h]   Duration of RCM test

t_{set} [h]   Setting time of the repair material

x_d [mm]   Chloride penetration depth

Roman capital letters

$A_{c,eff}$ [μm^2]   Effective contact area in HYMOSTRUC

$A_{c,spec}$ [μm^2/μm^3]   Specific effective contact area in HYMOSTRUC

$A_{c,spec,fail}$ [μm^2/μm^3]	Secific effective contact area in the failure region
$A_{wat}(\alpha)$ [cm^2/cm^3]	Wall area of water-filled pores in HYMOSTRUC
$A_{por}(\alpha)$ [cm^2/cm^3]	Total pore wall area in HYMOSTRUC
B [1/m]	The Raleigh-Ritz pore size distribution constant in HYMOSTRUC
$C(x,t)$ [-]	Chloride content at depth x at time t
C_s [-]	Surface chloride content
C_i [-]	Initial chloride content in the concrete
D [mm^2/s]	Non-steady-state chloride penetration coefficient
D_0 [mm^2/s]	Chloride penetration coefficient at the reference time t_0
E_{precr} [Gpa]	Pre-cracking Young's modulus of ECC
E_{postcr} [Gpa]	Post-cracking Young's modulus of ECC
E_r [GPa]	Young's modulus of the repair material
E_s [GPa]	Young's modulus of the concrete substrate
F_i (i = 1, 2) [-]	Temperature-related factors accounting for the effects of curing temperature in HYMOSTRCU
L_r [mm]	Length of the repair system
L_{RCM} [mm]	Thickness of the specimen used in RCM test
K [N/mm^3]	Shear stiffness of the interface
K_0 [-]	Basic rate factor in HYMOSTRUC
K_θ [(cm^3/cm^3)/(N×s)]	Volumetric unsaturated water permeability dependent on the water content in HYMOSTRUC
K_s [(cm^3/cm^3)/(N×s)]	Volumetric saturated water permeability in HYMOSTRUC
J_{tip} [J/m^2]	Crack tip toughness in ECC
J_b [J/m^2]	Complementary energy in ECC
R_a [mm]	Average profile of a surface
R_i [mm]	Measured profile of a surface
R_y [mm]	Maximum height of the surface profile
R_q [mm]	Parameter used to describe surface roughness
R [μm]	Average radius of the curvature of the liquid-vapor interface
S_w [-]	Degree of saturation
T [°C]	Temperature of the anolyte solution in RCM test
U [V]	Applied voltage in RCM test
V [cm^3/cm^3]	Volumetric porosity in HYMOSTRUC
V_{pen} [cm^3]	Volume of the penertrometer in MIP test
V_{sample} [cm^3]	Bulk volume of the sample in MIP test
V_{pore} [cm^3]	Pore volume in the sample in MIP test
$V_{0,ce}$ [cm^3/cm^3]	Initial volume of cement in a unit volume of cement paste
$V_{0,w}$ [cm^3/cm^3]	Initial volume of water in a unit volume of cement paste
V_{ex} [cm^3/cm^3]	Change of water content due to moisture exchange in HYMOSTRUC
V_{ab}(x,y,z) [cm^3/cm^3]	Volumetric water loss in the repair material due to the water absorption of the concrete substrate
V_{fr} [cm^3/cm^3]	Volume of the free capillary water in HYMOSTRUC
V_{cp} [μm^3]	Volume of cement paste
W_i [g]	Initial weight of specimen
W_s [g]	Weight of specimen after saturation
W_d [g]	Weight of specimen after drying
W_n [g]	Non-evaporable water content of hydrating cement paste
$W_{n,max}$ [g]	Maximum non-evaporable water content at complete hydration

W_{sample} [g]   Weight of sample for MIP test
W_{pen} [g]   Weight of the penertrometer
$W_{mercury}$ [g]   Weight of mercury
$W_{w,in}$ [g]   Initial weight of water in cement paste
$W_{c,in}$ [g]   Initial weight of Portland cement in cement paste

Greek letters

α [-]   Degree of hydration
β [cm^3/cm^3]   Volume of water consumed by hydration of a unit volume of cement
β_1 [-]   A constant in HYMOSTRUC
δ_0 [mm]   Crack opening corresponding to the maximum fiber bridging stress σ_0
δ_{ss} [mm]   Crack opening corresponding to the steady-state cracking stress σ_{ss}
δ_x [μm]   Thickness of the shell of the hydration products in HYMOSTRUC
$\delta_{in,x}$ [μm]   Thickness of the inner hydration products in HYMOSTRUC
δ_{tr} [μm]   Transition thickness in HYMOSTRUC
ε_{sh} [-]   Shrinkage of the repair material
ε_{fc} [-]   First cracking strain of ECC
ε_u [-]   Ultimate tensile strain of the repair material
ϕ [-]   Porosity
γ [-]   A coefficient
γ_{sv} [N/m]   Solid-vapor interfacial energy
γ_{sl} [N/m]   Solid-liquid interfacial energy
γ_{lv} [N/m]   Liquid-vapor interfacial energy (i.e. the surface tension of liquid)
λ [-]   Factor depending on rate-controlling mechanism in HYMOSTRUC
μ [Pa×s]   Water viscosity
v [1/cm^3]   Volumetric rate of water flow
θ_c [°]   Equilibrium contact angle between the liquid and the solid
θ [cm^3/cm^3]   Volumetric Water content
$\dfrac{\partial \theta_{hy}}{\partial t}$ [cm^3/(cm^3×s)]   Rate of the change of the water content due to cement hydration
$\dfrac{\partial \theta_{mex}}{\partial t}$ [cm^3/(cm^3×s)]   Rate of the change of the water content due to moisture exchange
$\rho_{mercury}$ [g/cm^3]   Density of mercury
ρ_{ce} [g/cm^3]   Density of Portland cement
ρ_w [g/cm^3]   Density of water
$\sigma_{x,re}$ [MPa]   Tensile stress in the repair material induced by differential shrinkage
$\sigma_{y,in}$ [MPa]   Debonding stress at the interface induced by differential shrinkage
σ_0 [MPa]   Maximum fiber bridging stress
σ_{ss} [MPa]   Steady-state cracking stress
$\tau_{x,in}$ [MPa]   Shear stress at the interface induced by differential shrinkage
ω [-]   Water-to-cement ratio
ω_0 [-]   Initial water-to-cement ratio of cement paste
ω_{res}(x,y,z) [-]   Resultant water-to-cement ratio of the repair material
ξ [-]   A constant used in the calculation of water permeability
Ω_i (i = 1, 2, 3) [-]   Reduction factors accounting for the different effects of water

List of Abbreviations

AgCl	Silver chloride
AgNO$_3$	Silver nitrate
BFS	Blast furnace slag
BSE	Backscattered electron
CaCO$_3$	Calcium carbonate
Ca(OH)$_2$	Calcium hydroxide
ECC	Engineered cementitious composite
ESEM	Environmental scanning electron microscope
FRPM	Fiber-reinforced polymer-modified
MIP	Mercury intrusion porosimetry
NaCl	Sodium chloride
NaOH	Sodium hydroxide
PC/BFS	Portland cement-to-BFS
PVA	Polyvinyl alcohol
RCM	Rapid chloride migration
RH	Relative humidity
w/c	water-to-cement

Chapter 1

General Introduction

1.1 Background

The concrete repair, rehabilitation and retrofitting industry grows rapidly, driven by deterioration of, damage to and defects in concrete structures. In U.S. only, the annual cost for the repair, maintenance and strengthening of concrete structures is estimated between \$18 and \$21 billion [Emmons and Sordyl 2006]. However, it is well known that realizing durable concrete repairs is very difficult. McDonald and Campbell [1985] reported that only slightly more than 50% of the concrete repairs carried out by the U.S. Army Corps of Engineers performed satisfactorily (Figure 1.1). Failure of concrete repairs causes high economical, social and environmental impacts.

Figure 1.1 Performance of concrete repairs [McDonald and Campbell 1985].

To understand the durability of concrete repairs, we must refer to the compatibility between repair material and concrete substrate. The compatibility is defined as a balance of deformations and physical, chemical and electrochemical properties between the repair material and the substrate concrete [Vaysburd and Emmons 2006]. This balance ensures that the repair system as a whole withstands stresses induced by restrained volume changes, chemical and electrochemical effects without premature deterioration/distress over a designed period of time. One of the most important components is the dimensional compatibility. Most repair materials have a tendency to shrink, especially at the early stage, while the volume change of substrate concrete is negligible. The shrinkage of the repair material is, therefore, restrained by the concrete substrate. As a result, the differential shrinkage between repair material and concrete substrate induces tensile stress in the repair material and shear and debonding stresses at the interface. These stresses can lead to cracking in the repair material and the interface delamination. Moreover, the cracking of the repair material and the interface

delamination accelerate the penetration of water, oxygen, chlorides, alkalis or sulphates into the repair system. This can cause the corrosion of reinforcement and the deterioration of concrete. Finally, the concrete repair fails.

Another crucial parameter for the durability of concrete repairs is the bond strength between repair material and concrete substrate [Emmons and Vaysburd 1994]. The repair-substrate interface in concrete repairs is often subjected to stresses due to the differential shrinkage or external loadings. On the other hand, the repair-substrate interface is relatively weak, compared with the repair material and the concrete substrate themselves [Bijen and Salet 1994]. When these stresses exceed the bond strength, the repair material debonds from the concrete substrate. Therefore, sufficient bond strength is required to withstand the stresses at the repair-substrate interface and to ensure the monolithic action of the repair material and the concrete substrate.

Engineered cementitious composite (ECC) has been proposed to be one of the most promising repair materials [Li 2004]. It is a micromechanically designed cement-based material reinforced with short random fibres. Unlike common cement-based materials, ECC shows a tensile strain-hardening behaviour with the strain capacity in the range of 3-7%. The high ductility of ECC is achieved by multiple cracking with crack width self-limited to about 60 μm. When ECC is used as a repair material, its high ductility and multiple cracking behavior can release the stresses induced by differential shrinkage. The differential shrinkage, therefore, causes cracking in ECC rather than interface delamination [Li and Li 2009]. This phenomenon has been demonstrated both in the laboratory [Li and Li 2009] and in the field [Lepech and Li 2006]. Moreover, the small crack width in ECC can significantly reduce the penetration of water, oxygen, chlorides, alkalis or sulphates into the repair system. Therefore, the use of ECC improves both the mechanical performance and durability of concrete repairs.

1.2   Objectives of this thesis

The first goal of this project is to develop a "green" Engineered Cementitious Composites (ECC) and to demonstrate the good performance of this "green" ECC. In this thesis, "green" refers to sustainable and environmental-friendly. The second goal is to develop a numerical tool, which can simulate the bond strength between the repair material and the concrete substrate, to assist engineers in designing a durable concrete repair with good bond.

1.3   Research strategy and outline of this thesis

To achieve the goal discussed in previous section, this research is carried out in subsequent steps which are described as follows.

In Chapter 2, this research started with exploring the reasons causing the cracking in repair material and the debonding of repair material from concrete substrate. The stresses in repair systems under differential shrinkage were investigated analytically. The analytical study has shown that differential shrinkage induces relatively lower stresses in the ECC repair system, compared with conventional repair materials. For this reason, ECC was chosen as a repair material in this research, and its performance in concrete repairs was investigated in the following chapters.

In Chapter 3, a new version of ECC, produced with limestone powder and blast furnace slag (BFS), was developed. In order to lower the shrinkage of ECC, the cement content in ECC was reduced by replacing a portion of cement with limestone powder and BFS. ECC mix

composition was designed, based on the ECC material design theory. The properties of the new versions of ECC were investigated experimentally.

The performance of the newly developed ECC repair system was studied in Chapter 4. After a layer of ECC was cast on the top of a concrete beam, the shrinkage of ECC caused cracking in ECC and debonding of ECC from the concrete substrate. The crack pattern in ECC and the interface delamination were measured. The chloride penetration profile of the cracked ECC was investigated using rapid chloride migration (RCM) test. Based on the measured chloride penetration coefficients, the service life of the ECC repair system was predicted. Due to the low bond strength between ECC and the concrete substrate, a large interface delamination was observed. This can cause the failure of the ECC repair system.

In order to enhance the bond strength between the repair material and the concrete substrate, an experimental study was then carried out to explore the microstructure development and the bond strength. The literature review revealed that the moisture transport between repair material and concrete substrate and the surface roughness of concrete substrate are two crucial factors affecting the bond strength. The influence of these two factors was investigated experimentally.

In Chapter 6, based on the experimental results, the cement hydration model HYMOSTRUC [van Breugel, 1991] was extended to simulate the microstructure development of the repair material. In the simulation, the moisture transport between repair material and concrete substrate was taken into consideration. The numerical model was verified by the experimental results. This model was then used to investigate the influence of several factors on the cement hydration and microstructure development. These factors included water content of the concrete substrate, porosity of the concrete substrate and thickness of the repair material.

In Chapter 7, the correlation between the bond strength and the microstructure of the repair material and of the interface was explored. The microstructure of the repair material and of the interface simulated in Chapter 6 was used as input in the calculation of the bond strength. The influence of various factors on the bond strength was also investigated.

Based on the results described in the previous chapters, some general conclusions were drawn in Chapter 8.

Chapter 2

Stresses Induced by Differential Shrinkage

2.1   Introduction

The differential shrinkage between repair material and concrete substrate is considered to be the main cause of the failure of concrete repairs. It can induce high stresses in the repair system and result in the cracking of the repair material and the debonding of the repair material from the concrete substrate as illustrated in Figure 2.1. The cracking in the repair material and the interface delamination accelerate the penetration of water, oxygen, chlorides, alkalis and sulphates into the repair system. This causes reinforcement corrosion and concrete deterioration. Finally, the concrete repair fails, and new repair activities will have to be carried out.
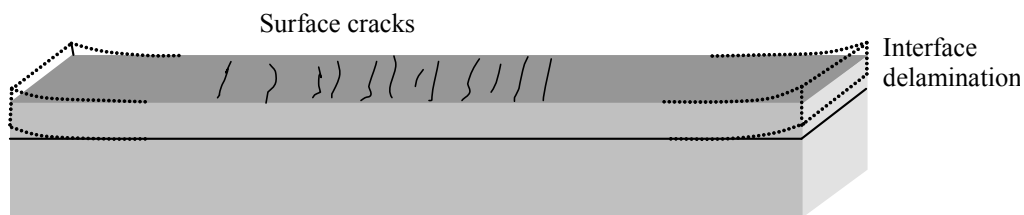
Figure 2.1 Repair material cracking and interface delamination due to differential shrinkage [Li and Li 2006].

The properties of the repair material influence the magnitude of the stresses induced by differential shrinkage. In this chapter, the properties and performance of various repair materials were first reviewed and discussed. The distribution and magnitude of the stresses induced by differential shrinkage in concrete repairs were calculated analytically. The influence of various factors on the stresses was then investigated. Finally, the performance of the conventional repair materials and ECC subjected to differential shrinkage was evaluated.

2.2   Repair materials

Repair materials can generally be grouped into cementitious materials, polymer modified cementitious materials and polymer concrete. These repair materials have a wide variety of properties as shown in Table 2.1. In general, the repair material is required to have a good workability, adequate compressive and tensile strength, high bond strength and good durability. Apart from the conventional repair materials, ECC has recently become a promising repair material due to its excellent mechanical properties and good durability [Li 2004]. Since concrete repairs are subjected to different structural and environmental loads,

each repair creates different demands on the properties of the repair material. To achieve a durable repair, the repair material should be properly selected to meet these demands. It is, therefore, necessary to know the properties of the repair material before decisions are made. The properties of the commonly used repair materials are discussed in the following paragraphs.

Table 2.1 Typical properties of repair materials [Mays and Wilkinson 1987].

Material properties	Cementitious material	Polymer-modified cementitious material	Polymer concrete
Compressive strength [MPa]	20-50	30-60	50-100
Tensile strength [MPa]	2-5	5-10	10-15
Young's modulus [GPa]	20-30	15-25	10-20
Thermal expansion coefficient [10^{-6} °C^{-1}]	10	10-20	25-30
Maximum service temperature [°C]	300	100-300	40-80

2.2.1   Cementitious materials

Conventional mortar and concrete are often used as repair materials in relatively thick sections and large areas, such as the repairs of slabs, walls, columns, piers, hydraulic structures and the full-depth repairs of bridge decks and parking structures. In order to reduce shrinkage, repair materials often have a low water-to-cement (w/c) ratio and a high percentage of aggregates [ACI 546.3R 2006]. Admixtures, such as water-reducing admixtures, expansive agents and accelerators, are often used to reduce water requirements, improve workability, lower shrinkage, accelerate strength gain and adjust other properties. Pozzolanic materials, such as silica fume, fly ash and blast furnace slag, are sometimes mixed in the cementitious repair materials. Silica fume is an ultra fine material. When mixed in the cementitious repair materials, silica fume can improve the particle packing both in the repair material and in the repair-substrate interface and it reacts with the products of cement hydration. Therefore, the addition of silica fume can improve the mechanical and durability properties of the repair material and can increase the bond strength between repair material and concrete substrate. Fly ash and blast furnace slag are used to replace portion of cement to reduce the heat of hydration and the shrinkage and to improve the durability. Recently, fiber-reinforced mortar and concrete are often used as repair materials due to their high tensile strength, low shrinkage and good durability [ACI 546.3R 2006].

In order to achieve durable concrete repairs, the properties of the repair material should match those of the concrete substrate as much as possible, such as pore structure and coefficient of thermal expansion [Cusson and Mailvaganam 1996]. Cementitious materials are considered the best choice of repair materials, since they have similar properties as the substrate concrete and they can be designed to match the properties of concrete substrate. In addition, they are readily available and relatively cheap. Cementitious materials are also easy to be produced, placed, finished and cured.

On the other hand, the cementitious repair materials have some limitations:
- The large shrinkage of the cementitious materials can induce high tensile stress in the repair material and shear and debonding stresses at the interface. Compared with the

polymer modified cementitious materials, the cementitious repair materials have low tensile and bond strength.

- Cementitious materials cannot be used in aggressive environments. For instance, when the deterioration of original concrete is caused by acid and salt attack, the cementitious materials should not be used, unless the causes of deterioration are removed.
- The long curing duration for reaching the targeted strength limits the application of cementitious materials.

2.2.2 Polymer-modified cementitious materials and polymer concrete

Polymers have been used in producing mortar and concrete for many years. There are two ways to use polymers, and the two resultant materials are polymer-modified cementitious materials and polymer concrete. The polymer-modified cementitious materials are made by partially replacing Portland or blended cement by polymers, at the rate of 10-20% by mass. The polymers have relatively small particle size and lead to good particle packing. The polymers react with the cement [ACI 548.3R 1994]. Therefore, the addition of the polymers can improve the mechanical properties, permeability and durability of the repair materials. Polymer concrete is a composite material, in which aggregates are bound together by a dense polymer binder. Portland cement is sometimes used in polymer concrete. But it acts as an aggregate or filler, and it does not react because of the absence of water. Polymer-modified cementitious materials and polymer concrete are mainly used in the repairs of bridges, parking decks and floors. They are especially suited for the use in areas where concrete is subjected to chemical attack and where closing time of a repair area is limited.

Polymer-modified cementitious materials and polymer concrete have many advantages, such as high compressive and tensile strengths, excellent bond properties, low shrinkage, good durability and rapid hardening [ACI 546.3R 2006]. However, the use of these materials has not been studied extensively yet. Therefore, it is difficult to control their properties and to predict their performance in concrete repairs. Polymer-modified cementitious materials and polymer concretes cannot be used in the concrete repairs serving in high temperature, since high temperature affects the physical properties of some polymer materials and results in softening. These materials have poor fire resistance compared to conventional concrete. Polymer-modified cementitious materials and polymer concrete are more difficult to place and finish than conventional concrete. The high cost of polymer also limits the use of these repair materials.

2.2.3 ECC

ECC, short for Engineered Cementitious Composites, is a class of ultra ductile fiber reinforced cementitious composites originally invented at the University of Michigan in the early 1990s [Li 1993]. This group of materials is characterized by high ductility in the range of 3-7%, tight crack width of around 60 μm and relatively low fiber content of 2% or less by volume. Figure 2.2 shows a typical tensile stress-strain curve of ECC and its tight crack width control [Weimann and Li 2003]. Unlike normal concrete and fiber reinforced concrete, ECC shows a metal-like property after the first cracking. This unique tensile strain-hardening behavior results from an elaborate design using a micromechanics model taking into account the interactions among fiber, matrix and fiber-matrix interface [Li and Leung 1992].
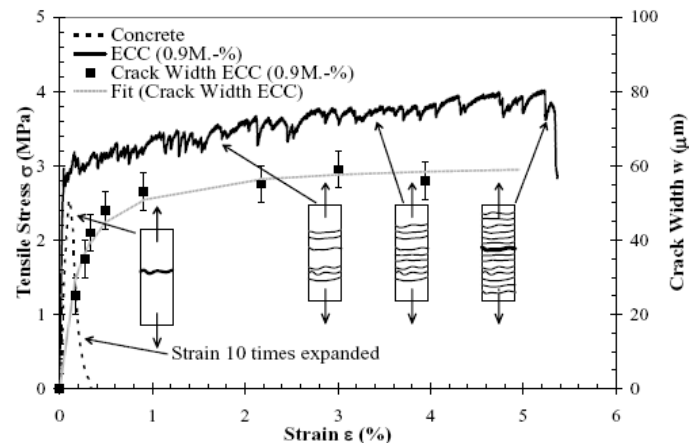
Figure 2.2 Tensile stress-strain curve and tight crack width control of ECC [Weimann and Li 2003].

When ECC is used as a repair material, its high ductility and multiple cracking behavior can release the stresses induced by differential shrinkage in concrete repairs. When ECC has adequate bond strength with the concrete substrate, differential shrinkage causes cracking of ECC. Once ECC cracks, its effective Young's modulus decreases and the further increase in differential shrinkage leads to further cracking of the repair material rather than interface delamination [Li and Li 2009]. This phenomenon has been demonstrated both in the laboratory [Li and Li 2009] and in the field [Lepech and Li 2006].

The crack width in the ECC repair layer is of vital importance for the durability of the repair system. ECC has a tight crack width, self-controlled to around 60 μm without the presence of steel reinforcement. This crack width is much smaller than the typical crack width observed in steel reinforced concrete and normal fiber reinforced concrete. ECC, therefore, shows a water permeability several orders of magnitude lower than the steel reinforced mortar, after the same pre-tension deformation of 1.5% [Lepech and Li 2005]. The small crack width of ECC can significantly reduce the penetration of water and harmful substances, such as oxygen, chlorides, alkalis or sulphates. ECC can, therefore, improve the durability of structures exposed to aggressive environments, such as freezing-thawing cycles, hot water immersion, chloride immersion, deicing-salt exposure and alkali-silicate reaction [Li 2007, Sahmaran and Li 2008, Sahmaran et al. 2008]. Therefore, the use of ECC not only improves the mechanical performance of concrete repairs, but also prolongs the service life of structures and reduces the maintenance and repair costs.

2.3   Shrinkage of the repair materials

Shrinkage is a result of the various types of shrinkage. Drying shrinkage and autogenous shrinkage are main concerns for repair materials, and they will be discussed in the following. Drying shrinkage is the volume change due to the loss of adsorbed water from cement pastes. It is the major part of total shrinkage of normal strength concrete. When concrete is subjected to drying conditions, the loss of free water takes place first which causes little or no shrinkage. As drying continues, adsorbed water is removed from the cement paste. This causes a pronounced volume change, and, for example, values up to 4000 μstrain have been observed

[Neville 1995]. Drying shrinkage develops over a long period of time and thus influences the long-term performance of repair materials.

   A high w/c ratio can lead to high drying shrinkage. According to Brooks [Brooks 1989], the drying shrinkage of hardened cement paste is proportional to its w/c ratio, when the w/c ranges from 0.2 to 0.6. An increase in aggregate content can lead to the reduction of shrinkage, because aggregates work as the inner restraint of the shrinkage of hardened cement paste. The thickness of repair materials has an influence on drying shrinkage. The drying shrinkage of thin repair materials grows relatively rapidly, because the water loss is faster in thin sections. Rapid drying shrinkage does not allow the relief of stresses by relaxation and the development of strength of repair materials. Therefore, repair materials with a smaller thickness are more susceptible to cracking. The environment conditions, such as ambient relative humidity, temperature, and wind speed, have an effect on the rate of drying shrinkage. In general, a low relative humidity, a high temperature and a high wind speed accelerate the rate of water loss and hence increase drying shrinkage. Therefore, a proper curing is helpful to reduce and delay drying shrinkage.

   The autogenous shrinkage is the consequence of withdrawal of water from the capillary pores by cement hydration and this process is known as self-desiccation. In concrete with a high w/c ratio, autogenous shrinkage is negligible compared to drying shrinkage [Neville 1995]. In high performance concrete, which is often used in concrete repairs, as the w/c ratio decreases and silica fume is used, autogenous shrinkage becomes substantial.

2.4   Analytical calculation of the stresses induced by differential shrinkage

Many analytical models have been developed to calculate the stresses in concrete repairs induced by differential shrinkage [Birkeland 1960, Silfwerbrand 1997, Beushausen and Alexander 2007]. The analytical models can easily be implemented in practice, without the need of specialized software and need less calculation time than finite element program. In this study, the distribution and magnitude of the stresses induced by the differential shrinkage is studied analytically. The classic plate theory [Timoshenko and Woinowsky-Krieger 1989] is used to calculate these stresses in the layered concrete repairs, and the calculation procedure is described in detail in Appendix A1.

   Differential shrinkage can induce tensile stresses in the repair material and the shear as well as debonding stresses at the interface as shown in Figure 2.3. These stresses are calculated using Eqs. A1.16-18 and presented graphically in Figure 2.4. The maximum value of the tensile stress $\sigma_{x,re}$ [MPa] locates at the middle section of repair material, while the maximum values of the shear stress $\tau_{x,in}$ [MPa] and the debonding stress $\sigma_{y,in}$ [MPa] locate at the end of the interface. The high tensile stress $\sigma_{x,re}$ can lead to the cracking of the repair materials. The combination of the shear stress $\tau_{x,in}$ and the debonding stresses $\sigma_{y,in}$ can lead to the debonding of the interface. Therefore, the observed failures of concrete repairs are always in two modes: the cracking at the middle of repair material and the interface delamination at the end of the interface.
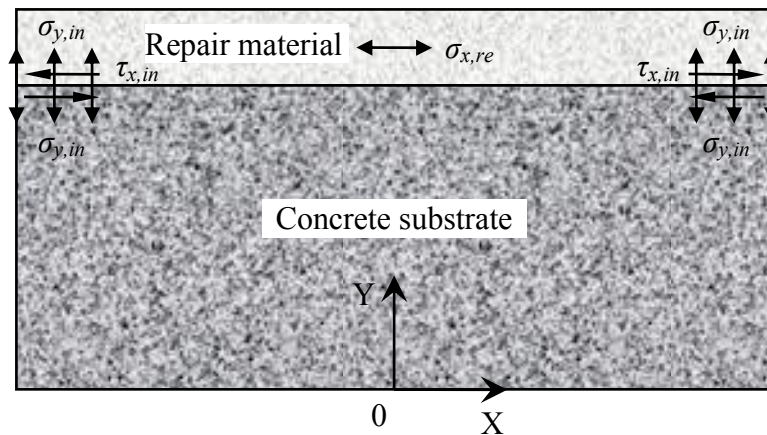
Figure 2.3 Stress distribution induced by differential shrinkage.
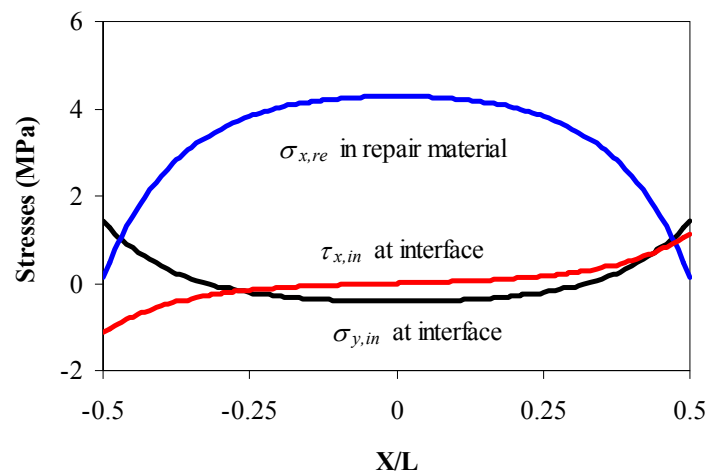
Figure 2.4 Differential shrinkage-induced stresses in the repair system calculated by Eq. A1.16-18 (linear elastic analysis).

2.5   Factors influencing the stresses induced by differential shrinkage

According to Eq. A1.31-33, the stresses induced by differential shrinkage are determined by the shrinkage of the repair material, the size of the repair system, the Young's moduli of the repair material and the concrete substrate and the shear stiffness of the interface. The influence of these factors is investigated analytically in this section.

In the analysis, a layered repair system with the length L_r of 2000 mm is used as a reference. The repair system consists of a layer of repair material with the Young's modulus E_r of 20 GPa and the thickness h_r of 50 mm and a layer of concrete substrate with the Young's modulus E_s of 30 GPa and the thickness h_s of 200 mm. The shrinkage of the repair material ε_{sh} was 200×10^{-6} and is constant over the depth of the repair material. The shear stiffness K of 5 N/mm^3 is used in this study.

2.5.1   Shrinkage of the repair material

According to Eqs. A1.31-33, the maximum values of the stresses induced by a differential shrinkage are linearly proportional to the shrinkage of the repair material until cracking. This indicates that the large shrinkage leads to high stresses in the repair system and hence large probability of cracking in the repair material and of debonding of the repair material from the concrete substrate. A repair material with a low shrinkage is, therefore, desirable. The shrinkage of repair materials is limited in many concrete repair standards. For example, the Hong Kong Housing Authority specifies a limit of 300 μstrain free shrinkage for specimens with dimensions of 25 × 25 × 285 mm at 7 days under 27°C and 55% RH [Hong Kong Housing Authority 1991].

2.5.2   Size of the repair system

Figure 2.5 shows the influence of the length of the concrete repair. The stresses increase fast as the length increases up to 4000 mm. Then they increase further only slightly, and $\sigma_{x,re}$ approaches the highest value of 3.6 MPa. This means that the shrinkage of the repair material is restrained at the interface within a critical length. When the length of repair system exceeds this critical length, it is not the crucial factor any more. The value of the critical length is influenced by the shear stiffness. When the shear stiffness is large, the shear stresses are high, $\sigma_{x,re}$ increases fast, and thus the critical length becomes small.
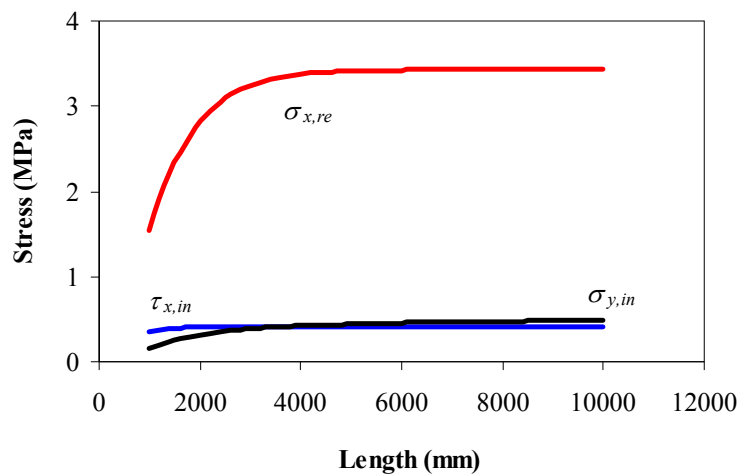
Figure 2.5 Influence of the length L_r of the repair system on the differential shrinkage-induced stresses by a linear elastic analysis.

The influence of the thickness ratio of the repair material h_r to the concrete substrate h_s on the differential shrinkage-induced stresses is plotted in Figure 2.6. As the thickness ratio increases, the maximum value of $\sigma_{x,re}$ decreases and the maximum values of $\sigma_{y,in}$ and $\tau_{x,in}$ increase. This indicates that a thinner repair material is more likely to crack, while the probability of interface delamination is higher in the concrete repair with a thicker repair material.

Figure 2.6 Influence of the thickness of the repair material h_r and of the concrete substrate h_s on the differential shrinkage-induced stresses by a linear elastic analysis.

2.5.3   Young's modulus

The influence of the ratio of the Young's moduli of the repair material E_r to the concrete substrate E_s on the differential shrinkage-induced stresses is plotted in Figure 2.7 and Figure 2.8. The increase in the ratio of the Young's moduli E_r/E_s causes a small increase in the maximum values of $\sigma_{y,in}$ and $\tau_{x,in}$ and hence an increase in the probability of interface delamination. When the ratio of the Young's moduli E_r/E_s increases, the maximum value of $\sigma_{x,re}$ increases, and the maximum value of the tensile strain $\varepsilon_{x,re}$ of the repair material decreases. Since cracking is governed by the ultimate strain, it can be expected that the repair material with smaller Young's modulus is more likely to crack due to differential shrinkage. This coincides with Mangat and O'Flaherty's conclusion [2000].
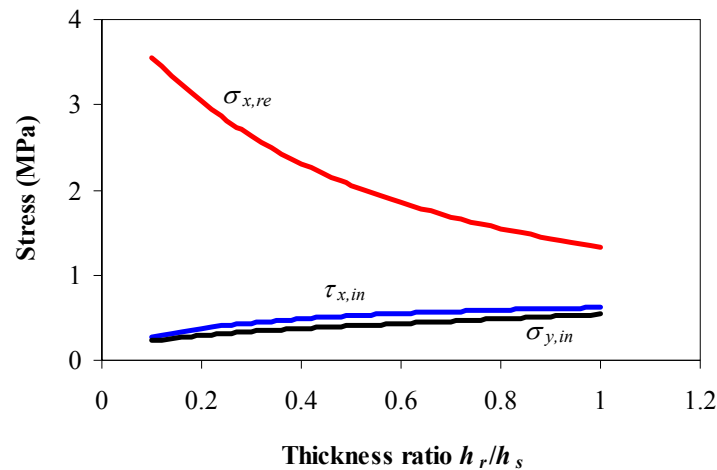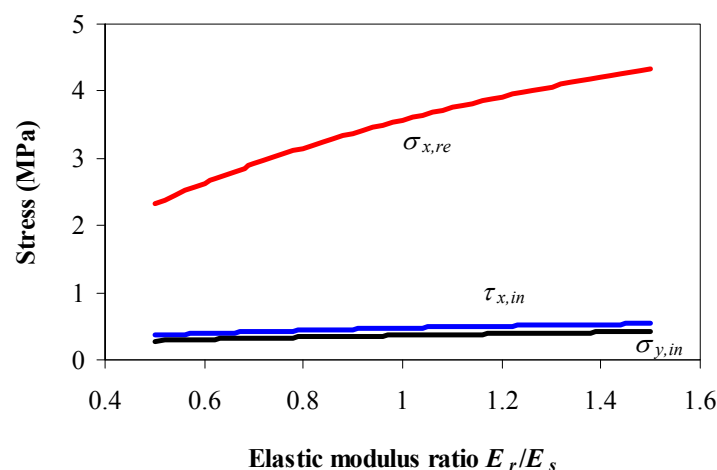

Figure 2.7 Influence of the Young's modulus of the repair material E_r and of the concrete substrate E_s on the differential shrinkage-induced stresses by a linear elastic analysis.
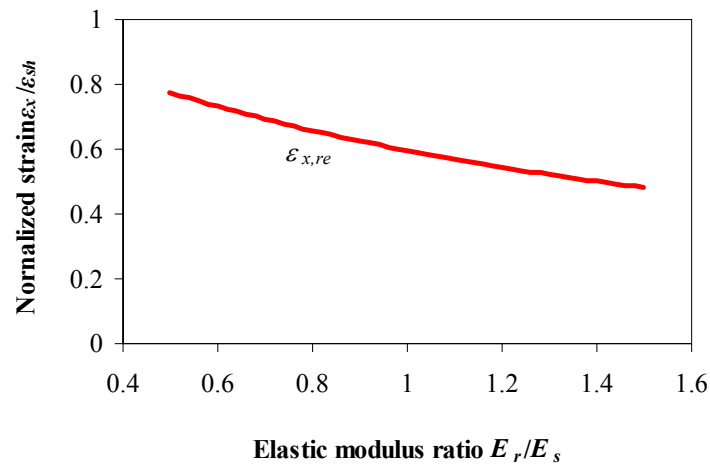
Figure 2.8 Influence of the Young's modulus of the repair material E_r and of the concrete substrate E_s on the resulting tensile strain of the repair material by a linear elastic analysis.

The creep of the repair material and the concrete substrate causes a decrease in their Young's moduli E_r/E_s. Consequently, the stresses in the repair system are reduced. Beushausen [2006] summarized that the creep of the repair material can reduce the tensile stress in the repair material by approximately 40-60%.

2.5.4   Shear stiffness

Figure 2.9 shows the influence of the shear stiffness of the interface on the maximum values of the stresses. The increasing shear stiffness results in a higher $\sigma_{x,re}$ and thus a larger probability of cracking. This explains why the cracking is more serious in the concrete repair with a rougher interface, which has large shear stiffness [Li and Li 2006].

Figure 2.9 Influence of the shear stiffness K of the interface on the differential shrinkage-induced stresses by a linear elastic analysis.

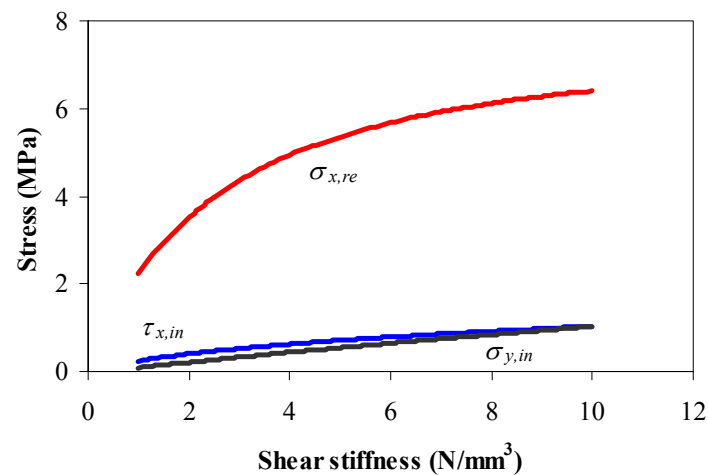## 2.6   Performance of the conventional repair materials and ECC

2.6.1   Stresses in the different repair systems

The conventional repair materials, such as cementitious material and polymer-modified material, are brittle materials. Once the tensile stress reaches its tensile strength, the repair material cracks and it cannot carry high load. Under uniaxial tensile load, ECC shows a strain-hardening behavior as shown in Figure 2.2. When the tensile stress is lower than the first cracking strength f_{fc} [MPa], ECC behaves the same as normal concrete, and the tensile stress is proportional to the tensile strain. Beyond the first cracking strength, ECC cracks sequentially, and the stresses increase only slightly. The multiple cracking results in a large strain capacity. In the calculation of the differential shrinkage-induced stresses, the tensile behavior of brittle materials is simplified as shown in Figure 2.10 (a), and the softening behavior after cracking is not taken into consideration. The tensile strain-hardening behavior of ECC can be modeled as a bilinear curve as shown in Figure 2.10 (b). The calculation of the differential shrinkage-induced stresses is discussed in detail in Section A1.4. As shown Figure 2.11, the differential shrinkage-induced stresses in the ECC repair system also appear bilinear to the shrinkage of ECC. Beyond the first cracking strength, the shrinkage leads to the multiple cracking of ECC and only a small increase in the stresses.

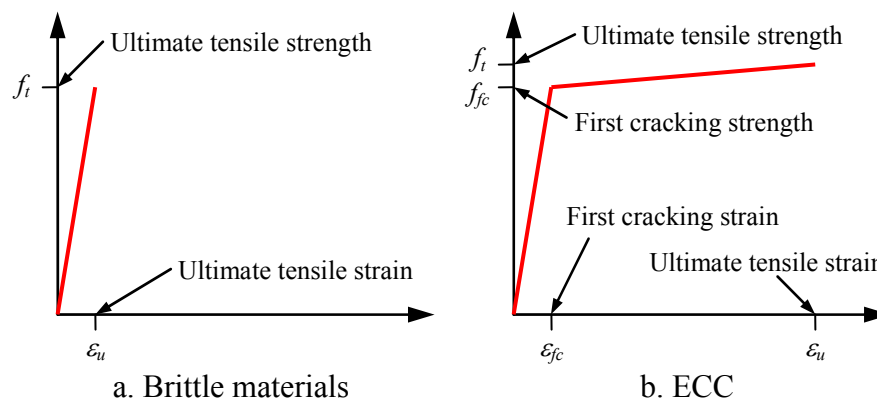a. Brittle materials   b. ECC

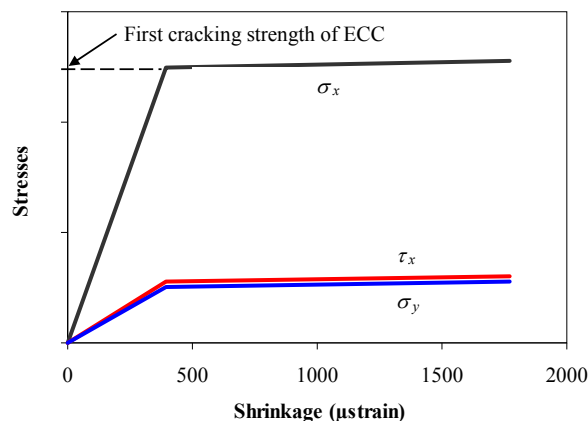Figure 2.10 Tensile stress-strain curves of (a) brittle repair materials and (b) ECC.

Figure 2.11 Differential shrinkage-induced stresses in the ECC repair system.

In order to compare the performance of ECC with the conventional repair materials, the differential shrinkage-induced stresses in the differential repair systems is calculated. In the calculation, a two-layer repair system with the length of 2000 mm is investigated. This repair system consists of a layer of the concrete substrate with the thickness of 200 mm and a layer of repair materials with the thickness of 50 mm. The repair materials, including cementitious materials, polymer-modified cementitious materials and ECC, are investigated. The Young's modulus of the concrete substrate was assumed to be 30 GPa. The shrinkage and creep of the concrete substrate were not taken into account. The properties of the conventional repair materials and ECC are given in Table 2.2 and Table 2.3, respectively. The shear stiffness of 5 N/mm^3 [Ackermann 1994], was used in this study. In the calculation, the shrinkage of repair materials is assumed to be constant through the depth.

Table 2.2 Properties of the conventional repair materials at the age of 28 days [Emberson and Mays 1990].

Repair materials	Tensile strength f_t [MPa]	Young's modulus E_r [GPa]	Bond strength f_b [MPa][*]	Free shrinkage ε_{sh} [$\times 10^{-6}$][#]
Cementitious material	3.1	38.6	1.21	700
Polymer modified material	6.5	43.1	1.45	540

[*] Bond strength was measured by pull-out test.
[#] The shrinkage was measured from unrestrained prisms ($40 \times 40 \times 160$ mm^3) cured under a temperature varying from 12°C to 22°C and a relative humidity varying from 55% to 95%.

Table 2.3 Properties of ECC at the age of 28 days.

First cracking strength f_{fc} [Mpa][*]	Ultimate tensile strength f_t [Mpa][*]	Pre-cracking Young's modulus E_{precr} [Gpa][*]	Post-cracking Young's modulus E_{postcr} [Gpa][*]	Free shrinkage ε_{sh} [$\times 10^{-6}$][*]	Bond strength f_b [MPa][#]
4.5	5.6	23.2	0.024	2400	1.1

[*] After Li and Li [2009].
[#] After van Zijl and Stander [2008].

The calculated stress-to-strength ratios in the different repair systems subjected to a differential shrinkage are given in Figure 2.12. The cementitious material shows the highest stress-to-strength ratios due to its high shrinkage and low tensile and bond strengths. The polymer modified material also shows high tensile and debonding stress-to-strength ratios, which exceed 1. Large differential shrinkage can cause the failure of these two repair materials in the forms of cracking and/or interface delamination. Among three repair materials, although ECC has very high shrinkage, it shows the lowest stress-to-strength ratios. It can be expected that ECC has a relatively low probably to fail in tension and to debond from concrete substrate.
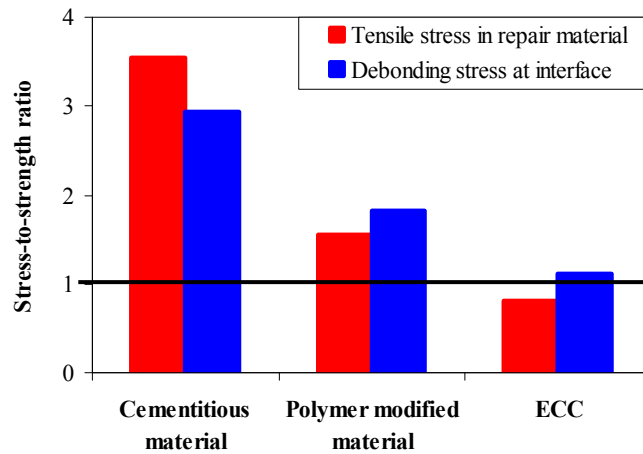
Figure 2.12 Calculated stress-to-strength ratios in the repair system subjected to differential shrinkage by a linear elastic analysis.

2.6.2   Performance of the differential repair materials after cracking

If the tensile stress in the repair material exceeds its tensile strength before the stresses at the interface reach the bond strength, the repair material cracks. The repair material often cracks at the middle, where the tensile stress is highest. In the brittle repair material, after cracking, the repair material cannot carry tensile load, and the repair material is separated into two parts as shown in Figure 2.13 (a). Where the repair material cracks, the tensile stress drops to zero, and the stresses at the interface increase dramatically as shown in Figure 2.13 (b), (c), and (d). The cracking of the repair material also results in the maximum tensile stress moving to the middle of the separated repair material as shown in Figure 2.13 (b). As the shrinkage continuously increases, the maximum tensile stress increases. When the tensile stress in the repair material exceeds its tensile strength, another crack forms.

a. Cracking of the brittle repair material

b. Tensile stress $\sigma_{x,re}$ in the repair material

c. Shear stress $\tau_{x,in}$ at the interface

d. Debonding stress $\sigma_{y,in}$ at the interface

Figure 2.13 (a) Cracking of the brittle repair material due to the differential shrinkage. Comparison of (b) the tensile stress $\sigma_{x,re}$ in the repair material, (c) the shear stress $\tau_{x,in}$ and (d) the debonding stress $\sigma_{y,in}$ at the interface before and after cracking.

After ECC cracks, it can carry a higher tensile load, and new cracks form. Finally, the ECC repair layer shows multiple cracking as shown in Figure 2.14 (a). Since the shrinkage of ECC is eliminated by the multiple cracking, the stresses in the repair system increase slightly as shown in Figure 2.14 (b), (c) and (d). When ECC cracks before debonding from the concrete substrate, the cracking can avoid the increase in the stresses at the interface due to the further shrinkage, and the interface is, therefore, "protected". Moreover, due to the strain-hardening behavior of ECC, after the cracking of ECC the repair system can keep or even increase its load-carrying capacity.

a. Multiply cracking in ECC

b. Tensile stress $\sigma_{x,re}$ in ECC

c. Shear stress $\tau_{x,in}$ at the interface
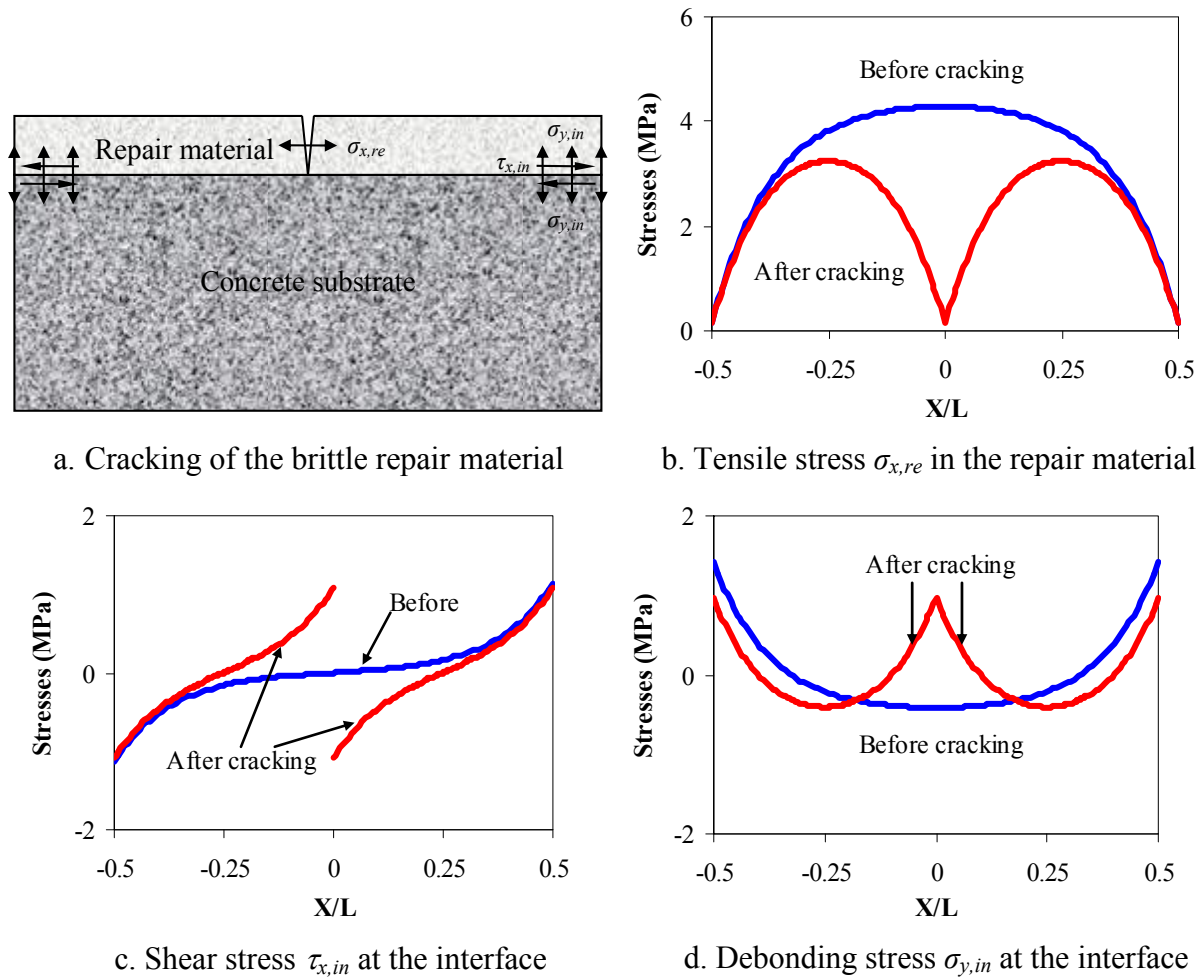

d. Debonding stress $\sigma_{y,in}$ at the interface
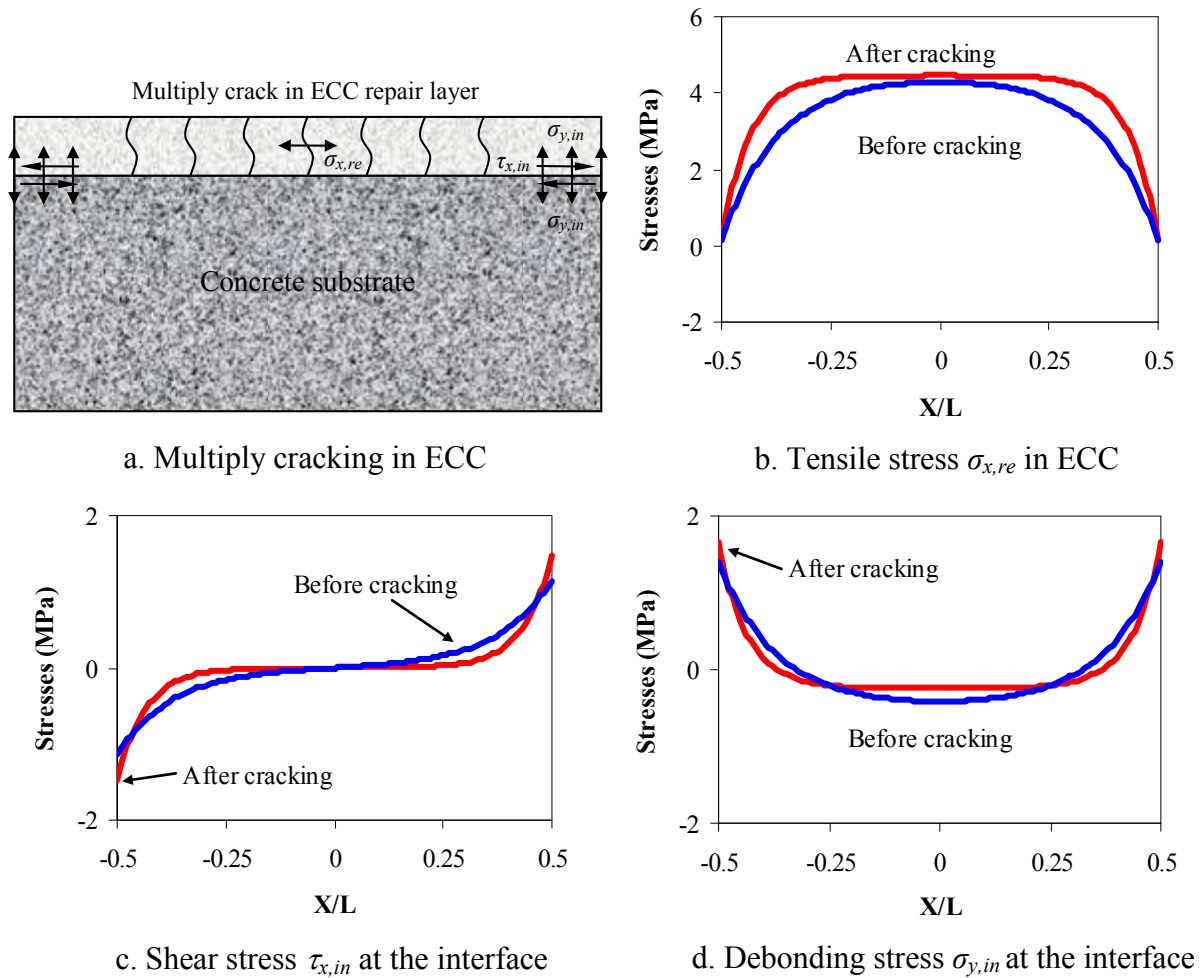
Figure 2.14 (a) Multiple cracking of ECC due to the differential shrinkage. Comparison of (b) the tensile stress $\sigma_{x,re}$ in ECC, (c) the shear stress $\tau_{x,in}$ and (d) the debonding stress $\sigma_{y,in}$ at the interface before and after cracking.

2.6.3   Performance of the differential repair materials after debonding

When the bond strength between repair material and concrete substrate is low, the repair material debonds from the concrete substrate before it cracks. Either in the conventional repair system or in the ECC repair system, the debonding causes a decrease of the stresses in the repair material. As the shrinkage increases, the stresses at the interface increase as well and cause further debonding. Therefore, in the ECC repair system the debonding is more critical than cracking. If the debonding occurs before ECC cracks, the tensile stress in ECC $\sigma_{x,re}$ cannot reach its first cracking strength. As a result, ECC does not show the multiple cracking behavior, and its high ductility cannot be utilized. Therefore, ECC should have high bond strength, so that ECC cracks before debonding occurs.
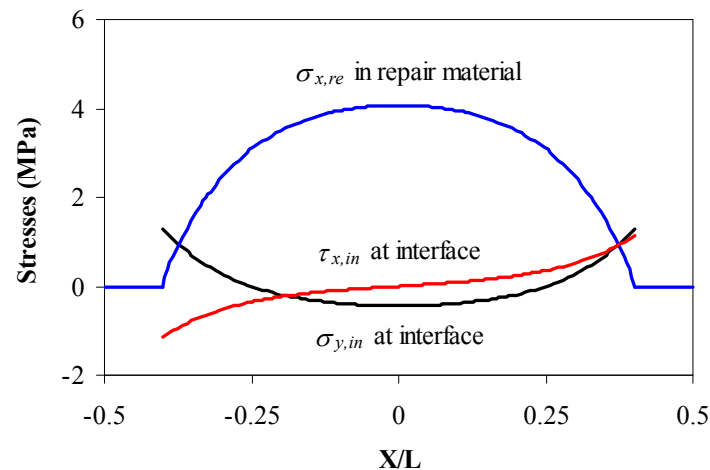
Figure 2.15 Stresses in the repair system after the repair material debonds from the concrete substrate.

2.7   Conclusions

Based on the above discussion, the following conclusions can be drawn:
- Repair materials have a wide variation of properties.
- The stresses induced by differential shrinkage are determined by the shrinkage of the repair material, the size of the repair system, the Young's moduli of the repair material and the concrete substrate and the shear stiffness at the interface.
- The analytical calculation reveals that ECC shows lower probability of failure in tension and debonding, compared with the conventional repair materials. After ECC cracks, as the shrinkage of ECC increases, the differential shrinkage-induced stresses increase slightly.
- The debonding of ECC is a crucial factor influencing the performance of the ECC repair system, and the bond strength between ECC and concrete substrate should be high enough to prevent the debonding before cracking.

From the discussion presented in this chapter, it can be concluded that ECC is potentially a good repair material. Therefore, ECC is chosen as a repair material to be investigated in this study. A version of ECC with locally available materials will be designed in Chapter 3. In Chapter 4, the mechanical and durability performance of the ECC repair system will be investigated experimentally, and its service life will be predicted.

Chapter 3

ECC with Limestone Powder and Blast Furnace Slag

3.1 Introduction

Based on the results and discussion in Chapter 2, it is found that after ECC cracks, as the shrinkage of ECC increases, the differential shrinkage-induced stresses increase only slightly. As a result, the potentials of the cracking and the interface debonding are reduced. It can be expected that ECC has a superior performance in concrete repairs and the use of ECC prolongs the service life of concrete repairs.

   To achieve strain hardening, the matrix fracture toughness of ECC has to be limited so that multiple cracking could occur before reaching maximum fiber bridging stress. Large aggregates can cause an increase in the matrix fracture toughness. They cannot, therefore, be used in the mixture [Wang and Li 2007]. As a consequence, ECC has considerably high cement content, typically two to three times higher than conventional concrete [Qian and Li 2007]. The high cement content in ECC results in high hydration heat and shrinkage. When used in concrete repairs, the high hydration heat and shrinkage can induce high stresses in the repair material and at the interface and may, therefore, cause failure of the concrete repairs. Moreover, the high cement content also has negative effects on environmental aspects and material cost. A solution could be to replace a portion of cement in ECC by environmental-friendly materials, such as limestone powder and BFS.

   In this chapter, a new version of ECC with locally available materials, including Portland cement, limestone powder and BFS, is designed. In the following sections, ECC material design theory is firstly described, and ECC mix design is discussed. Then, the properties of different ECC mixtures are investigated experimentally. The experimental results of four-point bending test, uniaxial tensile test, loaded crack width measurement and compressive test are reported. The images captured under environmental scanning electron microscope (ESEM) are used to interpret the microstructural properties of ECC.

3.2 Fiber-bridging properties and multiple-cracking behavior

The fiber-bridging properties play a crucial role on the tensile strain-hardening behavior of ECC. One of the typical fibers used in ECC is polyvinyl alcohol (PVA) fiber with a diameter of 39 μm and a length of 6-12 mm. Figure 3.1 illustrates the single fiber pullout behavior of PVA fiber [Yang et al. 2008]. Before the fiber is pulled out, it first debonds from the surrounding cement-based matrix, which is reflected by the drop after the first load peak. After debonding stage, the fiber is in the pullout stage and shows a slip-hardening behavior. As the fiber slips out of the matrix, the frictional force between the fiber and the matrix increases. During the debonding and pullout stages, the fiber may rupture if the pullout load

exceeds the fiber tensile strength, often observed in the case of large embedment length as shown in Figure 3.2.
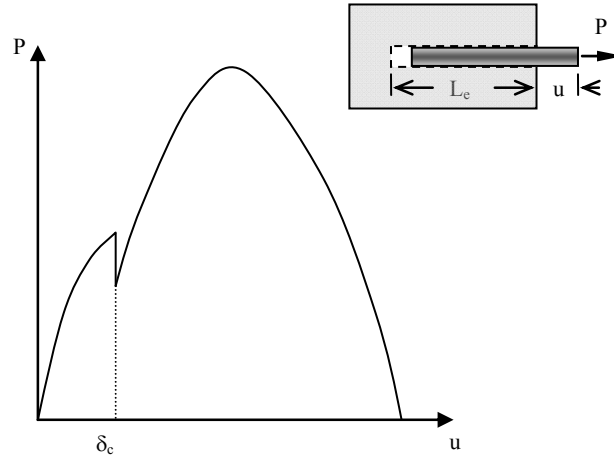
Figure 3.1 Single fiber pullout behavior of the PVA fiber [Yang et al. 2008].
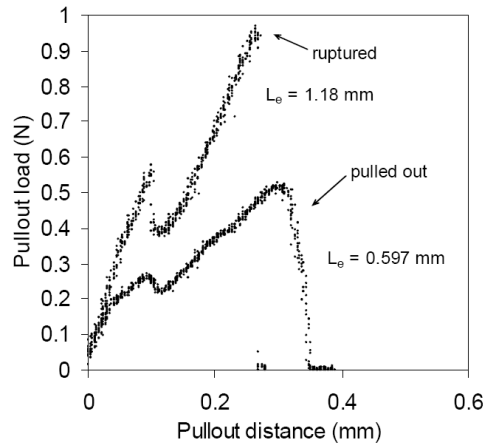
Figure 3.2 Single fiber pullout curves of PVA fiber [Yang et al. 2008].

When ECC is loaded in tension, the matrix starts to crack in its weakest cross-section. Then the fibers crossing this crack take over the tensile load. As the fibers slip out of the matrix, the crack progressively opens. Due to the slip-hardening behavior of fibers, ECC can carry an increasing load, which generates new cracks at other sites. By repeating this process ECC exhibits multiple-cracking behavior. The sequential development of multiple cracking results in the strain-hardening behavior of ECC. This is referred to as the strength criterion:

$$f_m \leq f_0 \tag{3.1}$$

where f_m [MPa] and f_0 [MPa] are the tensile strength of ECC matrix and the maximum fiber bridging strength on each potential crack plane, respectively. The strength criterion determines the initiation of cracks.

Another requirement for the multiple-cracking behavior is the steady-state flat crack propagation under tension. This is referred to as the energy criterion. A flat crack forms after

initiating from a defect site and extends infinitely through the matrix [Li and Leung 1992, Li 1993, Wang and Li 2006]. This requires the crack tip toughness J_{tip} [J/m^2] to be lower than the complementary energy $J_b^{'}$ [J/m^2]:

$$J_{tip} \leq J_b^{'}$$ (3.2)

The crack tip toughness J_{tip} and the complementary energy $J_b^{'}$ can be calculated from the bridging stress σ [MPa] versus crack opening δ [mm] curve as shown in Figure 3.3:

$$J_b^{'} = \sigma_0 \delta_0 - \int_0^{\delta_0} \sigma(\delta) d\delta$$ (3.3)

$$J_{tip} = \sigma_{ss} \delta_{ss} - \int_0^{\delta_{ss}} \sigma(\delta) d\delta$$ (3.4)

where δ_0 [mm] is the crack opening corresponding to the maximum fiber bridging stress σ_0 [MPa]; δ_{ss} [mm] is the crack opening corresponding to the steady-state cracking stress σ_{ss} [MPa].
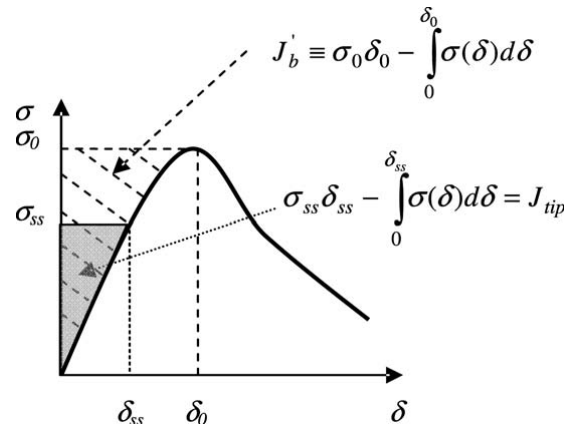
Figure 3.3 Typical tensile $\sigma(\delta)$ curve. Hatched area represents complimentary energy $J_b^{'}$. Shaded area represents crack tip toughness J_{tip} [Wang and Li 2006].

3.3   ECC mixture design

3.3.1   Materials used in ECC

The standard ECC is made of Portland cement, fine silica sand and fly ash as shown in Table 3.1 [Qian and Li 2007]. In this mixture, the Portland cement content is as high as 33.3% by weight. The high Portland cement content causes high shrinkage and high heat evolution. When used in concrete repairs, these may result in the cracking of ECC and the interface debonding, especially at early age. Fine silica sand is made by finely grinding silica sand to an average size about 110 μm. Since silica sand is very hard, the grinding costs a lot of energy, and the price of fine silica sand, therefore, increases dramatically. In order to reduce the

Portland cement content and to replace fine silica sand by low-cost materials, locally available materials, including Portland cement CEM I 42.5 N, limestone powder and BFS, are used to produce ECC.

Table 3.1 Mix composition of the standard ECC mixture M45 (weight %) [Qian and Li 2007].

Type I cement	Fine silica sand	Fly ash	Water/powder ratio	Super-plasticizer	PVA fiber (by volume)
1	0.8	1.2	0.2	0.013	2%

Limestone powder is produced by grinding limestone, and it consists principally of calcium carbonate ($CaCO_3$). When mixed with Portland cement and water, only a little limestone powder reacts with cement clinker or hydration products, and it is usually considered as an inert filler material [Poppe and De Schutter 2005]. The incorporation of limestone powder with Portland cement has many advantages on early compressive strength, durability and workability of concrete [Tsivilis et al. 2000]. BFS is a by-product in the manufacture of pig iron, and it is the main cement replacement material in the Netherlands. Due to the amorphous glassy-like microstructure consisting of mono-silicates, BFS shows a potential of pozzolanic reaction [Bijen 1996]. BFS accelerates the hydration of Portland cement and reacts with the calcium hydroxide, one of the hydration products of Portland cement. The addition of BFS results in a more homogeneous fiber distribution, because BFS particles can enhance the viscosity of fresh cement paste [Kim et al. 2007]. Therefore, the use of limestone powder and BFS in ECC not only reduces the cost and increases the greenness, but also improves the workability and mechanical properties of ECC.

BFS is usually used in concrete as main constituent of BFS cement. BFS cement is produced by mixing Portland cement clinker and BFS and then grinding them together. According to BFS fractions, the family of BFS cements can be divided into three types, i.e. CEM III/A, CEM III/B and CEM III/C [EN 197-1 2000]. Table 3.2 gives the composition of the three types of BFS cements. BFS cement was also used to produce ECC by replacing Portland cement and BFS.

The chemical compositions of Portland cement (CEM I 42.5N), limestone powder, BFS and BFS cement (CEM III/B 42.5N) are given in Table 3.3. The densities of Portland cement (CEM I 42.5N), limestone powder, BFS and BFS cement (CEM III/B 42.5N) are 3150 kg/m^3, 2700 kg/m^3, 2850 kg/m^3 and 2960 kg/m^3, respectively. Figure 3.4 shows the particle size distribution curves of Portland cement (CEM I 42.5N), limestone powder, BFS and BFS cement (CEM III/B 42.5N), which were measured with laser-diffraction technique. The mean particle sizes of CEM I 42.5N, limestone powder, BFS and BFS cement (CEM III/B 42.5N) are 16.2 μm, 13.4 μm, 10.6 μm and 20.4 μm, respectively.

Table 3.2 Compositions of BFS cements (weight %) [EN 197-1 2000].

Types of BFS cement	Clinker	BFS	Minor additional constituents
CEM III/A	35-64	36-65	0-5
CEM III/B	20-34	66-80	0-5
CEM III/C	5-19	81-95	0-5

Table 3.3 Chemical compositions of Portland cement (CEM I 42.5N), limestone powder, BFS and BFS cement (CEM III/B 42.5N) (weight %).

Compound	Portland cement	Limestone powder	BFS	BFS cement
CaO	64.1	-	40.8	47
SiO_2	20.1	0.3	35.4	30
Al_2O_3	4.8	0.1	13	9
Fe_2O_3	3.2	0.1	0.5	1
MgO	-	0.2	8.0	-
K_2O	0.5	-	0.5	-
Na_2O	0.3	-	0.2	-
SO_3	2.7	-	0.1	3.2
$CaCO_3$	-	98.8	-	-
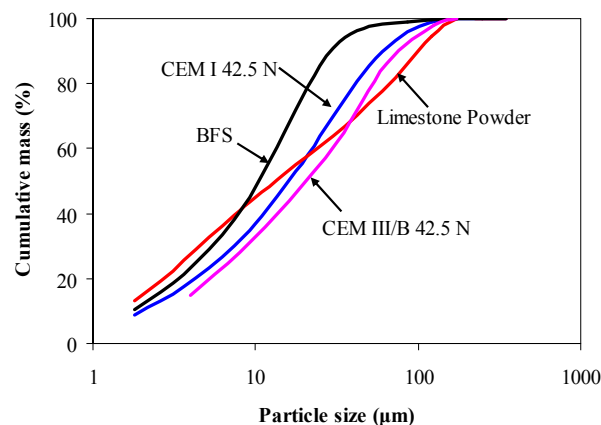
Figure 3.4 Particle size distribution of Portland cement (CEM I 42.5N), limestone powder, BFS and BFS cement (CEM III/B 42.5N), measured with laser-diffraction technique.

3.3.2 ECC mix design

When blended with Portland cement, limestone powder and fine silica sand behave as inert materials. BFS and fly ash have a potential of pozzolanic reaction and these reactions need to be activated by the hydration products of Portland cement. In ECC mix design, Portland cement and BFS are considered as cementitious materials, and limestone powder is considered as inert filler material. The mix composition of a standard ECC mixture M45 as shown in Table 3.1 [Qian and Li 2007] is used as a reference in the ECC mix design. Table 3.4 gives the mix composition of the ECC made of Portland cement, limestone powder and BFS. M1 is a trial mixture, and its mix composition came from that of M45 by replacing fine silica sand and fly ash by limestone powder and BFS, respectively. A higher water-to-powder ratio was used because of the higher water demand of BFS compared with fly ash. The mixtures M1-4 were used to investigate the effect of limestone powder and to find out the optimum limestone powder content. Limestone powder with a mean particle size of 13.4 μm

had a smaller particle size than the fine silica sand used in M45 with a mean particle size of 110 μm [Yang et al. 2007]. The small particle of limestone powder results in a decrease in the matrix toughness, which is conducive to the ductility of ECC [Li and Leung 1992]. Increasing limestone powder contents were used in the mixtures M1-4. In order to obtain good workability, the superplasticizer content was slightly adjusted. Among these four mixtures, M3, in which the cementitious materials-to-limestone powder ratio was 1.1, exhibited the highest tensile strain capacity. Then, the cementitious materials-to-limestone powder ratio of 1.0 was used in M5 and M6. In these two mixtures, Portland cement-to-BFS (PC/BFS) ratios of 1.0 and 0.43 were used, since these two ratios match the typical values in BFS cements CEM III/A and CEM III/B, respectively.

The experimental study revealed that among the above six mixtures, M6, in which the PC/BFS ratio was 0.43, has the highest tensile strain capacity. Therefore, BFS cement CEM III/B 42.5N was used to replace Portland cement CEM I 42.5N and BFS in M6. Table 3.5 gives the mix composition of the ECC mixture mixed with CEM III/B 42.5N and limestone powder.

In all mixtures, the PVA fiber content was 2% by volume. The PVA fiber had a length of 8 mm and a diameter of 40 μm. The tensile strength of the PVA fiber was 1600 MPa and the density was 1300 kg/m^3. The fiber surface was coated with 1.2% oil by weight to reduce the chemical and friction bond between the PVA fiber and the matrix.

Table 3.4 Mix composition of the ECC with Portland cement, limestone powder and BFS.

Mixture	LP[#]/PC[*]	BFS/PC	PC [kg/m^3]	LP [kg/m^3]	BFS [kg/m^3]	Water [kg/m^3]	SP[$] [kg/m^3]	PVA fiber [kg/m^3]
M1	0.8	1.2	534	427	640	416	13.3	26
M2	1.5	1.2	431	646	517	414	9.9	26
M3	2	1.2	379	758	455	414	6.8	26
M4	3	1.2	305	914	366	412	6.1	26
M5	2	1	398	795	398	414	7.2	26
M6	3.3	2.3	237	790	553	411	7.9	26

[#] LP represents limestone powder.
[*] PC represents Portland cement CEM I 42.5N.
[$] SP represents superplasticizer.

Table 3.5 Mix composition of the ECC with BFS cement and limestone powder.

LP[#]/BFSC[*]	BFSC [kg/m^3]	LP [kg/m^3]	Water [kg/m^3]	SP[$] [kg/m^3]	PVA fiber [kg/m^3]
1	790	790	411	7.9	26

[#] LP represents limestone powder.
[*] BFSC represents BFS cement CEM III/B 42.5N.
[$] SP represents superplasticizer.

3.3.3   Mixing and Curing

Cement, limestone powder and BFS were first mixed with a HOBART® mixer for 1 minute. Then water and superplasticizer were added and mixed for 3 minutes. Finally, PVA fibers were added and mixed for another 2 minutes.

The fresh ECC was cast into six coupon specimens with the dimension of $240 \times 60 \times 10$ mm^3 and a prism with the dimension of $160 \times 40 \times 40$ mm^3. After 1 day curing in moulds covered with plastic paper, the specimens were demoulded and cured under sealed condition at a temperature of 20°C for 27 days.

3.4   Experiments

3.4.1   Compressive test

After 28 days of curing, the prism specimens were sawn into three cubes with the dimension of $40 \times 40 \times 40$ mm^3. These cubes were used for compressive tests. Three parallel measurements were done for each mixture.

3.4.2   Four-point bending test

After 28-day curing, the coupon specimens were sawn into four pieces with the dimension of $120 \times 30 \times 10$ mm^3. These specimens were used in four-point bending test. The support span of the four-point bending test set-up was 110 mm, and the load span was 30 mm as shown in Figure 3.5. Two LVDTs were fixed on both sides of the test set-up to measure the flexural deflection of the specimen. The test was conducted deformation controlled at a speed of 0.01 mm/s. Three measurements were done for each mixture.
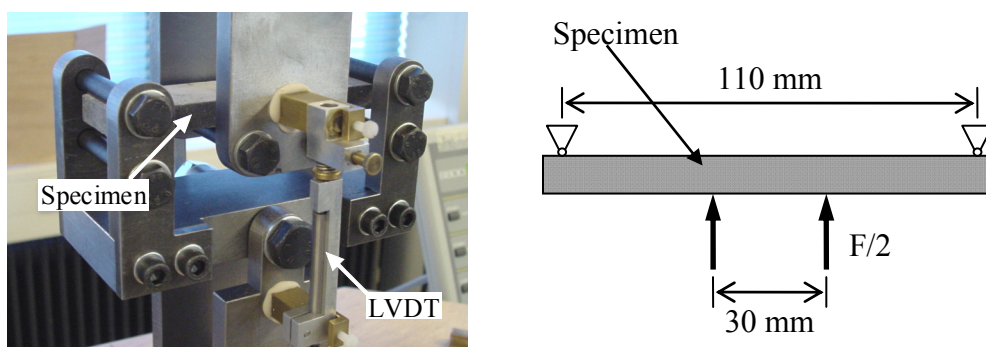
Figure 3.5 Four-point bending test set-up.

3.4.3   Uniaxial tensile test

Figure 3.6 shows the uniaxial tensile test set-up designed for ultra ductile fiber reinforced concrete, such as ECC. The specimen is clamped by four steel plates, one pair at each end. Each pair of steel plates is tightened with four bolts. Two pairs of steel plates are fixed on the loading device with four steel bars, two for each pair. Between the pairs of steel plates and the loading device, there is a ±3 mm space. It is used to diminish the eccentricity in the direction

perpendicular to the plate of the specimen by moving the steel plates along the steel bar. The tensile force is transferred to the specimen by the friction force between the steel plates and the specimen. Four aluminum plates, 1 mm thick each, are glued on both sides of the ends of specimen in order to improve the friction force, to ensure the clamped area work together and to prevent the local damage on the specimen caused by high clamping force.
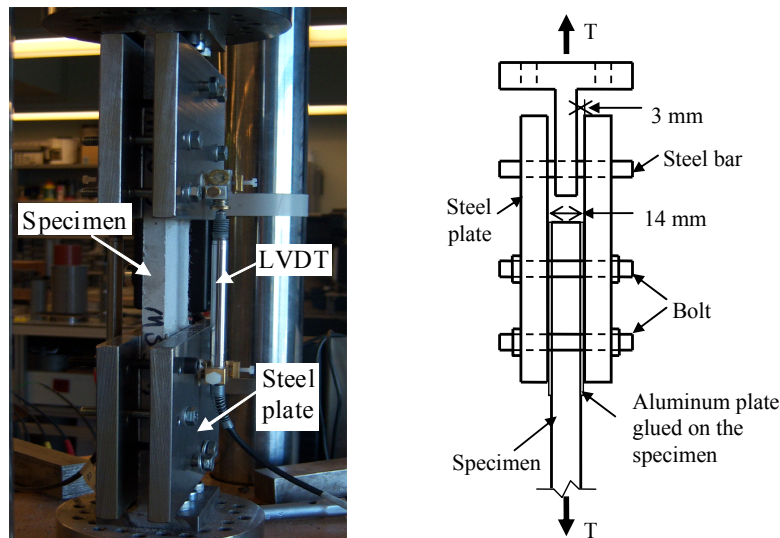
Figure 3.6 Uniaxial tensile test set-up.

The coupon specimens were sanded to obtain a flat surface with a higher bond strength with the aluminum plates. After cleaning the specimen surface and the aluminum plate with acetone, the aluminum plates were glued on the specimen. The glue was cured for 1 day before testing. Before placing the specimen in the test set-up, two pairs of steel plates were connected to the bottom and the top parts of loading device, respectively. The lower end of the specimen was first clamped with the steel plates by tightening four bolts. Then the upper end of the specimen was clamped with the other pair of steel plates. Finally, two LVDTs were mounted on both sides of the specimen. The testing gauge length was 70 mm. The tests were conducted under deformation control with a loading speed of 0.005 mm/s. Five specimens were tested for each mixture.

3.4.4   Loaded crack width measurement

The crack width was measured on the coupon specimens after the uniaxial tensile test. Three lines parallel to the loading direction were drawn on the specimen. These lines were uniformly spaced on the width of specimen as shown in Figure 3.7. Under the microscope, the number of cracks crossing each line was counted. The average crack number of each specimen was calculated by averaging the number of cracks crossing these three lines. Since ECC deforms several hundred times larger than the matrix, the tensile deformation of the matrix contributes little to the overall tensile deformation of ECC. Therefore, the overall tensile deformation of ECC can be related only to the crack opening. Accordingly, the average crack width w can be calculated by dividing the measured tensile deformation at the peak load Δl by the average crack number N, viz:

$$w = \frac{\Delta l}{N} \qquad (3.5)$$

The calculated crack width is the crack width under tensile load. This is different from the residual crack width in the previous studies [Yang et al. 2007], in which the crack width is measured after partial crack closure after unloading. According to Yang et al. [2007], the crack width under tensile load is roughly twice of the residual crack width.
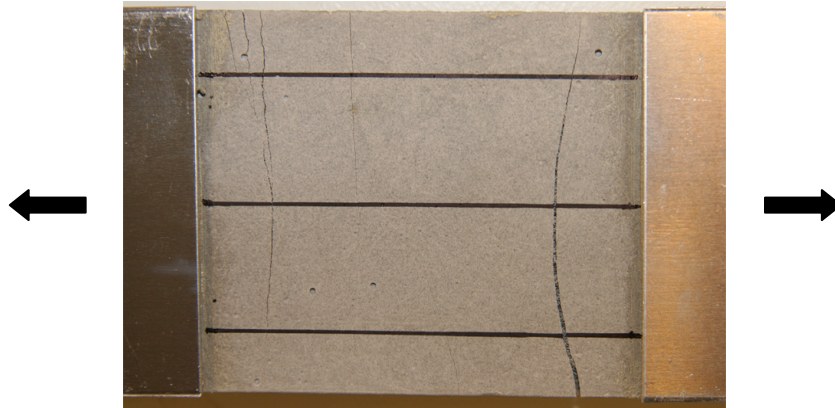

Figure 3.7 Illustration of the measurement of the crack width under tensile load.

3.4.5   ESEM observation

The ESEM study was conducted to investigate the microstructural properties of ECC. After the four-point bending test, the specimens were freeze-dried. The dried specimens were placed in a vacuum chamber and impregnated with a low-viscosity epoxy. After the hardening of epoxy, the specimens were carefully ground on the middle-speed lap wheel with p120, p220, p320, p500, p1200 and p4000 sand papers and were then polished on the lap wheel with 6, 3, 1 and 0.25 μm diamond pastes. The final polishing was done with a low-relief polishing cloth. Each grinding and polishing step took 2 minutes. The images were taken on the prepared section using a backscattered electron (BSE) detector with vapor mode. The acceleration voltage of 20 kV was used in order to obtain a high contrast image.

3.5   Results and Discussion

In this section, the experimental results of compressive strength test, four-point bending test, uniaxial tensile test and the measurement of crack width under tensile load are presented. Based on the experimental results, the factors influencing the properties of different ECC mixtures are discussed.

3.5.1   ECC mixed with Portland cement, limestone powder and BFS

3.5.1.1 Compressive strength
The compressive strength of ECC at 28 days is summarized in Figure 3.8. The increasing limestone powder content results in a decrease in the compressive strength in M1-4. Comparing the compressive strength of mixtures M5 and M6, the high cement replacement by

BFS causes little decrease in the compressive strength. The mixtures M3, M5 and M6 with good tensile property all show compressive strengths higher than 38 MPa. This value can fulfill engineering requirements in most projects.
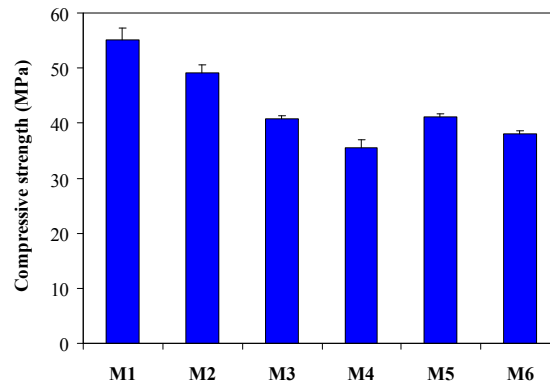
Figure 3.8 Compressive strength of ECC at 28 days.

3.5.1.2 Flexural and uniaxial tensile performance

Under four-point bending load and uniaxial tensile load, the mixtures M1-6 all exhibit multiple-cracking behavior as shown in Figure 3.9. Among the six mixtures, M6 shows the highest flexural deflection capacity and tensile strain capacity. M6 has the lowest cement content of 15% of powder materials by weight, which is more or less the same as the cement content in normal concrete. Figure 3.10 shows the flexural load-deflection curves and the tensile stress-strain curves of M6. In the flexural load-deflection curves, the maximum flexural stress is defined as the flexural strength, and the corresponding deflection is defined as the flexural deflection capacity. In the tensile stress-strain curves, the stress at the first drop associated with the first cracking is defined as the first cracking strength. Similarly, the maximum stress is defined as the ultimate tensile strength, and the corresponding strain is defined as the tensile strain capacity. The flexural deflection capacity and tensile strain capacity of M6 can be calculated by averaging the results of three four-point bending measurements and four uniaxial tensile measurements, and they are 3.9 mm and 3.3%, respectively. Although M1 exhibits the smallest deformation capacity, its tensile strain capacity is already as high as 1.7%, which is much higher than that of conventional concrete (about 0.01%).
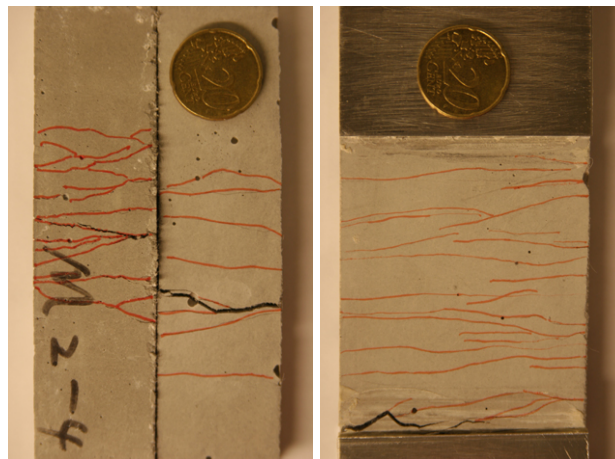
Figure 3.9 Multiple cracking of the specimens under four-point bending load (left) or uniaxial tensile load (right).
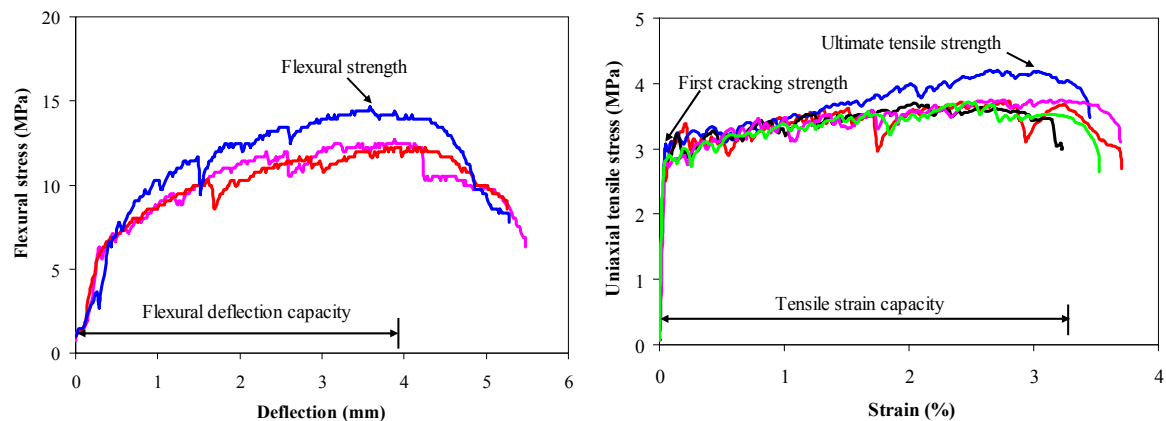
Figure 3.10 Flexural load-deflection curves and tensile stress-strain curves of M6 with the average flexural deflection capacity of 3.9 mm and the average tensile strain capacity of 3.3%.

The flexural deflection capacity and the tensile strain capacity of ECC with different limestone powder contents and BFS contents are summarized in Figure 3.11. The results of the four-point bending test and the uniaxial tensile test indicate a linear correlation between the flexural deflection capacity and the tensile strain capacity as shown in Figure 3.12. This linear correlation between the flexural deflection capacity and the tensile strain capacity agrees with the ECC flexural beam analysis [Maalej and Li 1994, Qian and Li 2007]. For these six mixtures (M1-6) mixed and cured at different times, the standard deviations of the tensile strain capacity within each mix design are lower than 0.6%, which is less than 20% of the tensile strain capacity. It can be concluded that the material properties of ECC with limestone powder and BFS are relatively robust.
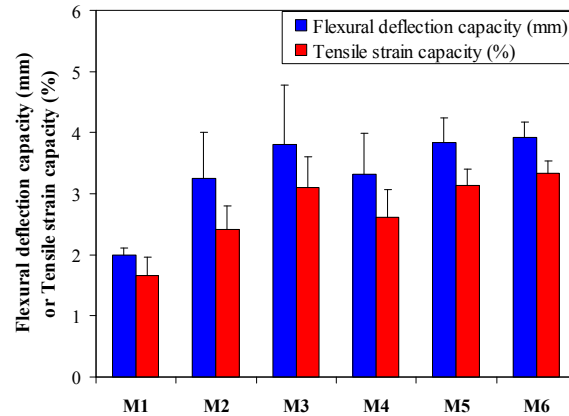
Figure 3.11 Flexural deflection capacity and tensile strain capacity of ECC at 28 days.
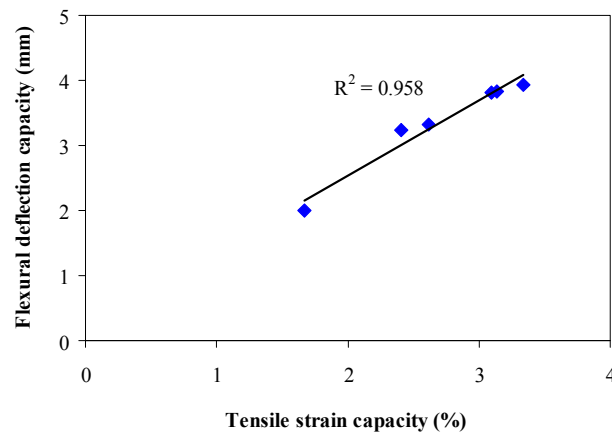
Figure 3.12 Correlation between the tensile strain capacity and the flexural deflection capacity.

   As the limestone powder content increases, the flexural deflection capacity and the tensile strain capacity first increase (from M1 to M3) and then decrease (from M3 to M4). Since the limestone powder behaves as inert filler materials, the addition of limestone powder results in a lower tensile strength of the matrix. Besides, due to the low hardness of limestone powder, the large limestone powder particle is easy to break, and the crack crosses the big limestone particles (Figure 3.13). Therefore, the addition of the limestone powder results in the decrease in the toughness of the matrix, reflected by the decrease in the first cracking strength as shown in Figure 3.14. The decreasing matrix toughness is conducive to the high ductility of the ECC composite [Li and Leung 1992]. On the other hand, the addition of too much limestone powder leads to a weak fiber-matrix interface. Li [2003] suggested that excessively weak interface has a negative effect on the strain-hardening behavior of ECC. The experimental results reveal that M3 has the optimum limestone powder content in terms of deformation capacity.
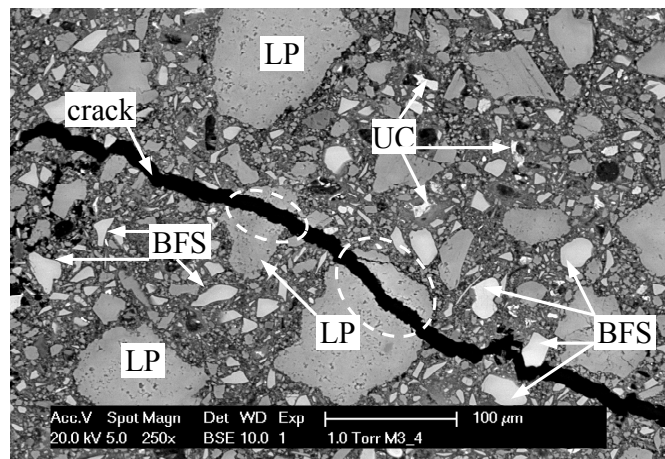
Figure 3.13 BSE image of M3 at 28 days shows a crack crossing the limestone powder particles, under bending. Here, LP indicates limestone powder particle and UC indicates the unhydrate cement particles.
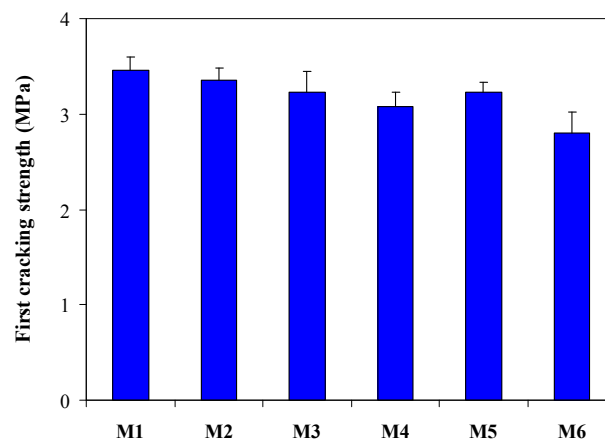
Figure 3.14 First cracking strength of ECC from uniaxial tensile test at 28 days.

As shown in Figure 3.11, both M5 and M6 show a tensile strain capacity higher than 3%. The decrease in the PC/BFS ratio results in the increase in the flexural deflection capacity and in the increase in the tensile strain capacity. This can be attributed to the lower matrix toughness and the better fiber-matrix interface due to the addition of BFS [Kim et al. 2007]. The replacement of Portland cement by BFS lowers the overall degree of hydration of cement paste [Zhou 2006]. In mixture M5 and M6, as the BFS content increases, the first cracking strength decreases as shown in Figure 3.14, and therefore the toughness of the matrix decreases. Under ESEM, a dense matrix-fiber interface is observed as shown in Figure 3.15. The reason is that the relatively small BFS particles improve the particle packing in the fiber-matrix interface. In addition, BFS reacts with calcium hydroxide to produce calcium silicate hydrate and little calcium hydroxide exists in the interface. Since the calcium silicate hydrate has a relatively denser microstructure than the calcium hydroxide, the transformation of calcium hydration to calcium silicate hydrate could increase the friction bond between fiber and matrix.
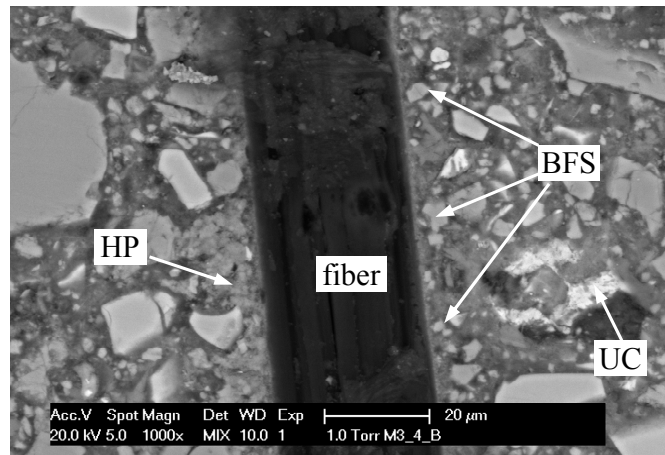
Figure 3.15 BSE image showing the fiber-matrix interface. Here, HP indicates hydration products and UC indicates the anhydrate cement particles.

The multiple cracking behavior of ECC results from the interaction among fiber, matrix and interface. One of the criteria for having the multiple-cracking behavior is that the matrix tensile strength must be lower than the fiber bridging strength across the crack plane [Li 2003]. Consequently, after the matrix cracks, the fibers can carry the increasing tensile load, which generates new cracks. When the tensile load exceeds the minimum fiber bridging strength in ECC, the fibers in this crack plane are pulled out of the matrix or rupture, and ECC fails. The minimum fiber bridging strength is recorded as the ultimate tensile strength in the uniaxial tensile test. Obviously, a larger margin between the ultimate tensile strength and the first cracking strength gives the matrix more chances to crack and results in a higher tensile strain capacity. The experimental results confirm this, and the tensile strain capacity shows a strong relation with the margin between the ultimate tensile strength and the first cracking strength as shown in Figure 3.16.

Figure 3.16 Correlation between the tensile strain capacity and the margin between the ultimate tensile strength and the first cracking strength.

3.5.1.3 Loaded crack width

The loaded crack width of ECC determines the transport properties in the loaded state, and it is, therefore, a crucial parameter for the durability of ECC. Figure 3.17 shows the loaded crack width of the ECC with limestone powder and BFS. All mixtures show a loaded crack width smaller than 100 μm. Among six mixtures M6 shows a very tight crack width of 57 μm. It can be expected that M6 has relatively low water permeability and good durability.
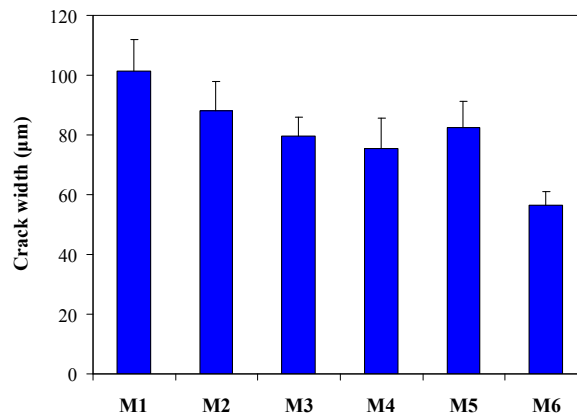
Figure 3.17 Loaded crack width of ECC at 28 days.

The increasing limestone powder and BFS contents lead to a smaller loaded crack width. As shown in Figure 3.4, limestone powder and BFS have higher contents of small particles (ranging from 1 μm to 10 μm) than Portland cement. The higher contents of small particles result in a better packing at the fiber-matrix interface and in a better interfacial property [Yang et al. 2007]. For M4, the low ultimate tensile strength results in a small fiber slipping out of the matrix. As a result, the crack width is small.

3.5.2 ECC mixed with BFS cement and limestone powder

BFS cement CEM III/B 42.5N was used to produce ECC with limestone powder. Table 3.6 gives the results of BFS cement-ECC compared with M6. At 28 days, the properties of BFS cement-ECC show a good agreement with those of M6, except the loaded crack width. The larger loaded crack width may be because of the difference between particle size distributions of BFS in the interground CEM III/B 42.5N and the blended M6 [Oner 2000].

Table 3.6 Properties of BFS cement-ECC and M6 (Portland cement + BFS).

Mixture	Compressive strength [MPa]	Ultimate tensile strength [MPa]	Tensile strain capacity [%]	Loaded crack width [μm]
BFS cement-ECC	40	4.0	3.1	76
M6 (PC + BFS)	38	4.0	3.3	57

3.6   Conclusions

A set of new ECC was developed with Portland cement Portland cement (CEM I 42.5N), BFS and limestone powder. The mix composition was designed experimentally by adjusting the amount of limestone powder and BFS, accompanied by four-point bending test and uniaxial tensile test. The loaded crack width and the compressive strength were also measured. ESEM study was used to investigate the microstructure of ECC. Furthermore, a ECC mixture with BFS cement and limestone powder was proposed and evaluated experimentally in order to reduce the matrix materials from three to two and to simplify the mixing of ECC. The following conclusions can be drawn from the experimental study:

- Under four-point bending load and uniaxial tensile load, all specimens exhibit multiple-cracking behavior. For the six mixtures with different limestone powder and BFS contents, the flexural deflection capacity ranges from 2.0 mm to 3.9 mm, and the tensile strain capacity ranges from 1.7% to 3.3% at 28 days. It is found that there is a stron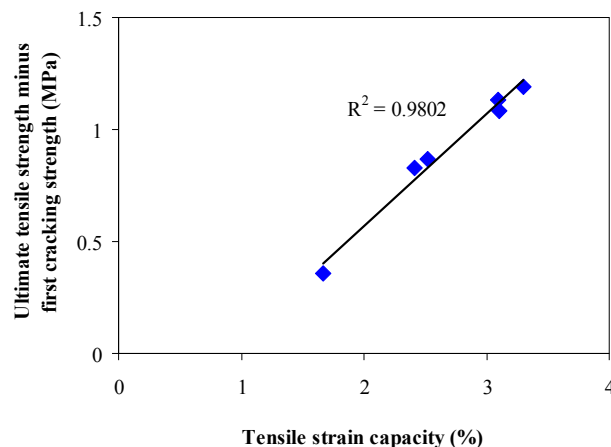g correlation between the tensile strain capacity and the margin between the ultimate tensile strength and the first cracking strength. As the margin increases the tensile strain capacity increases.
- As the limestone powder content increases, the flexural deflection capacity and the tensile strain capacity first increase and then decrease. With the same limestone powder content, as the cement replacement with BFS increases from 50% to 70%, the flexural deflection capacity and the tensile strain capacity increase.
- The increasing limestone powder and BFS contents lead to a smaller loaded crack width. All mixtures show a loaded crack width smaller than 100 μm.
- BFS cement-ECC was also developed with BFS cement (CEM III/B 42.5N) and limestone powder. BFS cement-ECC shows properties in agreement with the ECC made of Portland cement, limestone powder and BFS.

The experimental study results in an ECC mix composition with a Portland cement content as low as 15% of powder materials by weight. This mixture, at 28 days, shows high tensile strain capacity of 3.3%, a moderate compressive strength of 38 MPa and a tight crack width of 57 μm. It can be expected that this mixture might be a durable repair material, no matter under mechanical load or environmental load. The performance of this mixture in concrete repairs will be investigated in Chapter 5. Based on the measured chloride penetration profile, the service life of concrete repairs will be predicted.

Chapter 4

Performance of the ECC Repair System Subjected to Differential Shrinkage

---

4.1   Introduction

In this chapter, the performance of the ECC repair system is investigated compared to a fiber-reinforced polymer-modified (FRPM) mortar, which is one of the most widely used repair materials in the Netherlands. ECC and FRPM mortar were cast on concrete beams. The surface cracking in the repair materials and the delamination of the interface caused by the differential shrinkage between repair material and concrete substrate were monitored. The properties of the two repair materials, including free shrinkage and repair-substrate bond strength, were also measured. In order to interpret the behavior of the repair materials, the analytical calculations discussed in Chapter 2 were used to calculate the stresses induced by differential volume changes with the measured material properties as inputs.

Further, the durability of the repair systems is investigated by measuring the chloride penetration profile in the repair system. The chloride penetration profile in the cracked repair materials were measured by rapid chloride migration (RCM) test. Based on the experimental data, the chloride penetration coefficient was calculated. The pore structure of the repair materials was studied by mercury intrusion porosimetry (MIP). The service life of concrete repairs in land and marine environments was predicted using the DuraCrete model.

4.2   Materials and Methods

4.2.1   Substrate concrete

The substrate concrete was a three-year-old concrete. The binder was blast furnace slag cement CEM III/B 42.5 LH with a cement amount of 350 kg/m^3 and a water-to-cement ratio of 0.48. The substrate concrete was steel fiber reinforced concrete. The compressive strength and Young's modulus, given by the supplier, were 88.9 MPa and 36.3 GPa, respectively.

4.2.2   Repair materials

The newly developed ECC mixture M6 was used as a repair material in this chapter. The mix proportion of M6 is given in Table 3.4, and the ECC mixing procedure is presented in detail in section 4.3.3. The FRPM mortar is one of the most widely used repair materials in the Netherlands. The water-to-solid ratio of the FRPM mortar was 0.14. Compressive strength test (see section 4.4.1) and uniaxial tensile test (see section 4.4.3) were used to investigate the

mechanical properties of these two repair materials at the ages of 3, 7, 28 and 90 days. The mechanical properties of the two repair materials are given in Table 4.1.

Table 4.1 Mechanical properties of ECC and FRPM mortar.

Repair material	Age [days]	Compressive strength f_c [MPa][*]	Ultimate tensile strength f_t [MPa][#]	Tensile strain capacity ε_u [%][#]	Young's modulus E [GPa][#]
ECC	3	14.3 ± 0.1	3.7 ± 0.2	5.1 ± 0.7	9.9 ± 1.2
	7	23.9 ± 1.5	4.2 ± 0.4	3.6 ± 0.2	14.9 ± 0.6
	28	40.1 ± 1.2	4.6 ± 0.5	3.1 ± 0.7	18.5 ± 0.9
	90	50.3 ± 0.8	4.8 ± 0.3	2.6 ± 0.3	20.8 ± 1.9
FRPM mortar	3	58.2 ± 0.4	3.9 ± 0.4	< 0.03	13.9 ± 1.5
	7	69.0 ± 1.0	-	-	-
	28	76.8 ± 0.6	5.6 ± 0.8	< 0.03	26.4 ± 1.6
	90	82.3 ± 1.2	-	-	-

[*] Compressive strength was obtained from averaging the results of three measurements on cubic specimens with a dimension of $40 \times 40 \times 40$ mm^3, as discussed in Section 4.4.1.
[#] Ultimate tensile strength, tensile strain capacity and Young's modulus were obtained from the uniaxial tensile test, as discussed in Section 4.4.3.

4.2.3   Surface cracking and interface delamination due to differential shrinkage

The surface cracking and interface delamination of composite beams due to differential shrinkage were investigated experimentally. As shown in Figure 4.1, the composite beams consisted of a layer of repair material bonded on top of concrete substrate. The concrete substrate had a dimension of $1000 \times 200 \times 200$ mm^3. The thickness of the repair material was 50 mm.
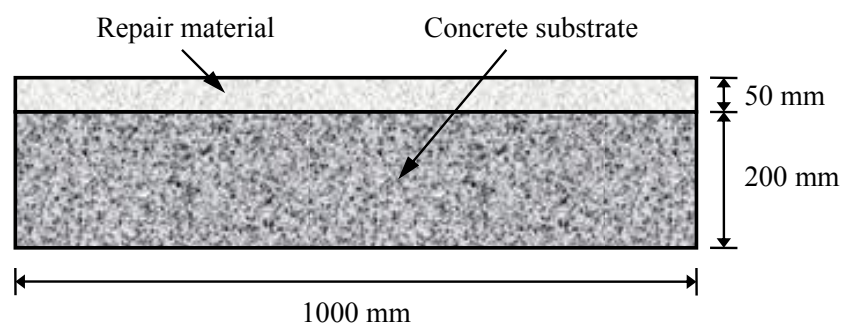
Figure 4.1 Composite beam with a layer of repair material and a layer of concrete substrate.

Before placing the repair materials, the surface of the concrete substrate was grit-blasted. The injecting air pressure was 0.8 MPa and the blasting speed was 10 cm^2/min. After the concrete substrates were moist-cured for 7 days, the substrate surfaces were dried and cleaned with high-pressure air, aiming at a saturated substrate with a dry and clean surface. After placing the repair materials, the fresh repair materials were vibrated by a vibrating needle to remove air bubbles especially at the interface, which are detrimental to interfacial bonding. Then, the repair materials were covered with plastic sheet and cured for 24 hours. After

demolding, the composite beams were moved into a room with ambient conditions of 20°C and 50% RH. Under these ambient conditions, the shrinkage of the repair materials developed and caused the debonding of the repair material from the concrete substrate and the cracking of the repair material.

The interface delamination was measured with two LVDTs, which were attached on the ends of the composite beams as shown in Figure 4.2. The strain gauges and LVDTs were connected to a computer and the data were recorded automatically. The surface cracking on the repair materials was observed with a portable microscope. The number of cracks and the crack width were measured manually. The measurements on the composite beams lasted for 90 days.

Figure 4.2 LVDT measuring the interface delamination.

4.2.4   Free shrinkage of repair materials

The free shrinkage of the repair materials was measured according to European standard EN 12617-4 [2002]. The fresh repair materials were cast into three prisms with a dimension of $160 \times 40 \times 40$ mm^3. After 24-hour sealed curing under a temperature of 20°C, the specimens were exposed to a temperature of 20°C and RH of 50%, the same exposure conditions as that of the composite beams. The length change of the specimens was measured with a length gauge from 1 to 90 days. The free shrinkage was calculated by averaging the results of three measurements of each repair material.

4.2.5   Tensile bond strength test

The bond strength of the repair-substrate interface was measured by a direct tensile test according to European standard EN 14488-4 [2002]. The tested specimens were layered cylinders with a diameter of 60 mm. The thicknesses of the repair material and the concrete substrate were both 60 mm. The substrate preparation and the specimen curing condition were the same as those of the composite beams. After 28-day curing, the top and bottom surfaces of the specimens were sanded and cleaned with acetone, aiming at a good bond between the specimens and the steel dollies. The specimens were then glued on the steel dollies, which were fixed on the loading device, as shown in Figure 4.3. After the glue hardened, an increasing tensile load was applied on the specimens, and the loading speed was controlled to be 0.05 MPa/s. The tensile load and the corresponding displacement were recorded by computer automatically. The tensile bond strength was calculated as the maximum load divided by the cross-sectional area. Three parallel measurements were done.
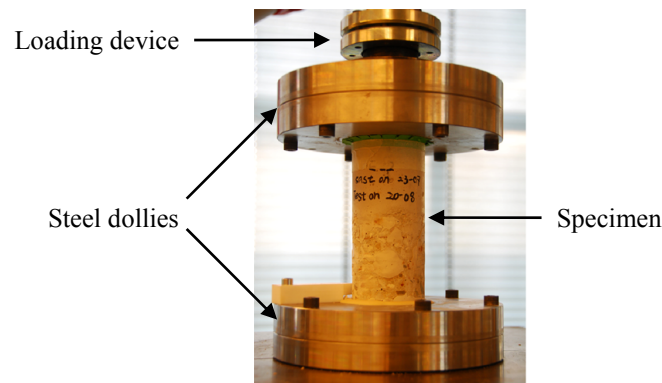
Figure 4.3 Test set-up of direct tensile tests.

4.2.6   RCM test

From literature, the method to investigate the durability and service life of cracked concrete can not be found, and most methods focus on the uncracked concrete. In this study, the RCM test used for uncracked concrete is, therefore, used to investigate the resistance against chloride penetration in the cracked repair material. The RCM test was carried out according to the Nordic standard NT BUILD 492 [1999].

After 90-day subjected to differential shrinkage, three cylinders with a diameter of 100 mm were drilled out of each composite beam at the locations with cracks. As shown in Figure 4.4, the specimens consist of a layer of repair material with a thickness of 50 mm and a layer of concrete substrate with a thickness of 20 mm. More than 4 cracks were observed in each ECC specimen and only one crack in each FRPM mortar specimen. The surface crack width was measured. The specimens were then saturated with calcium hydroxide ($Ca(OH)_2$) solution for 24 hours.

Figure 4.4 FRPM specimen for RCM tests.

After $Ca(OH)_2$ solution saturation, the specimens were put in a rubber sleeve and fastened with two stainless steel clamps to ensure that no water goes along the edge of the specimens, as shown in Figure 4.5. The RCM test set-up is illustrated in Figure 4.6. The substrate surface was immersed in the anolyte solution of 0.3 M NaOH and the cracked repair surface was immersed in the catholyte solution of 10% NaCl. A voltage of 60 V was then applied on the anolyte solution and catholyte solution for 3 days. The room temperature during testing was $24.6 \pm 0.2°C$.
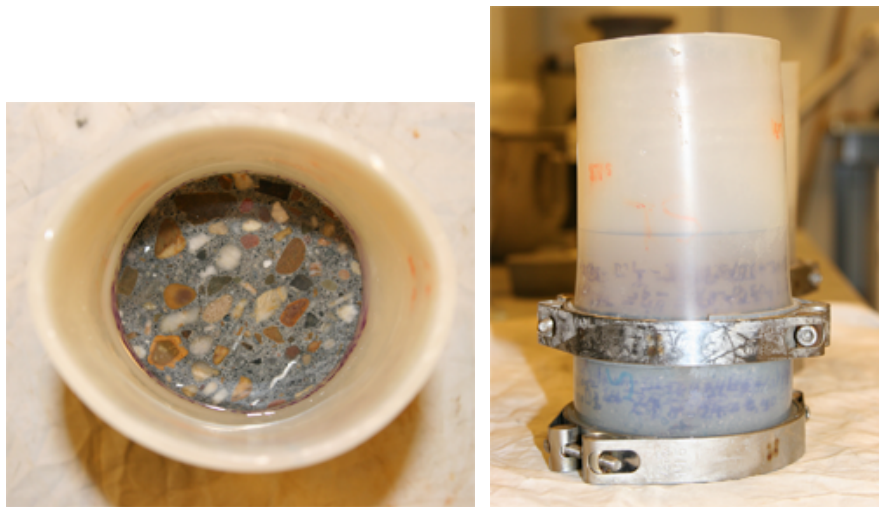
Figure 4.5 Specimen sealed with rubber sleeve and stainless steel clamps.

a. Rubber sleeve
b. Solution of 0.3 M NaOH
c. Anode: stainless steel
d. Concrete specimen
e. Solution of 10% NaCl
f. Cathode: stainless steel
g. Direction of chloride penetration
h. Plastic support
i. Container
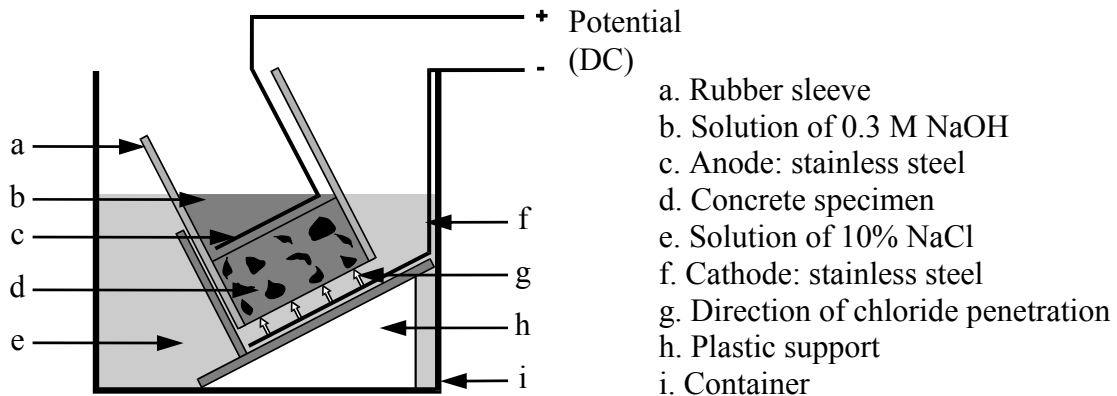
Figure 4.6 RCM test set-up.

After a 3-day exposure to chloride solution, the rubber sleeve and stainless steel clamps were removed, and the specimens were split into two pieces perpendicularly to the surface cracks. A 0.1 M $AgNO_3$ solution was sprayed on the freshly split sections. $AgNO_3$ reacts with NaCl and produces AgCl. AgCl appears white and indicates chloride penetration depth. After around 15 minutes of spraying $AgNO_3$ solution, the penetration depth was measured at 7 locations on every section. The average penetration depth was calculated by averaging the measured values from each specimen. The maximum penetration depth in the specimens was also measured.

4.2.7   MIP

In order to interpret chloride transport properties of the repair materials, MIP tests were conducted to investigate the pore structure of the repair materials. At the age of 90 days, the repair materials were sawn into pieces of 0.5 cm^3 and were then dried by freeze-drying method. The samples were quickly frozen by immersing in liquid nitrogen for 5 minutes. Then, they were moved into a freeze-dryer with temperature of -24ºC and vacuum at 0.1 Pa. The sample was considered to be dry, until the water loss was below 0.01%/day. This period lasted for 10-20 days depending on w/c ratio and curing age of the samples. Ye [2003]

suggested that this method caused less damage on the pore structure of cement paste compared with the other common drying methods, i.e. oven drying and vacuum drying.

The dried samples with a known weight were put into a penetrometer. The penetrometer was closed with a steel cap. After the weight of the penetrometer with the samples was measured, it was placed into a low-pressure chamber. The chamber was evacuated to a pressure of 50 μmHg, and mercury then filled the penetrometer. Pressure was gradually increased from 0.004 MPa to 0.15 MPa. The penetrometer was removed from the low-pressure chamber and was then weighted. After the penetrometer was placed in a high-pressure chamber, pressure was gradually increased to the maximum value of 200 MPa. In total, 125 pressure steps in logarithmic distribution were taken. Equilibrating time in every step was 30 seconds.

4.3   Mechanical performance of repair materials subjected to differential shrinkage

4.3.1   Experimental results

Figure 4.7 shows the free shrinkages of repair materials in the first 90 days. In the curves, each value represents the average shrinkage of three measurements. Because of the high cementitious material content and the absence of aggregates, ECC shows a free shrinkage about 2 times higher than RFPM mortar in the first 90 days.
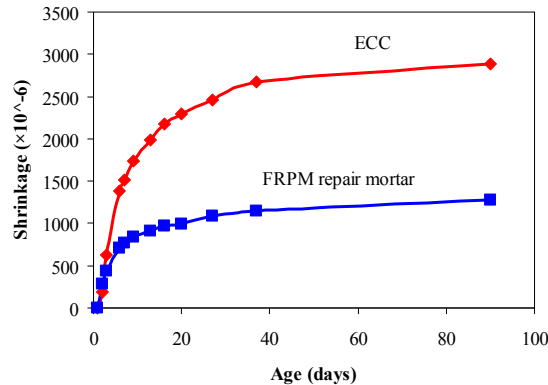
Figure 4.7 Free shrinkages of repair materials in the first 90 days.

Table 4.2 gives the measured bond strength between repair material and concrete substrate. The values were the average of three measurements. The experiment results show that the bond strength of ECC is 47% lower than that of FRPM mortar. ECC specimens all failed in the interface as shown in Figure 4.8 (a), while FRPM mortar specimens all failed in the substrate as shown in Figure 4.8 (b).

Table 4.2 Repair-substrate bond strength of ECC and FRPM mortar.

Repair material	ECC	FRPM mortar
Bond strength [MPa]	1.35 ± 0.10	2.57 ± 0.12
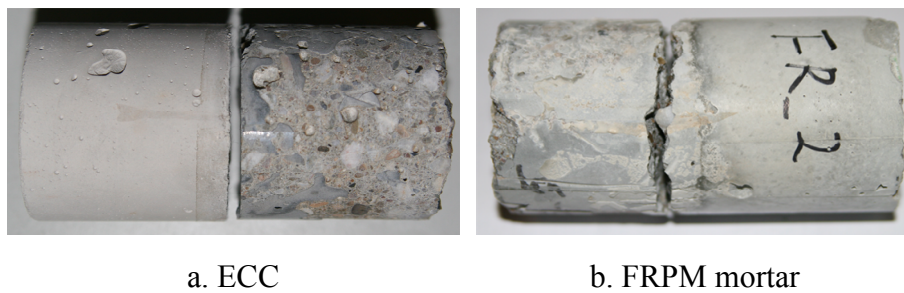
a. ECC   b. FRPM mortar

Figure 4.8 Failure modes of (a) ECC specimen and (b) FRPM mortar specimen under uniaxial tensile load.

The differential shrinkage between repair material and concrete substrate causes the cracking of repair materials and interface debonding in these two beams. The average crack width and crack number measured at the surface of repair materials are shown in Figure 4.9 and Figure 4.10. The first surface crack in ECC was observed after 3 days, while it was after 5 days in FRPM mortar. During 90-day measurement period, ECC exhibits smaller crack width and a larger number of cracks than FRPM mortar. At 90 days, 51 cracks with the width ranging from 10 μm to 60 μm were formed on the surface of ECC, while only 9 cracks with the width ranging from 100 μm to 130 μm were formed on the surface of FRPM mortar. The two repair materials show different crack patterns:

- In ECC, as the curing age increases, the average crack width keeps a value of around 38 μm, except a slight increase in the first 7 days, and the number of cracks however gradually increases from 15 to 51.
- In FRPM mortar, the average crack width gradually increases and the increase is more pronounced in the first month, while no more cracks are formed after 7 days.
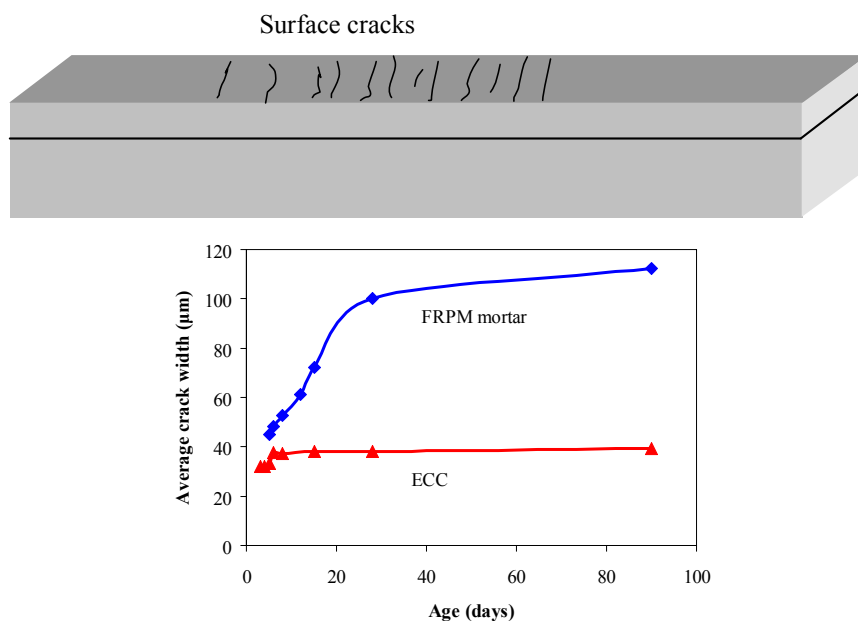
Figure 4.9 Average crack width at the surface of the repair materials.
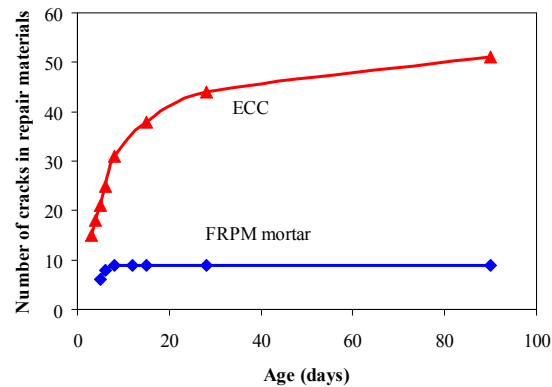
Figure 4.10 Number of cracks on the surface of the repair materials.

The interface delamination of composite beams is illustrated in Figure 4.11 and their values measured by LVDTs are given in Figure 4.12. The ECC composite beam shows an earlier and larger interface delamination than the FRPM mortar composite beam. The interface delamination in the ECC composite beam was initiated at 1.5 days, while the interface delamination in the FRPM mortar beam was initiated at 4 days. After 90 days, the ECC composite beam exhibited an average interface delamination of 0.11 mm, while the FRPM mortar composite beam exhibited an average interface delamination of 0.035 mm. In the ECC composite beam, the interface delamination occurs mainly in the first 20 days and reaches the average value of 0.094 mm, which is 85% of the average interface delamination at 90 days. Afterwards, the interface delamination in the ECC composite beam does not show a big increase. However, in the FRPM mortar composite beam, the differential shrinkage results in a continuous increase in the interface delamination during the 90-day measurement period.

a. ECC   b. FRPM mortar
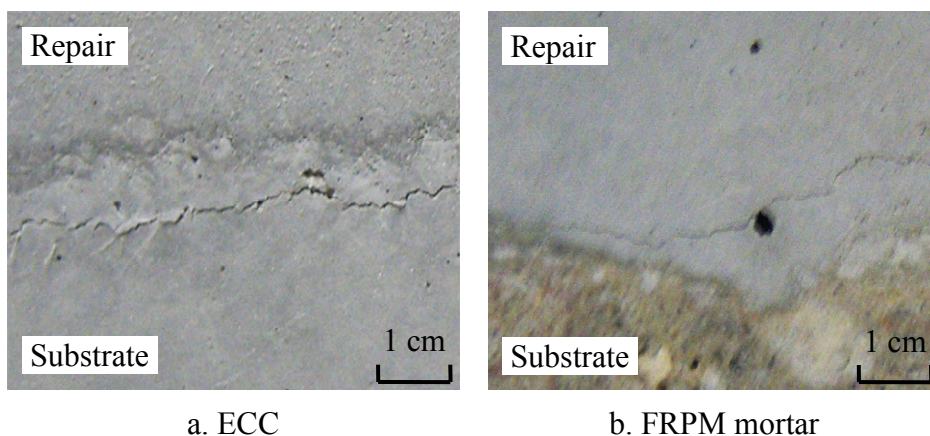
Figure 4.11 Interface delamination in (a) the ECC composite beam and (b) the FRPM mortar composite beam at the age of 90 days.
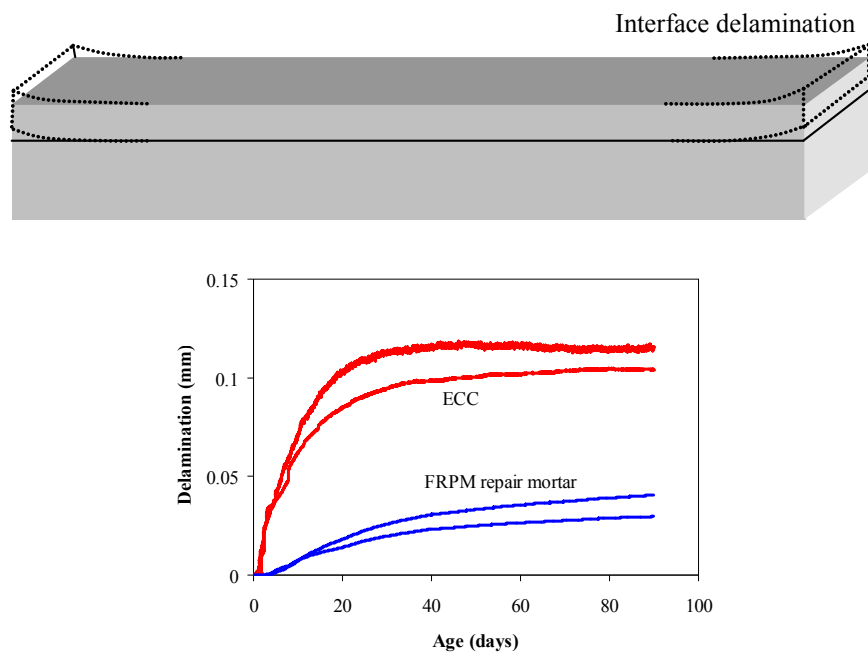
Figure 4.12 Interface delamination at the ends of composite beams in the first 90 days.

4.3.2   Stresses calculated by the analytical tool

The stresses in composite beams are calculated by the analytical tool discussed in Chapter 3. The dimension of composite beams and the properties of substrate and interface are given in Table 4.3. In the ECC composite beam, the tensile stress in the ECC, the shear stress and debonding stress at the interface are calculated using Eq. 3.41-43 with the mechanical properties of ECC given in Table 4.4. Figure 4.13 shows the calculated stresses in the ECC at the age of 28 days. When the shrinkage of ECC is lower than 364×10^{-6}, the tensile stress in ECC is lower than the first cracking strength of 3.6 MPa, and ECC does not crack. When the shrinkage becomes higher than this value, the tensile stress in ECC exceeds the first cracking strength, and ECC starts to crack. The 830% increase in shrinkage only results in a small increase in the critical stresses due to the small post-cracking Young's modulus.

The calculated critical stresses in the ECC composite beam versus the ages of ECC are given in Figure 4.14 and Table 4.5. The stresses increase dramatically in the first 28 days and afterwards the increase becomes relatively small. Although the shrinkage increases by 360% from 3 days to 90 days, the tensile stress in ECC shows an increase of 58%. The shear and debonding stresses at interface show an increase of 12%. In the first 90 days, the calculated tensile stress in ECC is a bit higher than its first cracking strength and quite lower than its ultimate tensile strength. In addition, the utilized tensile strain of ECC is not higher than 0.21%, while ECC has a tensile strain capacity higher than 2.6%. It means that ECC cracks but it is far from the final failure of ECC. ECC can still carry a higher tensile load and large tensile strains. The shear and debonding stresses at the interface range from 0.8 to 1.1 and from 0.8 to 0.9 MPa, respectively. At the early stage these values may already exceed the bond strength, since the bond strengths develop relatively slower. This can cause the debonding of the interface, as observed in experiments. At the later stage, the stresses increase slightly. This explains why the interface delamination was mainly measured at the first 28 days.

Table 4.3 Input values used to calculate stresses in composite beams.

Thickness of repair material h_r [m]	Thickness of substrate h_s [m]	Length of beam L [m]	Young's modulus of substrate E_s [GPa]	Shear stiffness of interface K [N/mm^3]
0.05	0.2	1	36.30	10 [Ackermann 1994]

Table 4.4 Mechanical properties of ECC.

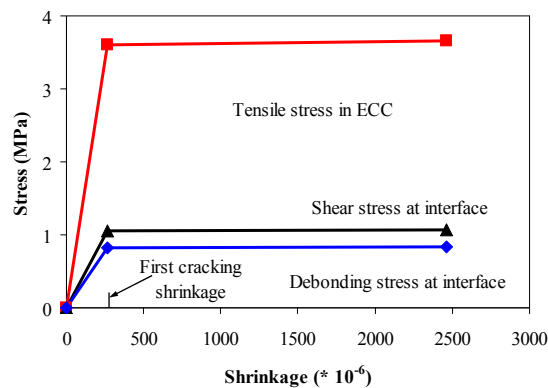| Age [Day]	Shrinkage ε_{sh} [$\times 10^{-6}$]	First cracking strength f_{fc} [MPa]	Ultimate tensile strength f_t [MPa]	Young's modulus before first cracking E_{precr} [GPa]	Young's modulus after first cracking E_{postcr} [GPa]
3	630	2.45	3.68	9.94	0.024
7	1520	3.12	4.23	14.85	0.031
28	2460	3.58	4.59	18.50	0.032
90	2880	3.79	4.85	20.77	0.041

Figure 4.13 Calculated critical stress in the ECC composite beam at the ECC age of 28 days.
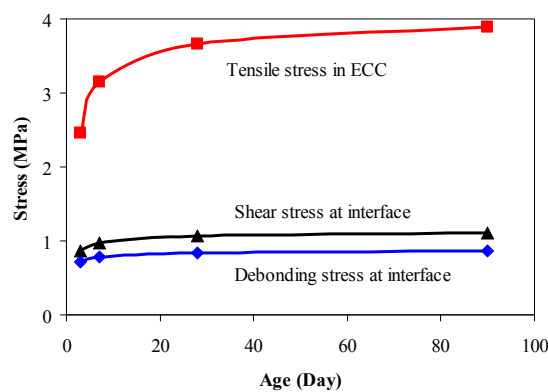

Figure 4.14 Calculated critical stresses in the ECC composite beam.

Table 4.5 Calculated critical stresses in the ECC composite beam.

Age [Day]	Tensile stress in ECC [MPa]	Shear stress at interface [MPa]	Debonding stress at interface [MPa]	Utilized tensile strain
3	2.46	0.87	0.71	0.03%
7	3.15	0.98	0.78	0.11%
28	3.66	1.07	0.84	0.18%
90	3.89	1.10	0.86	0.21%

Table 4.6 gives the mechanical properties of FRPM mortar used in the calculation of the stresses in the FRPM mortar composite beam. The calculated critical stresses are given in Table 4.7. At the age of 3 days, the calculated tensile stress in FRPM mortar is lower than its ultimate tensile strength and no cracks are, therefore, formed. As observed in experiments, no crack was observed until 5 days. The shear and tensile stresses at the interface of the FRPM mortar composite beam are lower than that in the ECC composite beam. In addition, FRPM mortar has a stronger interfacial bond than ECC. Therefore, the FRPM mortar composite beam showed later interface delamination than the ECC composite beam did. The calculated stresses show a big increase from 3 to 28 days. At 28 days, the tensile stress in FRPM mortar is much higher than its ultimate tensile strength, as observed in the experiments that FRPM mortar cracked severely between 3 and 28 days.

Table 4.6 Mechanical properties of FRPM mortar.

Age [Day]	Shrinkage ε_{sh} [$\times 10^{-6}$]	Ultimate tensile strength f_t [MPa]	Young's modulus E [GPa]
3	330	3.91	13.88
28	1090	5.60	26.41

Table 4.7 Calculated critical stresses in the FRPM mortar.

Age [Day]	Tensile stress in FRPM mortar [MPa]	Shear stress at interface [MPa]	Debonding stress at interface [MPa]
3	3.08	0.81	0.51
28	14.00	3.30	1.92

4.3.3   Discussion on the mechanical performance of the ECC repair

Plain concrete and ordinary fiber-reinforced concrete show a tensile-softening response. Once it cracks, the specimen reaches the peak load. Beyond this peak load, the single crack keeps opening until it can not carry any load and the final failure of specimen occurs. When used as repair material, the restraint of the increasing shrinkage results in the increase in crack width rather than further cracking in FRPM mortar. The differential shrinkage, therefore, causes the failure of FRPM mortar in tension, and reinforcement is needed to carry tensile load in the repair material.

On the contrary, under tensile load, ECC shows a unique tensile strain-hardening behavior and tight crack width control. The increasing tensile load results in a sequential cracking of the matrix rather than crack opening. When ECC is used as repair material, once the tensile stress reaches its tensile strength, ECC cracks sequentially and generates large deformation. The multiple cracking of ECC releases the shear and debonding stresses at the interface. Therefore, after the first cracking of ECC, the further shrinkage causes a small increase in stresses but more cracks, hence large tensile deformation in ECC. And thus the potential of interface debonding is reduced. Crack width in ECC is normally smaller than 60 μm. The tight crack width in ECC can greatly reduce the water permeability, slow down the chloride penetration and, therefore, improve the durability of the repair system. The chloride penetration results in these two repair materials are discussed in section 4.4.1. Furthermore, the shrinkage of ECC is much lower than its tensile strain capacity, which are 0.21% and 2.6% at the age of 90 days, respectively. Without the presence of reinforcement, ECC can still carry more load or further deformation and gives a better load bearing capacity of the repair system.

A crucial condition for reduced interface debonding is that ECC cracking takes place earlier than interface delamination, i.e. the stresses at interface should not exceed their strength. If this condition is not met, differential shrinkage may cause severe interface delamination rather than cracking, as observed in ECC in the first 3 days. The interface is, therefore, the weakest point of ECC regarding the performance of concrete repairs. In order to avoid the interface debonding, the bond strength between ECC and concrete substrate should be enhanced.

4.4   Durability of the repair systems

Chloride-induced reinforcement corrosion is often considered the major cause of deterioration of reinforced concrete structures [DuraCrete 2000]. The chloride penetration profile in concrete is, therefore, often used as an index to predict the service life of concrete structures. In the most concrete repairs, the differential shrinkage results in the cracking of the repair material. The cracking of the repair material has a big influence on the durability of the repair system. Therefore, the durability of the cracked repair system was investigated in this section.

4.4.1   Chloride penetration profile

As indicated in Figure 4.15, surface cracking facilitates chloride penetration in the repair materials, and the peaks in chloride penetration front were all observed in cracks. Due to the presence of more than 4 cracks, the chloride penetration front in ECC shows several peaks. In FRPM mortar, there is one major peak in the chloride penetration front, and this peak is more pronounced than those in ECC. The chloride penetration depth in the cracks shows a good linear relationship with its crack width as shown in Figure 4.16. In the repair materials, as the crack width increases, the chloride penetration depth in this crack increases.
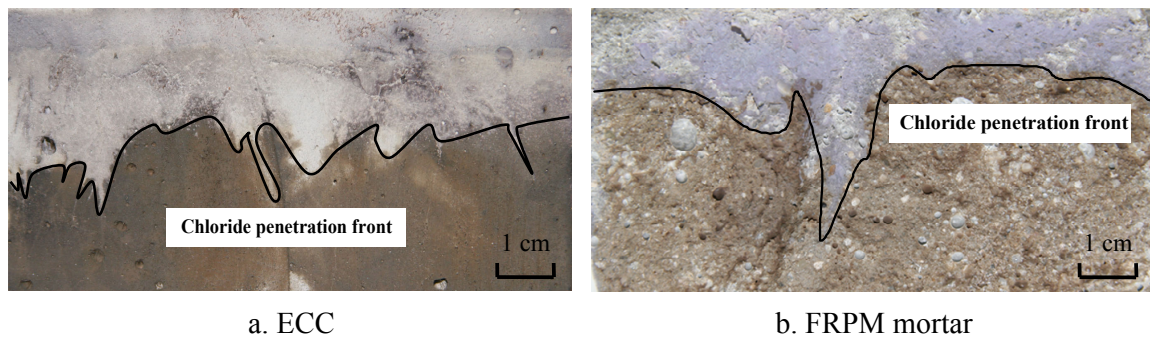
a. ECC   b. FRPM mortar

Figure 4.15 Chloride penetration profile in (a) ECC and (b) FRPM mortar at the age of 90 days.
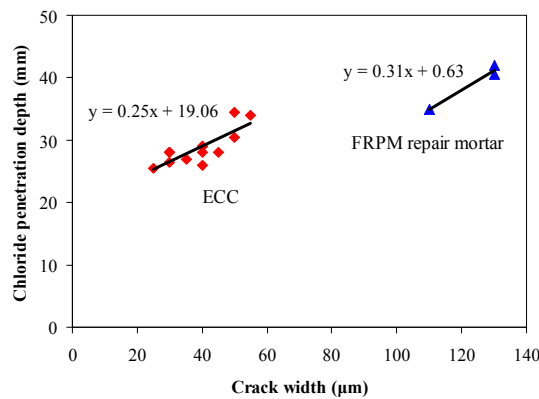
Figure 4.16 Relationship between the chloride penetration depth in cracks and the crack width.

Besides the maximum chloride penetration depth in the cracks, the average chloride penetration depths in the two repair materials are calculated by averaging the results at 7 locations in each specimen. The values of the average and maximum chloride penetration depths are given in Table 4.8. The average chloride penetration depth in ECC is larger than that in FRPM mortar. However, ECC shows a maximum chloride penetration depth smaller than FRPM mortar.

Table 4.8 Average and maximum chloride penetration depths in repair materials.

Repair material	Average chloride penetration depth [mm]	Maximum chloride penetration depth [mm]
ECC	22.3 ± 0.8	33.0 ± 2.2
FRPM mortar	12.6 ± 1.3	39.2 ± 3.7

In order to explain the chloride transport in the repair materials, the pore structures of the repair materials were investigated by MIP. The MIP results of the two repair materials are shown in Figure 4.17. The experimental results show that ECC is much more porous than FRPM mortar. The total porosities of uncracked ECC and FRPM mortar are 26.2% and 12.1%, respectively. The differential curve of ECC shows two major peaks located at the pore diameters of 0.52 μm and 0.04 μm. The differential curve of FRPM mortar shows only one

major peak located at the pore diameter of 0.07 μm. Since the addition of fibers induces porous fiber-matrix interface, the porosity is increased. The presence of the peaks corresponding to larger pore diameter might be attributed to the large pores at the fiber-matrix interface.
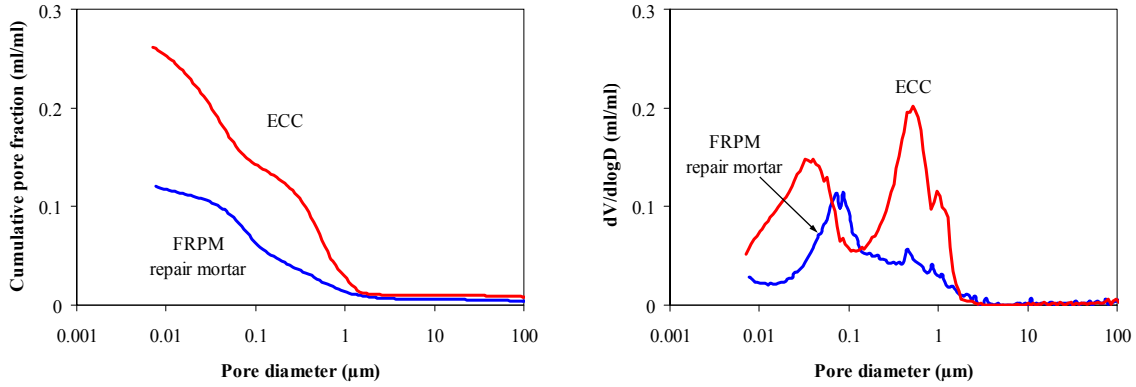
Figure 4.17 Pore size distributions of the repair materials at the age of 90 days.

Chloride ions penetrate into concrete through the pore system, if there are no cracks. The pore sizes determine the rate of chloride penetration. The larger the pore sizes are, the faster the chloride penetration is. As a result, ECC shows a larger average chloride penetration depth. Besides the pore system, cracks also facilitate the chloride ingress in concrete. Usually, the chloride penetration in the cracks is much faster than that in the pore structure, because the cracks have a larger size than pores. The experimental results also show a larger penetration depth in the cracks. The penetration depth in the cracks is correlated with the crack width. The larger crack width in FRPM mortar results in a larger maximum penetration depth. Consequently, ECC shows a higher average chloride penetration coefficient and lower maximum chloride penetration coefficient.

4.4.2   Chloride penetration coefficient

In this section, the method used to calculate the chloride penetration coefficient of uncracked concrete is borrowed to calculate the chloride penetration coefficient of the cracked repair materials. The non-steady-state chloride penetration coefficients of the cracked repair materials can be calculated with the following equation [NT BUILD 492 1999]:

$$D = \frac{0.0239 \times (273+T) \times L_{RCM}}{(U-2) \times t} \times \left(x_d - 0.0238 \times \sqrt{\frac{(273+T) \times L_{RCM} \times x_d}{U-2}} \right) \qquad (4.1)$$

where D [mm^2/s] is the non-steady-state chloride penetration coefficient, T [°C] is the temperature in the anolyte solution, L_{RCM} [mm] is the thickness of the specimen, x_d [mm] is the chloride penetration depth, U [V] is the applied voltage and t [h] is the test duration.

The non-steady-state chloride penetration coefficients calculated with the average and maximum penetration depths are given in Table 4.9. The average chloride penetration coefficient of ECC is higher than that of FRPM mortar. However, when calculated with the

maximum penetration depth, ECC shows a lower maximum chloride penetration coefficient than FRPM mortar.

Table 4.9 Non-steady-state chloride penetration coefficients calculated with the average and maximum penetration depths.

Repair material	Chloride penetration coefficient calculated with average penetration depth [$\times 10^{-12}$ m^2/s]	Chloride penetration coefficient calculated with maximum penetration depth [$\times 10^{-12}$ m^2/s]
ECC	2.4 ± 0.1	3.6 ± 0.2
FRPM mortar	1.3 ± 0.1	4.3 ± 0.4

4.4.3   Service life prediction of the concrete repairs

When the repair material does not debond from the concrete substrate, the service life is defined as the duration from placing repair materials until the initiation of chloride-induced reinforcement corrosion. Once the chloride content at the surface of the rebar has exceeded the critical value, the service life of the structure is considered to end. The DuraCrete model is used to calculate the service life of the concrete repairs. The DuraCrete model is a transport property-based model, adopting the semi-probabilistic approach. The concept of this model, its validation and application has been presented and discussed in details in [Polder et al. 2006, van Breugel and Polder 2009]. In the DuraCrete model, the chloride penetration process is calculated as:

$$C(x,t) = C_s - \left(C_s - C_i\right) \times erf\left(\frac{x}{\sqrt{4ktD(t)}}\right) \tag{4.2}$$

where $C(x,t)$ [-] is the chloride content at depth x at time t, C_s [-] is the surface chloride content, C_i [-] is the initial chloride content in the concrete, k [-] is a correction factor and $D(t)$ is the chloride penetration coefficient at time t.

The critical chloride content is set to be 0.6% by mass of the repair material [Gaal et al. 2003]. The surface chloride content is often taken equal to 3.0% for marine structures [de Rooij and Polder 2005] and 1.5% for land structures [Gaal et al. 2003]. The initial chloride content in the repair material is assumed to be 0.1% [van Breugel and Polder 2009]. The correction factor k depends on the type of binder, the environmental factors and curing conditions. According to [DuraCrete 2000], the k-values of ECC and FRPM mortar are taken equal to 2.97 because of high slag content in the two repair materials. The chloride penetration coefficient is a time-dependent factor, and it decreases with time. This phenomenon can be described with an aging coefficient as follows:

$$D(t) = D_0 \left(\frac{t_0}{t}\right)^n \tag{4.3}$$

where D_0 [mm^2/s] is the chloride penetration coefficient at the reference time t_0 (90 days in this study) and n [-] is the aging coefficient. The value of the aging coefficient depends on the

type of binder, the rate of cement hydration and environmental factors. In moderately wet environment, the *n*-values of ECC and FRPM mortar are taken to be 0.85 [DuraCrete 2000].

The minimum cover depth required for the service life of 100 years, exposed to marine and land environments is determined using Eq. 5.2 and summarized in Table 4.10. Because of the high chloride content in seawater, the repair materials in the marine environment need a thicker cover compared to those in the land environment. No matter in land or marine environment, ECC needs smaller cover depth compared to the FRPM mortar due to its tiny crack width and low chloride penetration coefficient.

Table 4.10 The minimum cover depth [mm] required for the service life of 100 years. Exposure classes XD1, XD2 and XD3 represent land environment, and XS2, XS3 represent marine environment.

Repair materials	Exposure class	
	XD1, XD2, XD3	XS2, XS3
ECC	18.6	26.7
FRPM mortar	20.4	30.2

Nowadays, the service life of concrete structures is mainly calculated with the material properties of uncracked concretes. In reality, most structural concretes perform in the presence of cracks, particularly in concrete repairs subjected to differential shrinkage. Cracks can adversely affect the durability by facilitating the ingress of aggressive substances, such as chloride ions and cause a decrease in service life. The service life might be overestimated when the uncracked material properties are used for the cracked concretes. Sahmaran et al. [2008] suggested that, even after the corrosion of reinforcement rebar ECC structures showed a small loss of the loading capacity. Therefore, ECC probably exhibits a better durability and longer service life than FRPM mortar, although the latter has more porous microstructure and higher average chloride penetration coefficient.

4.5   Conclusion

The performance of the newly developed ECC in concrete repairs subjected to differential volume change was experimentally investigated, compared to a FRPM mortar. Based on the experimental results, the following conclusion can be drawn:
- The differential shrinkage results in an increase in the number of cracks in the ECC repair system and an increase in crack width in the FRPM mortar repair system. And, ECC has much smaller crack width than FRPM mortar.
- Although ECC has a high shrinkage, the calculated stresses in the ECC composite beam are lower than those in the FRPM mortar composite beam. Although differential shrinkage generates many cracks in ECC, the calculated strain is much lower than its tensile strain capacity, so that ECC can carry more load and further strains.
- The surface cracking facilitates chloride penetration in repair materials. The maximum chloride penetration depths are all located along cracks. Due to the tight crack width, ECC exhibits a relatively smaller maximum chloride penetration depth.

- Due to the smaller crack width, ECC has a higher chloride resistance than FRPM mortar. To achieve the same service life, ECC, therefore, needs smaller cover depth than FRPM mortar.

Based on the experimental results and discussion, it can be concluded that ECC is a good repair material. The high ductility and tight crack width control of ECC can significantly improve the mechanical and durability performance of the ECC repair system. It was also found that the bond strength is a crucial factor influencing the performance of the ECC repair system. To enhance the bond strength becomes more meaningful on achieving durable concrete repairs. The properties of the repair-substrate interface and the bond strength will be investigated experimentally and numerically in Chapters 5-7.

Chapter 5

Experimental Study on Microstructure and Bond Strength of the Repair-Substrate Interface

5.1 Introduction

As discussed in Chapter 4, the bond strength between ECC and concrete substrate is the key factor for the performance of the ECC repair system. Sufficient bond strength is required to withstand the stresses at the interface induced by environmental and/or mechanical loads. In order to enhance the bond strength, this chapter aims at exploring the fundamental bond mechanisms between repair material and concrete substrate and at indentifying the factors influencing the bond strength.

To understand the fundamental bond mechanisms, the cement hydration and microstructure at the repair-substrate interface were investigated experimentally, since they affect the mechanical properties of the interface. The influence of the surface roughness of the concrete substrate was also studied. In the experiments, a Portland cement paste was used as a repair material instead of ECC. Firstly, the cement paste is the most important part in ECC and the cement-based repair material. The properties of the cement paste determine the microstructure and mechanical properties at the interface. The bond strength between the repair material and the concrete substrate mainly depends on the properties of the cement paste in the repair material. Secondly, the techniques used to study cement hydration and microstructure, for example non-evaporable water test and BSE image analysis, are difficult to use for blended cement-based material, such as ECC. The fundamental understanding of the phenomena happening at the interface obtained in this research can be employed for the conventional cement-based repair material and in the old-new concrete interface.

In the following sections, the literature review on the bond strength between repair material and concrete substrate is first discussed. The characterization of the concrete substrate is presented. Then, the cement hydration process and microstructure at the interface are experimentally investigated in order to interpret the bond properties of different repair-substrate interfaces.

5.2 Literature review on the bond strength between repair material and concrete substrate

The bond strength is commonly referred to the stresses required to separate the repair material from the concrete substrate [Beushausen 2006]. The bonding between repair material and substrate concrete is a result of the combination of adhesion and mechanical interlocking [Courard 2000]. The adhesion results from chemical and physical interactions between the repair material and the concrete substrate [Fiebrich 1994]. After placing the repair material on

the concrete substrate, the fresh repair material penetrates into the cavities and pores on the substrate. When this repair material hardens, the resultant mechanical anchorage will contribute to the bond strength.

The cement hydration of the repair material determines the microstructure and mechanical properties of the interface and it, therefore, affects the quality of bond. According to Courard and the co-worker [Courard 2000, Courard and Nelis 2003, Courard and Degeimbre 2003, Courard 2005, Garbacz et al. 2005, Garbacz et al. 2006], the roughness of the concrete substrate has a significant influence on the mechanical interlocking, since it affects the geometric profile of the interface and the contact area between the two materials.

5.2.1   Moisture exchange and cement hydration

Moisture exchange between repair material and concrete substrate plays an important role in the development of the properties of the repair-substrate interface. The moisture exchange has influences on the cement hydration and microstructure development of the repair material, which determine the mechanical properties of the repair-substrate interface. The moisture exchange can be divided into two stages.

Before setting of the repair material, the concrete substrate absorbs water from the repair material driven by capillary absorption [Courard and Degeimbre 2003]. This causes a water loss of the repair material and thus a reduction of the w/c ratio. The water loss shortens the setting time of the repair material and decelerates cement hydration, while the reduced w/c ratio leads to a dense pore structure of the repair material and probably high strength of the repair material and the repair-substrate interface. However, if capillary absorption is too large, the left water may be not enough for the hydration of the repair material, particularly when the initial water content of the repair material is low and when the volume of the repair material is small [Beushausen 2006]. Therefore, the degree of hydration is lowered and lots of large pores are formed in the repair material.

After setting of the repair material, moisture exchange between repair material and concrete substrate continues driven by capillary pressure gradients in the two materials. At the early age, moisture normally moves from the repair material to the concrete substrate due to the high water content in the repair material. The degree of cement hydration in the repair material, therefore, decreases. As water is gradually consumed, the water content in the repair material decreases, and the capillary pressure in the repair material thus increases. When the capillary pressure in the repair material exceeds that in the concrete substrate, water is forced to flow back to the repair material. The water gain then accelerates the cement hydration of the repair material.

Moreover, capillary absorption plays an important role in the mechanical interlocking, since it facilities the penetration of the liquid repair material into the cavities of the concrete substrate and increases the contact area of the two materials [Courard 2000].

5.2.2   The "wall effect" on microstructure of the repair-substrate interface

The "wall effect" is a well-known phenomenon at the interface between cement matrix and aggregate [Larbi 1992]. Due to the "wall effect", the interfacial zone between cement paste and aggregates has a loose packing of cement particles, and the w/c ratio of cement paste locally increases. Therefore, the cement matrix-aggregate interfacial zone shows a high porosity and poor microstructure. Pigeon and Saucier [1992] reported that the repair-substrate interface is very similar to the aggregate-cement matrix interface depending very much on the

type of aggregates in the substrate. The "wall effect" also exists at the repair-substrate interface and causes a porous microstructure. Therefore, it can be expected that the interface is a weak point in concrete repairs.

5.2.3 Roughness of the concrete substrate

The aim of the surface preparation of the concrete substrate is to increase the surface roughness and to remove the defects on the surface of the concrete substrate. There are many techniques used to roughen the surface of the concrete substrate, such as grit-blasting, shot-blasting, milling, grinding and so on. Different techniques result in different profiles of the surfaces. Some surface treatments, including shot-blasting and milling, can cause microcracks in the surfaces [Garbacz et al. 2005]. The presence of cracks results in a poor repair-substrate interface and a low bond strength. In general, without the presence of microcracks, the increase in roughness results in an increase in the bond strength of the repair-substrate interface, especially the shear bond strength [Austin et al. 1995, Santos et al. 2007, Courard 2005]. The increase in the bond strength can be attributed to the modifications of the mechanical interlocking and increase in the contact area between repair material and concrete substrate [Fiebrich 1994, Courard 2000].

5.2.4 Summary of the literature review

From literature, the cement hydration process and microstructure of the interface have not been studied extensively. Few studies were carried out to interpret the bonding of the interface from the microstructural point of view. This chapter has the aim to study the cement hydration and the microstructure development of the repair-substrate interface, taking into consideration the moisture exchange and the "wall effect".

5.3 Characterization of the concrete substrate

The concrete substrate was a 3-year-old concrete, which was cured at a temperature of 20°C and a relative humidity of 99.9%. The mix proportion the concrete substrate is given in Table 5.1.

Table 5.1 Mix proportion of the concrete substrate.

Coarse aggregate [kg/m^3]	Fine aggregate [kg/m^3]	Cement [kg/m^3]	Water [kg/m^3]	w/c ratio	Maximum aggregate size [mm]
1177.2	633.9	375	187.5	0.5	16

5.3.1 Preparation of concrete substrate

Two techniques were used to roughen the surface of the concrete substrates:
- Cutting (as shown in Figure 5.1 (a)).
- Grit-blasting (as shown in Figure 5.1 (b)). The injecting air pressure was 0.8 MPa, and the blasting speed on the surface of the concrete substrate was 10 cm^2/minute.
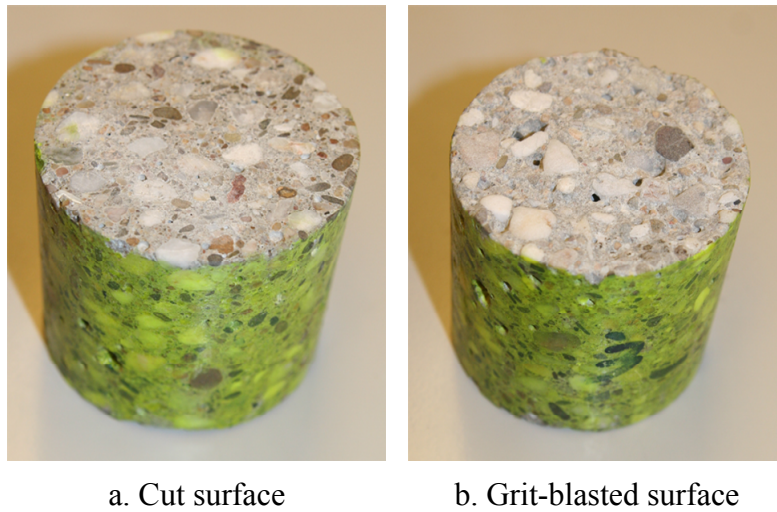
a. Cut surface   b. Grit-blasted surface

Figure 5.1 Substrate specimens with (a) a cut surface and (b) a blasted surface.

After the surface treatment, the substrate specimens were placed in two moisture conditions for 7 days, i.e. 50% relative humidity (RH) and 99.9% RH, to obtain the unsaturated and saturated concrete substrates, respectively. The preparations of the concrete substrates are summarized in Table 5.2.

Table 5.2 Preparation of the concrete substrates.

Concrete substrate	Surface treatment	Moisture condition
C1	Cutting	50% RH
C2	Grit-blasting	50% RH
C3	Cutting	99.9% RH

5.3.2   Degree of saturation of the concrete substrate

The degree of saturation of the substrate specimens is determined. The weight of the specimens is first measured and recorded as W_i [g]. Then, the specimens are vacuum-saturated for 6 hours, and the weight of the saturated specimens W_s [g] is measured. Finally, the specimens are dried at a temperature of 105°C for 24 hours, and the weight of dried specimens is recorded as W_d [g]. The degree of saturation of the concrete substrate S_w [-] is calculated as follows:

$$S_w = \frac{W_i - W_d}{W_s - W_d} \tag{5.1}$$

The calculated degree of saturation of the concrete substrates exposed to different moisture conditions are given in Table 5.3. After 7-day exposure to 99.9% RH, the specimen got almost fully saturated. The specimen placed in 50% RH shows a lower degree of saturation, which is 14.4%. It can be expected that the unsaturated substrates C1 and C2 has a high potential to absorb water, while the saturated concrete substrate C3 can only absorb little water.

Table 5.3 Degree of saturation of the concrete substrates after 7-day exposure to 50% RH and 99.9% RH (see Table 5.2).

Concrete substrate	Degree of saturation S_w
C1 (cut, unsaturated)	14.4%
C2 (blasted, unsaturated)	14.4%
C3 (cut, saturated)	99.0%

5.3.3   Capillary absorption of the concrete substrate

The capillary absorption of the unsaturated substrates C1 (cut) and C2 (blasted) was investigated according to the European standard EN 480-5 [2005]. The specimen was a cylinder with a diameter of 60 mm and thickness of 60 mm. The perimeters of the cylinder specimens were first coated with a thin layer of epoxy to avoid lateral water penetration and evaporation as shown in Figure 5.2. After the epoxy hardened, the specimens were suspended on a balance and then immersed into water as shown in Figure 5.3. The immersed level was 5 mm. After the specimen got contact with water, water was absorbed into the specimen and the weight of the specimens increased continuously. The weight change of the specimen was measured for 10 hours. Three parallel measurements were done.

   The water absorption of the cut and blasted specimens is illustrated in Figure 5.4. Each value represents the average of the three measurements, and the standard deviations are all lower than 0.015 g. In the first 2 hours the blasted specimen absorbs more water than the cut specimen. There is no difference on the water absorption between the two specimens in the later stage. After 10 hours, the two concrete substrates both absorb 0.32 g/cm^2 water on average. This amount of water leads to an increase in the degree of saturation of the unsaturated substrate from 14.4% to 90.4%.

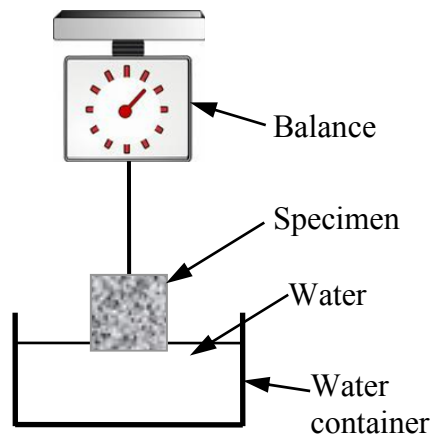Figure 5.2 Specimen for capillary absorption test.

Figure 5.3 Test set-up of capillary absorption [EN 480-5 2005].
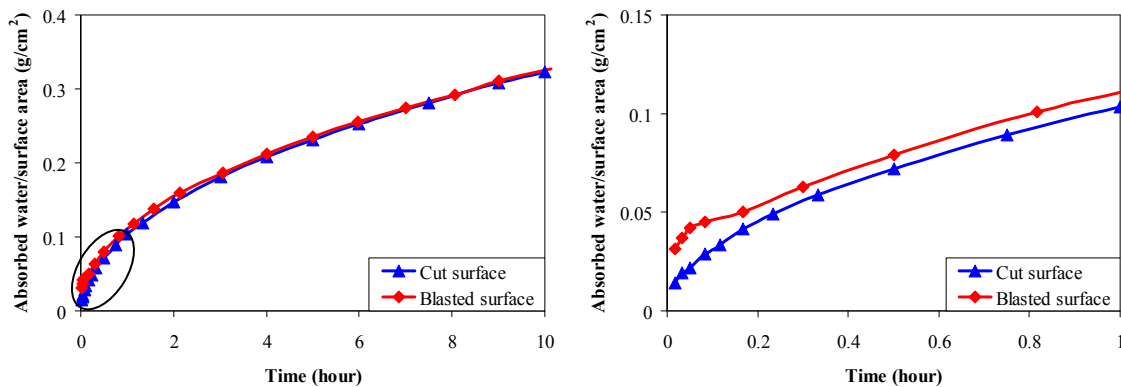
Figure 5.4 Water absorption of the unsaturated concrete substrates C1 (cut) and C2 (blasted).

5.3.4   Surface roughness measured by laser profilometry

Laser profilometry was used to investigate the surface roughness of the concrete substrates. The surfaces with a size of $100 \times 100 \text{ mm}^2$ were scanned over a distance of 0.5 mm (*X*-axis) × 0.5 mm (*Y*-axis) using a laser beam triangulation mode with a vertical resolution of 1 μm.

Figure 5.5 shows a typical surface profile of the concrete substrate measured by laser profilometry. Based on the experimental data, several parameters can be defined to quantify the surface roughness [Mummery 1992]. The average profile R_a [mm] is defined as the mean value of local profile R_i [mm], and it holds that:

$$R_a = \frac{1}{n} \sum_{i=1}^{n} R_i \tag{5.2}$$

The maximum height of the profile R_y [mm] is defined as the distance between the highest and the lowest points as shown in Figure 5.5. R_q [mm] is a parameter often used to describe surface roughness [Courard and Nelis 2003, Garbacz et al. 2006]. It is defined as the root mean square deviation of the profiles:

$$R_q = \sqrt{\frac{1}{l_m} \int_0^{l_m} \left(R(x) - R_a \right)^2 dx}$$ (5.3)

where l_m [mm] is the evaluation length of the profile.

Figure 5.5 Surface profile of the concrete substrate measured by laser profilometry.
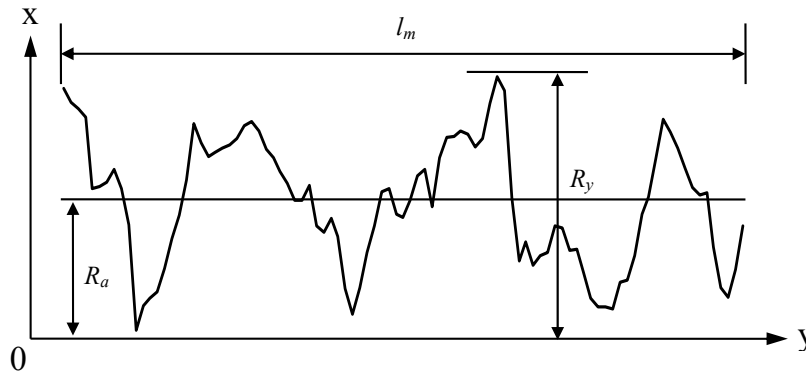
The laser profilometry results of the concrete substrates prepared by different surface treatments are shown in Figure 5.6, and the parameters calculated by Eqs. 5.3 and 5.4 are given in Table 5.4. The experimental results show that the cut surface is much smoother than the blasted surface. The average profile R_a and the maximum profile R_y in the cut surface are 0.60 mm and 1.95 mm, respectively, while those of the blasted surface are 3.50 mm and 6.64 mm, respectively. The calculated R_q of the blasted surface is 5.3 times of that of the cut surface.

Table 5.4 Laser profilometry results.

Surface treatment	R_a [mm]	R_y [mm]	R_q [mm]
Cutting	0.60	1.95	0.31
Grit-blasting	3.50	6.64	1.65

Figure 5.7 shows the surface profile and the aggregate distribution in the same blasted specimen. After grit-blasting, most aggregates have a higher profile than the surrounding cement matrix as indicated by circles in Figure 5.7. The reason is that most aggregates have a compressive strength above 80 MPa [Neville 1995], which is considerably higher than the strength of cement matrix. Therefore, when subjected to the grit-blasting, the cement matrix is more easily removed than the aggregate. However, there are also some aggregates, such as sandstone, which are week and have a similar strength as the cement matrix [Neville 1995]. These aggregates can be removed as easily as the cement matrix, and they thus show a lower profile as indicated by squares in Figure 5.7.

a. Cut surface   b. Grit-blasted surface
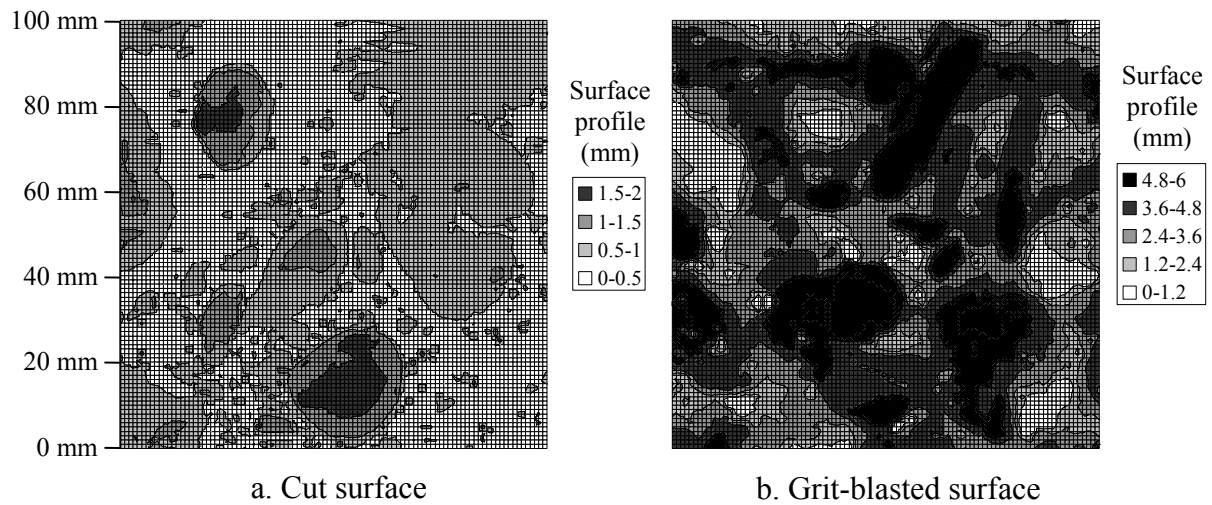
Figure 5.6 Surface profiles of (a) the cut surface and (b) the grit-blasted surface.

a. Surface profile   b. Aggregate distribution
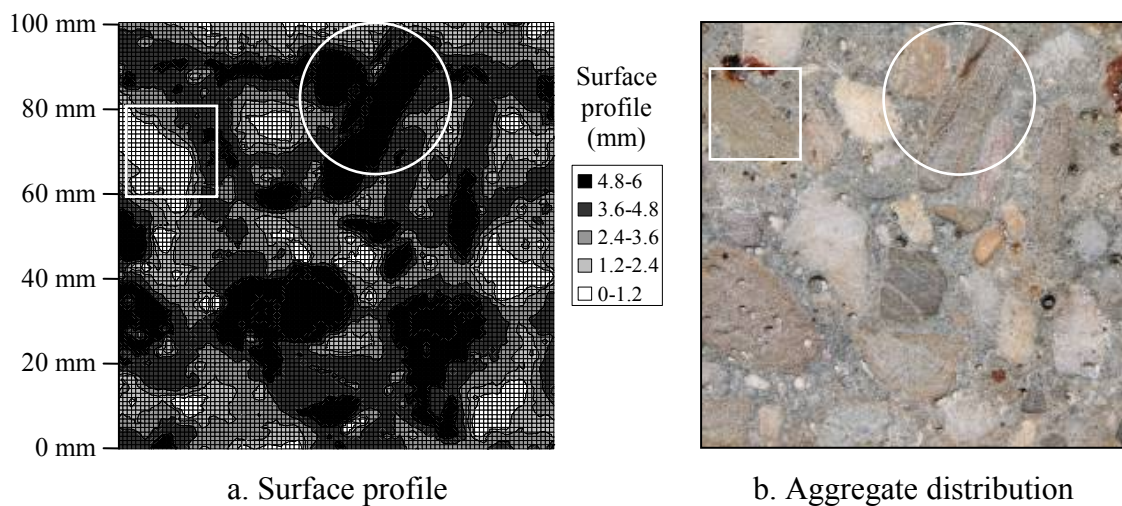
Figure 5.7 Comparison between (a) the surface profile and (b) the aggregate distribution on the grit-blasted specimen.

5.4   Experiments to investigate the microstructure and bond strength of the repair-substrate interface

At the repair material age of 28 days, the degree of hydration and porosity in the repair material, the microstructure at the repair-substrate interface and the bond strength were investigated by non-evaporable water test, MIP, SEM and direct tensile test, respectively. Powers and Brownyard [1946] found that in cement paste, the degree of hydration has a linear relationship with the non-evaporable water content. Accordingly, the degree of hydration is often studied by measuring the non-evaporable water content [Parrott et al. 1990, Escalante-Garcia 2003]. MIP is one of the most popular methods used to investigate the pore structure of the cement based materials. It can provide valid measurement on the total porosity. It is difficult to take samples from the interface for non-evaporable water and MIP test, since the

samples for these two techniques are much larger than the interface itself. Therefore, these two techniques are limited to investigate the degree of hydration and porosity in the repair material rather than at the interface. Instead, SEM is used to study the microstructure, degree of hydration and porosity at the interface by taking images from the interface, which is 20 μm wide. The experimental procedures will be presented in detail in the following.

5.4.1   Repair material

In this study, an ordinary Portland cement (CEM I 42.5N) paste with a w/c ratio of 0.4 was used as repair material.

5.4.2   Sample preparation for non-evaporable water, MIP, SEM and bond strength tests

The substrate specimen was a cylinder with a diameter of 60 mm and thickness of 60 mm. Before casting the repair material, the top perimeter of the concrete substrate was encircled by adhesive tape to avoid the leakage of the mixing water from the gap between the specimens and the molds as shown in Figure 5.8 (a and b). The specimens were then enclosed in two pieces of half PVC pipes as shown in Figure 5.8 (c). The PVC pipes were tightened by adhesive tape as shown in Figure 5.8 (d). The fresh repair material was cast on the prepared surface of the substrate specimen, and the thickness of the repair material was 60 mm. The repair material was then vibrated to remove air bubbles. As a reference, a plain Portland cement paste was cast with a thickness of 60 mm. The specimens were cured at a temperature of 20°C and in a sealed condition for 28 days.

   After curing, the samples for non-evaporable water, MIP and SEM tests were taken from the specimens as shown in Figure 5.9 (a). The other three specimens were used for bond strength test. The samples for non-evaporable water and MIP tests were sawn into pieces of 0.5 cm^3, and the samples for SEM test were sawn into pieces of $4 \times 2 \times 1$ cm^3. In the reference specimen, the samples for non-evaporable water and MIP tests were taken at the same locations as shown in Figure 5.9 (b). Some samples were also taken from the concrete substrates and sawn into pieces of 0.5 cm^3 for MIP test.

   The freeze-drying was used to dry the samples for non-evaporable water, MIP and SEM tests, since this method causes less damage on the microstructure of cement paste compared with the other common drying methods, such as oven drying and vacuum drying [Ye 2003]. The samples were quickly frozen by immersing in liquid nitrogen for 5 minutes. Then, they were placed in a freeze-dryer with a temperature of -24ºC and a vacuum of 0.1 Pa. The samples were considered to be dry, until the water loss was less than 0.01%/day. This period lasted for 10-20 days depending on the w/c ratio and the curing age of the samples.

Figure 5.8 Preparation for casting the repair material.
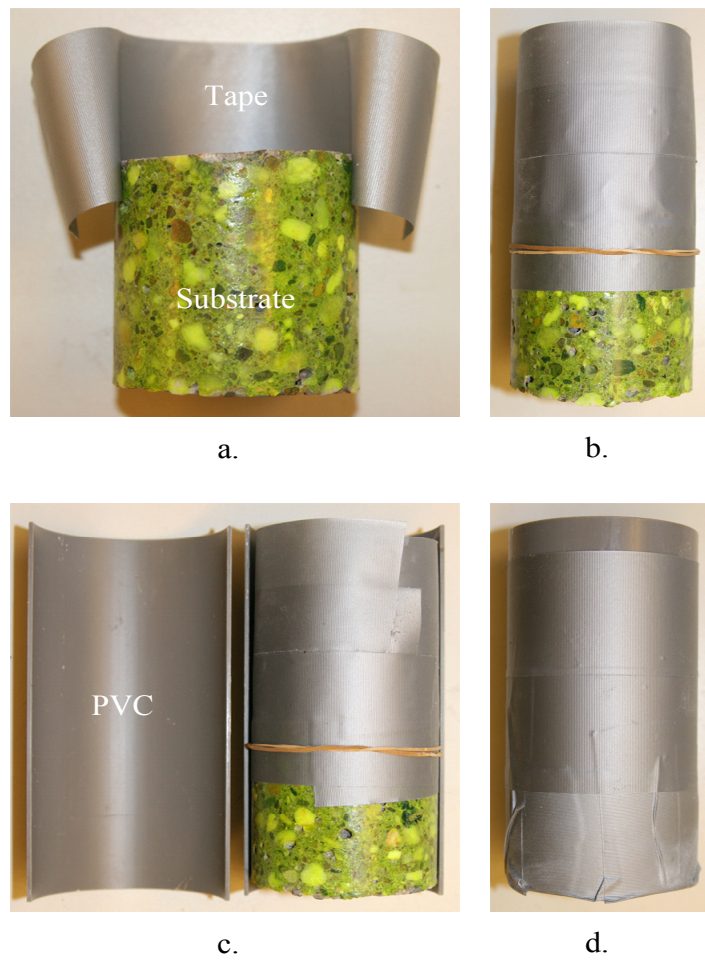

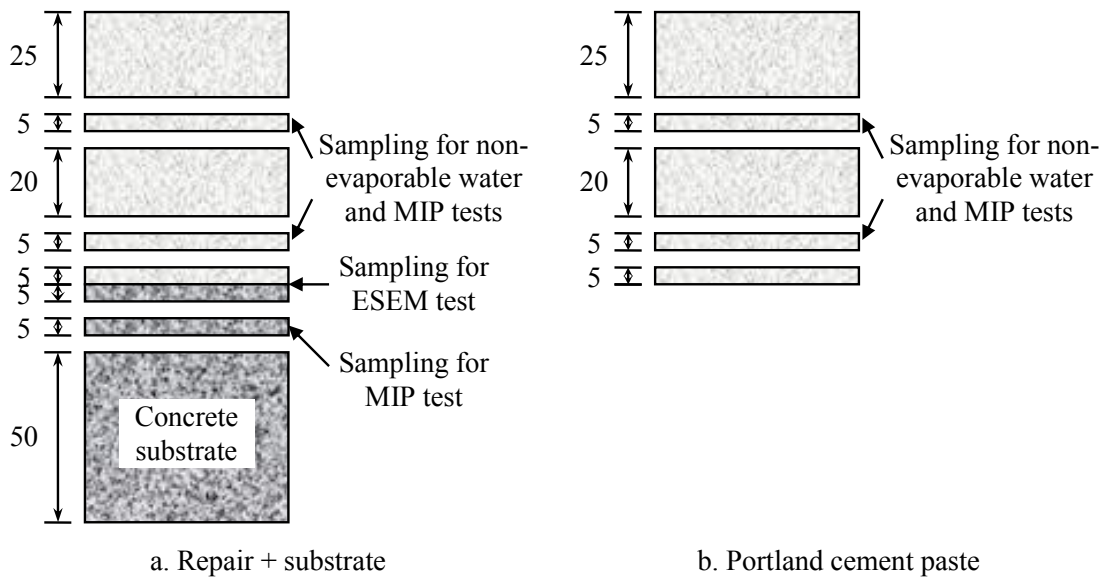a. Repair + substrate   b. Portland cement paste

Figure 5.9 Sampling for non-evaporable water, MIP and SEM tests from (a) the layered
specimens and (b) the reference (dimension in mm).

5.4.3 Non-evaporable water test

The degree of hydration of the repair material was determined by measuring its non-evaporable water content. The freeze-dried samples were ground into powder in order to remove the non-evaporable water efficiently. The powder was further dried at a temperature of 105ºC for 24 hours to remove the evaporable water. Simultaneously, the crucibles were dried in a furnace at a temperature of 1000°C for 2 hours and the weight of the crucibles W_1 [g] was measured. Around 1.1 g powder (W_2 [g]) was added into the crucibles. The crucibles were placed in a furnace at a temperature of 1000°C for 3 hours to remove the non-evaporable water. The weight of the crucibles with the sample was measured and recorded as W_3 [g]. Three parallel measurements were done. The non-evaporable water content W_n [g] per gram of the cement W_c [g] can be calculated as:

$$\frac{W_n}{W_c} = \frac{W_1 + W_2 - W_3}{W_3 - W_1} \qquad (5.4)$$

The degree of hydration α [-] can be calculated by dividing the measured non-evaporable water content by the maximum non-evaporable water content at complete hydration $W_{n,\max}$ [g]:

$$\alpha = \frac{W_n}{W_{n,\max}} \qquad (5.5)$$

The maximum non-evaporable water content at complete hydration is a cement composition dependent parameter. According to Copeland et al. [1962], the maximum non-evaporable water content can be calculated as follows:

$$W_{n,\max} = W_{C_3S} \times (C_3S) + W_{C_2S} \times (C_2S) + W_{C_3A} \times (C_3A) + W_{C_4AF} \times (C_4AF) \qquad (5.6)$$

where W_{C3S}, W_{CsS}, W_{C3A} and W_{C4AF} are the non-evaporable water contents of the major constituents of Portland cement given in Table 5.5. (C_3S) (C_2S) (C_3A) and (C_4AF) are the content the major constituents in Portland cement CEM I 42.5N, which is given in Table 5.6. The calculated non-evaporable water content at complete hydration is 0.225 g/g.

Table 5.5 Non-evaporable water contents of the major constituents of Portland cement [Powers and Brownyard 1946].

Cement phase	Coefficient [g water/g cement phase]
C_3S	0.187
C_2S	0.158
C_3A	0.665
C_4AF	0.213

Table 5.6 Major constituents of Portland cement CEM I 42.5N. The data were from the manufacturer.

Cement phase	Weight [%]
C_3S	65.8
C_2S	14.8
C_3A	8.3
C_4AF	11.1

5.4.4   MIP test

The porosities of the repair material and the concrete substrates were measured by means of MIP. The freeze-dried samples with a known weight W_{sample} [g] were put into a penertrometer and the penertrometer was closed with a steel cap. After the weight of the penertrometer with the samples $W_{sample} + W_{pen}$ [g] was measured, it was placed in the low-pressure chamber. The chamber was evacuated to a pressure of 50 µmHg, and mercury was then filled in the penertrometer. Pressure gradually increased from 0.004 MPa to 0.15 MPa. The penertrometer was removed from the low-pressure chamber, and its weight $W_{sample} + W_{pen} + W_{mercury}$ [g] was measured. The penertrometer was then placed in the high-pressure chamber, and pressure was gradually increased to the maximum value of 200 MPa. The mercury intrusion volume at every pressure step was recorded. In total, 125 pressure steps in logarithmic distribution were carried out, and equilibrating time in every step was 30 seconds.

Based on the experimental data, the bulk volume of the sample V_{sample} [cm^3] can be calculated:

$$V_{sample} = V_{pen} - \frac{W_{mercury}}{\rho_{mercury}}$$

(5.7)

where V_{pen} [cm^3] is the volume of the penertrometer, and $\rho_{mercury}$ [g/cm^3] is the density of mercury. It is assumed that all pores in samples can be filled by mercury at the maximum pressure, and the pore volume V_{pore} [cm^3] is, therefore, equal to the total mercury intrusion volume $V_{intrusion}$ [cm^3]. The porosity ϕ [-] can be calculated by dividing the total mercury intrusion volume by the bulk volume of the sample:

$$\phi = \frac{V_{intrusion}}{V_{sample}}$$

(5.8)

5.4.5   SEM observation

SEM observation was used to investigate the microstructure at the repair-substrate interface. The specimens were firstly pre-ground in a grinding machine and freeze-dried. The dry specimens were then epoxy-impregnated. The dried specimens were placed in a chamber and the chamber was evacuated for 4 hours. Keeping under vacuum, the freshly mixed epoxy resin was poured on the prepared surfaces. The chamber was still evacuated for 5 minutes. Then, air was slowly released into the chamber to force the epoxy resin to impregnate the specimens.

The penetration depth, varying with the pore structure of the samples and the viscosity of epoxy resin [Diamond 2007], is often very small, particularly in the samples with a low w/c ratio. Kjellsen et al. [2003] reported that the penetration depth in a 0.4-w/c-ratio cement paste was only 120 μm. Therefore, grinding and polishing should be done very carefully and not beyond the epoxy penetration depth. The samples were finely ground in a grinding machine, which can control the ground thickness by 7 μm. Each sample was ground for about 5 minutes until a 50 μm-thick surface was removed. The last grinding was done on a middle-speed lap wheel with a p4000 sand paper for 2 minutes. Then the samples were polished on lap wheels with 6, 3, 1 and 0.25 μm diamond pastes for 8 minutes (2 minutes for each step). Last, the samples were cleaned with a low-relief polishing cloth.

The images were taken on the prepared samples using the backscattered electron (BSE) detector with the vapor mode. The acceleration voltage of 20 kV was used in order to obtain high-contrast images. The spot size was 4.0 nm and the magnification was 500×. The working distance between the final condenser lens and the specimen was 10 mm. The pressure inside the chamber was set at 0.5 Torr.

BSE observation can provide two-dimensional information of the microstructure. A typical BSE image of hardening Portland cement paste is shown in Figure 5.10 (a). The main phases in microstructure of the cement paste, i.e. pores, hydration products and unhydrated cement, can be distinguished by their grey levels as shown in Figure 5.10 (b). Since the pores are filled by epoxy and epoxy does not scatter electrons, the pore space appears black. Hydration products appear grey, and unhydrated cement particles appear bright. With a commercial image processing program, the area of each phase can be determined by counting the number of pixels. The number of pixels of the pore space and the unhydrated cement is first counted, since they can easily be distinguished from the other phases. Then, the number of pixels of the hydration products is calculated by subtracting the pixels of the former two phases from the total pixels. According to Ye [2003], more than 12 images are needed for BSE image analysis.

a. Typical BSE image   b. Grey level histogram
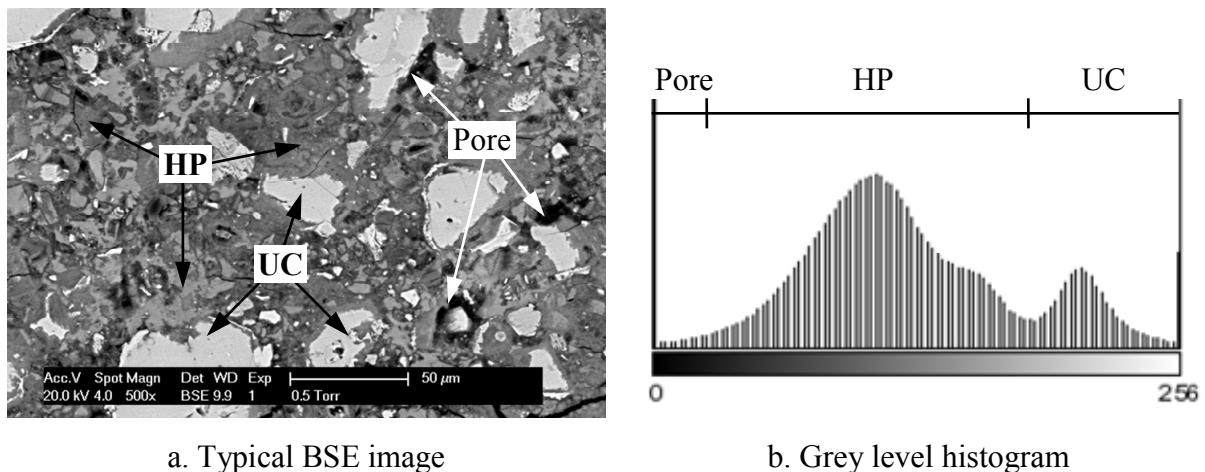
Figure 5.10 Illustration of pore space, hydration products (HP) and unhydrated cement (UC) in (a) a typical BSE image and (b) its grey level histogram.

According to the stereology theory [Underwood 1970, Diamond and Leeman 1995], the three-dimensional information of microstructure can be derived from the two-dimensional BSE images. The volume fraction of each phase is assumed to be equal to their area fraction in the BSE images. The porosity ϕ can be calculated by dividing the number of pixels of the pores n_{pore} [-] by the number of total pixels n_{total} [-]:

$$\phi = \frac{n_{pore}}{n_{total}} \tag{5.9}$$

According to Powers' model [Powers and Brownyard 1946], for Portland cement the hydration products have a volume 2.1 times larger than that of the hydrated cement particles. Therefore, the number of pixels of the hydrated cement n_{hc} [-] holds:

$$n_{hc} = \frac{n_{hp}}{2.1} \tag{5.10}$$

where n_{hp} [-] is the number of pixels of the hydration products. The degree of hydration can be calculated by dividing the pixel of the hydrated cement particles by the total number of the pixels of the cement particles before hydration:

$$\alpha = \frac{n_{hp}/2.1}{n_{hp}/2.1 + n_{uc}} \tag{5.11}$$

where n_{uc} [-] is the number of pixels of the unhydrated cement.
The w/c ratio ω can also be calculated as follows:

$$\omega = \frac{W_{w,in}}{W_{c,in}} = \frac{\left(n_{total} - n_{hp}/2.1 - n_{uc}\right)\rho_w}{\left(n_{hp}/2.1 + n_{uc}\right)\rho_c} \tag{5.12}$$

where $W_{w,in}$ [g] is the initial weight of water, $W_{c,in}$ [g] is the initial weight of Portland cement, ρ_w is the density of water (1 g/cm^3) and ρ_{ce} is the density of Portland cement (3.15 g/cm^3).

5.4.6   Tensile bond strength test

The tensile bond strength of the repair-substrate interface was measured by a direct tensile test according to European standard EN 14488-4 [2002]. The test procedures were presented in detail in Section 4.2.5.

5.5   Experimental results

5.5.1   Degree of hydration of the repair material

The non-evaporable water test can provide an accurate estimation of the degree of hydration, and the standard deviations of the three parallel measurements are all lower than 0.2%. The degree of hydration of the reference and of the repair material at the age of 28 days is given in Figure 5.11. As shown in Figure 5.11 (a), there is no big difference between the degree of hydration at the two layers in the reference. Therefore, the difference in the degree of hydration between the middle and bottom layers of in the reference and the repair material can be ignored.

Compared with the reference, the repair material cast on the unsaturated concrete substrates C1 and C2 shows a lower degree of hydration, while the repair material cast on the

saturated concrete substrate C3 shows a higher degree of hydration. As the repair material hydrates, water is gradually consumed. The saturated concrete substrate can provide additional water for the hydration of the repair material, and this increases the degree of hydration of the repair material. On the contrary, the unsaturated concrete substrate absorbs water from the repair material. The water loss in the repair material results in a reduction of the w/c ratio and lowers the degree of hydration.

As shown in Figure 5.11 (d), when cast on the saturated concrete substrate C3, the repair material close to the interface shows a slightly higher degree of hydration than that far from the interface. As shown in Figure 5.11 (b) and (c), when cast on the unsaturated concrete substrates C1 and C2, the repair material close to the interface shows a slightly lower degree of hydration than that far from the interface. The water exchange between the repair material and the concrete substrate takes place through the interface and spreads further into the two materials. Therefore, the water gain and loss have a bigger influence on the cement hydration closer to the interface.

The different surface treatment techniques do not result in significant difference on the degree of hydration of the repair materials.
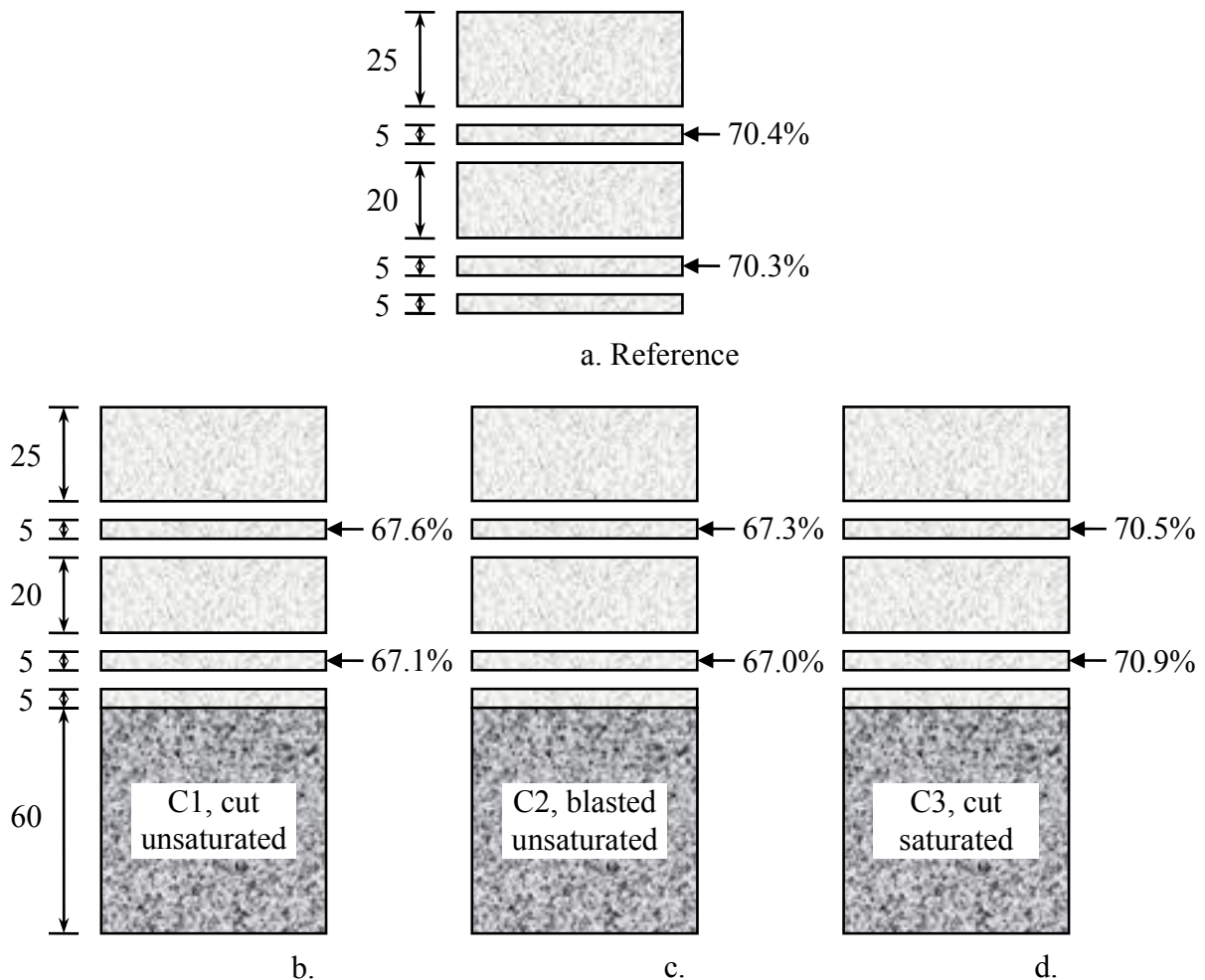

Figure 5.11 Degree of hydration of the reference and of the repair material at the age of 28 days measured by non-evaporable water test (dimension in mm).

5.5.2   Porosities of the concrete substrate and the repair material

The measured porosity of the concrete substrate by MIP is 8.0%. Considering that the coarse aggregates do not contribute to the porosity and the volumetric fraction of the aggregates is 44.4%, the porosity of the mortar in the concrete substrate becomes 14.4%.

The measured porosities of the reference and the repair material are illustrated in Figure 5.12. As shown in Figure 5.12 (a), there is no big difference between the porosities at the two layers in the reference. Therefore, the difference in the porosity between the middle and bottom layers in the reference can be ignored.

Compared with the reference, the repair material cast on the unsaturated concrete substrates C1 and C2 shows a considerably lower porosity, while the repair material cast on the saturated concrete substrate C3 shows a slightly lower porosity. For the unsaturated concrete substrate, the water loss in the repair material results in a large reduction of the w/c ratio of the repair material, and the porosity of the repair material, therefore, decreases. The saturated concrete substrate does not absorb water from the repair material. Therefore, there is little reduction in the w/c ratio of the repair material cast on the saturated concrete substrate. At the later stage, the saturated concrete substrate can provide water for the hydration of the repair material, and this accelerates the cement hydration and, therefore, lowers the porosity of the repair material.

As shown in Figure 5.12 (d), when cast on the saturated concrete substrate, the repair material close to the interface shows a slightly lower porosity than that far from the interface. As shown in Figure 5.12 (b) and (c), when cast on the unsaturated concrete substrate, the repair material close to the interface shows a slightly higher porosity than that far from the interface. The same as the cement hydration, the water gain and loss have a larger influence on the porosity closer to the interface.

The different surface treatment techniques do not result in significant difference on the porosity of the repair materials.

5.5.3   Microstructure of the repair-substrate interface

Figure 5.13 shows the BSE images taken at the repair-substrate interfaces. On the BSE images, the repair material and the concrete substrate can be distinguished by their microstructures. The repair material, on the left hand side of the BSE images, contains more unhydrated cement (white space) and more porosity (black space) than the concrete substrate, on the right hand side of the BSE images. Adjacent to the concrete substrate, there is an interfacial transition zone with relatively more black space. This indicates that this interfacial transition zone has a higher porosity and probably lower strength.

Figure 5.13 (a) and (c) show that the cut concrete substrate results in a smooth surface. It can be expected that the smooth surface does not contribute to the mechanical interlocking between the repair material and the concrete substrate. For a blasted concrete substrate, the repair material can be embedded in the concrete substrate as shown in Figure 5.13 (b). Therefore, the repair material and the concrete substrate might have a strong mechanical interlocking.

Table 5.7 gives the degree of hydration, porosities and w/c ratios at the repair-substrate interface and in the repair material obtained by BSE image analysis. In the three specimens, the degree of hydration, porosity and w/c ratio at the repair-substrate interface are all higher than those in the repair material. Due to the "wall effect" [Bijen and Salet 1994], cement particles have a poor packing on the surface of the concrete substrates. The poor packing

causes a lower volume fraction of cement particles at the repair-substrate interface, and the repair-substrate interface, therefore, shows a w/c ratio around 48% (on average) higher than in the repair material as given in Table 5.8. The high w/c ratio results in a high porosity and a high degree of hydration.

No matter in the repair material or at the repair-substrate interface, the saturated concrete substrate results in a higher porosity, a higher degree of hydration and a higher w/c ratio compared with the unsaturated concrete substrate, while the surface treatment does not have a significant influence on these data. This is in a good agreement with the observation from non-evaporable water test and MIP test.
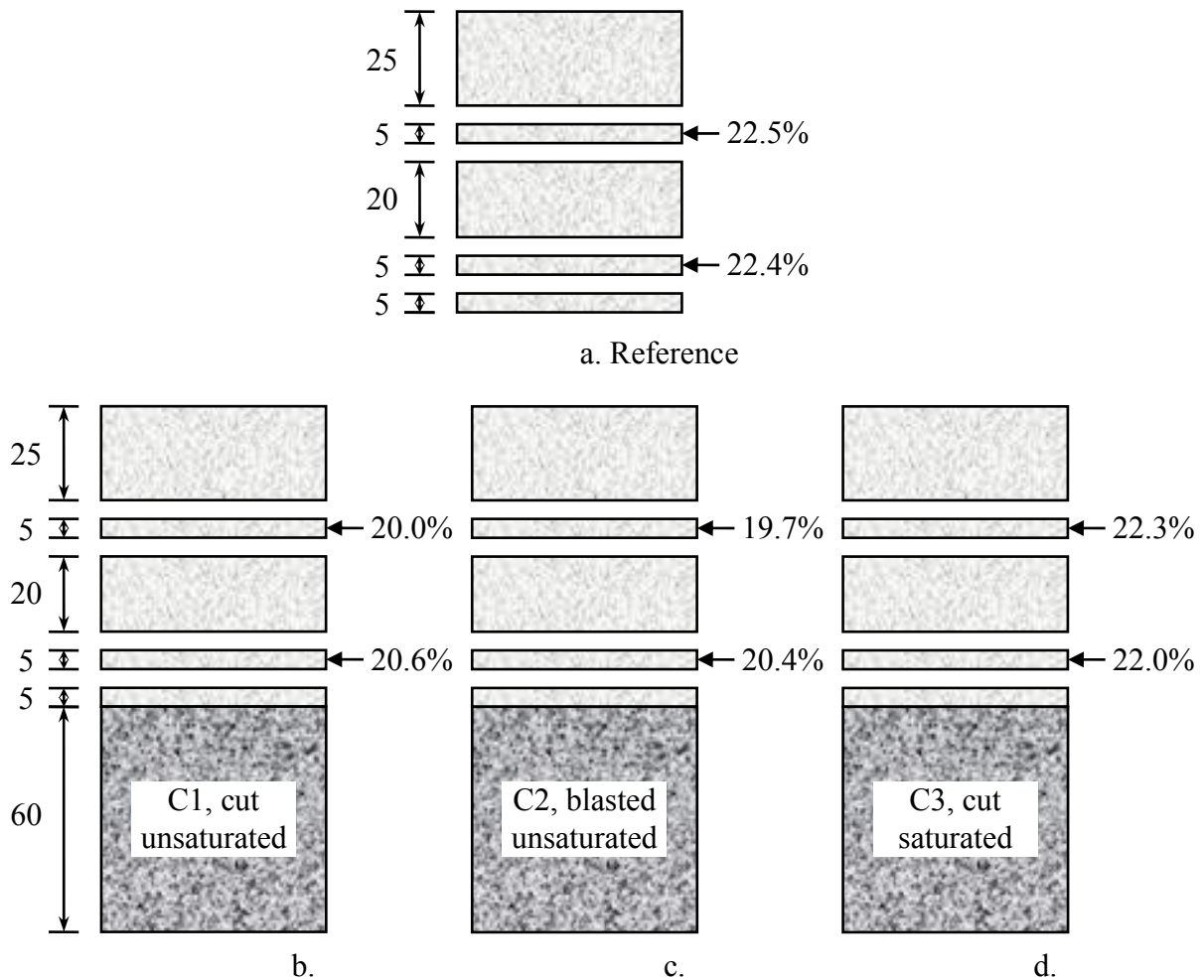

a. Reference

b.   c.   d.

Figure 5.12 Porosity of the reference and of the repair material at the age of 28 days measured by MIP (dimension in mm).

a. C1 (cut, unsaturated)   b. C2 (blasted, unsaturated)
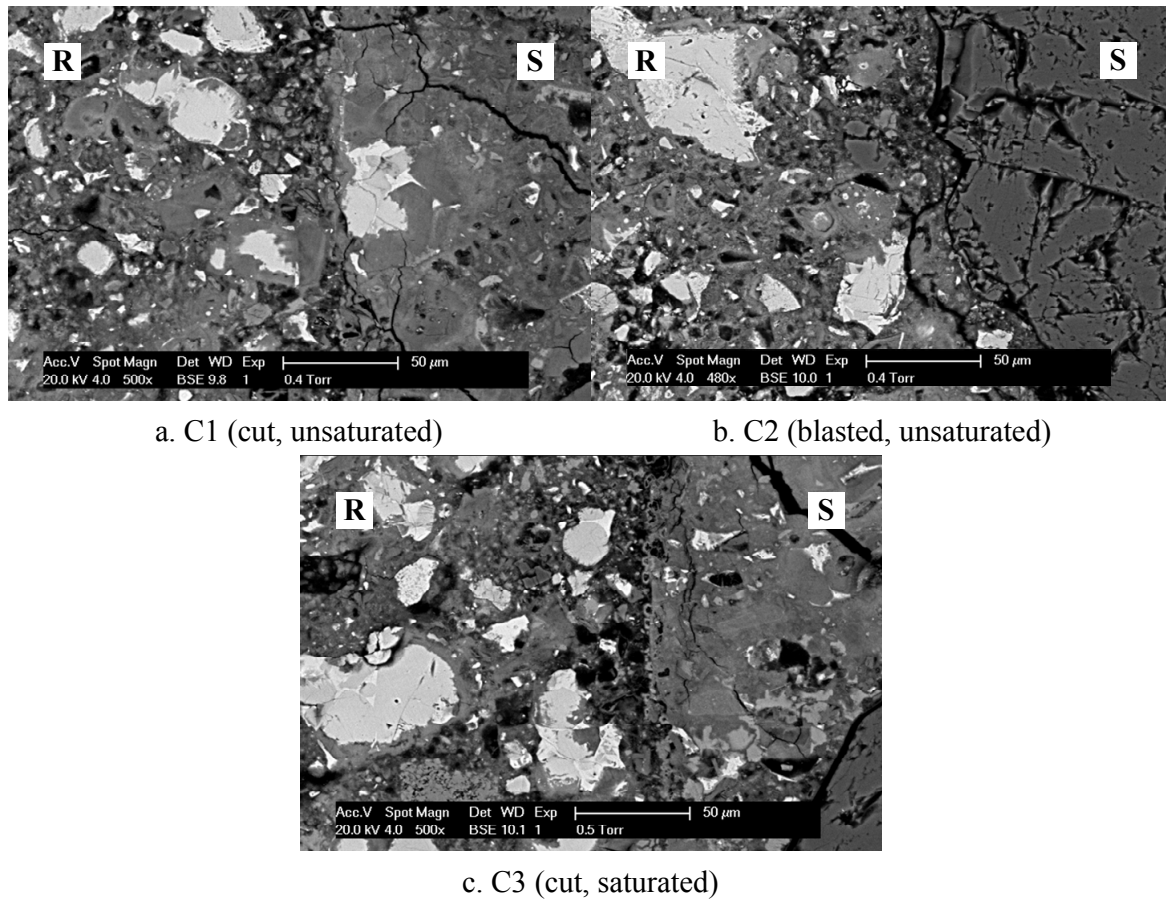

c. C3 (cut, saturated)

Figure 5.13 BSE images of the repair (R)-substrate (S) interface at the age of 28 days.

Table 5.7 Degree of hydration α, porosities ϕ and w/c ratios ω at the repair-substrate interface (20 µm wide) and the repair material at 28 days obtained by BSE image analysis.

Concrete substrate	Repair-substrate interface			Repair material		
	α [%]	ϕ [%]	ω	α [%]	ϕ [%]	ω
C1 (cut, unsaturated)	76.4 ± 2.3	24.0 ± 3.7	0.45 ± 0.03	65.4 ± 3.2	13.2 ± 2.6	0.31 ± 0.02
C2 (blasted, unsaturated)	78.0 ± 4.5	24.4 ± 3.0	0.46 ± 0.03	66.5 ± 5.5	13.0 ± 2.0	0.32 ± 0.03
C3 (cut, saturated)	80.8 ± 3.3	30.6 ± 2.3	0.55 ± 0.04	70.6 ± 2.4	16.9 ± 2.1	0.36 ± 0.02

Table 5.8 Proportions of the data at the repair-substrate interface to those in the repair material.

Concrete substrate	α	ϕ	ω
C1 (cut, unsaturated)	1.17	1.82	1.46
C2 (blasted, unsaturated)	1.17	1.87	1.47
C3 (cut, saturated)	1.14	1.81	1.51

5.5.4 Comparison of the degree of hydration and the porosity in the repair material measured by different techniques

The degree of hydration in the repair material was measured by means of non-evaporable water test and BSE image analysis. There is no significant difference between the experimental results measured by these two techniques.

The porosity in the repair material measured by the BSE image analysis is lower than that measured by the MIP test. Due to the resolution limit of BSE images, the pores with a diameter smaller than 0.25 μm are not detectable. Therefore, the lower porosity obtained by BSE image analysis can be attributed to the limited resolution of BSE measurement.

The calculated w/c ratio might be overestimated. For instance, in the specimen with the saturated substrate, the w/c ratio of the repair material should be 0.4, since the saturated substrate does not absorb water from the repair material. However, the w/c ratio obtained from BSE image analysis is 0.36, which is 10% lower than the expected value. Since the number of pixels of the hydration products is calculated by subtracting the numbers of pixels of the pores and the unhydrated cement particles from the number of total pixels, the underestimation of the porosity causes an overestimation of the hydration products. According to Eqs. 5.10-13, the overestimation of the hydration products results in a lower w/c ratio. Similarly, the porosity and the w/c ratio at the interface might be underestimated by BSE image analysis.

The w/c ratio in the repair material was recalculated using Eqs. 5.10-13 with the porosity measured by MIP test. The results are given in Table 5.9. The w/c ratio of the repair material cast on the saturated concrete substrate increases to 0.398, which is almost the same as the expected value of 0.4. The water absorption by the unsaturated concrete substrate causes a reduction of the w/c ratio from 0.4 to 0.36 (on average).

Table 5.9 Recalculated w/c ratios of the repair material using Eqs. 5.10-13 with the porosity measured by MIP test.

Concrete substrate	ϕ from MIP test	ω
C1 (cut, unsaturated)	20.6%	0.359
C2 (blasted, unsaturated)	20.4%	0.362
C3 (cut, saturated)	22.0%	0.398

5.5.5 Bond strength of the repair-substrate interface

Table 5.10 gives the results of the bond strength between the repair material and the concrete substrate. Each value is the average result of three parallel measurements. For the specimens with the unsaturated substrate, the blasted substrate results in a higher bond strength than the cut substrate. For the specimens with the cut substrate, the bond strength of the specimen with the unsaturated concrete substrate is higher than that with the saturated concrete substrate. Under uniaxial tensile load, the specimens with the cut substrates all failed at the repair-substrate interface as shown in Figure 5.14 (a) and (c), while those with blasted substrates failed in the repair material as shown in Figure 5.14 (b). It implies that the cut concrete substrate results in a poor interface, which is the weakest point in the specimens. For the specimens with the blasted substrate, the measured bond strength is the tensile strength of the repair material, and the real interfacial bond strength should be higher than this.

Table 5.10 Bond strength of the repair-substrate interface.

Concrete substrate	Bond strength [MPa]
C1 (cut, unsaturated)	1.13 ± 0.27
C2 (blasted, unsaturated)	1.64 ± 0.24
C3 (cut, saturated)	0.92 ± 0.23

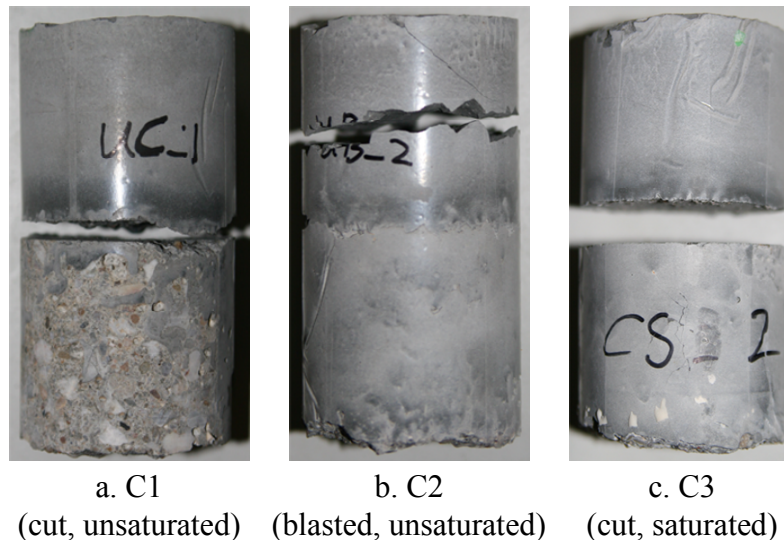| a. C1	b. C2	c. C3
(cut, unsaturated)	(blasted, unsaturated)	(cut, saturated)

Figure 5.14 Failure modes of the specimens under uniaxial tensile load.

5.6   Discussion

5.6.1   Influence of the water content of the concrete substrate

In the repair material, the cement hydration gradually consumes water, and the water content in the repair material decreases. Therefore, the capillary pressure in the repair material gradually increases. When the capillary pressure in the repair material exceeds that in the concrete substrate, water is forced to flow to the repair material. The saturated concrete substrate works as a "water reservoir" for the later cement hydration. The supply of the additional water accelerates cement hydration and leads to a denser pore structure. Since the repair material closer to the interface gains more water, it shows a higher degree of hydration and a lower porosity.

When the concrete substrate is unsaturated, it can absorb water from the repair material, and the water absorption causes a decrease in the w/c ratio of the repair material. The resultant w/c ratio has two effects on properties of the repair material. Firstly, the resultant w/c ratio decelerates the cement hydration and lowers the degree of hydration. Secondly, a low w/c ratio leads to a low porosity and a denser pore structure.

The w/c ratio is a crucial parameter determining the ultimate strength of cementitious materials. At the same age, a lower w/c ratio leads to a higher tensile strength and, therefore, a higher bond strength. When the concrete substrate is dry, it absorbs more water from the

repair material and causes a larger reduction in w/c ratio. As a result, the unsaturated substrate results in a higher bond strength, although repair material has a lower degree of hydration.

5.6.2 The "wall effect"

Due to the "wall effect", cement particles have a poor packing on the surface of the concrete substrate. The w/c ratio of the repair material locally increases at the repair-substrate interface, which contains relatively more pore space. The main hydration product, calcium-silicate hydrate, forms on the original cement particles and slowly grows to the pore space [van Breugel 1991]. Therefore, the pore space at the repair-substrate interface is more difficult to fill up with the hydration product. As a result, the repair-substrate interfacial zone has high porosity and low strength.

5.6.3 Influence of the surface roughness of the concrete substrate

Grit-blasting can be used to produce a rougher surface of the concrete substrate compared with cutting. The experimental results show that there is little difference between the water absorption of the concrete substrates prepared by different surface treatments. The surface roughness of the concrete substrate does not cause big difference on the decrease in the w/c ratio of the repair material. Therefore, the repair materials cast on the concrete substrate with different roughness have more or less the same degree of hydration and porosity.

The surface roughness has a big influence on the bond strength of the repair-substrate interface. The rougher the surface of the concrete substrate is, the higher the bond strength is. The reason is that the microscopic roughness can improve the mechanical interlocking between the repair material and the concrete substrate. Secondly, as the surface roughness increases, the contact area between the repair material and the concrete substrate increases.

5.7 Conclusions

The cement hydration and microstructure of the repair material and the bond strength of the repair-substrate interface were studied experimentally. Based on the experimental results and discussion, the following conclusions can be drawn:

- When the concrete substrate is unsaturated, it absorbs water from the fresh repair material and causes a decrease in w/c ratio of the repair material. The resultant w/c ratio results in a decrease in degree of hydration and a decrease in porosity.
- When the concrete substrate is saturated, it can provide additional water for the hydration of the repair material. The degree of hydration in the repair material, therefore, increases.
- Due to the "wall effect", the cement particles have a poor packing at the repair-substrate interface and the w/c ratio locally increases. This increased w/c ratio results in a porous interfacial zone and poor mechanical properties.
- The surface roughness does not cause big difference of the capillary absorption of the concrete substrate and the change of the w/c ratio. The degree of hydration and pore structure of the repair material show little difference. The increased roughness results in a higher bond strength, since a rougher surface leads to a greater mechanical interlocking.

Numerical Study on Cement Hydration and Microstructure of the Repair-Substrate Interface

6.1   Introduction

As discussed in Chapter 5, after placing repair material on a concrete substrate, the moisture exchange between these two materials takes place. The moisture exchange can result in the change of the water content in the repair material and at the interface, and affects the cement hydration and the microstructure. In this chapter, the cement hydration and the microstructure in the repair material and at the interface are investigated numerically, taking into consideration of the moisture exchange. The cement hydration model HYMOSTRUC is used to simulate the cement hydration process and the microstructure development at the interface. A module to simulate the moisture exchange process is added to the HYMOSTRUC model. Then, this model is validated by the experimental results discussed in Chapter 5. Moreover, this model is used to investigate the influence of some factors on the cement hydration and microstructure development, but not limited to these factors.

The HYMOSTRUC model is briefly described in Section 6.2. Section 6.3 presents the algorithm, which describes the cement hydration and the moisture exchange in the repair system. The implementation of the algorithm is discussed in Section 6.4. The simulations are presented in Section 6.5. This model is validated by comparing the simulation and experimental results. In Section 6.6, based on the simulation results, the influence of various factors on the cement hydration and microstructure development in the repair material and at the interface is discussed.

6.2   HYMOSTRUC

The HYMOSTRUC model was established by van Breugel [1991] for the simulation of the reaction process and of the formation of the microstructure in cement-based materials with different mixing composites (w/c ratio, cement particle size, chemical composition of cement and blended materials) at different scales (micro and macro). This model was further developed by Koenders [1997] and Ye [2003]. It has been demonstrated that this model is a good numerical tool for understanding the cement hydration process and the microstructure development of the cement-based materials [Ye 2003].

In the HYMOSTRUC model, the cement particles are modeled as a group of spheres. The spheres are randomly distributed in a three-dimensional body according to a given w/c ratio. At the beginning, the cement particles are surrounded by water. As the cement hydrates, the hydration products are formed in the vicinity of the hydrating cement particles [Taylor 1990], and the hydration products have a volume around 2.1 times larger than the hydrating cement

particles [Powers and Brownyard 1946]. The hydration process of individual cement particles is simulated as the growth of the spheres, which consists of a growing shell of hydration products and a shrinking unhydrated cement core as shown in Figure 6.1, left [van Breugel 1991]. As the shell of hydration products grows outwardly, the smaller cement particles, located in the vicinity of the larger cement particles, become embedded in the outer shell of the larger cement particles as shown in Figure 6.1, right [van Breugel 1991]. As the hydration process progresses, solid phases occupy more and more volume and the growing cement particles become more and more connected as depicted in Figure 6.2. This is considered the basis for simulating the development of the microstructure.
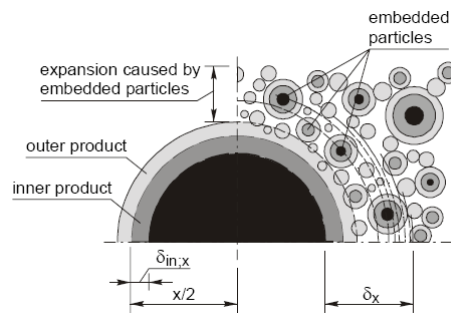

Figure 6.1 Schematic illustration of the growth mechanism of the HYMOSTRUC model [van Breugel 1991]. Left part shows the growth of a single cement particle and the formation of inner and outer products; right part shows the embedding of the small cement particles in the out shell of a large cement particle. Here, x is the diameter of the original cement particle; δ_x [μm] is the thickness of the shell of the hydration products, including the inner and outer products; $\delta_{in,x}$ [μm] is the thickness of the inner hydration products.

a. $\alpha = 0$

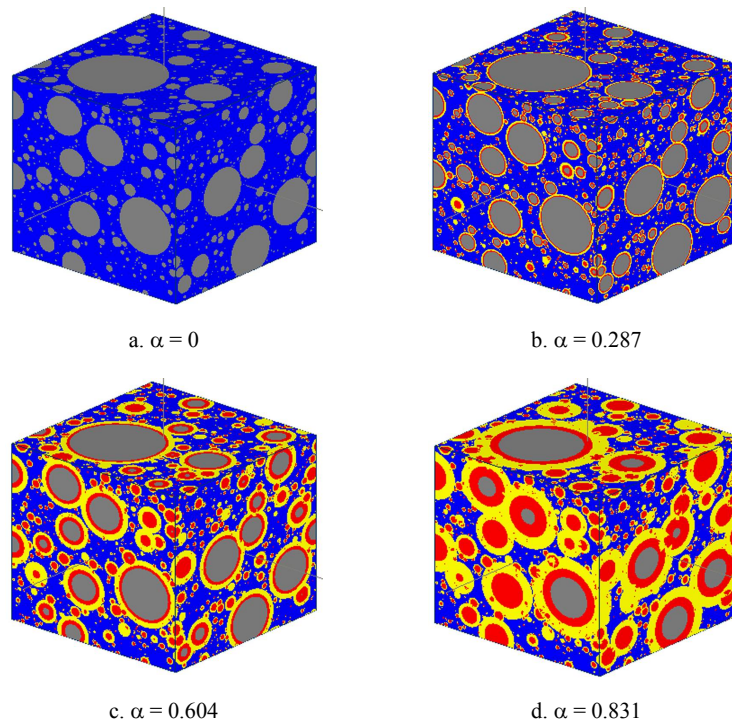b. $\alpha = 0.287$

c. $\alpha = 0.604$

d. $\alpha = 0.831$

Figure 6.2 Development of the microstructure of a hydrating cement paste [Sun et al. 2005].

6.3 Modeling

In this section, the cement hydration and the moisture exchange are discussed separately and described mathematically. Since these two processes can both result in the change of the water content in the repair system, these two processes are coupled, while taking into account the mass conservation of water.

6.3.1 Cement hydration

As cement hydration proceeds, water is gradually consumed and the hydration products form in the pore structure. Consequently, the influence of the cement hydration on the moisture transport has two aspects. Firstly, the water loss due to the continuous hydration leads to a decrease in the water content in the paste. Secondly, the formation of hydration products results in a reduction in the porosity and a change of the pore size distribution. These two aspects are both dependent on the degree of hydration and are discussed as follows.

6.3.1.1 Water consumed by the cement hydration

For a certain initial w/c ratio ω_0 [-], the initial volume of cement in a unit volume of the cement paste $V_{0,ce}$ [cm^3/cm^3] can be calculated as:

$$V_{0,ce} = \frac{\rho_w}{\rho_w + \rho_{ce}\omega_0} \tag{6.1}$$

According to Powers' model [Powers and Brownyard 1946], the amount of water consumed by the cement hydration can be calculated approximately:

$$\frac{\partial \theta_{hy}}{\partial t} = -\beta V_{0,ce} \frac{\partial \alpha}{\partial t} \tag{6.2}$$

where $\dfrac{\partial \theta_{hy}}{\partial t}$ [cm^3/(cm^3×s)] is the rate of the change of the water content due to cement hydration, β [cm^3/cm^3] is the volume of water consumed by the hydration per unit volume of cement, and α [-] is the degree of hydration.

Based on the measurement on the total and non-evaporable water content in hardening cement paste, Power and Brownyard [1946] proposed that complete hydration of 1 g of cement consumes approximately 0.4 g of water. Therefore, β can be calculated as follows:

$$\beta = 0.4 \times \frac{\rho_{ce}}{\rho_w} \tag{6.3}$$

where ρ_{ce} [g/cm^3] is the density of cement, which is 3.15 g/cm^3; ρ_w [g/cm^3] is the density of water, which is 1 g/cm^3.

6.3.1.2 Degree of hydration with moisture transport

Water plays a very important role in the cement hydration process. In the case with moisture exchange, the moisture transport affects the rate of cement hydration. When water moves out of the cement paste, less water is left for cement hydration and leads to a lower degree of

hydration. Inversely, when water moves into the hydrating cement paste, the additional water is available for cement hydration and this leads to a higher degree of hydration.

The basic formula for determining the rate of hydration of the individual cement particle can be described as [van Breugel 1991]:

$$\frac{\partial \delta_{in,x}}{\partial t} = K_0 \times \Omega_1 \times \Omega_2 \times \Omega_3 \times F_1 \times \left(F_2 \times \left(\frac{\delta_{tr}}{\delta_x} \right)^{\beta_1} \right)^{\lambda}$$ (6.4)

where $\delta_{in,x}$ [μm] is the penetration depth of the reaction front in cement particle x; K_0 [-] is the basic rate factor depending on the rate-controlling mechanism, on the cement composition and on the degree of hydration; Ω_i ($i = 1, 2, 3$) [-] are reduction factors accounting for the different effects of water, which will be discussed in details in the following; F_i ($i = 1, 2$) [-] are temperature-related factors accounting for the effects of curing temperature; δ_{tr} [μm] is the transition thickness; δ_x [μm] is the total thickness of the product layer; β_1 [-] is a constant and λ [-] is the factor depending on the rate-controlling mechanism.

The degree of hydration of cement particle x can be calculated by dividing the incrementally decreased volume of the hydrated cement by the initial volume of the cement particle:

$$\alpha_x = 1 - \left(1 - \frac{\delta_{in,x}}{0.5 d_{0,x}} \right)^3$$ (6.5)

where α_x [-] is the degree of hydration of cement particle x, and $d_{0,x}$ [μm] is the initial diameter of cement particle x.

By integrating the degree of hydration of all cement particles, the overall degree of hydration α is obtained:

$$\alpha = \frac{1}{G(x-1)} \sum_{z=x_{min}}^{x-1} \alpha_z \times W(z)$$ (6.6)

where $G(x-1)$ [g] is the sum of the initial amount of cement and $W(z)$ [g] is the mass of cement particle z.

In Eq. 6.4, there are three water-related factors Ω_1, Ω_2 and Ω_3. Ω_1 covers the so-called water withdrawal mechanism. When some small cement particles are embedded in the product shell of the central cement particles, the embedded cement particles have an influence on the water penetration into the central cement particles and reduce the cement hydration rate of the central cement particles. The amounts of water available for the embedded cement particles and the central cement particle, therefore, depend on the distribution of small cement particles around the large cement particles and the degree of hydration of individual cement particles.

Ω_2 is defined as the reduction factor referring to the water distribution in the pore system. The cement hydration gradually consumes water and empties pores starting from the large ones. The emptying of pores retards the cement hydration, since the ions involved in the reaction process have to travel to reach the cement particles located adjacent to the wall of empty pores [van Breugel 1991]. Ω_2 is determined by dividing the wall area of the water-filled pores $A_{wat}(\alpha)$ [cm^2/cm^3] by the total pore wall area $A_{por}(\alpha)$ [cm^2/cm^3]:

$$\Omega_2(\alpha) = \frac{A_{wat}(\alpha)}{A_{por}(\alpha)} \tag{6.7}$$

For the water-filled pores and the total pores, the wall area can be calculated as follows:

$$A_{wat}(\alpha) = 4 \times a \times \phi(\alpha) \times \left(\frac{1}{r_0} - \frac{1}{r_{wat}(\alpha)} \right) \tag{6.8}$$

$$A_{por}(\alpha) = 4 \times a \times \phi(\alpha) \times \left(\frac{1}{r_0} - \frac{1}{r_{por}(\alpha)} \right) \tag{6.9}$$

where a [-] is a pore size distribution constant; $\phi(\alpha)$ [-] is porosity; r_0 [μm] is radius of the minimum capillary pore (0.002 μm); $r_{por}(\alpha)$ [μm] is the radius of the largest pore; $r_{wat}(\alpha)$ [μm] is the radius of the largest water-filled pore. Inserting Eq. 6.8 and Eq. 6.9 into Eq. 6.7 yields:

$$\Omega_2 = \frac{r_{wat}(\alpha) - r_0}{r_{por}(\alpha) - r_0} \times \frac{r_{por}(\alpha)}{r_{wat}(\alpha)} \tag{6.10}$$

van Breugel [1991] proposed that the parameters can be determined as follows:

$$r_{por}(\alpha) = r_0 \times \exp\left(\frac{\phi(\alpha)}{a} \right) \tag{6.11}$$

$$r_{wat}(\alpha) = r_0 \times \exp\left(\frac{V_{fr}(\alpha)}{a} \right) \tag{6.12}$$

where $V_{fr}(\alpha)$ [cm^3/cm^3] is the volume of the free capillary water.

If the moisture exchange takes place between the cement paste and the surrounding materials, the amount of free capillary water can be calculated by subtracting the amount of water consumed by cement hydration and the change of water content due to moisture exchange from the initial amount of water:

$$V_{fr}(\alpha) = \frac{\rho_{ce}}{\rho_w + \rho_{ce}\omega_0} \times (\omega_0 - 0.4\alpha) + V_{ex} \tag{6.13}$$

where V_{ex} [cm^3/cm^3] is the change of water content due to moisture exchange.

Ω_3 is defined as the reduction factor referring to the availability of pore water. As the cement is dissolved in water, a corresponding amount of ions exist in the pore water. When the ion concentration remains constant, there should be a balance between the rate of ion dissolving into water and the rate of ion consumption for product formation. Therefore, a gradual decrease in the amount of water leads to a decrease in the amount of ions dissolved in water and thus a decrease in the amount of product formation. Assuming a constant ion concentration in pore water, Ω_3 can be calculated as follows:

$$\Omega_3 = \frac{\omega_0 - 0.4\alpha}{\omega_0} + \frac{V_{ex}}{V_{0,w}} \tag{6.14}$$

where $V_{0,w}$ [cm^3/cm^3] is the initial volume of water in a unit volume of cement paste, and it can be calculated as follows:

$$V_{0,w} = \frac{\rho_{ce}\omega_0}{\rho_w + \rho_{ce}\omega_0} \tag{6.15}$$

6.3.1.3 Pore structure

The cement hydration results in a change of the pore structure of the hardening cement paste. The pore structure of the cement paste in the repair material determines the moisture transport between the repair material and the concrete substrate (see Section 6.3.2.2 and 6.3.2.3). Therefore, the pore structure of the hardening cement paste is studied in this section.

In general, the hardening cement paste comprises three components from the volumetric standpoint, i.e. unhydrated cement, hydration products and capillary porosity. The capillary porosity is defined as the remnants of the initially water-filled space. The hydration products occupy more space than the cement that has reacted. The hydration products gradually grow in the initially water-filled space. Therefore, as the cement hydration proceeds, the total porosity decreases and the pore sizes become smaller. According to Powers' model, the porosity can be calculated by subtracting the volumes of the unhydrated cement and the hydration products from the total volume of the hardening cement paste, given as:

$$\phi(\alpha) = 1 - \frac{\rho_w}{\rho_w + \rho_{ce}\omega_0}(1 + 1.1\alpha) \tag{6.16}$$

As hydration proceeds, the capillary pores are generally filled with hydration products. The formation of hydration products results in a reduction in the size of the capillary pores and a change of pore size distribution. In general, the size of capillary pores in the hardening cement paste is distributed over several orders of magnitude, ranging from 10 nm to 10 μm. The pore size distribution in the hardening cement paste is often assumed to be in a simplistic Raleigh-Ritz distribution, expressed as:

$$V = 1 - \exp(-Br) \tag{6.17}$$

$$dV = Br \exp(-Br)d \ln r \tag{6.18}$$

where V [cm^3/cm^3] is the volumetric porosity; B [1/m] is the Raleigh-Ritz pore size distribution constant, which represents the peak of the pore size distribution on a logarithmic scale; r [μm] is the pore radius. As the cement hydration proceeds, the hydration products form in the pore structure and this process results in a reduction in porosity and a change of pore size distribution. Therefore, B is a degree of hydration dependent parameter, which can be determined from the MIP results.

6.3.2   Moisture exchange

Moisture transport takes place in the porous medium in the form of liquid and vapor. At low relative humidity, water exists mainly in the form of vapor. The main mechanism for moisture transport is diffusion of vapor. At high relative humidity, the capillary action dominates the water transport. This process is quite rapid compared with the vapor diffusion. A study [Crausse et al. 1981] conducted on a sand column shows that when the relative humidity in the pore system exceeds 4%, the contribution of the vapor phase to the overall moisture transport is negligible. In cement paste and concrete, the relative humidity is normally higher than 75% [Neville 1995]. Therefore, the vapor transport in cement paste can be ignored in this study.

6.3.2.1   Change in the water content due to the moisture exchange

Darcy's law is usually used as the general equation describing the water transport, given as follows [Dullien 1992]:

$$q = -K_\theta (\nabla p - \rho_w g) \qquad (6.19)$$

where q [$1/(cm^2 \times s)$] is the volumetric flux of water, K_θ [$(cm^3/cm^3)/(N \times s)$] is the volumetric unsaturated water permeability dependent on the water content θ, p [N/cm^2] is the capillary pressure and g [N/g] is the acceleration of gravity. The pressure induced by gravity force is usually several orders of magnitude smaller than the capillary pressure. Therefore, the item ρg in the right hand side of Eq. 6.19 can be neglected. The moisture transport in a porous medium can be approximated as:

$$q = -K_\theta \nabla p \qquad (6.20)$$

The rate of the change of the water content due to moisture exchange $\dfrac{\partial \theta_{mex}}{\partial t}$ [$cm^3/(cm^3 \times s)$] can be calculated as:

$$\frac{\partial \theta_{mex}}{\partial t} = \nabla \bullet q \qquad (6.21)$$

6.3.2.2   Determining the unsaturated water permeability K_θ

Considering the steady-state laminar flow through the porous medium, Poiseuille's law provides a mathematical expression relating the water permeability to the pore geometry [Feldman 1986]:

$$K_s = \xi \frac{1}{\mu} \iint_{surface} v dv \qquad (6.22)$$

where K_s [$(cm^3/cm^3)/(N \times s)$] is the saturated water permeability, ξ [-] is a constant, μ [$Pa \times s$] is the water viscosity and v [$1/cm^3$] is the volumetric rate of water flow.

Based on a simple pore structure model considering porous medium as a set of cylindrical tubes with different radii as shown in Figure 6.3, the saturated water permeability can be calculated as follows [Maekawa et al. 1999]:

$$K_s = \frac{\phi^2}{50\mu}\left(\int_0^\infty rdV\right)^2$$
(6.23)

where r [µm] is the pore radius, and V [cm^3/cm^3] is the volumetric porosity.
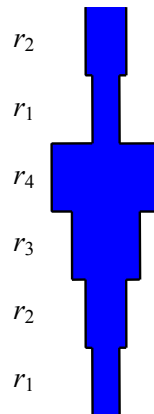

Figure 6.3 Imaginary pore structure consisting of a set of cylindrical tubes with different radii.

In an unsaturated porous medium as shown in Figure 6.4, the moisture transport is determined by the properties of the water-filled pores [Maekawa et al. 1999]. The unsaturated water permeability can be obtained from:

$$K_\theta = \frac{\phi^2}{50\mu}\left(\int_0^{r_c} rdV\right)^2$$
(6.24)

where r_c [µm] is the Kelvin equilibrium radius defined as the pore radius with which the equilibrated liquid-vapor interface is created. This pore radius is the maximum radius of the pores that are completely filled. The pores with a radius larger than r_c only contain a layer of the adsorbed water of which the thickness depends on the RH in the pore system.
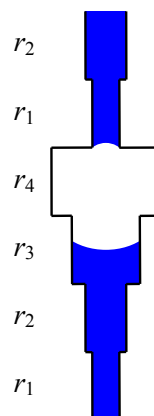

Figure 6.4 Partially saturated pore structure. r_1, $r_2 < r_c$; $r_3 = r_c$; $r_4 > r_c$.

At high relative humidity, the amount of the adsorbed water is relatively small compared with the free water. The water content θ can be calculated by integrating the volume of pores with radii smaller than r_c:

$$\theta = \int_0^{r_c} dV \tag{6.25}$$

With dV calculated by Eq. 6.18, the water content in the pore system can be calculated as follows:

$$\theta = \phi\left(1 - \exp(-Br_c)\right) \tag{6.26}$$

Substituting Eq. 6.18 into Eq. 6.24 yields the water-content dependent permeability of concrete:

$$K_\theta = \frac{\phi^2}{50B^2\mu}\left(1 - \left(1 - \ln\left(1 - \frac{\theta}{\phi}\right)\right) \times \left(1 - \frac{\theta}{\phi}\right)\right)^2 \tag{6.27}$$

when $\dfrac{\theta}{\phi} = 1$, $K_\theta = K = \dfrac{\phi^2}{50B^2\mu}$.

6.3.2.3 Determining the capillary pressure p

When a liquid meets a solid surface, a contact angle forms at the interface. The contact angle is defined by the planes tangent to the liquid-liquid interface and the liquid-solid interface as shown in Figure 6.5. At the interface, the contact angle and the surface tension forces satisfy a relationship described mathematically by the Young's equation:

$$\gamma_{sv} - \gamma_{sl} = \gamma_{lv}\cos\theta_c \tag{6.28}$$

where γ_{sv} [N/m] is the solid-vapor interfacial energy, γ_{sl} [N/m] is the solid-liquid interfacial energy, γ_{lv} [N/m] is the liquid-vapor interfacial energy (i.e. the surface tension of liquid) and θ_c [°] is the equilibrium contact angle between the liquid and the solid. Water has a contact angle between 20° and 30° with most solid materials [Aligizaki 2006].
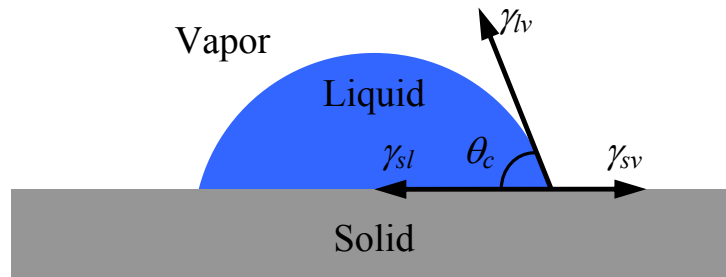

Figure 6.5 Illustration of contact angle forming at interface.

Surface tension also causes a pressure difference across the liquid-vapor interface. The pressure difference is balanced by the curved liquid-vapor interface as illustrated in Figure 6.5. The pressure difference is a function of curvature of the liquid-vapor interface, which can be calculated by the Laplace's equation:

$$p = -\frac{2\gamma_{lv}}{R} \tag{6.29}$$

where R [μm] is the average radius of the curvature of the liquid-vapor interface.

Since the liquid-vapor interface has a spherical shape in a tube (as shown in Figure 6.6), the radius of the sphere can be calculated as:

$$R = \frac{r_s}{\cos\theta_c} \tag{6.30}$$

where r_s [μm] is the maximum water-filled pore radius when the adsorbed water is not considered. When considering the water adsorption and condensation, this radius is smaller than the equilibrated interface radius r_c with which the equilibrated interface of liquid and vapor is created. An explicit equation was proposed to describe the relationship between these two values [Maekawa et al. 1999]:

$$r_c = Cr_s \tag{6.31}$$

where the constant C [-] was determined by numerous comparisons of the analytical predictions of the equilibrated interface radius r_c as obtained from the modified BET theory and the maximum water-filled pore radius r_s as given by Kelvin's equation [Maekawa et al. 1999]. The value of 2.15 is often quoted for the constant C.

Substituting Eqs. 6.26, 6.30 and 6.31 into Eq. 6.29, the pressure difference can be calculated as:

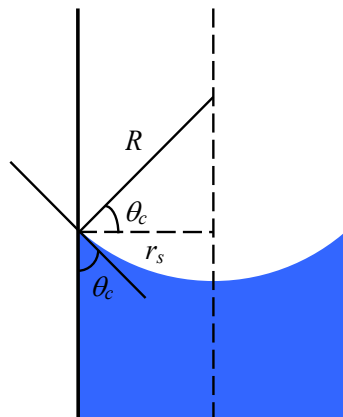$$p = \frac{2CB\gamma_{lv}\cos\theta_c}{\ln\left(1 - \dfrac{\theta}{\phi}\right)} \tag{6.32}$$

Figure 6.6 Spherical meniscus with contact angle less than 90°.

6.3.3   Interaction of cement hydration and moisture exchange

The cement hydration of the repair material consumes water, while the moisture exchange causes water redistribution in the repair material and the concrete substrate. Consequently, these two processes can both result in the change of the water content in the repair system. Considering mass conservation of water, the change of the water content can be calculated by summing up those caused by these two processes:

$$\frac{\partial \theta}{\partial t} = \frac{\partial \theta_{hy}}{\partial t} + \frac{\partial \theta_{mex}}{\partial t} \tag{6.33}$$

where $\frac{\partial \theta}{\partial t}$ [m^3/(m^3 × s)] is the rate of the change of the water content in the repair system.

Substituting Eq. 6.1 and Eq. 6.21 into Eq. 6.33, the expression for describing the moisture transport coupled with the cement hydration can be obtained:

$$\frac{\partial \theta}{\partial t} = -\beta V_{0,ce} \frac{\partial \alpha}{\partial t} - \nabla \bullet (K_\theta \nabla p) \tag{6.34}$$

6.4   Implementation

The numerical model for simulating the moisture transport and cement hydration of the repair system is programmed using Matlab. The procedures of the simulation on the cement hydration and the moisture exchange will be discussed in detail in the following.

6.4.1   Repair system

In order to compare the experiments presented in Chapter 5, the simulated repair system has a comparable structure as the specimens investigated in the experiments. The repair system consists of a layer of repair material bonded on a layer of concrete substrate as shown in Figure 6.7. The thickness of the repair material varies from 10 mm to 30 mm to 60 mm, and the thickness of the concrete substrate is 60 mm. The repair material is ordinary Portland cement paste. In the simulation, the concrete substrate is described as a two-phase material, i.e. mortar and coarse aggregates. Since the coarse aggregates have a very low porosity, it is assumed that only the mortar contributes to the porosity of the concrete substrate.
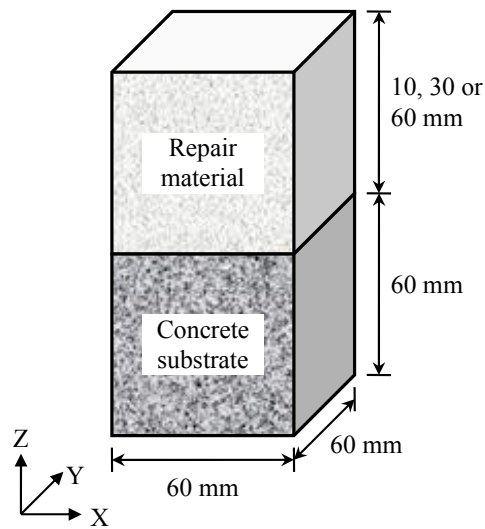
Figure 6.7 Dimension of the repair system used in the simulations.

6.4.2   Generating the concrete substrate

Table 6.1 gives the proportion of the coarse aggregates in the concrete substrate. The coarse aggregates occupy 44.4% volume of concrete. The coarse aggregates are simulated as a group of spherical particles with the size distribution given in Table 6.1. These spherical particles are randomly distributed in a cube with a dimension of 60^3 mm^3 as shown in Figure 6.8. The rest space is filled by the mortar, which consists of cement paste and sand.

Table 6.1 Proportion of the coarse aggregates in the concrete substrate.

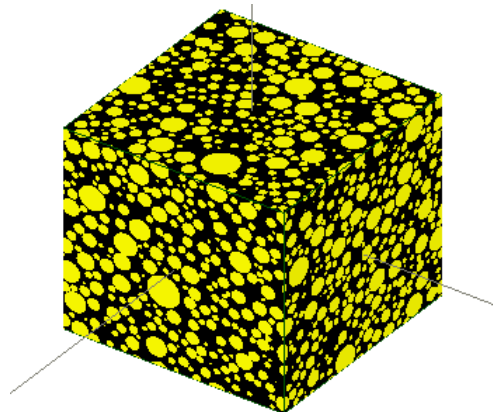| Aggregate size [mm]	Weight content [kg/m^3]
2-4	271.6
4-8	362.1
8-16	543.2

Figure 6.8 Aggregates in the concrete substrate ($60 \times 60 \times 60$ mm^3).

6.4.3   Generating the concrete substrate

The measured surface profile as discussed in Chapter 5 is used in the simulation of the surface roughness of the concrete substrate. The surface profile of the concrete substrate was measured by laser profilometry discussed in Section 5.3.4. It is found that the cut surface is smooth, and the average surface profile R_a is 0.6 mm. The grit-blasted surface is relatively rough, and the average surface profile R_a is 3.5 mm. In the simulation, the cut surface is assumed as a flat surface. The measured surface profile of the grit-blasted substrate is assigned to the simulated rough surface as shown in Figure 6.9.

The simulation of the surface profile of the grit-blasted substrate is illustrated in Figure 6.9. Firstly, the measured surface profile is divided into small parts in every 1 mm as shown in Figure 6.9 (b). Secondly, for each small part, the surface profile is averaged. Last, the simulated surface profile can be obtained by connecting the averaged profiles as shown in Figure 6.9 (c).

a. Measured profile of the grit-blasted surface
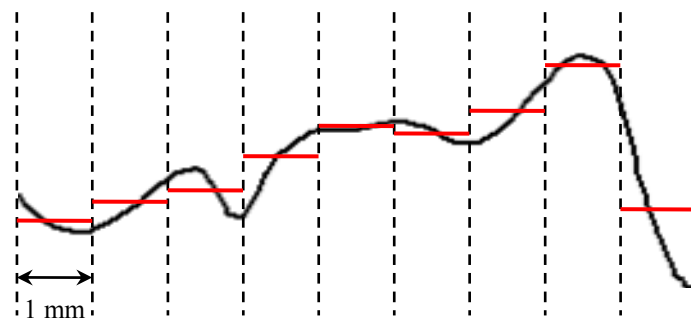
b. Dividing the surface profile and averaging it
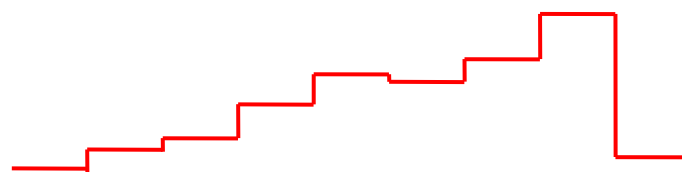
c. Simulated profile of the grit-blasted surface

Figure 6.9 Simulation the surface profile of the grit-blasted concrete substrate.

6.4.4   The "wall effect" on the repair-substrate interface

Due to the "wall effect", the cement particles have a loose packing at the surface of the concrete substrate. The w/c ratio is, therefore, locally increased. In the simulation, the cement particles are considered as a group of spheres. The distribution of these spheres on a rigid boundary is used to simulate the packing of cement particles at the surface of the concrete substrate as shown in Figure 6.10. The w/c volume ratio from the rigid boundary can be calculated by dividing the number of the voxels of cement by that of water. The w/c volume ratio is then converted to the w/c ratio by dividing the w/c density ratio.

Figure 6.11 shows the local w/c ratio over the distance from a rigid boundary. Close to the rigid boundary, the local w/c ratio is very high. As the distance from the concrete substrate increases, the local w/c ratio decreases. From the curves, it is found that when the w/c ratio ranges from 0.26 to 0.4, the thickness of the interfacial zone is about 20 μm. In the following discussion, this 20 μm-thick interfacial zone is called the "interface", which is distinguished from the "bulk repair material" itself as shown in Figure 6.12.
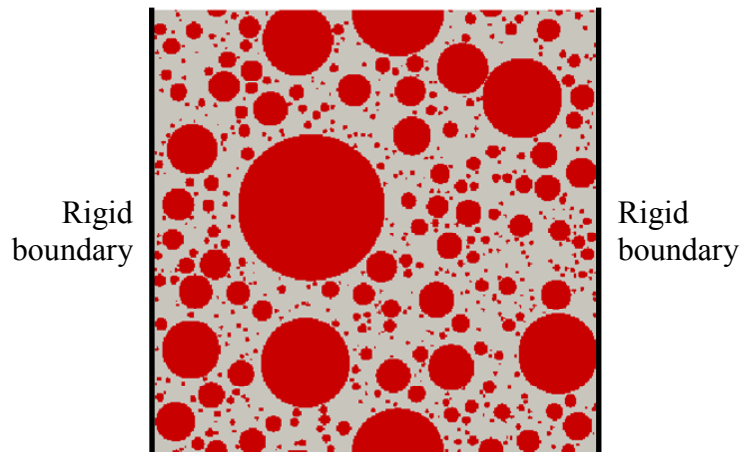

Figure 6.10 Cement particle packing at rigid boundaries (100^2 μm^2).
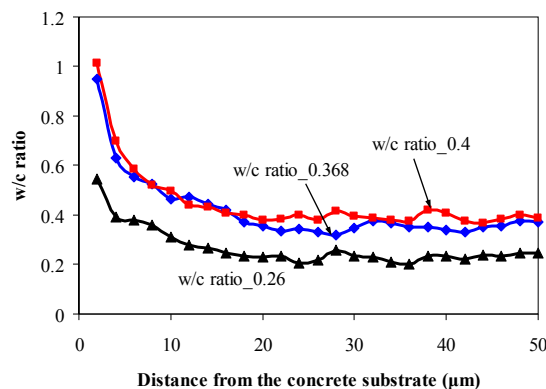

Figure 6.11 Local w/c ratio versus the distance from the concrete substrate in the cement pastes with the overall w/c ratios of 0.26, 0.368 and 0.4.
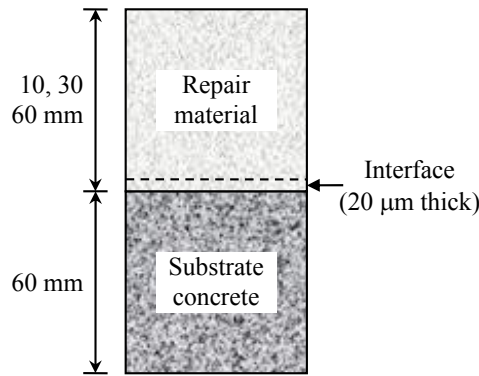
Figure 6.12 Definition of the "bulk repair material" and the "interface" for the following discussion.

6.4.5 Water absorption by the concrete substrate and resultant w/c ratio in the bulk repair material and at the interface

After the repair material is placed on the concrete substrate, the repair material needs several hours to harden. During this period, the repair material is still fresh and water is gradually absorbed by the concrete substrate. The water absorption is driven by the capillary pressure and the hydraulic pressure generated by the gravity force of the fresh repair material. Before the setting of the repair material, the solid phases, i.e. the cement particles and a small amount of the hydration products are suspended in water and isolated from each other. Consequently, the hydraulic pressure generated by the gravity force of the fresh repair material can be calculated as follows:

$$p_{presetting} = \frac{(\omega_0 + 1)\rho_{ce}}{\rho_w + \omega_0 \rho_{ce}} g h_r \qquad (6.35)$$

where h_r [mm] is the thickness of the repair material. The moisture transport inside the concrete substrate can be calculated with Eq. 6.21.

The loss of water in the repair material results in a reduction of the w/c ratio, called the resultant w/c ratio. The resultant w/c ratio of the repair material $\omega_{res}(x,y,z)$ [-] can be calculated as follows:

$$\omega_{res}(x,y,z) = \omega_0 \left(1 - \frac{V_{ab}(x,y,x)}{V_{0,w}} \right) \qquad (6.36)$$

where $V_{ab}(x,y,z)$ [cm^3/cm^3] is the volumetric water loss in the repair material due to the water absorption of the concrete substrate.

6.4.6 Setting of the repair material

The setting time of the repair material is calculated in this section. Setting refers to the change of cementitious materials from a fluid to a rigid stage. After setting of the repair material, the

solid framework forms. Therefore, the loss of water cannot result in any reduction of the w/c ratio of the repair material.

The setting time of the repair material depends on its w/c ratio. As shown in Figure 6.13, when the w/c ratio is between 0.3 and 0.5, the setting time is proportional to the w/c ratio. Consequently, the setting time of the repair material t_{set} [h] can be determined as:

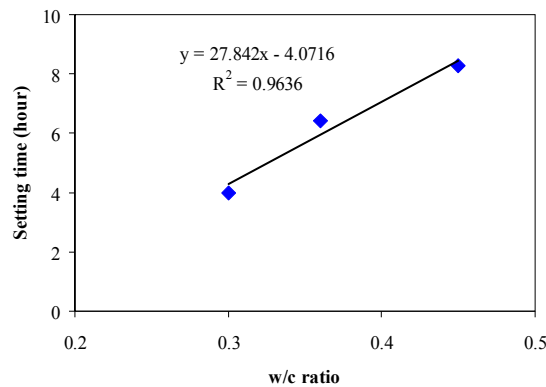$$t_{set} = 27.8 \times \omega_{res} - 4.1 \tag{6.37}$$

Figure 6.13 Setting time versus the w/c ratio of the cement paste (after Amziane [2006]).

6.4.7 Cement hydration and moisture transport after setting of the repair material

After setting of the repair material, the driving force for the moisture exchange becomes the capillary gradient in these two materials, and the moisture exchange process can be simulated using Eq. 6.35. In the simulation, the cement hydration and the change in the porosity in the concrete substrate are not taken into consideration. The degree of hydration and the porosity of the cement paste are calculated using Eq. 6.6 and Eq. 6.16, respectively.

6.5   Simulations

6.5.1   Inputs of the simulation

Table 6.2 summarizes the inputs of the simulations S1-S10. Among the ten simulations, S1 is set as a reference. The simulations S1-S3 are used to simulate the three repair systems, which were experimentally investigated in Chapter 5. By comparing the simulations S2-S10 with S1, the following five factors can be investigated:
- The surface roughness of the concrete substrate: S1 and S2
- The degree of saturation of the concrete substrate: S1, S3 and S4.
- The porosity of the mortar in the concrete substrate: S1, S5 and S6.
- The thickness of the repair material: S1, S7 and S8.
- The w/c ratio of the repair material: S1, S9 and S10.

The repair systems were cured at 20°C in a sealed condition. The cement hydration and porosity in the bulk repair material and at the interface in the first 28 days were simulated.

6.5.2 Water absorption by the concrete substrate

Before the setting of the repair material, the concrete substrate absorbs water from the repair material. Figure 6.14 shows a comparison of the calculated amount of water absorbed by an unsaturated concrete substrate obtained from the simulation S1 and from the water absorption test discussed in Chapter 5. The good agreement between the two curves indicates that the simulation gives a good prediction of the water absorption process of the concrete substrate.

Figure 6.15 shows the change of the water content profile in the concrete substrate due to the water absorption obtained from the simulation S1. The water absorption results in an increase in the water content of the concrete substrate. Water in the concrete substrate gradually moves from the surface exposed to the repair material to the bottom. The concrete substrate becomes more and more saturated.

Table 6.2 Inputs of the simulations S1-S10.

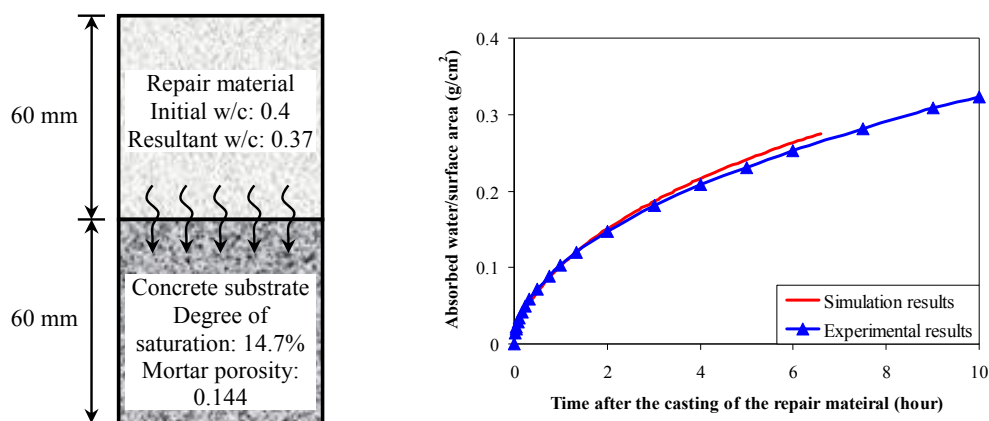| Simulation number	Thickness of repair material h_{rep} [mm]	w/c ratio of repair material ω_0	Thickness of concrete substrate h_{sub} [mm]	Degree of saturation of concrete substrate θ/ϕ	Mortar porosity in concrete substrate ϕ	Surface of concrete substrate
S1	60	0.4	60	14.7%	0.144	Smooth
S2	60	0.4	60	14.7%	0.144	Rough
S3	60	0.4	60	100%	0.144	Smooth
S4	60	0.4	60	50%	0.144	Smooth
S5	60	0.4	60	14.7%	0.2	Smooth
S6	60	0.4	60	14.7%	0.08	Smooth
S7	30	0.4	60	14.7%	0.144	Smooth
S8	10	0.4	60	14.7%	0.144	Smooth
S9	60	0.3	60	14.7%	0.144	Smooth
S10	60	0.5	60	14.7%	0.144	Smooth

Figure 6.14 Comparison of the amount of water absorbed by the concrete substrate obtained from the simulation S1 (see Table 6.2) and from the water absorption test (Section 5.3.3).
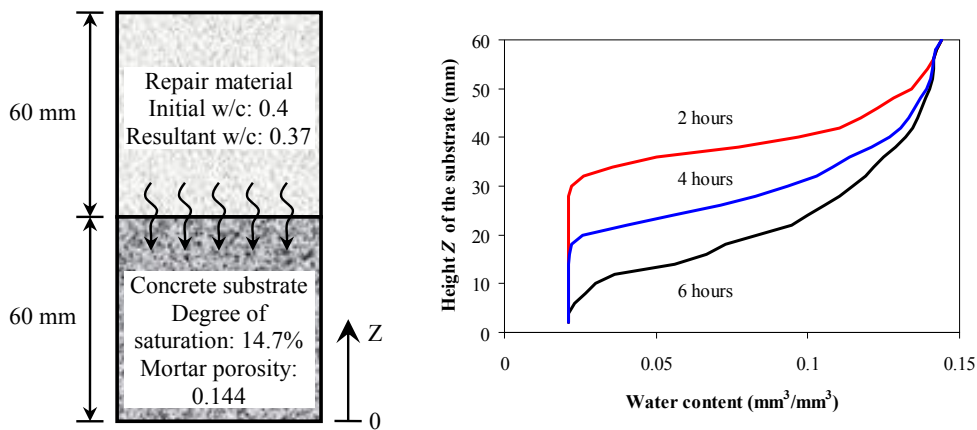
Figure 6.15 Change of the water content in the concrete substrate at 2, 4 and 6 hours after placing the repair material obtained from the simulation S1 (see Table 6.2).

6.5.3   Resultant w/c ratio in the bulk repair material and at the interface

The water absorption of the concrete substrate causes a reduction of the w/c ratio in the bulk repair material and at the interface. Table 6.3 lists the amount of water absorbed by the concrete substrate and the resultant w/c ratio in the bulk repair material and at the interface. As discussed in Section 6.4.3, due to the "wall effect", the interface has a relatively loose particle packing. Therefore, the resultant w/c ratio at the interface is higher than that in the bulk repair material.

   Figure 6.16 shows the resultant w/c ratio in the bulk repair material and at the interface obtained from the simulation S1. Within the 10 mm-thick bulk repair material above the concrete substrate, as the bulk repair material approaches to the concrete substrate, the resultant w/c ratio decreases. Above this zone in the bulk repair material (height from 10 mm to 60 mm), there is no difference in the resultant w/c.

Table 6.3 Simulated amount of the absorbed water by the substrate and the resultant w/c ratio in the bulk repair material and at the interface after setting of the repair material.

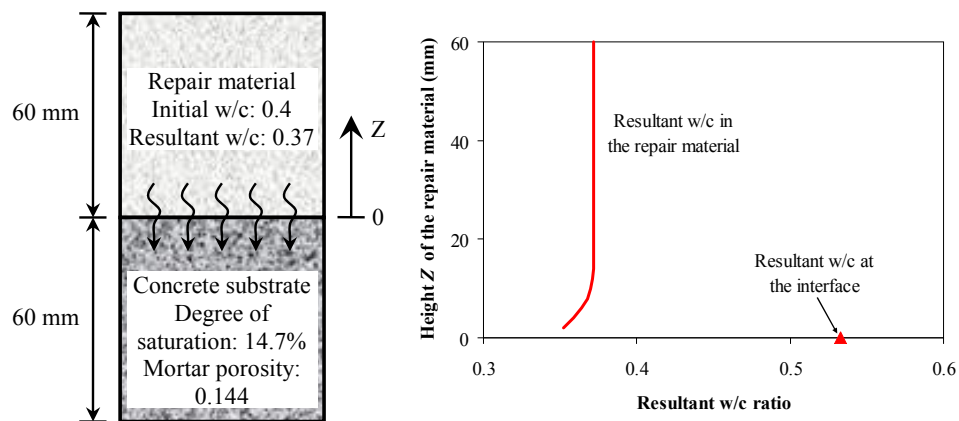|	Simulation number									
	S1	S2	S3	S4	S5	S6	S7	S8	S9	S10
Absorbed water by the substrate [g/cm^2]	0.28	0.28	0	0.18	0.52	0.03	0.26	0.18	0.19	0.31
Resultant w/c ratio in bulk repair material (half height)	0.37	0.37	0.40	0.38	0.34	0.39	0.34	0.27	0.28	0.46
Resultant w/c ratio at the interface (20 μm thick)	0.53	0.53	0.59	0.55	0.45	0.59	0.49	0.41	0.41	0.65

Figure 6.16 Resultant w/c ratio in the bulk repair material and at the interface after setting of the repair material obtained from the simulation S1 (see Table 6.2).

6.5.4 Moisture exchange between the repair material and the concrete substrate

Figure 6.17 shows the water content profile in the repair material and the concrete substrate at 1, 7, 21 and 28 days obtained from the simulation S1. As time elapses, the total water content in the repair material and in the concrete substrate decreases. The reason is that a part of water is consumed by the cement hydration in the repair material.

At 1 and 7 days, as shown in Figure 6.17 (left), in the concrete substrate, the closer to the interface, the higher the water content is. In the repair material, the closer to the interface, the lower the water content is. This implies that some water moves from the repair material to the concrete substrate driven by the capillary gradient.

At 21 days, the concrete substrate gets fully saturated, while the water content of the repair material decreased. The water content distribution in the repair material becomes more uniform, and the water content close to the interface is slightly lower than that at the top. This implies that the moisture transport process becomes slower and the repair-substrate system approaches to the balanced condition in terms of capillary potential.

At 28 days, as shown in Figure 6.17 (right), the water content in the concrete substrate decreases when approaching the repair-substrate interface. In the repair material, the water content close to the interface becomes higher than that at the top. The reason is that, as cement hydration proceeds, the water content decreases and the pore sizes become smaller. The capillary pressure, therefore, increases. When the capillary pressure in the repair material exceeds that in the concrete substrate, water is forced to flow from the concrete substrate to the repair material.

6.5.5 Simulated degree of hydration and porosity of the bulk repair material and of the interface

Figure 6.18 shows the evolution of the degree of hydration in the bulk repair material (at half height) and at the interface in the first 28 days obtained from the simulation S1. Due to the "wall effect", the interface has a higher w/c ratio than that of the bulk repair material (see Table 6.3). Therefore, the cement paste shows a higher degree of hydration at the interface.
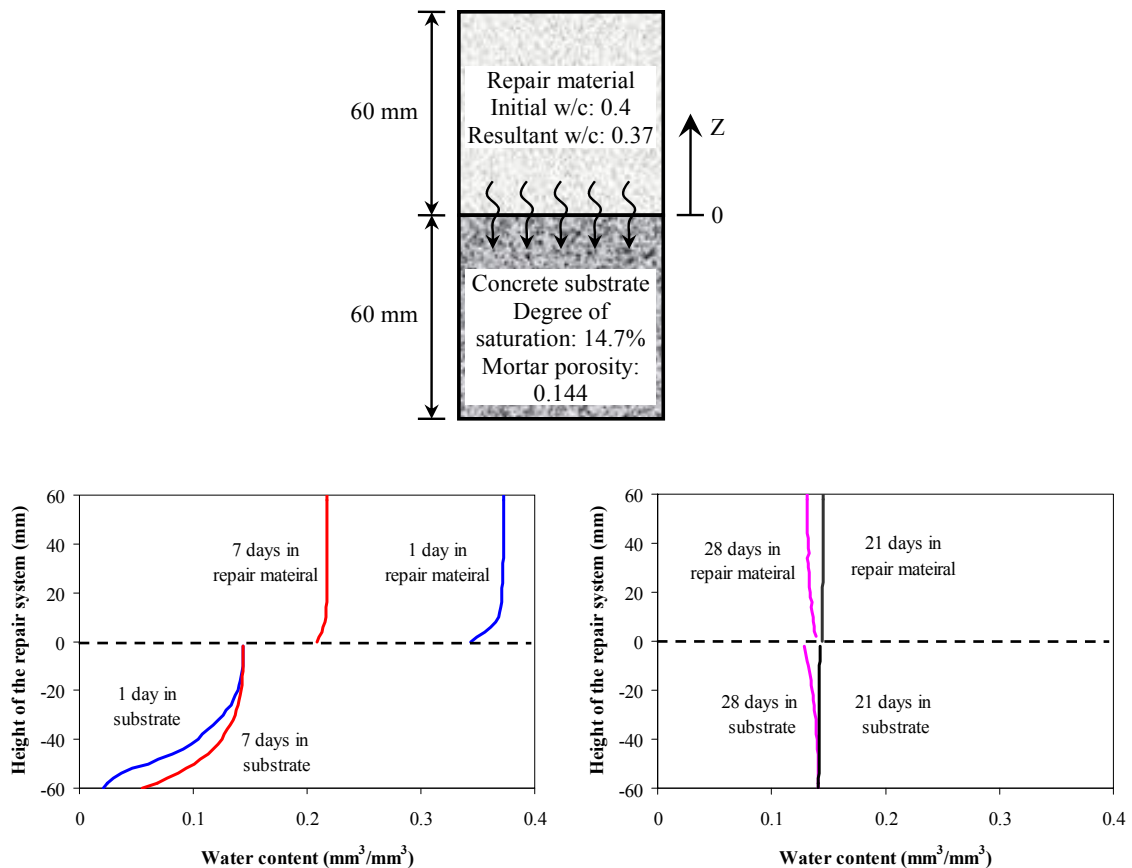
Figure 6.17 Change of the water content of the repair material and of the concrete substrate at 1, 7, 21 and 28 days obtained from the simulation S1 (see Table 6.2).

Figure 6.19 shows the degree of hydration of the bulk repair material and of the interface at 1, 7 and 28 days obtained from the simulation S1. Since the interface has a higher resultant w/c ratio than the bulk repair material, the degree of hydration at the interface is higher than that in the bulk repair material. At 1 and 7 days, bulk repair material has a lower degree of hydration, when approaching the interface. At 28 days, although the degree of hydration close to the interface remains lower, the difference between the top and bottom layers becomes smaller. This implies that at the early stage the cement hydration proceeds slower in the bulk repair material closer to the interface where the bulk repair material loses more water. At the later stage, the hydration process in the bulk repair material close to the interface becomes relatively fast, since some water flows back to the bulk repair material from the substrate concrete.

Figure 6.20 shows the simulated porosity of the bulk repair material and of the interface at 1, 7 and 28 days obtained from the simulation S1. Since the interface has a higher resultant w/c ratio than the bulk repair material, the porosity at the interface is higher than that in the bulk repair material. In the first 28 days, the bulk repair material closer to the interface shows a higher porosity, due to its lower resultant w/c ratio and lower degree of hydration.
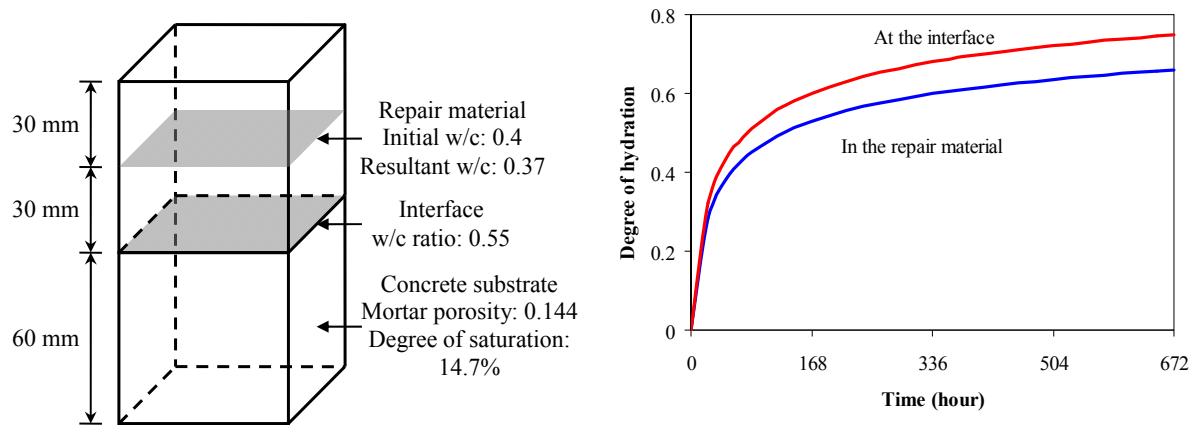
Figure 6.18 Degree of hydration in the bulk repair material (at half height) and at the interface obtained from the simulation S1 (see Table 6.2).
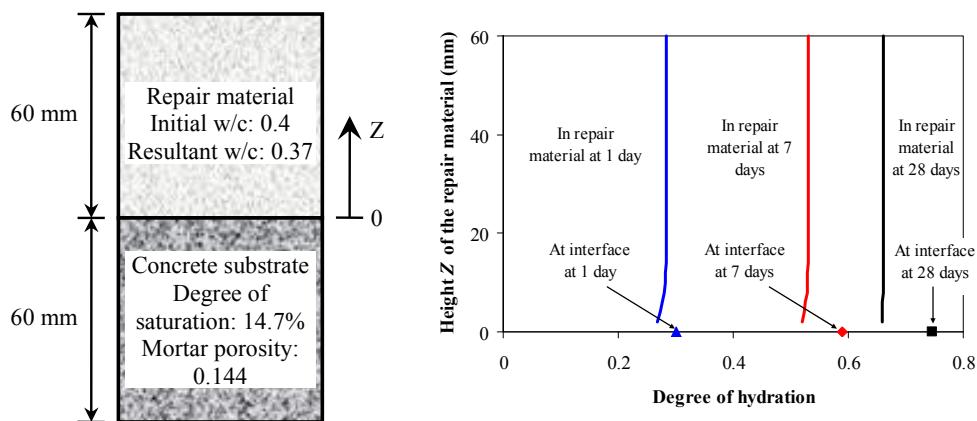

Figure 6.19 Degree of hydration of the bulk repair material and of the interface at 1, 7 and 28 days obtained from the simulation S1 (see Table 6.2).
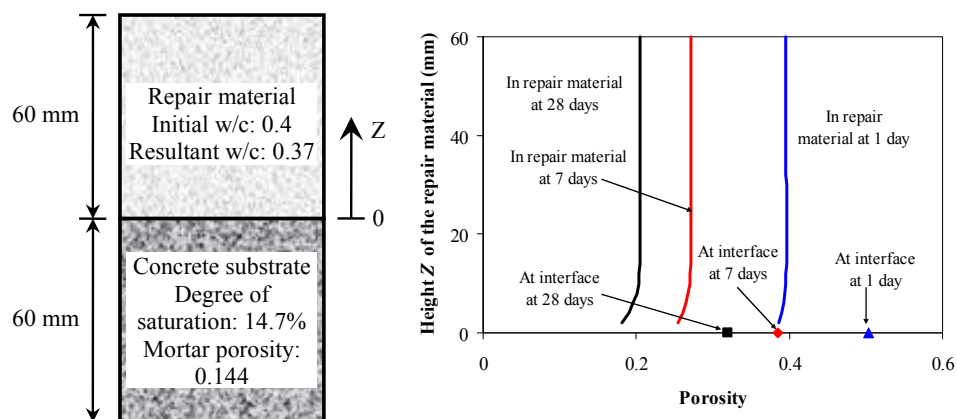

Figure 6.20 Porosity of the bulk repair material and of the interface at 1, 7 and 28 days obtained from the simulation S1 (see Table 6.2).

6.5.6   Comparison between the simulation results and experimental results of the degree of hydration and of the porosity

Table 6.4 gives a comparison between the simulation results and experimental results (Chapter 5) of the degree of hydration and of the porosity in the bulk repair material and at the interface. In general, the simulation results are in good agreement with the experimental results. The good agreement between the simulation results and experimental results indicates that the model can predict very well the cement hydration process and the microstructure development in the repair system.

Table 6.4 Comparison between the simulation results (S1-S3 in Table 6.2) and experimental results (see Section 5.5) of the degree of hydration and of the porosity in the bulk repair material and at the interface.

Simulation & experiment		Degree of hydration			Porosity	
		Simulation result	Non-evaporable water test	BSE image analysis	Simulation result	MIP
S1 & C1 cut, unsaturated	Repair	0.659	0.671	0.654	0.200	0.206
	Interface	0.747	-	0.764	0.318	-
S2 & C2 blasted, unsaturated	Repair	0.656	0.670	0.665	0.201	0.204
	Interface	0.747	-	0.780	0.318	-
S3 & C3 cut, saturated	Repair	0.698	0.709	0.706	0.219	0.220
	Interface	0.775	-	0.808	0.353	-

6.6   Influence of individual factors

6.6.1   Influence of the surface roughness of the concrete substrate

The concrete substrates in the simulations S1 and S2 have a smooth surface and a rough surface, respectively. These two simulations do not show significant difference on the degree of hydration and porosity in the bulk repair material and at the interface. This indicates that the surface roughness does not have influence on the cement hydration process and development of pore structure in the bulk repair material.

6.6.2   Influence of the degree of saturation of the concrete substrate

Figure 6.21 shows the influence of degree of saturation in the concrete substrate on the resultant w/c ratio in the bulk repair material and at the interface. When a concrete substrate has a lower degree of saturation, it absorbs more water from the bulk repair material, resulting in a lower resultant w/c ratio in the bulk repair material and at the interface.

Figure 6.22 shows the influence of the degree of saturation in the concrete substrate on the water content of the bulk repair material and the concrete substrate at 1, 7 and 28 days. When

the concrete substrate has a lower degree of saturation, the water content in the bulk repair material and in the concrete substrate is lower as well. At 28 days, the water content of the concrete substrate decreases, and water in the concrete substrate flows to the bulk repair material.

Figure 6.21 Influence of the degree of saturation (DoS) in the concrete substrate on the resultant w/c ratio in the bulk repair material and at the interface after setting of the repair material.

Figure 6.22 Influence of the degree of saturation (DoS) in the concrete substrate on the water content in the bulk repair material and in the concrete substrate at 1, 7 and 28 days.

The influence of the degree of saturation in the concrete substrate on the evolution of the degree of hydration of the bulk repair material and of the interface is not significant as shown in Figure 6.23. Since the concrete substrate with a lower degree of saturation results in a lower resultant w/c ratio of the bulk repair material and at the interface (Figure 6.21), the bulk repair material and the interface show a lower porosity as shown in and Figure 6.24.

a. Degree of hydration in the
repair material (at half height)

b. Degree of hydration
at the interface

Figure 6.23 Influence of the degree of saturation (DoS) in the concrete substrate on the degree of hydration (a) in the bulk repair material (at half height) and (b) at the interface.

a. Porosity in the repair material   b. Porosity at the interface
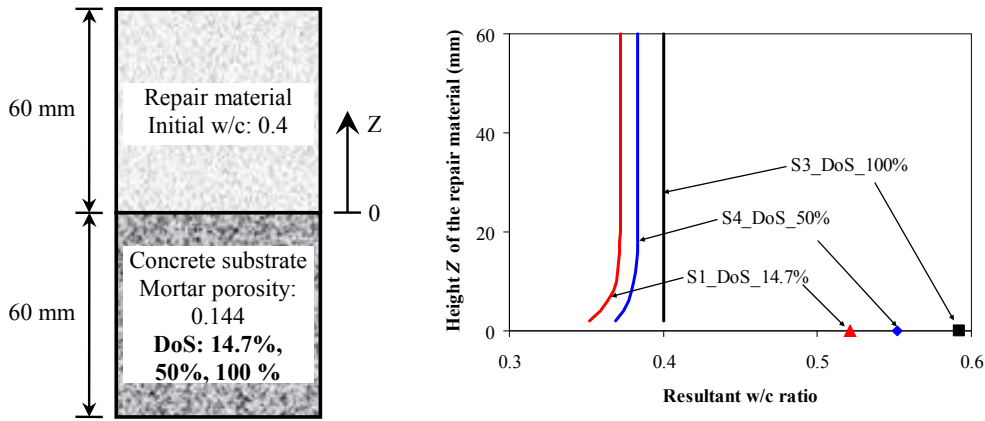
Figure 6.24 Influence of the degree of saturation (DoS) in the concrete substrate on the porosity (a) of the bulk repair material (at half height) and (b) at the interface.

6.6.3   Influence of the porosity of the mortar in the concrete substrate

In the simulations S1, S5 and S6, the mortar in the concrete substrate has different porosity. When the degree of saturation is the same, the concrete substrate with a higher porosity has more empty pores. This concrete substrate can absorb more water from the bulk repair material, resulting in a larger reduction of the w/c ratio in the bulk repair material and at the interface as shown in Figure 6.25.

When the bulk repair material has a lower resultant w/c ratio, it has a lower porosity and smaller pore sizes. The capillary pressure in the smaller pores is higher according to Eq. 6.32. Therefore, the capillary pressure in the bulk repair material with a lower resultant w/c ratio can easily exceed that in the concrete substrate. As a result, more water is forced to move from the concrete substrate to the bulk repair material. Consequently, for the concrete substrate with the highest porosity, the water content of the concrete substrate decreases relatively fast as shown in Figure 6.26.

Figure 6.27 and Figure 6.28 show the influence of the porosity of the mortar in the concrete substrate on the degree of hydration and on the porosity of the bulk repair material and at the interface, respectively. A lower porosity of the mortar in the concrete substrate leads to a higher degree of hydration and a higher porosity of the bulk repair material at the interface. In a later stage, for the concrete substrate with the highest porosity, the rate of cement hydration

in the bulk repair material becomes relatively fast. The reason is that more water moves from the concrete substrate to the bulk repair material. This accelerates the cement hydration of the bulk repair material and of the interface.
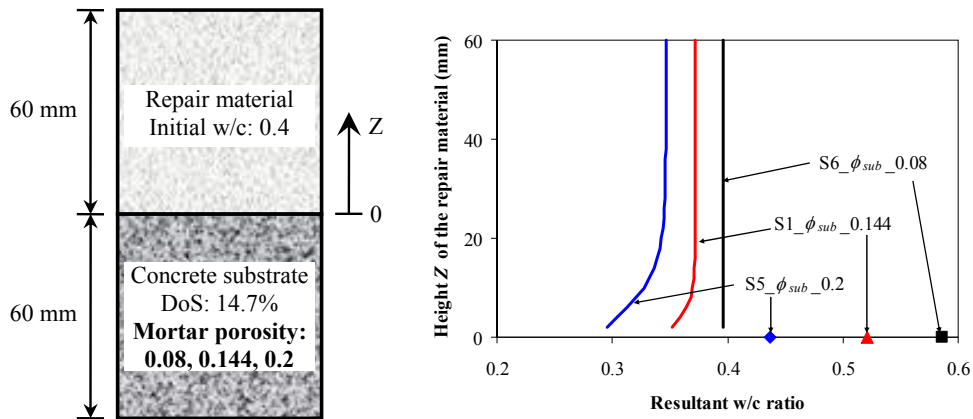
Figure 6.25 Influence of the porosity of the mortar in the concrete substrate ϕ_{sub} on the resultant w/c ratio in the bulk repair material and at the interface after setting of the repair material.
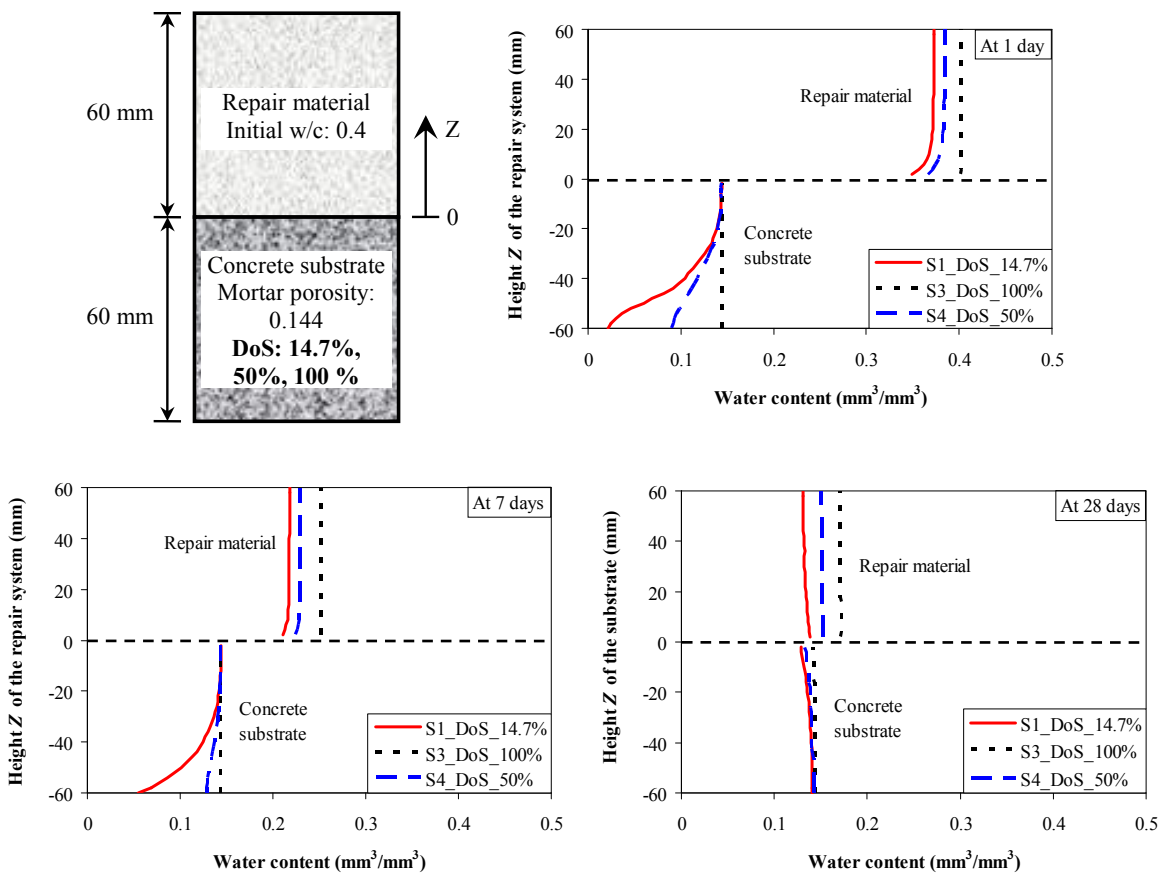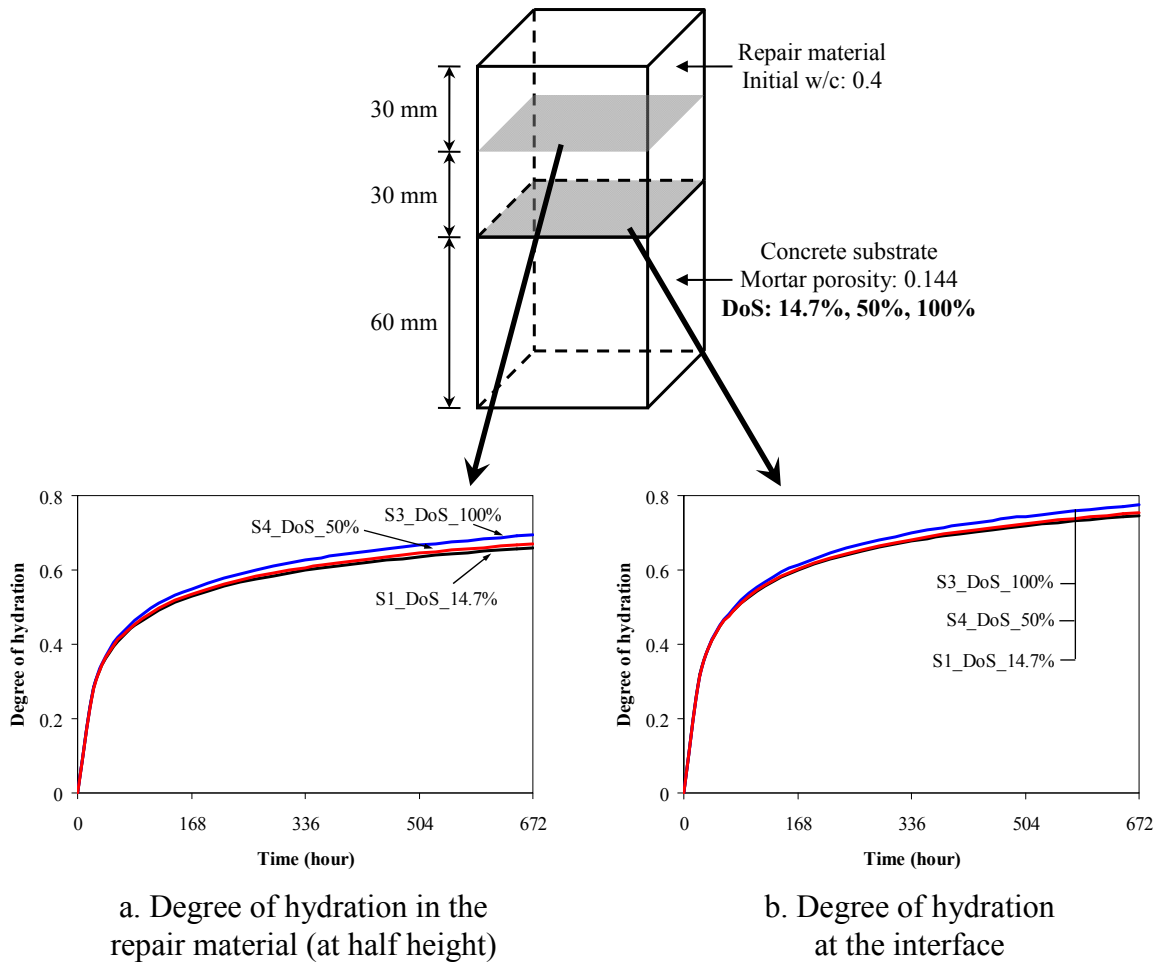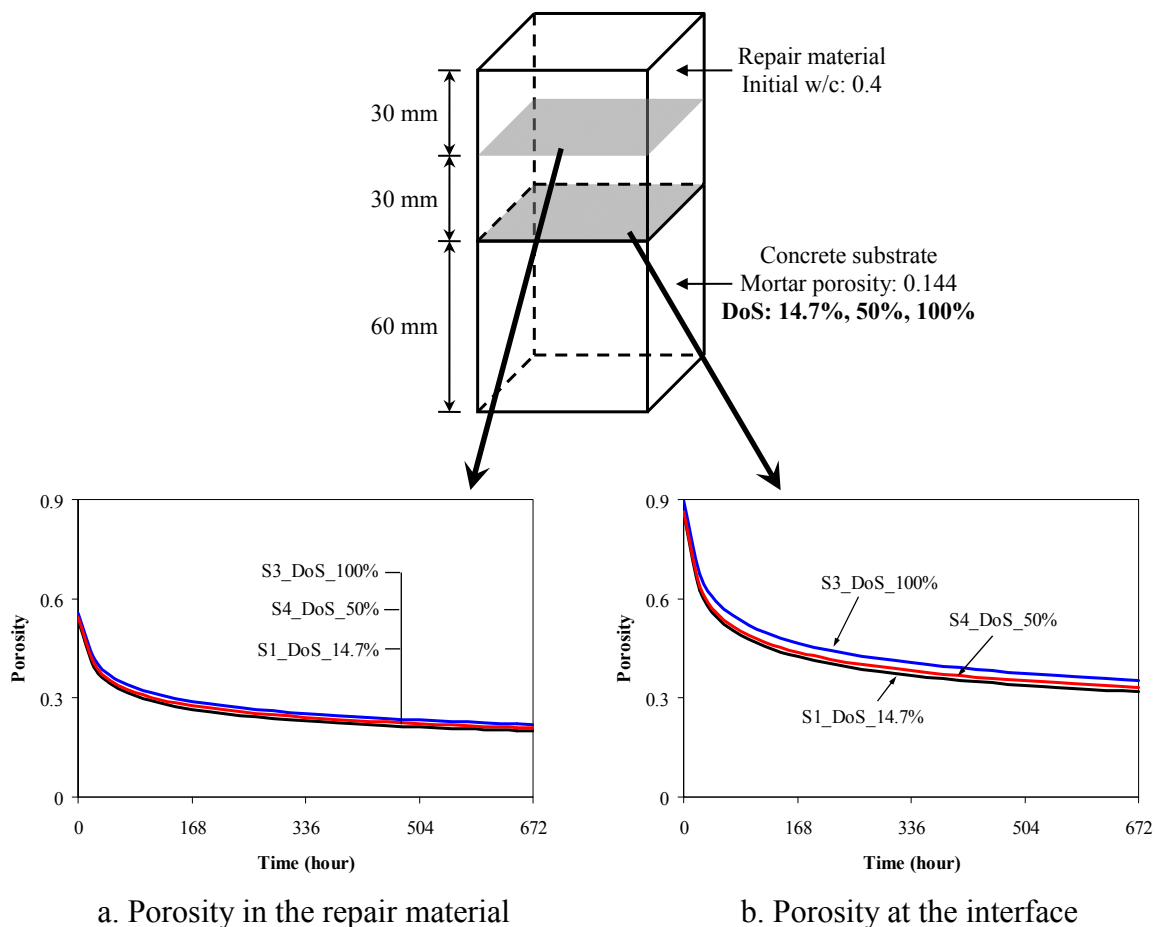

Figure 6.26 Influence the porosity of the mortar in the concrete substrate on the water content in the bulk repair material and in the concrete substrate at 1, 7 and 28 days.

a. Degree of hydration in the
repair material (at half height)

b. Degree of hydration
at the interface
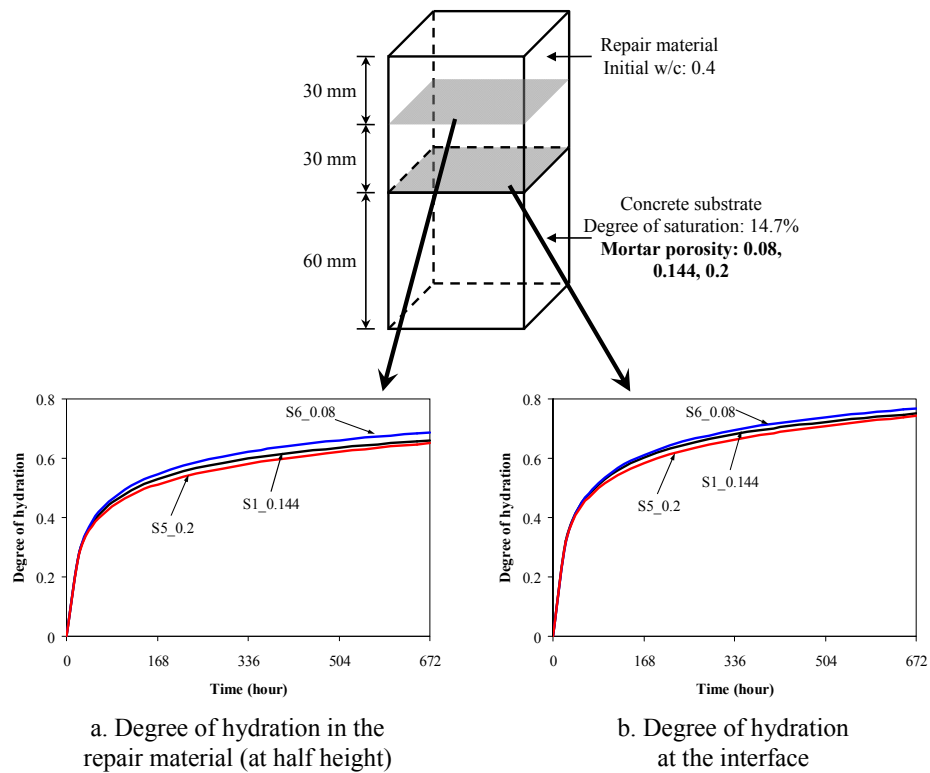
Figure 6.27 Influence the porosity of the mortar in the concrete substrate on the degree of
hydration (a) in the bulk repair material (at half height) and (b) at the interface.

a. Porosity in the repair material

b. Porosity at the interface
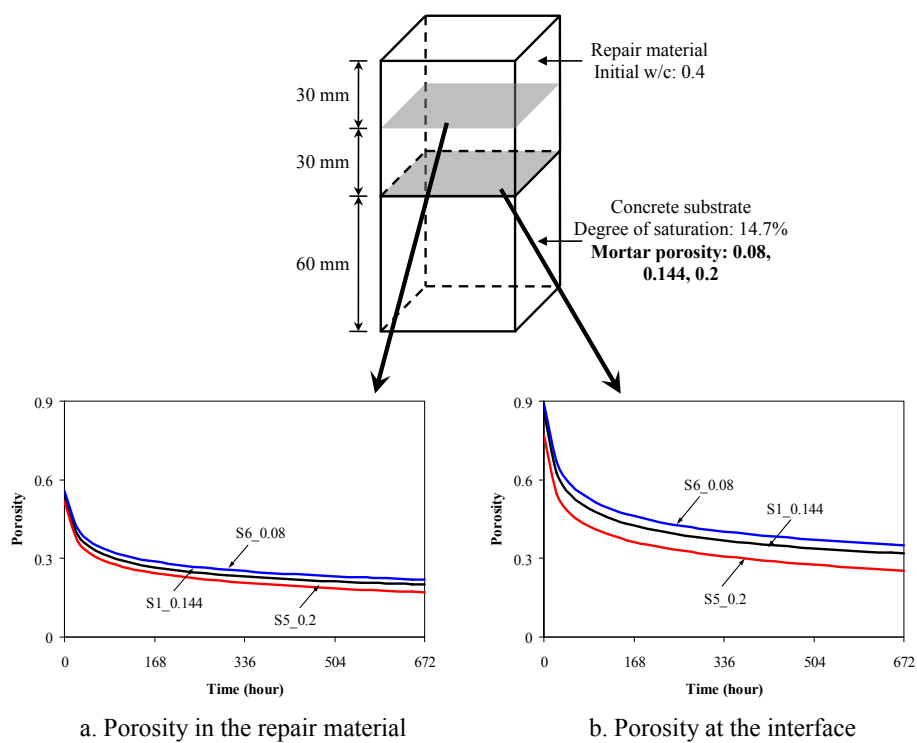
Figure 6.28 Influence the porosity of the mortar in the concrete substrate on the porosity (a) in
the bulk repair material (at half height) and (b) at the interface.

6.6.4   Influence of thickness of the bulk repair material

Figure 6.29 shows the influence of the thickness of the bulk repair material on the resultant w/c ratio in the bulk repair material and at the interface. As the thickness of the bulk repair material increases, the resultant w/c ratios in the bulk repair material and at the interface increase. When the bulk repair material has a low resultant w/c ratio, it has a small pore size and high capillary pressure. Therefore, for a thinner bulk repair material, at the later stage, more water flows from the substrate to the bulk repair material as shown in Figure 6.30. Due to the lower resultant w/c ratio, the thinner bulk repair material shows a lower degree of hydration and a lower porosity as shown in Figure 6.31 and Figure 6.32, respectively.

Figure 6.29 Influence of the thickness of the bulk repair material h_{rep} on the resultant w/c ratio in the bulk repair material and at the interface after setting of the repair material.
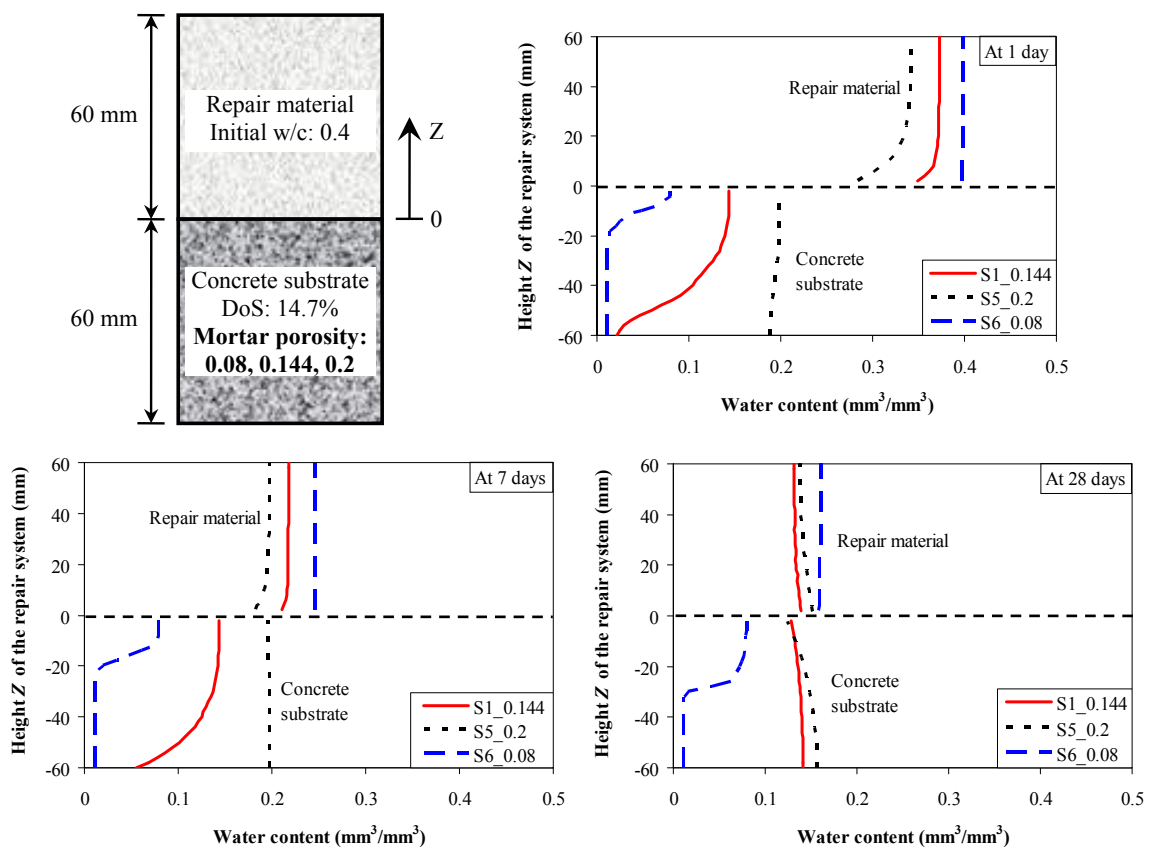

Figure 6.30 Influence of the thickness of the bulk repair material on the water content in the bulk repair material and in the concrete substrate at 1, 7 and 28 days.

a. Degree of hydration
in the repair material

b. Degree of hydration
at the interface
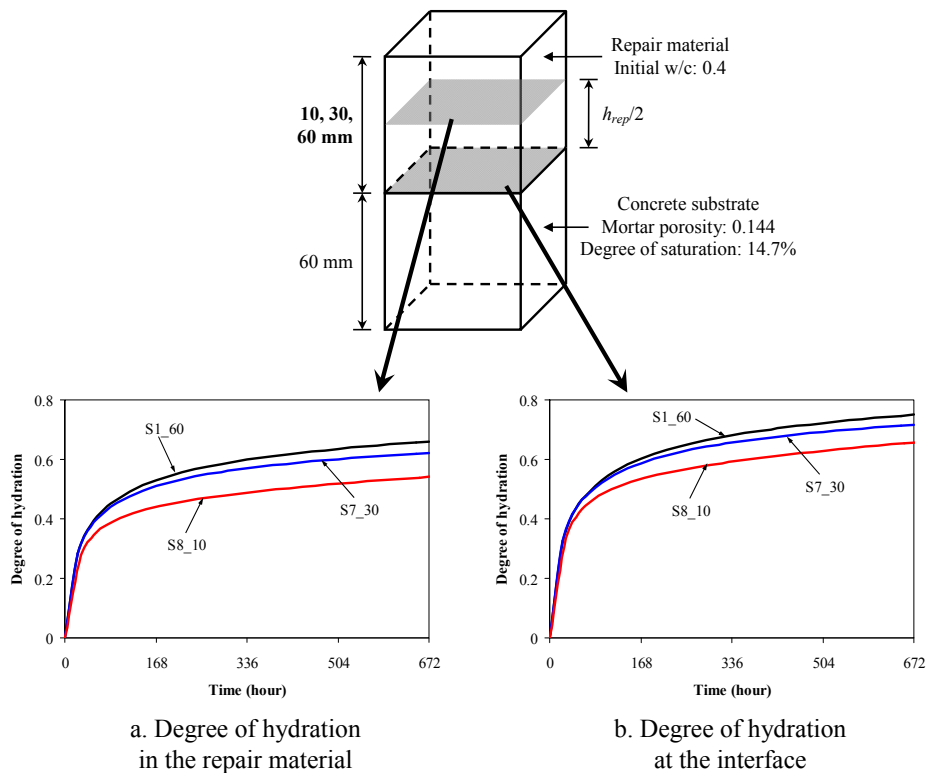
Figure 6.31 Influence of the thickness of the bulk repair material on the degree of hydration (a)
in the bulk repair material (at half height) and (b) at the interface.

a. Porosity in the repair material

b. Porosity at the interface
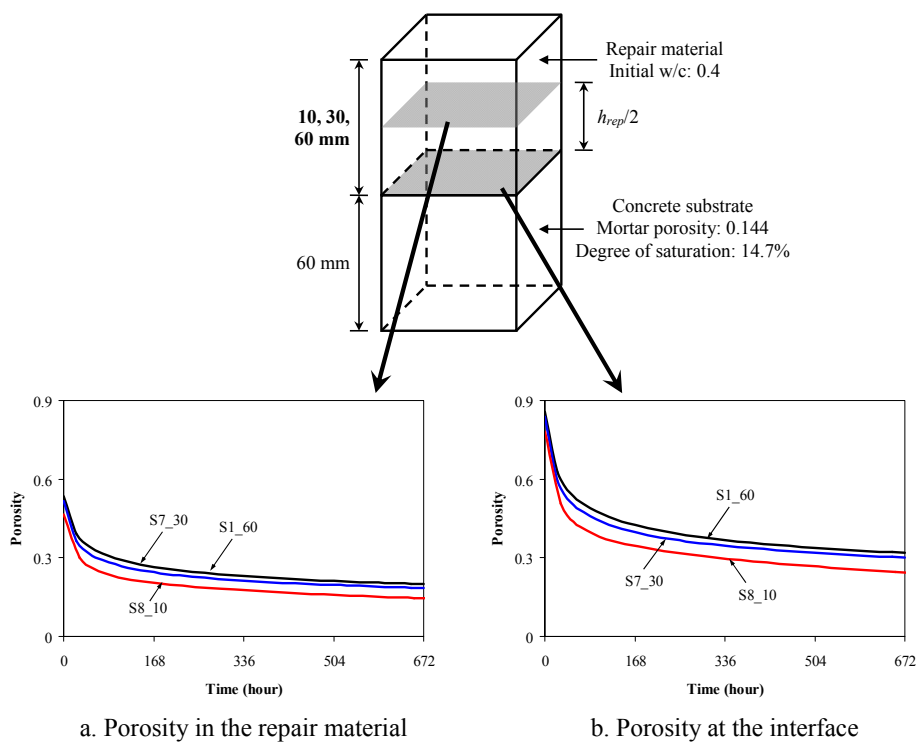
Figure 6.32 Influence of the thickness of the bulk repair material on the porosity (a) in the
bulk repair material (at half height) and (b) at the interface.

6.6.5   Influence of the initial w/c ratio of the bulk repair material

Figure 6.33 shows the influence of the initial w/c ratio of the bulk repair material on the resultant w/c ratio in the bulk repair material and at the interface. As the initial w/c ratio of the bulk repair material increases, the resultant w/c ratios in the bulk repair material and at the interface increase as well. The bulk repair material with a higher initial w/c ratio has a higher degree of hydration (as shown in Figure 6.34) and a higher porosity (as shown in Figure 6.35). When the bulk repair material has a lower resultant w/c ratio, the capillary pressure in the pores is higher. Therefore, more water flows from the concrete substrate to the bulk repair material driven by the capillary pressure gradient as shown in Figure 6.36.
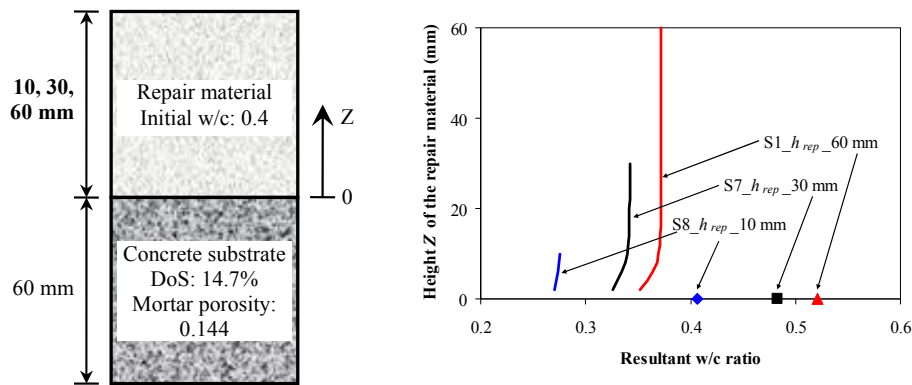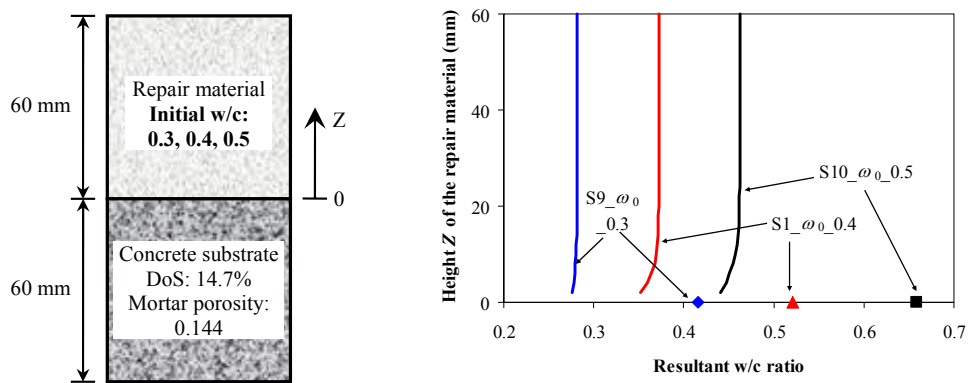

Figure 6.33 Influence of the initial w/c ratio of the bulk repair material ω_0 on the resultant w/c ratio in the bulk repair material and at the interface after setting of the repair material.

a. Degree of hydration
in the repair material

b. Degree of hydration
at the interface

Figure 6.34 Influence of the initial w/c ratio of the bulk repair material on the degree of hydration (a) in the bulk repair material (at half height) and (b) at the interface.

a. Porosity in the repair material   b. Porosity at the interface

Figure 6.35 Influence of the initial w/c ratio of the bulk repair material on the porosity (a) in the bulk repair material (at half height) and (b) at the interface.
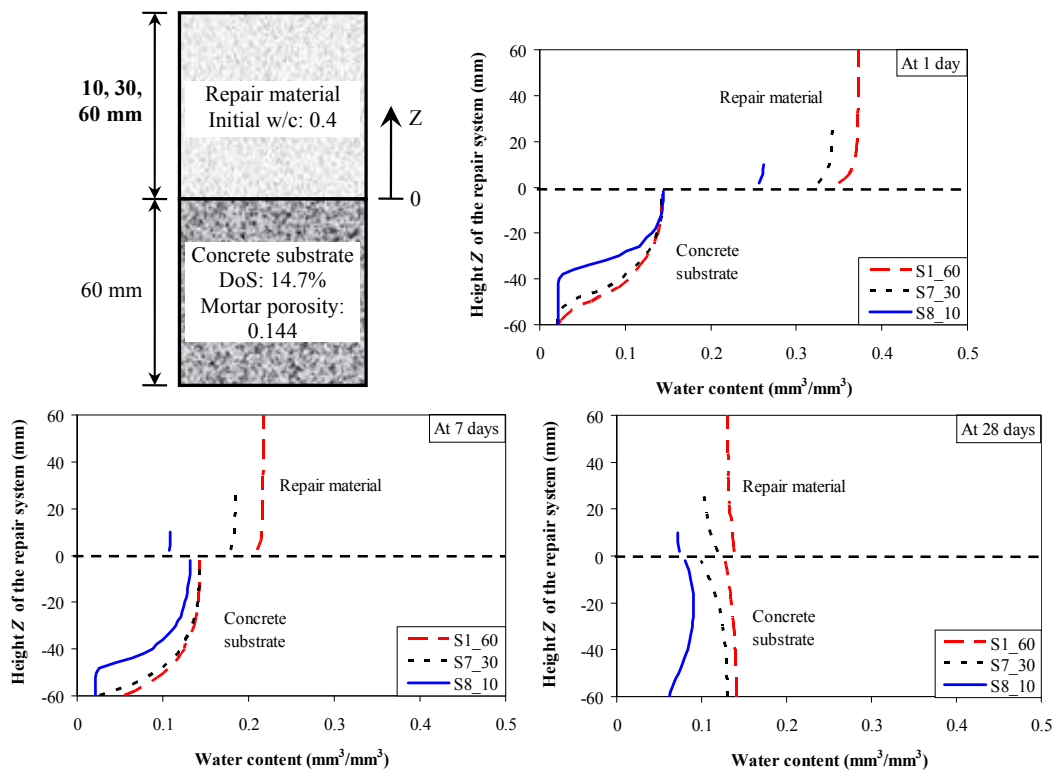

Figure 6.36 Influence of the initial w/c ratio of the bulk repair material on the water content in the bulk repair material and in the concrete substrate at 1, 7 and 28 days.

6.7   Discussion
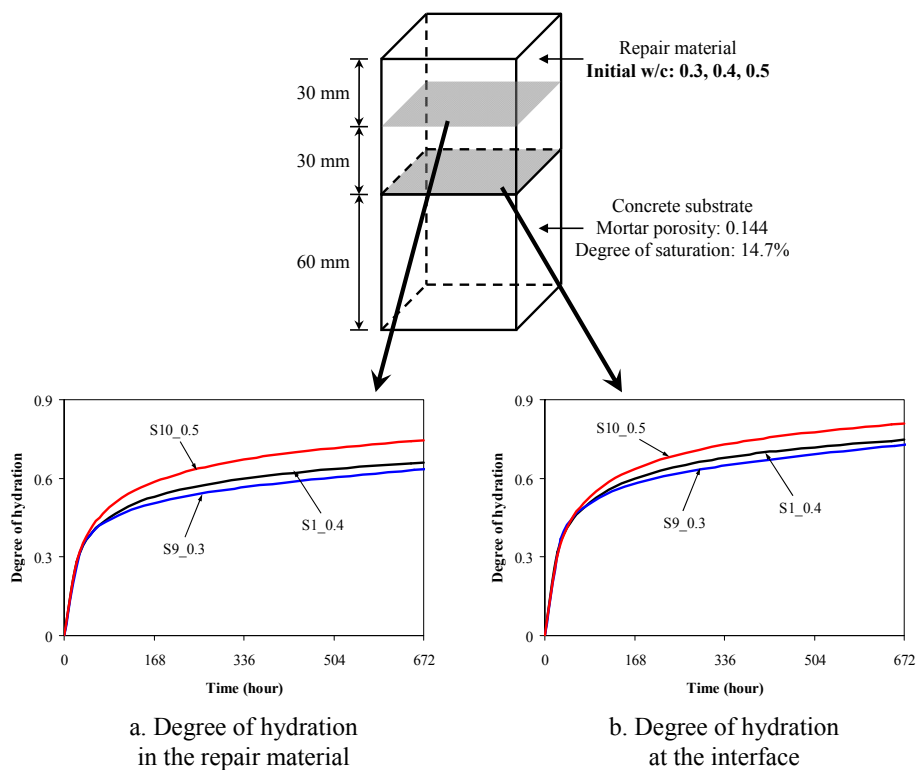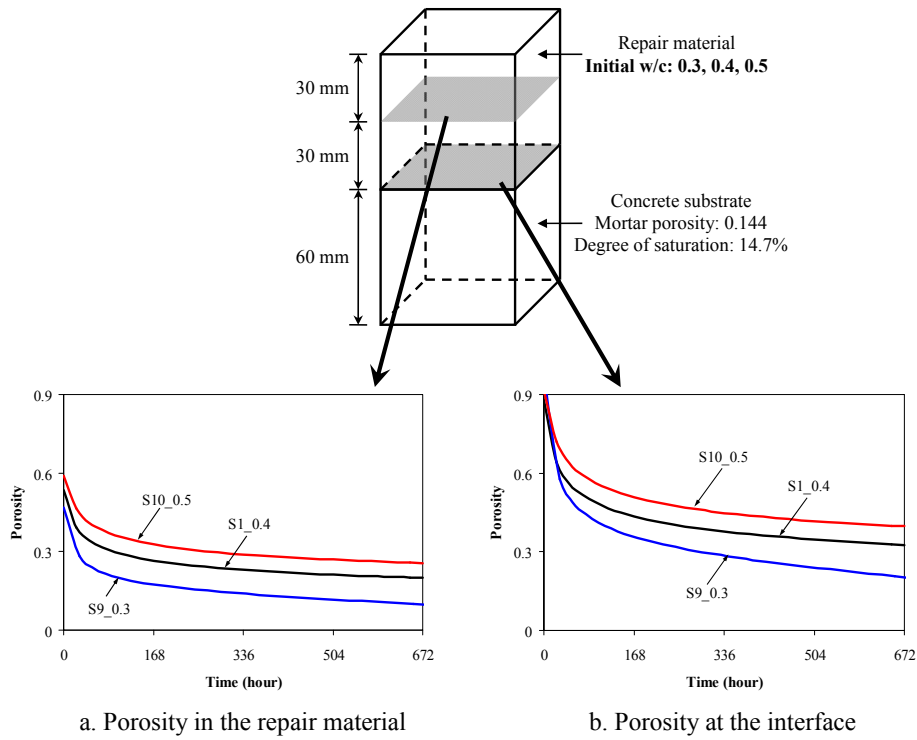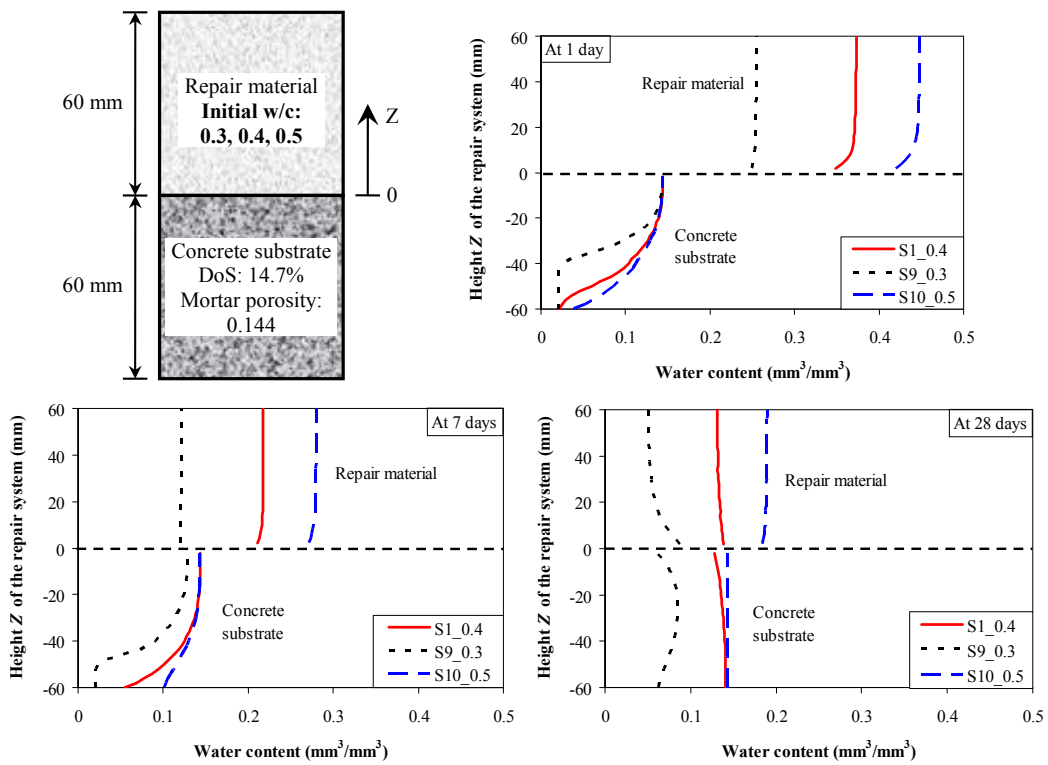
6.7.1   Water absorption

Immediately after placing repair material on an unsaturated substrate, the concrete substrate absorbs water from the repair material and gets more and more saturated. Since the repair material is still "liquid" (plastic stage), the water loss causes a reduction in the w/c ratio in the bulk repair material and at the interface. When the concrete substrate has a lower degree of saturation and a higher porosity, and the repair material has a small thickness, the reduction in the w/c ratio of the repair material is more pronounced. The resultant w/c ratio has two effects on the cement hydration of the repair material. On one hand, the reduced water content initially retards the cement hydration and results in a lower degree of hydration. On the other hand, a lower w/c ratio results in a lower porosity and a denser pore structure.

The water absorption also leads to the saturation of the concrete substrate and thus the reduction in the capillary pressure in the substrate. After setting of the repair material, the reduced capillary pressure in the substrate leads to less water loss of the repair material.

6.7.2   Interaction between cement hydration and moisture transport

After setting of the repair material, the capillary pressure gradient between the repair material and the concrete substrate drives the moisture transport between the two materials. When the concrete substrate is dry, water flows from the repair material to the concrete substrate through the interface as shown in Figure 6.17 (a). The moisture exchange reduces the capillary pressure difference between the two materials and the pressure gradually approaches to a balance. The moisture exchange, therefore, proceeds slowly as shown in Figure 6.17 (b).

When the capillary pressure gradient decreases to zero, the moisture transport will stop. However, the cement hydration consumes water in the repair material and breaks the balanced capillary pressure. As water is gradually consumed, the water content of the repair material decreases and the pore size in the repair material becomes smaller. The capillary pressure in the repair material, therefore, increases. When the capillary pressure in the repair material exceeds that in the concrete substrate, water is forced to move back to the repair material as shown in Figure 6.17 (d). Therefore, the concrete substrate may act as a "water reservoir" for the later cement hydration of the repair material. The supply of the additional water can promote or accelerate the cement hydration of the repair material.

When the concrete substrate is initially fully saturated, it will not absorb any water from the repair material. Instead, the saturated concrete substrate provides additional water for the hydration of the repair material at the beginning. The moisture transport from the concrete substrate to the repair material accelerates the cement hydration of the repair material from the very beginning.

In conclusion, the cement hydration works as a "motor" and generates the driving force for the moisture transport between the two materials, while water acts as "fuel", which is consumed by the "motor" and influences the efficiency of the "motor".

6.7.3   Influence of relevant factors on cement hydration and porosity in the bulk repair material and at the interface

Table 6.5 gives the influence of the factors (degree of saturation of the concrete substrate, porosity of the concrete substrate, thickness of the repair material and initial w/c ratio of the repair material) on the resultant w/c ratio in the bulk repair material and at the interface. When the concrete substrate has a lower degree of saturation and a higher porosity, it will absorb more water from the repair material and result in a lower resultant w/c ratio in the bulk repair material. When the repair material has a smaller thickness and a lower initial w/c ratio, the same amount of water loss, due to the water absorption, will result in a lower resultant w/c ratio. As shown in Figure 6.37 and Figure 6.38, the resultant w/c ratio has a strong correlation with the degree of hydration and the porosity in the bulk repair material and at the interface. It indicates that the water absorption before setting of the repair material has a great influence on the cement hydration and the porosity.

Table 6.5 Effect of factors on the resultant w/c ratio of the bulk repair material and at the interface

Factor	Degree of saturation of concrete substrate	Porosity of concrete substrate	Thickness of repair material	Initial w/c ratio of repair material
Resultant w/c ratio	+*	-	+	+

* "+" indicates positive effect, "-" indicates negative effect. For example, the increase of the degree of saturation in the concrete substrate results in an increase in the resultant w/c ratio of the bulk repair material.
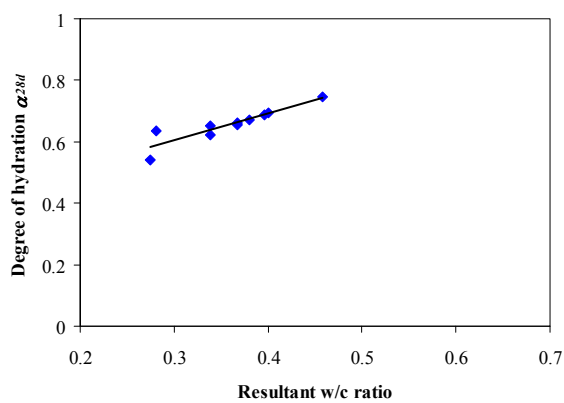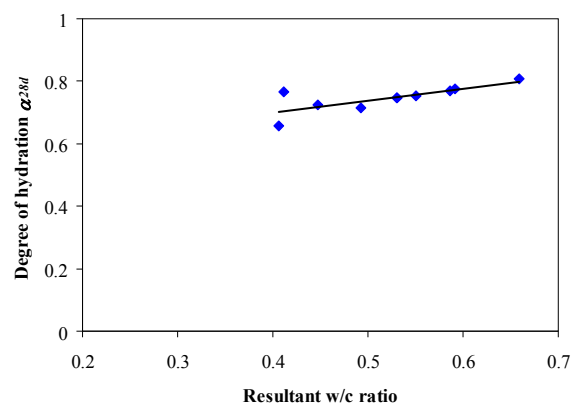
a. In the repair material   b. At the interface

Figure 6.37 Relationship between the resultant w/c ratio and the degree of hydration (a) in the bulk repair material (at half height) and (b) at the interface at the age of 28 days.

a. In the repair material   b. At the interface
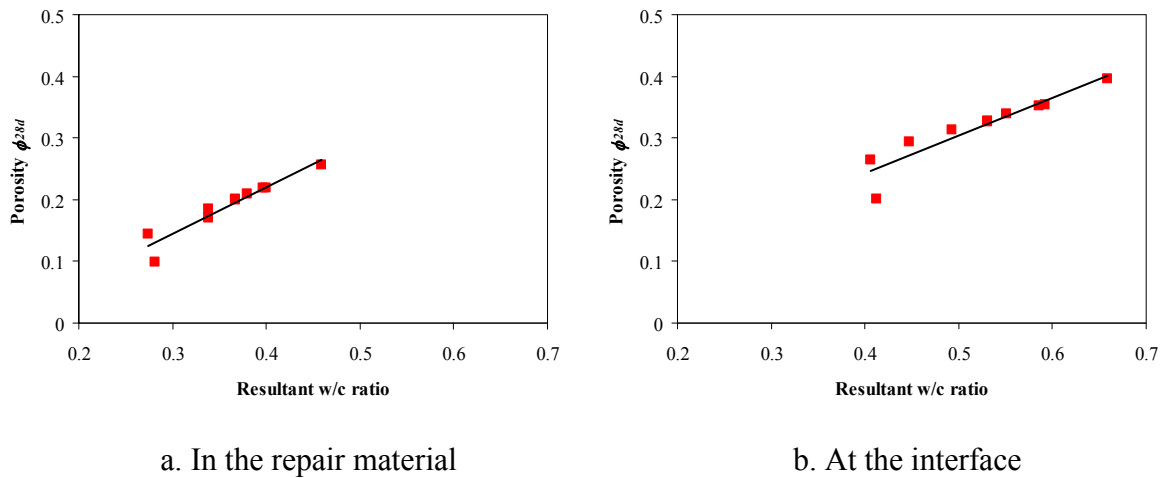
Figure 6.38 Relationship between the resultant w/c ratio and the porosity (a) in the bulk repair
material (at half height) and (b) at the interface at the age of 28 days.

6.8   Conclusions

In this chapter, a numerical study was conducted to investigate the cement hydration and
porosity of the repair material influenced by the moisture exchange between repair material
and concrete substrate. Based on the simulation results, some conclusions can be drawn:

- It is observed that the simulation results of the degree of hydration and the porosity of
  the repair system are in good agreement with the experimental results. This indicates
  that this model can predict very well the cement hydration process and the
  microstructure development in the repair system.
- Before setting of the repair material, the water absorption of an unsaturated concrete
  substrate causes a reduction of the w/c ratio in the repair material, called resultant w/c
  ratio. The resultant w/c ratio in the repair material has a great influence on the cement
  hydration and porosity of the repair material.
- After setting of the repair material, the cement hydration works as a "motor" and
  generates the driving force for the moisture transport in the two materials, while water
 acts as "fuel", which is consumed by the "motor" and influences the efficiency of the
  "motor".

The microstructure of the repair material and of the interface is numerically studied in this
chapter. The mechanical properties of a cementitious material are strongly dependent on its
microstructure. The correlation between the bond strength and microstructure will be
investigated in Chapter 7. The simulated microstructure in this chapter will be used as input in
this investigation.

Bond Strength between Repair Material and Concrete Substrate

7.1   Introduction

The development of the mechanical properties (strength and Young's modulus) of a hardening cementitious material results from the microstructural evolution due to cement hydration. It can be expected that the bond strength between the repair material and the concrete substrate is also determined by the microstructure in the repair material and at the interface. In this chapter, the correlation between the bond strength and microstructure is explored. The microstructure in the repair material and at the interface as discussed in Chapter 6 is used as input in the calculation of the bond strength. Last, the influence of various factors on the bond strength is investigated.

7.2   From microstructure to mechanical properties

The mechanical properties of cementitious materials have been found to depend strongly on their microstructure. Sun et al. [2005] suggested that the mechanical properties of cement paste correlate to the connectivity of the solid phase, which is a parameter used to describe the microstructure. The definition of this parameter will be described in detail in this section.

7.2.1   Connectivity of the solid phase

In the HYMOSTRUC3D model, the cement particles are randomly distributed in a three-dimensional body, depending on the given w/c ratio (see also Section 6.2). At the beginning, the cement particles are surrounded by water and are isolated from each other as shown in Figure 7.1 (a). As the cement hydrates, the hydration products are formed in the vicinity of the cement particles, and the cement particles, therefore, grow outwardly. Since the smaller cement particles are gradually embedded in the outer shell of the larger cement particles, isolated clusters are formed. These isolated clusters are the basis of the solid network. As the hydration process progresses, solid phases occupy more and more space, and the solid network becomes more and more connected as depicted in Figure 7.1 (b).

a. Initial status: cement
particles suspended in water

b. Percolation of cement
particles due to their growth
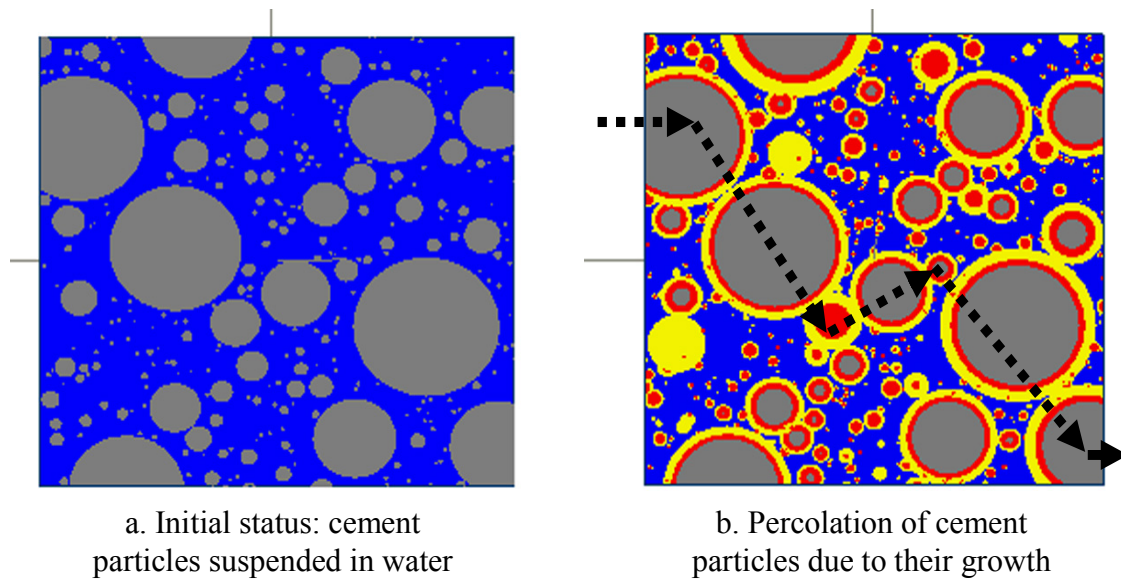
Figure 7.1 Development of connectivity of the solid phase in a hydrating cement paste [Sun et al. 2005].

The connectivity of the solid phase can be characterized by describing the extent of inter-particle bonding. Sun et al. [2004] has introduced a parameter, the contact area A_c [μm^2], to indicate this extent as shown in Figure 7.2. If a cluster of connected solid particles is considered, the contact area for this cluster is the sum of the areas that form the connection between the individual particles. The contact area between two or more particles increases with the increase in the degree of hydration.

a. Three connected
cement particles

b. Contact area A_c
between A and B

c. Contact area A_c
between B and C
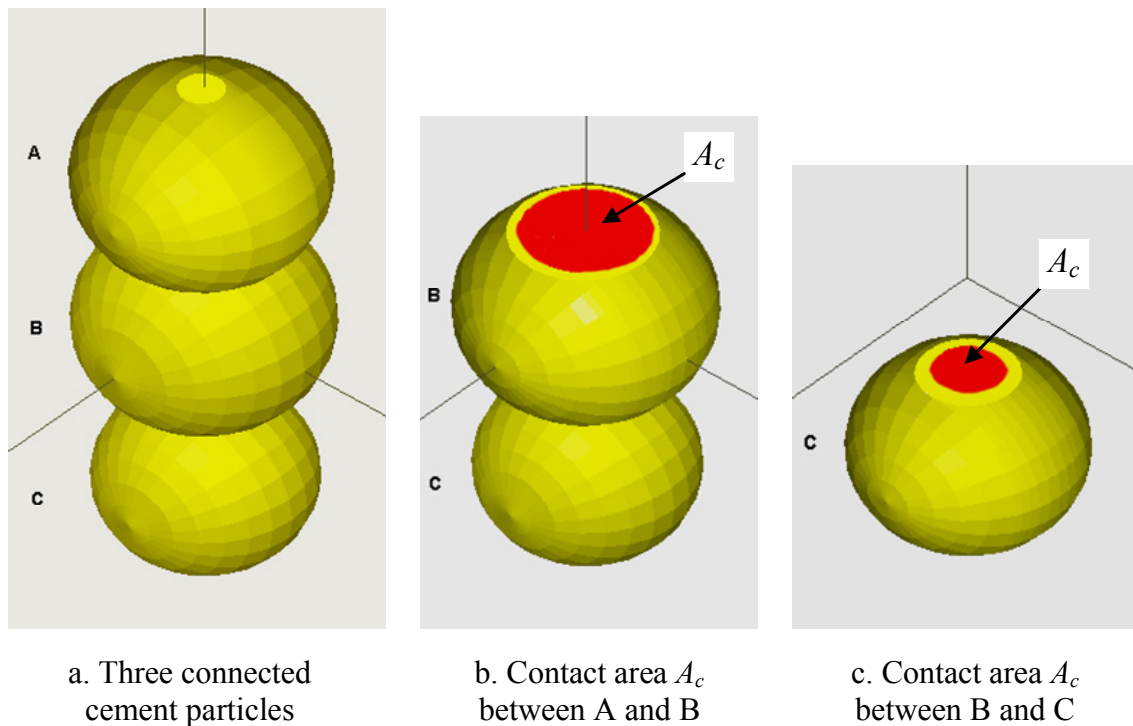
Figure 7.2 Contact area between cement particles [Sun et al. 2005].

The effective contact area $A_{c,eff}$ [μm^2] is defined as the contact area in the direction normal to the direction of the applied load [Sun et al. 2005]. Taking a load applied in the y direction as an example, the algorithm and criteria for calculating the effective contact area are shown in Figure 7.3. The phenomenon of particle connection can be divided into four cases, which are taken into consideration in calculations of the effective contact area normal to direction y. In case (a), when two particles are interconnected in a direction normal to the y axis, the effective contact area $A_{c,eff,y}$ equals the contact area A_c, which is the area of the contact circle. In case (b), when the two particles are not interconnected in a plane normal to the y direction, the effective contact area $A_{c,eff,y}$ is calculated by mapping the contact area onto a plane normal to the y direction. When three or more particles are interconnected, the doubly-overlapping contact area has to be subtracted from the total contact area (Figure 7.3 (c)). When a larger and a smaller particle are close together, the larger particle O_1 may grow sufficiently as hydration proceeds for it to completely contain the smaller particle O_2. In this case, the effective contact area $A_{c,eff,y}$ is the circle area with the radius equals to that of the smaller particle (Figure 7.3 (d)). The details of these algorithms are described in reference [Sun et al. 2004].

a. Contact area normal to y-axis   b. Contact area not normal to y-axis

c. Overlapping contact area

d. Small particle embedded in large particle
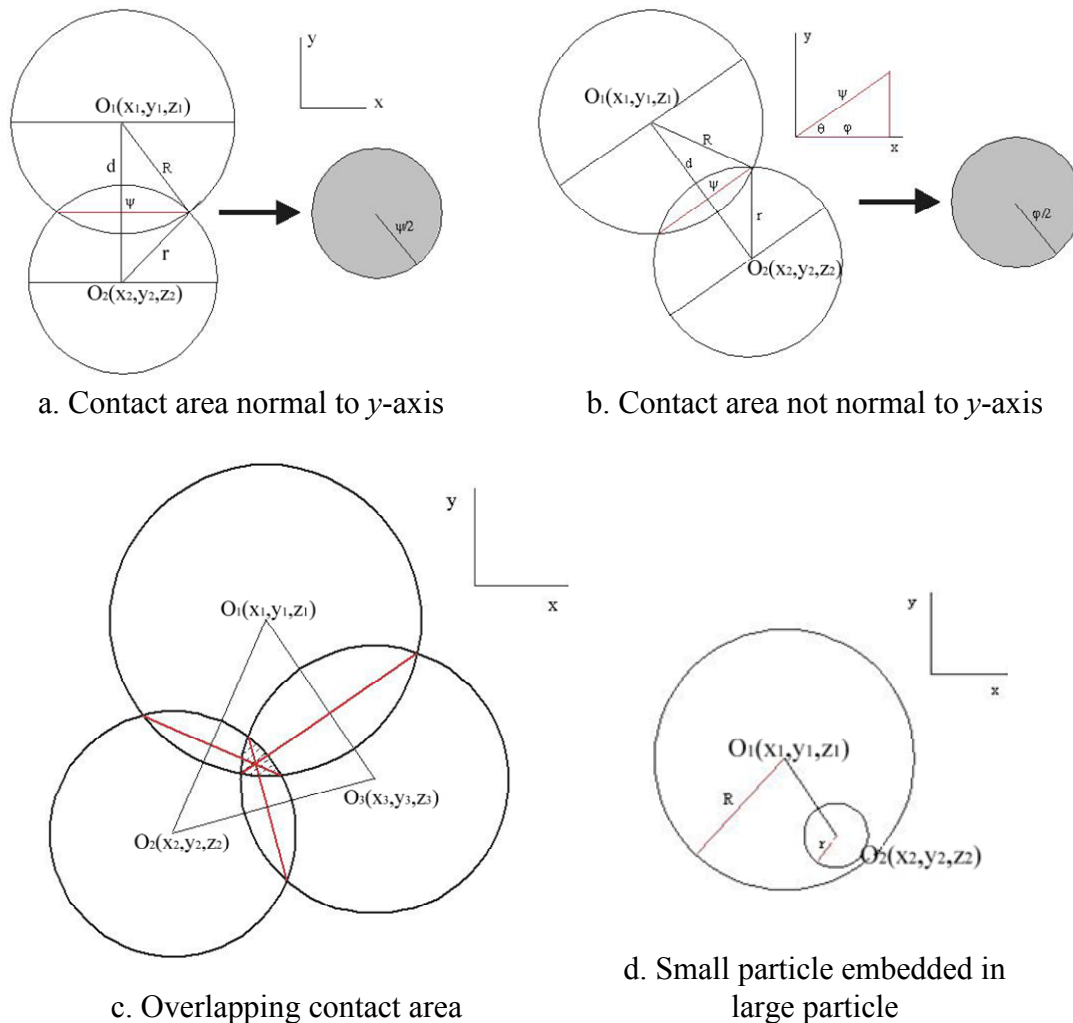
Figure 7.3 Effective contact area between cement particles in different cases [Sun et al. 2005].

The total effective contact area in a specific direction of the hydrating cement particles is the sum of the effective contact area in that direction for all particles within the cubic cell. The total effective contact area in the cement paste is assumed to be equal to the sum of the effective contact area in the x, y and z directions [Sun et al. 2005]:

$$A_{c,eff} = A_{c,eff,x} + A_{c,eff,y} + A_{c,eff,z} \qquad (7.1)$$

For convenience in the data analysis, the concept of the specific effective contact area $A_{c,spec}$ [$\mu m^2/\mu m^3$] is introduced. The specific effective contact area is defined as the effective contact area per unit volume of cement paste V_{cp} [μm^3]:

$$A_{c,spec} = A_{c,eff} / V_{cp} \qquad (7.2)$$

7.2.2 Correlation between the compressive strength and the specific effective contact area in cement paste

The specific effective contact area is a microstructure parameter which can be calculated by HYMOSTRUC3D. Although the specific effective contact area is not a directly measurable quantity, it provides an approach to quantify the degree of connection between the particles in the microstructure. The correlations among the compressive strength and the specific effective contact area of solid phase were investigated by Sun et al. [2005].

Figure 7.4 shows the correlation between compressive strength and the specific effective contact area. The compressive strength and the specific effective contact area show a good linear relationship, regardless the w/c ratio of cement paste. The linear compressive strength-specific effective contact area relationship suggests that the compressive strength develop differently under the same hydration conditions. Based on these observations, it appears that the compressive strength of cement pastes can be related directly to the degree of connectivity of the solid phase in cementitious materials. It is believed that the specific effective contact area in cement paste is an essential factor that determines the development of the mechanical properties of the cementitious materials.

Figure 7.4 Correlation between the compressive strength and the specific effective contact area [Sun et al. 2005].

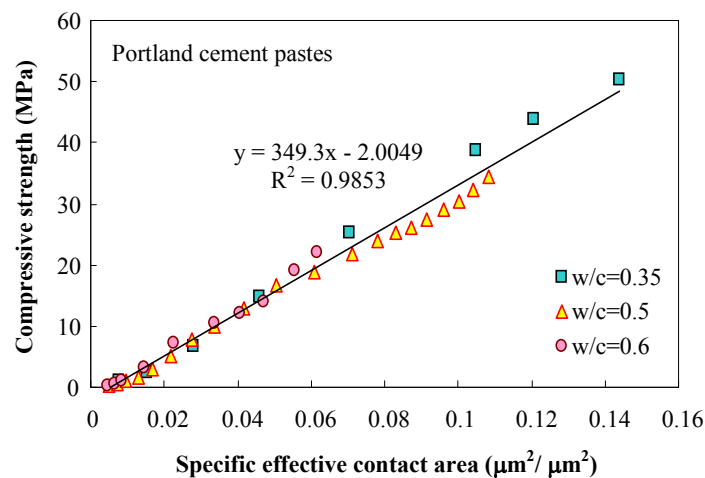### 7.2.3   Correlation between tensile strength and compressive strength

In this study, the bond strength is defined as the loading capacity between the repair material and the concrete substrate under a tensile load. The bond strength is closely related to the tensile properties of the repair material and the interface. The correlation between the tensile strength and the specific effective contact area is, therefore, explored in this section.

From the discussion on the strength of concrete, it is found that the compressive and tensile strengths are closely related [Neville, 1995]. In general, as the compressive strength f_c [MPa] increases, the tensile strength f_t [MPa] increases but at a decreasing rate. Among the empirical formulae connecting these two types of strength, many are in the form:

$$f_t = k \left(f_c \right)^n \tag{7.3}$$

where k [-] and n [-] are coefficients. Values of n between 0.5 and 0.75 have been suggested. Based on a large amount of test data (566 groups) assembled from various sources, Oluokun [1991] suggested a regression expression:

$$f_t = 0.2 \left(f_c \right)^{0.69} \tag{7.4}$$

Considering the linear compressive strength-specific effective contact area relationship, the tensile strength of hardening cement pastes can be calculated as follows:

$$f_t = \gamma \times \left(A_{c,spec} \right)^{0.69} \tag{7.5}$$

where γ [-] is a coefficient.

7.3   Bond strength between the repair material and the concrete substrate

In this section, the specific effective contact area in the repair material and at the interface is discussed. The specific effective contact area is used to calculate the bond strength using Eq. 7.5. In the prediction, the surface roughness of the concrete substrate is not taken into account. The contribution of the mechanical interlocking to the bond strength is assumed to be 0.

7.3.1   Specific effective contact area in the repair material and at the interface

The microstructure of the repair system simulated in Chapter 6 is used as input to calculate the specific effective contact area by the HYMOSTRUC3D model. In the simulations, the influence of various factors is taken into consideration, which includes the degree of saturation of the substrate θ/ϕ_s, the porosity of mortar in the substrate ϕ_s [-], the thickness of the repair material h_r and the initial w/c ratio of the repair material $\omega_{0,r}$ [-]. Table 7.1 gives the specific effective contact area in the repair material $A_{c,spec,r}$ [$\mu m^2/\mu m^3$] and at the interface $A_{c,spec,int}$ [$\mu m^2/\mu m^3$] at 28 days. As the specific effective contact area in the repair material increases, the specific effective contact area at the interface increases as well. For the same specimen at the same curing age, the repair material has a larger specific contact area than the interface.

Table 7.1 Specific effective contact area in the repair material and at the interface at 28 days calculated by the HYMOSTRUC3D model.

Simulation number	h_s	θ/ϕ_s	ϕ_s	h_r	$\omega_{0,r}$	$A_{c,spec,r,28}$	$A_{c,spec,int,28}$
S1	60	14.7%	0.144	60	0.4	0.229	0.118
S2	60	14.7%	0.144	60	0.4	0.229	0.118
S3	60	100%	0.144	60	0.4	0.204	0.098
S4	60	50%	0.144	60	0.4	0.214	0.112
S5	60	14.7%	0.2	60	0.4	0.268	0.175
S6	60	14.7%	0.08	60	0.4	0.204	0.099
S7	60	14.7%	0.144	30	0.4	0.247	0.128
S8	60	14.7%	0.144	10	0.4	0.314	0.179
S9	60	14.7%	0.144	60	0.3	0.430	0.225
S10	60	14.7%	0.144	60	0.5	0.167	0.084

The correlation between the specific effective contact area and the degree of hydration in the repair material (half height) and at the interface is shown in Figure 7.5. For a given w/c ratio, as the degree of hydration increases, the specific effective contact area increases at an increasing rate both in the repair material and at the interface. On the other hand, a low w/c ratio results in a low porosity and a low specific effective contact area. This can be attributed to the high volume concentration of cement particles in the low w/c-ratio cement paste. The simulation results show that the repair material has a higher specific contact area than the interface. This indicates that the w/c ratio is the dominate factor on the specific contact area rather than the degree of hydration.
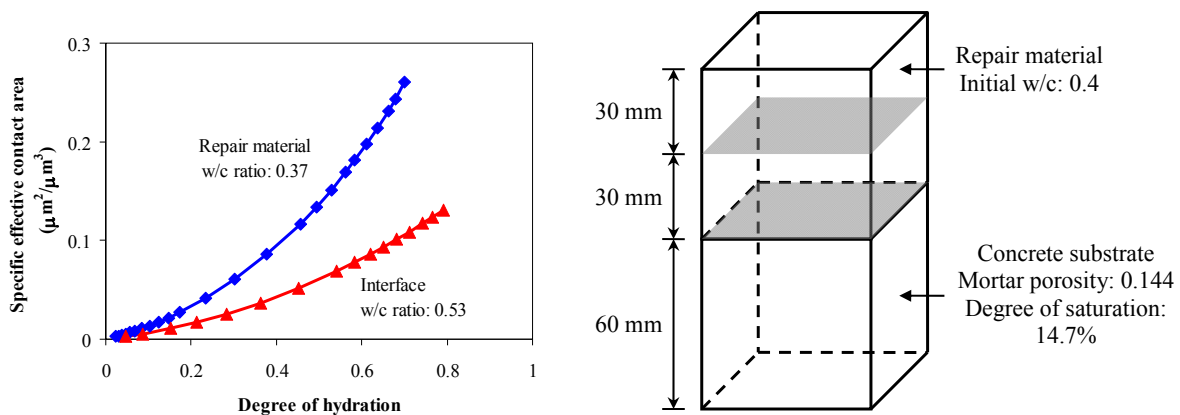
Figure 7.5 Correlation between the specific effective contact area and the degree of hydration in the repair material (half height) and at the interface.

7.3.2   Bond strength between the repair material and the concrete substrate

The bond strength between the repair material and the concrete substrate is often measured under a tensile load. When the concrete substrate is strong enough, the specimens fail either in the repair material or at the interface. In essence, the measured bond strength is the tensile

strength of the weakest point in the specimen, either the repair material or the interface. Based on the correlation between the tensile strength and the specific effective contact area in the cement paste described by Eq. 7.5, the tensile strength in the repair material and at the interface can be calculated. The bond strength between the repair material and the concrete substrate can, therefore, be predicted based on the microstructure in the repair material and at the interface.

In order to determine the coefficient γ in Eq. 7.5, the correlation between the measured bond strength (Chapter 5) and the simulated specific effective contact area in the failure region (calculated by the HYMOSTRUC3D model) is investigated. As discussed in Chapter 5, under a tensile load, when the concrete substrate had a cut surface (smooth), the repair system failed at the interface. When the concrete substrate had a grit-blasted surface (rough), the repair system failed in the repair material. The correlation between the measured bond strength and the simulated specific effective contact area in the failure region at 28 days is plotted in Figure 7.6. The measured bond strength and the specific effective contact area at the failure region show a good linear correlation. This linear correlation was used to determine the coefficient γ in Eq. 7.5. Accordingly, the value of 4.65, which is the slope in Figure 7.6, was assigned to the coefficient γ. The bond strength f_b [MPa] between the repair material and the concrete substrate can be calculated as follows:

$$f_b = 4.65\left(A_{c,spec,fail}\right)^{0.69} \tag{7.6}$$

where $A_{c,spec,fail}$ [$\mu m^2/\mu m^3$] is the specific effective contact area in the failure region.

As the specific effective contact area increases, the tensile strength increases. Therefore, the failure region should have the smallest specific effective contact area in the specimen. $A_{c,spec,fail}$ can be calculated as follow:

$$A_{c,spec,fail} = \min\left(A_{c,spec,r}, A_{c,spec,int}\right) \tag{7.7}$$
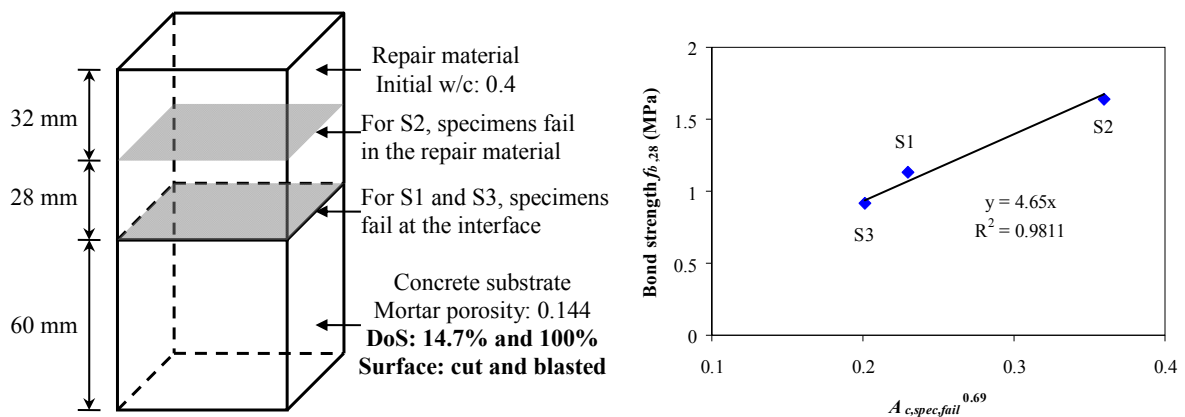

Figure 7.6 Correlation between the measured bond strength (see Chapter 5) and the simulated specific effective contact area in the failure region at 28 days.

The bond strength between the repair material and the concrete substrate at 28 days is calculated by Eq. 7.6. The simulated bond strength between the repair material and the concrete substrate is given in Table 7.2. The influence of various factors on the bond strength will be discussed in the next section.

Table 7.2 Bond strength and failure location between the repair material and the concrete substrate at 28 days obtained from the numerical simulation and the experiments (Chapter 5).

Simulation number	Simulation results					Experimental results	
	Contact area $A_{c,spec,28}$ [$\mu m^2/\mu m^3$]		Tensile strength $f_{c,28}$ [MPa]		Bond strength $f_{b,28}$ [MPa]	Failure location	Bond Strength [MPa]
	Repair	Interface	Repair	Interface			
S1	0.229	0.118	1.68	1.07	1.07	Interface	1.13
S2[#]	0.227	0.118	1.67	1.07	1.67[#]	Repair	1.64
S3	0.204	0.098	1.55	0.94	0.94	Interface	0.92
S4	0.214	0.112	1.60	1.02	1.02	-	-
S5	0.268	0.175	1.87	1.40	1.40	-	-
S6	0.204	0.099	1.56	0.94	0.94	-	-
S7	0.247	0.128	1.77	1.13	1.13	-	-
S8	0.314	0.179	2.09	1.42	1.42	-	-
S9	0.430	0.225	2.60	1.66	1.66	-	-
S10	0.167	0.084	1.35	0.84	0.84	-	-

[#] In the experiment, the specimen corresponding to the simulation S2 has a grit-blasted substrate. The mechanical interlocking between the repair material and the concrete substrate results in a strong interface. It is found that the specimen failed in the repair material. Therefore, the bond strength is equal to the tensile strength of the repair material.

7.3.3   Influence of various factors on the simulated bond strength

In this section, the influence of various factors on the simulate bond strength (as given in Table 7.2) is investigated. These factors include the degree of saturation and porosity of substrate and the thickness and initial w/c ratio of the repair material. Moreover, the correlation between the simulated bond strength and the resultant w/c ratio at the interface is also explored. Among the simulations, the specimens all fail at the interface.

A lower degree of saturation and a higher porosity of the concrete substrate result in a higher bond strength as shown in Figure 7.7 and Figure 7.8, respectively. The reason is that this concrete substrate absorbs more water from the repair material and, therefore, results in a larger reduction of the w/c ratio of the repair material, which is called the resultant w/c ratio see Chapter 6. The low resultant w/c ratio leads to a good bond. This agrees with the experimental results from van Zijl and Stander [2008]. They found that a lower water content (10-minute moistening) of the substrate leads to a higher bond strength compared with a higher one (24-hour submergence).
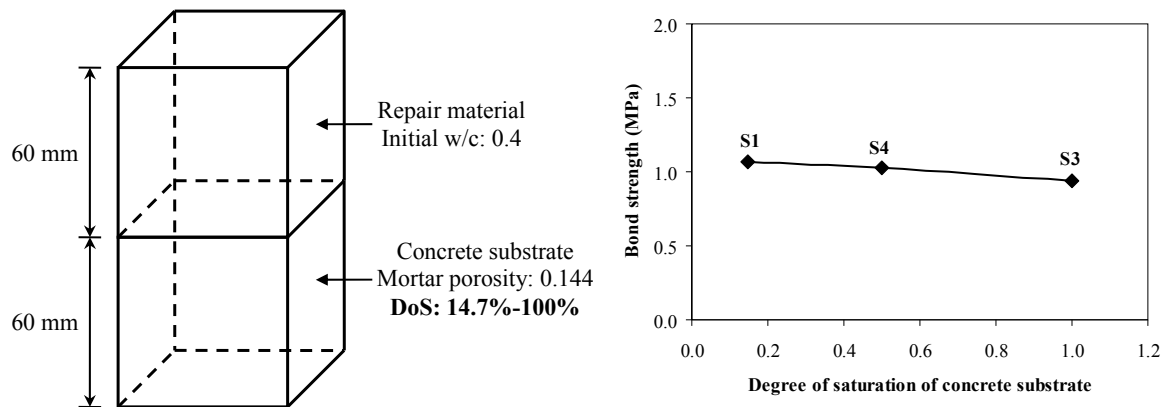
Figure 7.7 Influence of the degree of saturation (DoS) of the concrete substrate on the simulated bond strength between the repair material and the concrete substrate at 28 days. All specimens fail at the interface.
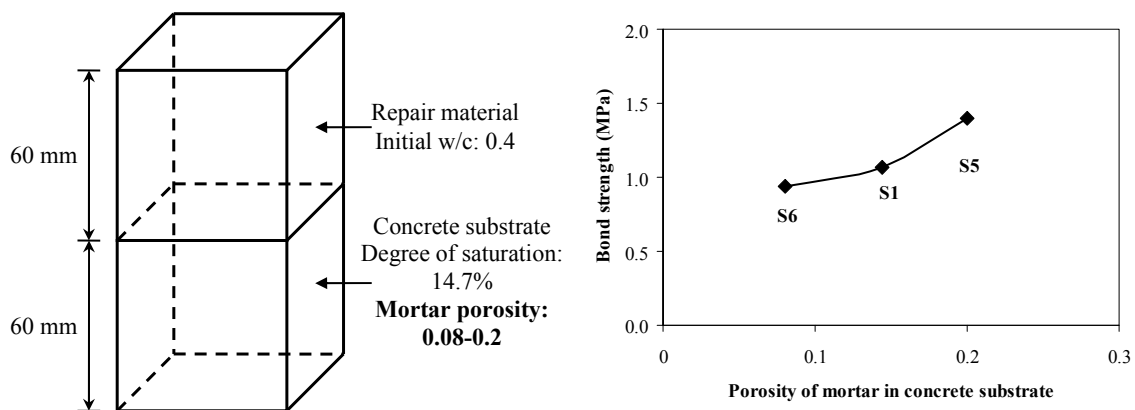
Figure 7.8 Influence of the porosity of the mortar in the concrete substrate on the simulated bond strength between the repair material and the concrete substrate at 28 days. All specimens fail at the interface.

Figure 7.9 shows the influence of the thickness of the repair material on the bond strength at 28 days. As discussed in Section 6.6.4, as the thickness of the repair material decreases, the resultant w/c ratio of the repair material decreases. This results in a higher bond strength.
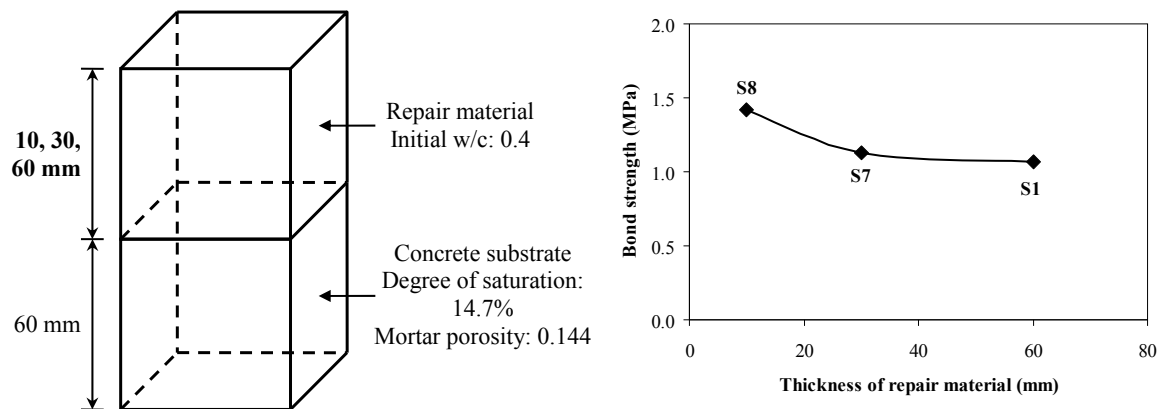
Figure 7.9 Influence of the thickness of the repair material on the simulated bond strength between the repair material and the unsaturated concrete substrate at 28 days. All specimens fail at the interface.

Figure 7.10 shows the influence of the initial w/c ratio of the repair material on the bond strength. When the repair material has a higher initial w/c ratio, it shows a higher resultant w/c ratio after more or less the same amount of water is absorbed by the concrete substrate. The higher w/c ratio leads to a lower tensile strength of the repair material and a lower bond strength.
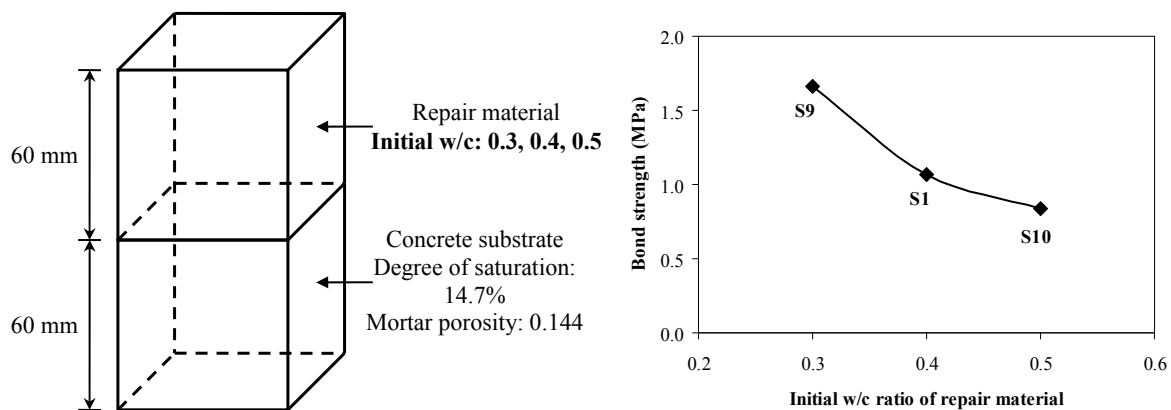
Figure 7.10 Influence of the initial w/c ratio of the repair material on the simulated bond strength between the repair material and the concrete substrate at 28 days. All specimens fail at the interface.

In Chapter 6, it is found that the resultant w/c ratio strongly correlates to the degree of hydration and the porosity at the interface. The resultant w/c ratio at the interface also shows a strong correlation with the simulated bond strength as shown in Figure 7.11. It indicates that when the specimen fails at the interface, the resultant w/c ratio at the interface is a crucial factor determining the bond strength between the repair material and the concrete substrate.
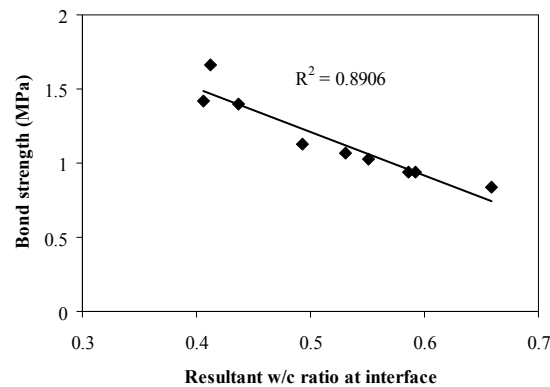
Figure 7.11 Correlation between the simulated bond strength at 28 days and the resultant w/c ratio at the interface.

7.4   Conclusions

The correlation between the bond strength and the microstructure of the repair material and the interface is explored in this chapter. Based on the simulation results and discussion, the following conclusions are drawn:

- The microstructure in the repair material and at the interface determines the bond strength between the repair material and the concrete substrate. The bond strength can be predicted by calculating the specific effective contact area in the repair material and at the interface.
- When the specimen fails at the interface, the simulated bond strength shows a strong correlation with the resultant w/c ratio of the interface. As the resultant w/c ratio decreases, the bond strength increases.
- It is possible to correlate the macro-level performance (bond strength) with the microstructure features (specific effective contact area).

Chapter 8

General Conclusions

8.1   Highlights of this thesis

It is well known that realizing durable concrete repairs is very difficult. The main reason of failures is that most repair materials and the repair-substrate interface cannot withstand the high stresses induced by differential shrinkage. Failures, therefore, manifest themselves by cracking in the repair material and debonding of the repair material from the substrate. The first goal of this thesis is to develop a "green" Engineered Cementitious Composite (ECC) and to demonstrate the good performance of this "green" ECC. The second goal is to develop a numerical tool, which can simulate the bond strength between the repair material and the concrete substrate, to assist engineers in designing a durable concrete repair with good bond.

The failure mechanisms of concrete repairs subjected to the differential shrinkage was first investigated analytically. The parameters, which influence the differential shrinkage-induced stresses, were studied. The analytical study has revealed that a ductile repair material, such as ECC, is desirable to reduce the possibility of failure of concrete repairs. For this reason, ECC is chosen as a repair material in this research.

This thesis demonstrates the feasibility of designing a "green" ECC with limestone powder and blast furnace slag (BFS). Conventional ECC contains a larger amount of cement than concrete, typically two or three times larger. The high cement content leads to a high shrinkage, high cost and poor sustainability. A "green" ECC with low cement content was developed by partially substituting Portland cement with limestone powder and BFS. The "green" ECC has a Portland cement content as low as 15% (by weight), which is about half the amount used in the standard ECC. The development of the "green" ECC can enhance the sustainability of concrete repairs and infrastructures. The mechanical and durability performance of the newly developed "green" ECC repair system was investigated experimentally. The experimental study has shown that the "green" ECC has a potential to improve the mechanical and durability performance of the repaired structures.

This thesis contributes to a better understanding of the bond mechanisms between the repair material and the concrete substrate. The cement hydration process and the degree of hydration of the repair material were investigated by determining the non-evaporable water content. The microstructure development and the bond mechanism in concrete repairs were investigated using mercury intrusion porosimetry (MIP), environmental scanning electron microscopy (ESEM) and direct bond strength test. A numerical tool was developed to simulate the microstructure development and the bond strength in the repair system. The moisture transport between the two materials (the repair material and the concrete substrate) and its effect on the cement hydration process of the repair material was taken into account.

This numerical tool enables designing a concrete repair with good bond, by optimizing the properties of the repair material and the concrete substrate, such as in the ECC repair systems.

8.2   General conclusions

The general conclusions with regards to the main goals of this thesis are given as follows:

1. Limestone powder and BFS can be used to develop "green ECC" by partially substituting Portland cement. At 28 days, the green ECC shows high tensile strain capacity of 3.3% and a moderate compressive strength of 38 MPa.

2. When the repair system is subjected to a differential shrinkage, the interface delamination is the dominate failure mode. The bond strength is, therefore, a crucial factor influencing the performance of the ECC repair system.

3. Before setting of the repair material, the water absorption of the concrete substrate from the repair material causes a reduction of the w/c ratio. What remains is a mixture with a so-called "resultant w/c ratio". The resultant w/c ratio strongly influences the degree of hydration and porosity of the repair material, as well as the bond strength.

4. The microstructure development of the repair material and the bond strength are influenced by many parameters, i.e. the porosity and water content of the concrete substrate, the w/c ratio of the repair material, and the thickness of the repair material and the concrete substrate.

5. Due to the "wall effect", the cement particles have a loose packing at the repair-substrate interface, and the w/c ratio locally increases. The increased w/c ratio results in a porous interfacial zone. The tensile strength of the interface is, in case of a smooth surface of the substrate, lower than that of the repair material.

6. When the specimen fails at the interface, in a case of smooth surface of the substrate, the simulated bond strength shows a strong correlation with the resultant w/c ratio of the interface. When the resultant w/c ratio decreases, the bond strength increases.

7. The surface roughness does not influence the moisture exchange and the cement hydration process. However, when the surface roughness increases, the contact area between the repair material and the concrete substrate increases as well. The increased contact area contributes to the bonding of the interface. As a result, the bond strength increases, and the failure location moves from the interface to the repair material (or maybe the concrete substrate).

8. Due to the small crack width as observed in the experiments, the maximum chloride penetration depth in ECC is smaller than that in the conventional cracked repair material. ECC has a potential to prolong the service life of the repaired structures.

8.3   Further research

From the experience obtained from this thesis, the following aspects appear important for further research:

- Although there are already several good examples of the application of ECC in concrete repairs, the on-site long term performance of ECC repair system needs more research.

- The sustainability of the "green" ECC as repair material needs to be evaluated in detail.

- Some additives, such as silica fume and polymers, are often used to improve the microstructure of the interface and the bond strength. The long-term performance of the interface in the presence of these additives needs to be studied experimentally and numerically.

- The numerical tool developed in this thesis needs to be extended in order to be able to investigate the influence of the roughness of substrate in the micro scale.

- The porosity and water content of the concrete substrate are two important parameters used for the optimization of the bond strength between the repair material and the concrete substrate. The technique, which can be used to test these parameters on construction sites, is needed.

References

ACI 546.3R-06 (2006), *Guide for the Selection of Materials for the Repair of Concrete*, ACI committee 546.

ACI 548.3R (1994), *Abstract of: State-of-the-Art Report on Polymer-Modified Concrete*, ACI Committee 548.

Ackermann, G. (1994), Structural behaviour of joints in composite structures of precast elements and in-situ concrete, *Proc. of the 2nd Bolomey Workshop on Adherence of Young on Old concrete*, p.115-127.

Aligizaki, K.K. (2006), *Pore Structure of Cement-Based Materials*, Taylor & Francis, Oxon, UK.

Amziane, S. (2006), Setting time determination of cementitious materials based on measurements of the hydraulic pressure variations, *Cement and Concrete Research* 36(2): 295-304.

Austin, S., Robins, P. and Pan, Y. (1995), Tensile bond testing of concrete repairs, *Materials and Structures* 28(5): 249-259.

Beushausen, H. (2006), *Long-Term Performance of Bonded Concrete Overlays Subjected to Differential Shrinkage*, PhD thesis, University of Cape Town, South Africa.

Beushausen, H. and Alexander, M.G. (2007), Localised strain and stress in bonded concrete overlays subject to differential shrinkage, *Materials and Structures* 40(2): 189-199.

Bijen, J. and Salet, T. (1994), Adherence of young concrete to old concrete – development of tools for engineering, *Proc. of the 2nd Bolomey Workshop on Adherence of Young on Old concrete*, pp.1-24.

Bijen, J. (1996), Benefits of slag and fly ash, *Construction and Building Materials* 10(5): 309-314.

Birkeland, H.W. (1960), Differential shrinkage in composite beams, *ACI Journal* 56(5): 1123-1136.

Brooks, J.J. (1989), Influence of mix proportions, plasticizer and superplasticizer on creep and drying shrinkage of concrete, *Magazine of Concrete Research* 41(148): 145-154.

Copeland, L.E., Kantro, D.L. and Verbeck, G. (1962), Chemistry of hydration of Portland cement, *Proc. of the 4th International Symposium on Chemistry of Cement*, pp.429.

Courard, L. (2000), Parametric study for the creation of the interface between concrete and repair products, *Materials and Structures* 33(1): 65-72.

Courard, L. (2005), Adhesion of repair systems to concrete: influence of interfacial topography and transport phenomena, *Magazine of Concrete Research* 57(5): 273-282.

Courard, L. and Degeimbre, R. (2003), A capillary action test for the investigation of adhesion in repair technology, *Canadian Journal of Civil Engineering* 30(6): 1101-1110.

Courard, L. and Nelis, M. (2003), Surface analysis of mineral substrates for repair works: roughness evaluation by profilometry and surfometry analysis, *Magazine of Concrete Research* 55(4): 355-366.

Crausse, P., Bacon, G. and Bories, S. (1981), Etude fondamentale des transferts couplés chaleur-masse en milieu poreux, *International Journal of Heat and Mass Transfer* 24(6): 991-1004.

Cusson, D. and Mailvaganam, N. (1996), Durability of repair materials, *Concrete International* 18(3): 34-38.

de Rooij, M.R. and Polder, R.B. (2005), *Durability of Marine Concrete Structures*, CUR report 215, (in Dutch).

Diamond, S. (2007), Measurement of the viscosity of resins used in SEM specimen preparation, *Materials and Structures* 40(9): 995-1000.

Diamond, S. and Leeman, M.E. (1995), Pore size distribution in hardened cement paste by SEM image analysis, *Proc. of Materials Research Society Symposia*, vol. 370, pp. 217-226.

Dullien, F.A.L. (1992), *Porous Media: Fluid Transport and Pore Structures*, 2nd ed., Academic Press, London.

DuraCrete (2000), The European Union – Brite EuRam III, *DuraCrete – Probabilistic Performance Based Durability Design of Concrete Structures*, DuraCrete Final Technical Report R 17, Document BE95-1347/R17, CUR, Gouda, the Netherlands.

Emberson, N.K. and Mays, G.C. (1990), Significance of property mismatch in the patch repair of structural concrete, Part 1: Properties of repair systems, *Magazine of Concrete Research* 42(152): 147-160.

Emmons, P.H. and Sordyl, D.J. (2006), The state of the concrete repair industry and a vision for its future, *Concrete Repair Bulletin*, July/August 2006, pp. 7-14.

Emmons, P.H. and Vaysburd, A.M. (1994), Factors affecting the durability of concrete repair: the contractor's viewpoint, *Construction and Building Materials* 8(1):5-16.

EN 197-1 (2000), *Cement - Part 1: Composition, Specifications and Conformity Criteria for Common Cements*.

EN 480-5 (2005), *Admixtures for Concrete, Mortar and Grout - Test Methods - Part 5: Determination of Capillary Absorption*.

EN 12617-4 (2002), *Products and Systems for the Protection and Repair of Concrete Structures - Test Methods - Part 4: Determination of shrinkage and expansion*.

EN 14488-4 (2002), *Testing Sprayed Concrete – Part 4: Bond Strength of Cores by Direct Tension.*

Escalante-Garcia, J.I. (2003), Nonevaporable water from neat OPC and replacement materials in composite cements hydrated at different temperatures, *Cement and Concrete Research* 33(11): 1883-1888.

Feldman, R.F. (1986), Pore structure, permeability and diffusivity as related to durability, *Proc. of the 8th International Congress on Chemistry of Cement*, vol. 1(4), pp. 336-356.

Fiebrich, M.H. (1994), Scientific aspects of adhesion phenomena in the interface mineral substrate-polymers, *Proc. of the 2nd Bolomey Workshop on Adherence of Young on Old concrete*, pp. 25-58.

Gaal, G.C.M., Walraven, J.C. and Polder, R.B. (2003), Critical chloride content – state of the art, *Proc. of the 10th International Conference on Structural Faults and Repair*, pp. 1-8.

Garbacz, A., Courard, L. and Kostana, K. (2006), Characterization of concrete surface roughness and its relation to adhesion in repair systems, *Materials Characterization* 56(4-5): 281-289.

Garbacz, A., Gorka, M. and Courard, L. (2005), Effect of concrete surface treatment on adhesion in repair systems, *Magazine of Concrete Research* 57(1): 49-60.

Hong Kong Housing Authority (1991), *Practice Notes for Concrete Repair*.

Kim, J.K., Kim, J.S., Ha, G.J. and Kim, Y.Y. (2007), Tensile and fiber dispersion performance of ECC (engineered cementitious composites) produced with ground granulated blast furnace slag, *Cement and Concrete Research* 37(7): 1096-1105.

Kjellsen, K.O., Monsoy, A., Isachsen, K. and Detwiler, R.J. (2003), Preparation of flat-polished specimens for SEM-backscatter electron imaging and X-ray microanalysis – importance of epoxy impregnation, *Cement and Concrete Research* 33(4): 611-616.

Koenders, E.A.B. (1997), *Simulation of Volume Changes in Hardening Cement-Based Materials*, PhD thesis, Delft University of Technology, the Netherlands. http://Microlab.citg.tudelft.nl

Larbi, J.A. (1992), *The Cement Paste-Aggregate Interfacial Zone in Concrete*, PhD thesis, Delft University of Technology, the Netherlands.

Lepech, M.D. and Li, V.C. (2005), Water permeability of cracked cementitious composites, *Proc. of the 11th International Conference on Fracture*, paper 4539.

Lepech, M.D. and Li, V.C. (2006), Long term durability performance of engineered cementitious composites, *International Journal for Restoration of Buildings and Monuments* 12(2): 119-132.

Li, M. and Li, V.C. (2006), Behavior of ECC/concrete layered repair system under drying shrinkage conditions, *International Journal for Restoration of Buildings and Monuments* 12(2): 143-160.

Li, M. and Li, V.C. (2009), Influence of material ductility on the performance of concrete repairs, *ACI Materials Journal* 106(5): 419-428.

Li, V.C. (1993), From micromechanics to structural engineering – the design of cementitious composites for civil engineering applications, *JSCE Journal of Structural Mechanics and Earthquake Engineering* 10(2): 37-48.

Li, V.C. (2003), On engineered cementitious composites (ECC), *Journal of Advanced Concrete Technology* 1(3): 215-230.

Li, V.C. (2004), High performance fiber reinforced cementitious composites as durable material for concrete structure repair, *International Journal for Restoration of Buildings and Monuments* 10(2): 163-180.

Li, V.C. (2007), Engineered cementitious composites (ECC) – material, structural and durability performance, in E. Nawy (ed.), *Concrete Construction Engineering Handbook*, Boca Raton: CRC Press, Chapter 24.

Li, V.C. and Leung, C.K.Y. (1992), Theory of steady state and multiple cracking of random discontinuous fiber reinforced brittle matrix composites, *ASCE Journal of Engineering Mechanics* 118(11): 2246-2264.

Maalej, M. and Li, V.C. (1994), Flexural/tensile strength ratio in engineered cementitious composite, *ASCE Journal of Materials in Civil Engineering* 6(4): 513-528.

Maekawa, K., Chaube, R. and Kishi, T. (1999), *Modelling of Concrete Performance: Hydration, Microstructure Formation and Mass Transport*, E&FN Spon, London.

Mangat, P.S. and O'Flaherty, F.J. (2000), Influence of elastic modulus on stress redistribution and cracking in repair patches, *Cement and Concrete Research* 30(1): 125-136.

Mays, G. and Wilkinson, W. (1987), Polymer repairs to concrete: their influence on structural performance, *ACI Special Publication SP-100-22*, pp. 351-375.

McDonald, J.E. and Campbell, R.L. (1985), *The Condition of Corps of Engineers Civil Works Concrete Structures*, Technical Report REMR-CS-2. http://www.wes.army.mil/REMR/reports.html

Mummery, L. (1992), *Surface Texture Analysis: The Handbook*, Hommelwerke GmbH, Thyssen.

Neville, A.M. (1995), *Properties of Concrete*, 4th ed., Longman, Harlow.

NT BUILD 492 (1999), *Concrete, Mortar and Cement-based repair materials: Chloride migration coefficient from non-steady-state migration experiments*.

Oluokun, F. (1991), Prediction of concrete tensile strength from its compressive strength: an evaluation of existing relations for normal weight concrete, *ACI Materials Journal* 88(3): 302-309.

Oner, M. (2000), A study of intergrinding and separate grinding of blast furnace slag cement, *Cement and Concrete Research* 30(3): 473-480.

Parrott, L.J., Geiker, M., Gutteridge, W.A. and Killoh, D. (1990), Monitoring Portland cement hydration: comparison of methods, *Cement and Concrete Research* 20(6): 919-926.

Pigeon, M. and Saucier, F. (1992), Durability of repaired concrete structures, *Proc. of International Symposium on Advances in Concrete Technology*, pp. 741-773.

Polder, R.B., de Rooij, M.R. and van Breugel, K. (2006), Validation of models for service life prediction – experiments from the practice, *Proc. of the International RILEM-JCI Seminar on Concrete Life'06*, pp. 292-301.

Poppe, A.M. and De Schutter, G. (2005), Cement hydration in the presence of high filler contents, *Cement Concrete Research* 35(12): 2290-2299.

Powers, T.C. and Brownyard, T.L. (1946), Studies of the physical properties of hardened Portland cement pastes, *Journal of American Concrete Institute* 18(2): 101-132.

Qian, S. and Li, V.C. (2007), Simplified inverse method for determining the tensile strain capacity of strain hardening cementitious composites, *Journal of Advanced Concrete Technology* 5(2): 235-246.

Sahmaran, M. and Li, V.C. (2008), Durability of mechanically loaded engineered cementitious composites under highly alkaline environment, *Cement and Concrete Composites* 30(2): 72-78.

Sahmaran, M., Li, V.C. and Andrade, C. (2008), Corrosion resistance performance of steel-reinforced engineered cementitious composite beams, *ACI Materials Journal* 105(3): 243-250.

Santos, P.M.D., Julio, E.N.B.S. and Silva, V.D. (2007), Correlation between concrete-to-concrete bond strength and the roughness of the substrate surface, *Construction and Building Materials* 21(8): 1688-1695.

Silfwerbrand, J. (1997), Stresses and strains in composite concrete beams subjected to differential shrinkage, *ACI Structural Journal* 94(4): 347-353.

Sun, Z., Ye, G., Voigt, T., Shah, S.P. and van Breugel, K. (2004), Early age properties of Portland cement pastes and investigated with ultrasonic shear waves and numerical simulation, *Proc. of the RILEM International Symposium on Advances in Concrete through Science and Engineering*, in CD-ROM.

Sun, Z., Ye, G. and Shah, S.P. (2005), Microstructure and early-age properties of Portland cement paste – Effects of connectivity of solid phases, *ACI Materials Journal* 102(2): 122-129.

Taylor, H.W.F. (1990), *Cement Chemistry*, Academic Press, London.

Timoshenko, S. and Woinowsky-Krieger, S. (1989), *Theory of Plates and Shells*, 2nd ed., McGraw-Hill, Auckland.

Tsivilis, S., Batis, G., Chaniotakis, E., Grigoriadis, Gr and Theodossis, D. (2000), Properties and behavior of limestone cement concrete and mortar, *Cement Concrete Research* 30(10): 1679-1683.

Underwood, E.E. (1970), *Quantitative Stereology*, Addison-Wesley, Massachusetts.

van Breugel, K. (1991), *Simulation of Hydration and Formation of Structure in Hardening Cement-Based Materials*, PhD thesis, Delft University of Technology, the Netherlands. http://Microlab.citg.tudelft.nl

van Breugel, K. and Polder, R. (2009), Probability-based service life design of structural concrete, *Proc. of the 2nd International RILEM Workshop on Concrete Durability and Service Life Planning-ConcreteLife'09*, pp. 383-391.

van Zijl, G.P.A.G. and Stander, H. (2008), SHCC repair overlays for RC: interfacial bond characterization and modeling, *Proc. of the 2nd International Conference on Concrete Repair, Rehabilitation and Retrofitting*, pp. 995-1003.

Vaysburd, A.M. and Emmons P.H. (2006), Concrete repair-a composite system: Philosophy, engineering and practice, *Proc. of the International Conference on Concrete Repair, Rehabilitation and Retrofitting*, pp. 9-11.

Wang, S. and Li, V.C. (2006), High-early-strength engineered cementitious composites, *ACI Materials Journal* 103(2): 97-105.

Wang, S. and Li, V.C. (2007), Engineered cementitious composites with high-volume of fly ash, *ACI Materials Journal* 104(3): 233-241.

Weimann, M.B. and Li, V.C. (2003), Hygral behavior of engineered cementitious composite (ECC), *International Journal for Restoration of Buildings and Monuments* 9(5): 513-534.

Yang, E.H., Wang, S., Yang, Y. and Li, V.C. (2008), Fiber-bridging constitutive law of engineered cementitious composites, *Journal of Advanced Concrete Technology* 6(1): 181-193.

Yang, E.H., Yang, Y. and Li, V.C. (2007), Use of high volumes of fly ash to improve ECC mechanical properties and material greenness, *ACI Materials Journal* 104(6): 620-628.

Ye, G. (2003), *Experimental Study and Numerical Simulation of the Development of the Microstructure and Permeability of Cementitious Materials*, PhD thesis, Delft University of Technology, the Netherlands. http://Microlab.citg.tudelft.nl

Zhang, M., Ye, G. and van Breugel, K. (2010), Study on representative elementary volume (REV) for diffusivity in cement paste based on numerical-statistical approach, accepted by *Materiales de Construcción*.

Zhou, J. (2006), *Microstructure and Permeability of Portland Cement Blended with Blastfurnace Slag, Fly Ash and Limestone Powder*, MSc thesis, Delft University of Technology, the Netherlands. http://Microlab.citg.tudelft.nl

Appendix 1

Analytical Calculation of Stresses Induced by Differential Shrinkage in Concrete Repairs

---

A1.1 Introduction

The first analytical model used to calculate the stresses induced by the differential shrinkage was developed by Birkeland [1960] in the 1960s. In this model, a compressive force is applied on the ends of the repair material. The absolute value of this compressive force is equal to that of the tensile force induced by the fully restrained shrinkage of the repair material. He assumed that the repair material is tightly bonded on the concrete substrate, and there is no slip at the interface. Employing the linear elasticity and the Bernoulli's hypothesis, the tensile stresses in the repair material and the compression stress in the substrate concrete can be calculated. Recently, Beushausen and Alexander [2007] also developed a model, based on the experimental results. There two models can only be used to calculated the tensile stresses in the repair material. Silfwerbrand [1997] introduced another model, and he assumed that that the shear stresses at the interface is linear to the slip between the repair material and the concrete substrate. This solved the calculation the shear stresses at the interface. However, the debonding stress at the interface, which is responsible for the interface delamination, can not be estimated.

In order to calculate the debonding stresses at the interface, the plate theory was used [Timoshenko 1989]. The analytical procedure will be discussed in detail. The method to calculate the stresses in ECC will also be developed.

A1.2 Analytical procedure

This section presents the development of the analytical model used for calculating the stresses in the layered concrete repair subjected to differential shrinkage. Figure A1.1 shows a concrete repair subjected to a differential shrinkage. The repair material with the Young's modulus of E_r [N/mm^2] and a thickness of h_r [mm] is bonded on the substrate concrete with a Young's modulus of E_s [N/mm^2] and a thickness of h_s [mm]. The length of the repair system is L [mm]. The shrinkage of the repair material is $\varepsilon_{sh}(y)$, and its positive value corresponds to contraction. The influence of lateral contraction is not taken into account, i.e. Poisson's ratio v is zero.
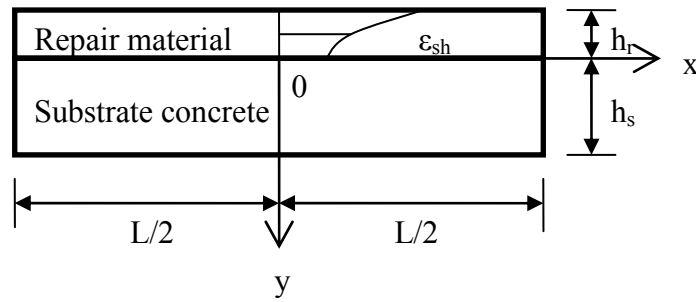
Figure A1.1 A layered concrete repair subjected to differential shrinkage.

The procedure of the model development can be divided into the following four stages:
- First, the repair material is assumed to be separated from the concrete substrate. The shrinkage of the repair material is restrained at the ends. A tensile stress $\sigma_{xx,sh}(y) = E_r \varepsilon_{sh}(y)$ is thus induced in the repair material.

- Secondly, the repair material is bonded on the concrete substrate. For the equilibrium of the repair system, a compressive stress $-\sigma_{xx,sh}(y)$ is then applied at the ends of the repair material. This stress is simplified to be constant over the depth of the repair material (Figure A1.2):

$$\sigma_{eq} = -\frac{1}{h_r} \int_{-h_r}^{0} E_r \varepsilon_{sh}(y) dy \qquad (A1.1)$$

- Thirdly, the stresses and strains in the repair system subjected to the external compressive stress σ_{eq} are calculated based on the assumption of the linear relation between shear stress and slip at interface [Yuan and Marosszeky 1994, Silfwerbrand 1997]:

$$\sigma_{xy}(x) = K\Delta u(x) \qquad (A1.2)$$

where K [N/mm^3] is the shear stiffness of the interface and $\Delta u(x)$ [mm] is the slip at the interface.
- Finally, the restrained shrinkage stress $\sigma_{sh}(y)$ is superimposed to the stresses calculated in the third stage.
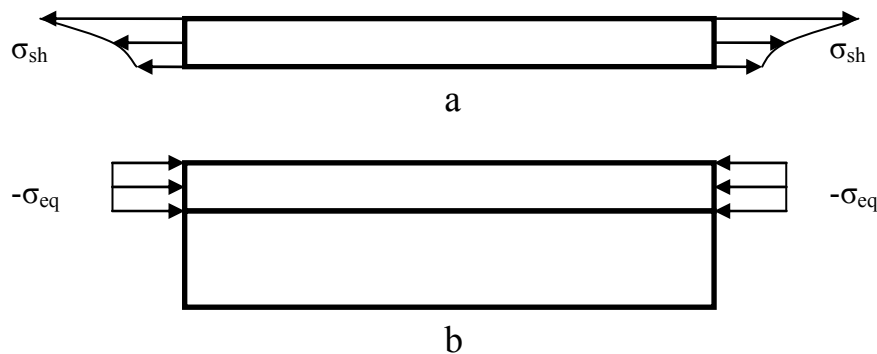
Figure A1.2 Modeling stresses induced by a differential shrinkage

The last two stages will be discussed in detail in the following. Figure A1.3 shows the displaced and deformed state of an element in concrete repairs. This rigid body has three displacements, i.e. a displacement in x-direction (u_x), a displacement in y-direction (u_y) and a rotation (ω_{xy}), and three deformations, i.e. a strain in x-direction (ε_{xx}), a strain in y-direction (ε_{yy}) and a shear deformation (γ_{xy}). The kinematic equations relating the displacements and the deformations can be written as:

$$\varepsilon_{xx} = \frac{\partial u_x}{\partial x} \tag{A1.3}$$

$$\varepsilon_{yy} = \frac{\partial u_y}{\partial y} \tag{A1.4}$$

$$\gamma_{xy} = \frac{\partial u_x}{\partial y} + \frac{\partial u_y}{\partial x} \tag{A1.5}$$
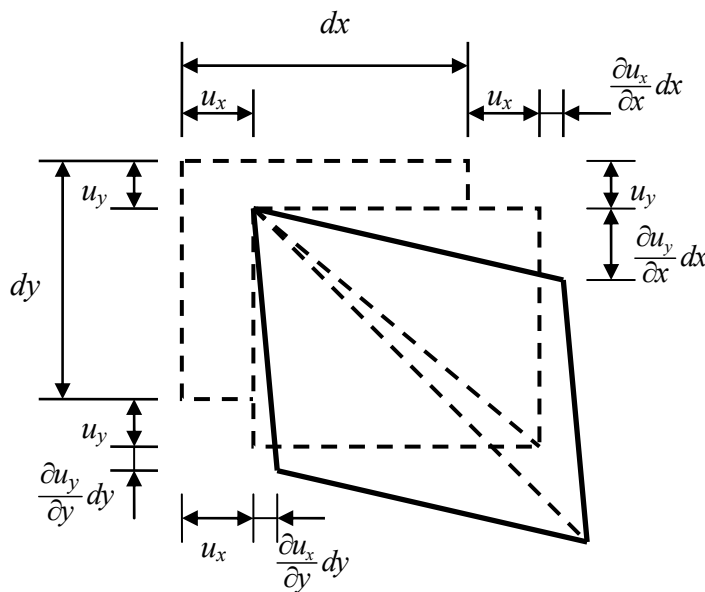
Figure A1.3 Displaced and deformed state of an element

According to Hooke's law, the constitutive equations, which describe the relations between the stresses and the strains, can be given:

$$\varepsilon_{xx} = \frac{1}{E}\sigma_{xx} \tag{A1.6}$$

$$\varepsilon_{yy} = \frac{1}{E}\sigma_{yy} \tag{A1.7}$$

$$\gamma_{xy} = \frac{2}{E}\sigma_{xy} \tag{A1.8}$$

where σ_{xx}, σ_{yy}, and σ_{xy} are the stresses in x-direction, in y-direction and the shear stress, respectively. Based on the equilibrium of this element (Figure A1.4), the equilibrium equations, which relate the loads to the stress resultants, can be obtained:

$$\frac{\partial \sigma_{xx}}{\partial x} + \frac{\partial \sigma_{xy}}{\partial y} = 0 \tag{A1.9}$$

$$\frac{\partial \sigma_{yy}}{\partial y} + \frac{\partial \sigma_{xy}}{\partial x} = 0 \tag{A1.10}$$

Figure A1.4 Equilibrium of an element

By combining the kinematic equations, the constitutive equations, and the equilibrium equations, three partial differential equations are derived:

$$E\left(\frac{\partial^4 u_x}{\partial x^4} + 2\frac{\partial^4 u_x}{\partial x^2 y^2} + \frac{\partial^4 u_x}{\partial y^4}\right) = 0 \tag{A1.11}$$

$$E\left(\frac{\partial^4 u_y}{\partial x^4} + 2\frac{\partial^4 u_y}{\partial x^2 y^2} + \frac{\partial^4 u_y}{\partial y^4}\right) = 0 \tag{A1.12}$$

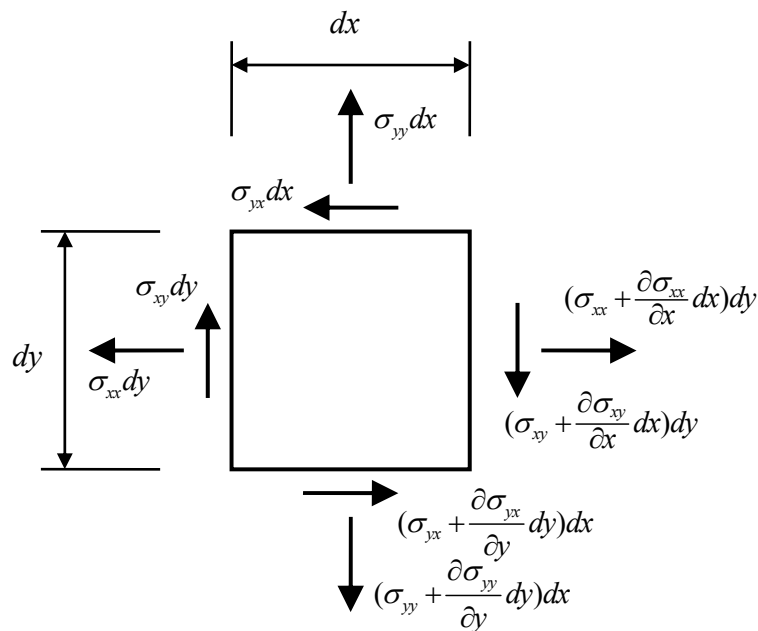$$\frac{\partial^2 u_x}{\partial x^2} + \frac{1}{2}\frac{\partial^2 u_x}{\partial y^2} + \frac{1}{2}\frac{\partial^2 u_y}{\partial x \partial y} = 0 \tag{A1.13}$$

With the solution in the form of $u_x = Ae^{\lambda x + \lambda y}$, the general solutions can be solved:

$$u_x = \left(A_1\left(e^{\lambda x} - e^{-\lambda x}\right) + A_2 x\left(e^{\lambda x} + e^{-\lambda x}\right)\right)\sin\left(\lambda y + A_3\right) + A_4 x \tag{A1.14}$$

$$u_y = \left(\frac{A_1 \lambda + 3A_2}{\lambda}\left(e^{\lambda x} + e^{-\lambda x}\right) + A_2 x\left(e^{\lambda x} - e^{-\lambda x}\right)\right)\cos\left(\lambda y + A_3\right) + A_5 y \tag{A1.15}$$

where A_i ($i = 1, 2, \ldots 5$) are constants.

To determine these constants, the following boundary conditions can be used:

1. The ends of the repair material are subjected to the compression stresses σ_{eq}, i.e. when $x = \pm\frac{L}{2}$, $\sigma_{xx}^r = \sigma_{eq}$.

2. The ends of the concrete substrate are free, i.e. when $x = \pm\frac{L}{2}$, $\sigma_{xx}^s = 0$.

3. The top of the repair material is not subjected to any load, i.e. when $y = -h_r$, $\sigma_{xy}^r = 0$ and $\sigma_{yy}^r = 0$.

4. The bottom of the concrete substrate is free in x-direction, i.e. when $y = h_s$, $\sigma_{xy}^s = 0$ and $u_y^s = 0$.

5. At the interface the normal stresses in the repair material are equal to those in the concrete substrate, and their sum is equal to zero, i.e. when $y = 0$, $\sigma_{yy}^r = \sigma_{yy}^s$ and $\int_{-\frac{L}{2}}^{\frac{L}{2}} \sigma_{yy}^r dx = 0$.

6. At the interface the shear stresses in the repair material and in the concrete substrate are equal and are proportional to the slip, i.e. when $y = 0$, $\sigma_{xy}^r = \sigma_{xy}^s = K(u_x^s - u_x^r)$.

where u_r, σ_r, u_s, and σ_s are the displacements and the stresses in the repair material and in the concrete substrate, respectively.

By superimposing $\sigma_{sh}(y)$ in the repair material, the stresses and the strains in this repair system are determined as follows:

$$\sigma_{xx}^r = \frac{\sigma_{eq}E_s \sin(\lambda h_s)\cos(\lambda y + \lambda h_r)\left(e^{\lambda x} + e^{-\lambda x}\right) + E_r \sin(\lambda h_r)\left(e^{\frac{\lambda L}{2}} + e^{-\frac{\lambda L}{2}}\right)}{\left(E_r \sin(\lambda h_r) + E_s \sin(\lambda h_s)\right)\left(e^{\frac{\lambda L}{2}} + e^{-\frac{\lambda L}{2}}\right)} + E_r \varepsilon_{sh} \quad \text{(A1.16)}$$

$$\sigma_{yy}^r = \frac{\sigma_{eq}E_s \cos(\lambda h_s)\left(\sin(\lambda y + \lambda h_r)\left(e^{\lambda x} + e^{-\lambda x}\right) - \frac{2}{\lambda L}\sin(\lambda h_r)\left(e^{\frac{\lambda L}{2}} - e^{-\frac{\lambda L}{2}}\right)\right)}{\left(E_r \sin(\lambda h_r) - E_s \cos(\lambda h_s)\right)\left(e^{\frac{\lambda L}{2}} + e^{-\frac{\lambda L}{2}}\right)} \quad \text{(A1.17)}$$

$$\sigma_{xy}^r = -\frac{\sigma_{eq}E_s \sin(\lambda h_s)\sin(\lambda y + \lambda h_r)\left(e^{\lambda x} - e^{-\lambda x}\right)}{\left(E_r \sin(\lambda h_r) + E_s \sin(\lambda h_s)\right)\left(e^{\frac{\lambda L}{2}} + e^{-\frac{\lambda L}{2}}\right)} \quad \text{(A1.18)}$$

$$\sigma_{xx}^s = -\frac{\sigma_{eq}E_s \sin(\lambda h_r)\left(\cos(\lambda y - \lambda h_s)\left(e^{\lambda x} + e^{-\lambda x}\right) - \left(e^{\frac{\lambda L}{2}} + e^{-\frac{\lambda L}{2}}\right)\right)}{\left(E_r \sin(\lambda h_r) + E_s \sin(\lambda h_s)\right)\left(e^{\frac{\lambda L}{2}} + e^{-\frac{\lambda L}{2}}\right)} \quad \text{(A1.19)}$$

$$\sigma_{yy}^s = \frac{\sigma_{eq}E_s \sin(\lambda h_r)\left(\cos(\lambda y - \lambda h_s)\left(e^{\lambda x} + e^{-\lambda x}\right) - \frac{2}{\lambda L}\cos(\lambda h_s)\left(e^{\frac{\lambda L}{2}} - e^{-\frac{\lambda L}{2}}\right)\right)}{\left(E_r \sin(\lambda h_r) - E_s \cos(\lambda h_s)\right)\left(e^{\frac{\lambda L}{2}} + e^{-\frac{\lambda L}{2}}\right)} \quad \text{(A1.20)}$$

$$\sigma_{xy}^s = \frac{\sigma_{eq}E_s \sin(\lambda h_r)\sin(\lambda y - \lambda h_s)\left(e^{\lambda x} - e^{-\lambda x}\right)}{\left(E_r \sin(\lambda h_r) + E_s \sin(\lambda h_s)\right)\left(e^{\frac{\lambda L}{2}} + e^{-\frac{\lambda L}{2}}\right)} \quad \text{(A1.21)}$$

where $\lambda = \dfrac{K\cos(\lambda h_r)}{E_r \sin(\lambda h_r)} + \dfrac{K\cos(\lambda h_s)}{E_s \sin(\lambda h_s)}$.

In the layered repair system, only the maximum values of the stresses and strains are responsible for the failure of concrete repairs. According to Eqs. A1.16-21, the highest σ_{xx} in the repair material is situated at the middle of the bottom, and the highest σ_{yy} and σ_{xy} at the interface are situated at the two ends. This explains why the cracking is often observed in the mid of the repair material and the delamination always starts from the ends of interface [Beushausen and Alexander 2007]. The equation for calculating the critical stresses can be derived from Eqs. A1.16-18:

$$\sigma_{xx}^{max} = \frac{\varepsilon_{sh} E_r E_s \sin(\lambda h_s)}{E_r \sin(\lambda h_r) + E_s \sin(\lambda h_s)} \times \left(1 - \frac{2}{e^{\lambda \frac{L}{2}} + e^{-\lambda \frac{L}{2}}}\right) \tag{A 1.22}$$

$$\sigma_{yy}^{max} = \frac{\varepsilon_{sh} E_r E_s \sin(\lambda h_r) \cos(\lambda h_s)}{E_r \sin(\lambda h_r) - E_s \cos(\lambda h_s)} \times \left(\frac{e^{\lambda \frac{L}{2}} - e^{-\lambda \frac{L}{2}}}{e^{\lambda \frac{L}{2}} + e^{-\lambda \frac{L}{2}}} \times \frac{2}{\lambda L} - 1\right) \tag{A1.23}$$

$$\sigma_{xy}^{max} = \frac{\varepsilon_{sh} E_r E_s \sin(\lambda h_r) \sin(\lambda h_s)}{E_r \sin(\lambda h_r) + E_s \sin(\lambda h_s)} \times \frac{e^{\lambda \frac{L}{2}} - e^{-\lambda \frac{L}{2}}}{e^{\lambda \frac{L}{2}} + e^{-\lambda \frac{L}{2}}} \tag{A1.24}$$

A1.3　Simplification of the analytical model

Since the calculated λ is very small, the following terms can be simplified as:

$$\sin(\lambda h_r) \approx \lambda h_r \tag{A1.25}$$

$$\cos(\lambda h_r) \approx 1 \tag{A1.26}$$

$$\sin(\lambda h_s) \approx \lambda h_s \tag{A1.27}$$

$$\cos(\lambda h_s) \approx 1 \tag{A1.28}$$

The λ is rewritten as:

$$\lambda \approx \frac{K}{E_r \lambda h_r} + \frac{K}{E_s \lambda h_s} \tag{A1.29}$$

The expression of λ is rewritten as

$$\lambda \approx \sqrt{\frac{K}{E_r h_r} + \frac{K}{E_s h_s}} \tag{A1.30}$$

Substitute Eqs. A1.22-25 into the Eqs. A1.28-30, the expression of the critical stresses can be simplified as:

$$\sigma_{xx}^{max} = \frac{E_r \varepsilon_{sh}}{\frac{E_r h_r}{E_s h_s} + 1} \times \left(1 - \frac{2}{e^{\lambda \frac{L}{2}} + e^{-\lambda \frac{L}{2}}} \right) \tag{A1.31}$$

$$\sigma_{yy}^{max} = \frac{E_r \varepsilon_{sh}}{\frac{E_r}{E_s} - \frac{1}{\lambda h_r}} \times \left(\frac{e^{\lambda \frac{L}{2}} - e^{-\lambda \frac{L}{2}}}{e^{\lambda \frac{L}{2}} + e^{-\lambda \frac{L}{2}}} \times \frac{2}{\lambda L} - 1 \right) \tag{A1.32}$$

$$\sigma_{xy}^{max} = \frac{E_r \varepsilon_{sh} \lambda h_r}{\frac{E_r h_r}{E_s h_s} + 1} \times \frac{e^{\lambda \frac{L}{2}} - e^{-\lambda \frac{L}{2}}}{e^{\lambda \frac{L}{2}} + e^{-\lambda \frac{L}{2}}} \tag{A1.33}$$

A1.4 Calculation of stresses in ECC repair systems

As shown in Figure A1.5, under tensile load, ECC behaves differently before and after the first cracking, which corresponds to the "yield point" in the tensile stress-strain curve. The response of ECC under uniaxial tensile load can be divided into two stages. When the tensile load is lower than the first cracking strength f_{fc}, ECC behaves like common cement-based materials. When the tensile load is between the first cracking strength f_{fc} and the ultimate strength f_t, ECC shows strain-hardening behavior. The bilinear behavior of ECC can be simplified by using different Young's moduli before and after the first cracking as shown in Figure A1.5.
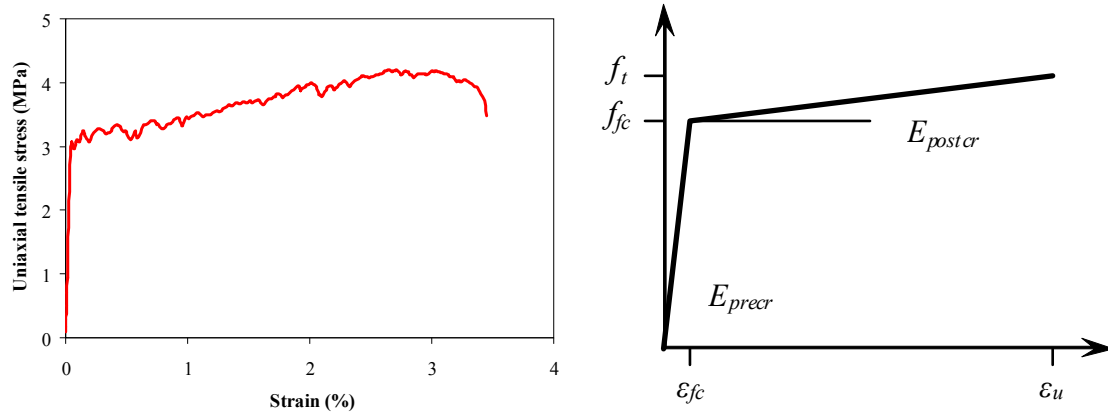
Figure A1.5 Simplified stress-strain curve of ECC

Accordingly, the calculation of stresses in the ECC repair system is divided into two stages. In the first stage, i.e. when the tensile stress in ECC is smaller than the first cracking strength of ECC, as the differential shrinkage increases, the stresses in ECC repair system increase. The stresses can be calculated by using Eqs. A1.31-33 with the Young's modulus of ECC, E_{precr}. The critical value of the differential shrinkage ε_{fc}, which corresponds to the stresses leading to the first cracking of ECC, can be calculated with the following equation:

$$\sigma_{xx}^{precr} = \frac{E_{precr}\varepsilon_{fc}}{\frac{E_{precr}h_r}{E_s h_s}+1} \times \left(1 - \frac{2}{e^{\lambda_{precr}\frac{L}{2}} + e^{-\lambda_{precr}\frac{L}{2}}}\right) = \sigma_{fc} \tag{A1.34}$$

where $\lambda_{precr} = \sqrt{\frac{K}{E_{precr}h_r} + \frac{K}{E_s h_s}}$. With the calculated value of the differential volume change ε_{fc}, the stresses at the interface can be calculated by:

$$\sigma_{yy}^{precr} = \frac{E_{precr}\varepsilon_{fc}}{\frac{E_{precr}}{E_s} - \frac{1}{\lambda_{precr}h_r}} \times \left(\frac{e^{\lambda_{precr}\frac{L}{2}} - e^{-\lambda_{precr}\frac{L}{2}}}{e^{\lambda_{precr}\frac{L}{2}} + e^{-\lambda_{precr}\frac{L}{2}}} \times \frac{2}{\lambda_{precr}L} - 1\right) \tag{A1.35}$$

$$\sigma_{xy}^{precr} = \frac{E_{precr}\varepsilon_{fc}\lambda_{precr}h_r}{\frac{E_{precr}h_r}{E_s h_s}+1} \times \frac{e^{\lambda_{precr}\frac{L}{2}} - e^{-\lambda_{precr}\frac{L}{2}}}{e^{\lambda_{precr}\frac{L}{2}} + e^{-\lambda_{precr}\frac{L}{2}}} \tag{A1.36}$$

Once the tensile stress in ECC exceeds the first cracking strength of ECC, ECC cracks and the calculation enters the second stage. It is assumed that the whole ECC layer turns into the strain-hardening stage after the first cracking, and the stress-strain gradient is E_{postcr}. The stresses induced by the increase in the differential shrinkage from ε_{fc} to ε_{sh} can be calculated by:

$$\sigma_{xx}^{postcr} = \frac{E_{postcr}\left(\varepsilon_{sh} - \varepsilon_{fc}\right)}{\dfrac{E_{postcr}h_r}{E_s h_s} + 1} \times \left(1 - \frac{2}{e^{\lambda_{postcr}\frac{L}{2}} + e^{-\lambda_{postcr}\frac{L}{2}}}\right) \qquad (A1.37)$$

$$\sigma_{yy}^{postcr} = \frac{E_{postcr}\left(\varepsilon_{sh} - \varepsilon_{fc}\right)}{\dfrac{E_2}{E_s} - \dfrac{1}{\lambda_{postcr}h_r}} \times \left(\frac{e^{\lambda_{precr}\frac{L}{2}} - e^{-\lambda_{precr}\frac{L}{2}}}{e^{\lambda_{precr}\frac{L}{2}} + e^{-\lambda_{precr}\frac{L}{2}}} \times \frac{2}{\lambda_{postcr}L} - 1\right) \qquad (A1.38)$$

$$\sigma_{xy}^{postcr} = \frac{E_{postcr}\left(\varepsilon_{sh} - \varepsilon_{fc}\right)\lambda_{postcr}h_r}{\dfrac{E_{postcr}h_r}{E_s h_s} + 1} \times \frac{e^{\lambda_{precr}\frac{L}{2}} - e^{-\lambda_{precr}\frac{L}{2}}}{e^{\lambda_{precr}\frac{L}{2}} + e^{-\lambda_{precr}\frac{L}{2}}} \qquad (A1.39)$$

where $\lambda_{postcr} = \sqrt{\dfrac{K}{E_{postcr}h_r} + \dfrac{K}{E_s h_s}}$.

By superimposing the stresses calculated in these two stages, the stresses in ECC repair system induced by differential shrinkage can be determined by the following equations:

$$\sigma_{xx} = \sigma_{xx}^{precr} + \sigma_{xx}^{postcr} \qquad (A1.40)$$

$$\sigma_{yy} = \sigma_{yy}^{precr} + \sigma_{yy}^{postcr} \qquad (A1.41)$$

$$\sigma_{xy} = \sigma_{xy}^{precr} + \sigma_{xy}^{postcr} \qquad (A1.42)$$

Summary

1. Background and goals of this thesis

The concrete repair, rehabilitation and retrofitting industry grows rapidly, driven by deterioration of, damage to and defects in concrete structures. However, it is well known that to achieve durable concrete repairs is very difficult. The failure of concrete repairs causes high economical, social and environmental impacts. The main reason of failures is that most repair materials and the repair-substrate interface cannot withstand the high stresses induced by differential shrinkage. Failures, therefore, manifest themselves by cracking in the repair material and debonding of the repair material from the substrate.

The first goal of this thesis is to develop a "green" Engineered Cementitious Composites (ECC) and to demonstrate the good performance of this "green" ECC. The second goal is to develop a numerical tool, which can simulate the bond strength between the repair material and the concrete substrate, to assist engineers in designing a durable concrete repair with good bond.

2. Research methodology

The stresses induced by differential shrinkage in repair systems were investigated analytically. The analytical study has shown that differential shrinkage induces lower stresses in the ECC repair system, compared with conventional repair materials. For this reason, ECC was chosen as a repair material in this research. Conventional ECC contains a larger amount of cement than concrete, typically two or three times larger. The high cement content leads a high shrinkage, high costs and poor sustainability performance. A "green" ECC with low cement content was developed by partially substituting Portland cement with limestone powder and blast furnace slag. The surface cracking and interface delamination of the "green" ECC repair system were investigated experimentally. In order to demonstrate the potential of ECC to prolong the service life of the repair structures, the rapid chloride migration (RCM) test was used to investigate the chloride penetration profile in the cracked ECC repair system.

In order to investigate the microstructure development and the bond mechanism in concrete repairs, the experimental techniques, including non-evaporable water test, MIP, ESEM and bond strength test, were applied. In order to quantitatively study the microstructure development and the bond strength in the repair system, the cement hydration model HYMOSTRUC was extended. The moisture transport between the two materials (the repair material and the concrete substrate) and the cement hydration process of the repair material was taken into account in this numerical tool.

3.   Summary of the results of this thesis

The analytical study has revealed that the shrinkage of the repair material, the size of the repair system, the Young's modulus and the roughness of the substrate influence the distribution and magnitude of the differential shrinkage-induced stresses. It was also found that differential shrinkage induces lower stresses in the ECC repair system compared with conventional repair materials.

This thesis demonstrates the feasibility of designing a "green" ECC with limestone powder and BFS. This mixture has a Portland cement content as low as 15% (by weight), which is about half of the standard ECC. At 28 days, the "green" ECC shows high tensile strain capacity of 3.3% and a moderate compressive strength of 38.

Subjected to a differential shrinkage, the "green" ECC repair system shows a larger number of cracks and smaller crack width (40 μm) than a conventional repair material, e.g. a fiber-reinforced polymer-modified repair mortar. Even though ECC cracks, it can carry more tensile load and accommodate larger tensile strain. Due to the smaller crack width, the maximum chloride penetration depth in ECC is much smaller than that in a conventional repair material. The service life prediction using the DuraCrete model revealed that, in order to achieve the same service life, the ECC repair system needs smaller cover thickness than the conventional repair material. It is also found that the bond strength is a crucial factor influencing the performance of the ECC repair system. To enhance the bond strength, therefore, is very important to realize durable ECC repairs.

The moisture transport shows a significant influence on the cement hydration and microstructure development of the repair material. Before setting of the repair material, the concrete substrate absorbs water from the repair material. This causes a reduction of the w/c ratio in the repair material. The reduction of the w/c ratio affects the degree of hydration and the porosity of the repair material as well as the bond strength. After setting of the repair material, the cement hydration works as a "motor" and generates the driving force for the moisture exchange in the two materials, while water acts as "fuel", which is consumed by the "motor" and influences the efficiency of the "motor".

The numerical study has shown that the microstructure development of the repair material and the bond strength are influenced by many parameters, i.e. the porosity and water content of the concrete substrate, the w/c ratio of the repair material, and the thickness of the repair material and the concrete substrate. The correlation between the bond strength and the microstructure of the repair material was observed numerically.

Due to the "wall effect", the cement particles have a loose packing at the interface, and the w/c ratio locally increases. The increased w/c ratio results in a porous interfacial zone. The tensile strength of the interface is, in case of a smooth surface of the substrate, lower than that of the repair material. As a result, under a tensile load, the specimen with a smooth surface of the substrate fails at the interface.

The surface roughness does not influence the moisture exchange and the cement hydration process. However, it has a significant influence on the bond strength. As the surface roughness increases, the contact area between the repair material and the concrete substrate increases as well. The increased contact area contributes to the bonding of the interface. As a result, the bond strength increases, and the failure changes from debonding at the interface to cracking of the repair material. Based on the above fact, ECC, with its high ductility and tight crack width, is a good choice.

Samenvatting

1. Achtergrond en doelstelling van het onderzoek

De betonreparatie-branche groeit snel, voortgestuwd door de veroudering van, schade aan en gebreken in betonnen constructies. Echter, het is bekend dat het realiseren van duurzame betonreparaties niet eenvoudig is. Vroegtijdig falen van betonreparaties brengt hoge kosten met zich mee en schaadt het milieu. De belangrijkste reden voor falen is dat de meeste reparatiematerialen en het contactvlak met de ondergrond geen weerstand kunnen bieden aan de hoge spanningen veroorzaakt door krimpverschillen. Falen manifesteert zich door scheuren in het reparatiemateriaal en onthechting van het reparatiemateriaal van de ondergrond.

Het eerste doel van dit onderzoek is het ontwikkelen van een "groen" Engineered Cementitious Composite[1]) (ECC), en het aantonen van de goede kwaliteit van dit "groene" ECC. Het tweede doel is het ontwikkelen van numeriek gereedschap, dat de aanhechtsterkte van het reparatiemateriaal aan de betonnen ondergrond kan simuleren. Dit gereedschap moet ontwerpers in staat stellen om gevoeligheidsanalyses uit te voeren en voorspellingen te doen over het gedrag van betonreparaties in de tijd.

2. Het onderzoek

Krimpverschillen, die de oorzaak zijn van spanningen in reparatiesystemen, zijn analytisch onderzocht. Deze studie heeft laten zien dat bij toepassen van ECC krimpverschillen tot lagere spanningen leiden in zowel het reparatiemateriaal als in het contactvlak tussen het reparatiemateriaal (ECC) en de ondergrond in vergelijking tot conventionele reparatiematerialen. Om deze reden is in dit onderzoek ECC gekozen als reparatiemateriaal. Het conventionele ECC bevat een grotere hoeveelheid cement dan gewoon beton. Dit kan wel twee tot drie keer zo groot zijn. Het hoge cementgehalte leidt tot grote krimp, hogere kosten en is ongunstig vanuit duurzaamheidoogpunt gezien (niet "sustainable"). Een "groen" ECC met een laag cementgehalte is verkregen door Portlandcement gedeeltelijk te vervangen door kalksteenmeel en hoogovenslakken (HOS). De scheurvorming in het ECC en onthechting in het contactvlak van het "groene" ECC-reparatiesysteem zijn experimenteel onderzocht. De mogelijkheden van ECC om de levensduur van met ECC gerepareerde betonconstructies te verlengen zijn aangetoond met behulp van de Rapid Cloride Migration Test[2]) (RCM-proef). Met de RCM-proef is het indringprofiel van chloride in het gescheurde ECC-reparatiesysteem onderzocht.
    De ontwikkeling van de microstructuur en de aanhechtingsmechanismen in betonreparaties zijn experimenteel onderzocht: hydratatiegraad, porieverdeling (MIP), microscopieonderzoek

---

1) ECC is ontwikkeld door professor Victor Li van de universiteit van Michigan, USA
2) NB: De RCM –proef is ontworpen voor het bepalen van Cl-indringing in ongescheurd beton.

(ESEM) en aanhechtproeven. De ontwikkeling van de microstructuur en de aanhechtingssterkte van het reparatiesysteem zijn numeriek gesimuleerd met het cementhydratatie-model HYMOSTRUC. Daarmee zijn tevens onderzocht het vochttransport tussen de twee materialen (het reparatiemateriaal en de betonondergrond) en het hydratatieproces in het reparatiemateriaal.

3.   Samenvatting van de resultaten van het onderzoek

De grootte en het verloop van de door de verschilkrimp veroorzaakte spanningen zijn afhankelijk van de eigenschappen van het reparatiemateriaal, de afmetingen van het reparatiesysteem, de elasticiteitsmoduli van de betrokken materialen en de ruwheid van de ondergrond. Uit een parameterstudie volgde dat bij toepassing van ECC als reparatiemateriaal de spanningen als gevolg van krimpverschillen kleiner zijn dan bij toepassing van conventionele reparatiematerialen.

Vastgesteld is dat de "groene" ECC-mengsels met kalksteenpoeder en HOS goed reproduceerbaar zijn. Het mengsel heeft een Portlandcementgehalte van slechts 15% (gewicht), wat ongeveer de helft is van dat van conventionele ECC. Na 28 dagen laat de "groene" ECC een hoge rekcapaciteit zien van 3,3% (trek), een bescheiden druksterkte van 38 MPa.

Onderworpen aan een opgelegde krimpvervorming laat het "groene" ECC een groter aantal scheuren en kleinere scheurwijdten (40 μm) zien dan een conventioneel reparatiemateriaal, zoals een vezelversterkte polymeergemodificeerde reparatiemortel. Hoewel ECC scheurt, kan het zelfs meer trekbelasting opnemen en grotere trekrek verdragen. Door de kleinere scheurwijdten is de maximale indringdiepte van chloride in ECC kleiner dan in een conventioneel reparatiemateriaal. Een voorspelling van de levensduur van een ECC-reparatie met het DuraCrete-model gaf aan dat, om dezelfde levensduur te bereiken, het ECC-reparatiesysteem een kleinere dekking nodig heeft dan een conventioneel reparatiemateriaal. Ook de aanhechtingssterkte blijkt een cruciale factor te zijn die de kwaliteit van het ECC reparatiesysteem beïnvloedt. Vergroten van de aanhechtsterkte is daarom heel belangrijk voor het bereiken van duurzame ECC-reparaties.

Vochttransport heeft een significante invloed op de cementverharding en de ontwikkeling van de microstructuur van het reparatiemateriaal. Voordat het reparatiemateriaal zich zet, absorbeert de betonnen ondergrond water uit het reparatiemateriaal. Dit veroorzaakt een reductie van de w/c-factor in het reparatiemateriaal. De reductie van de w/c-factor beïnvloedt de mate van hydratatie en de porositeit van het reparatiemateriaal ter plaatse van het aanhechtoppervlak en daarmee ook de aanhechtsterkte. Na begin binding van het reparatiemateriaal werkt de cementhydratatie als een "motor", die de drijvende kracht vormt voor vochtuitwisseling tussen de twee materialen, terwijl het water optreedt als brandstof welke gebruikt wordt door de motor en de efficiëntie van de motor beïnvloedt.

De numerieke studie heeft laten zien dat de ontwikkeling van de microstructuur van het reparatiemateriaal en de aanhechtsterkte worden beïnvloed door veel parameters, zoals de porositeit en het watergehalte van de betonondergrond, de w/c-factor van het reparatiemateriaal, de dikte van het reparatiemateriaal en de dikte van de betonondergrond. De correlatie tussen de aanhechtsterkte en de microstructuur van het reparatiemateriaal is numeriek vastgesteld.

Door het "wandeffect" in de grenslaag tussen reparatiemateriel en ondergrond hebben de cementdeeltjes een losse pakking nabij het contactvlak en neemt de w/c-factor locaal toe. De hogere w/c-factor resulteert in een poreuze grenslaag. De treksterkte van de grenslaag is in het

geval van een glad oppervlak van de ondergrond lager dan dat van het reparatiemateriaal. Het gevolg is dat bij trekbelasting een proefstuk met een gladde ondergrond bezwijkt in de grenslaag.

De oppervlakteruwheid heeft geen invloed op de vochtuitwisseling en het hydratatieproces van het cement. Het heeft daarentegen een significante invloed op de aanhechtingssterkte. Bij toenemende oppervlakteruwheid neemt het contactoppervlak tussen het reparatiemateriaal en de betonnen ondergrond toe. Het toegenomen contactoppervlak draagt bij aan de aanhechting van het grensvlak. Het gevolg is dat de aanhechtsterkte toeneemt en de plaats van bezwijken verplaatst van het grensvlak naar het reparatiemateriaal (of misschien de betonnen ondergrond).

Publications

Journal papers

1. **Zhou, J.**, Ye, G., Schlangen, E. and van Breugel, K., Measurement of the advancing and receding contact angles between mercury and cement-based materials, submitted to *Cement and Concrete Research*.
2. **Zhou, J.**, Qian, S., Ye, G., Copuroglu, O., van Breugel, K. and Li, V.C., Improved fiber distribution and mechanical properties of Engineered Cementitious Composites by adjusting mixing sequence, submitted to *Cement and Concrete Composites*.
3. **Zhou, J.**, Ye, G. and van Breugel, K., Influence of moisture exchange on cement hydration, microstructure and bond strength in concrete repairs, Journal of the Chinese Ceramic Society 38(9) 69-75, 2010.
4. Qian, S., **Zhou, J.** and Schlangen, E., Influence of curing regime and precracking time on the self-healing behavior of Engineered Cementitious Composites, *Cement and Concrete Composite* 32(9) 686-693, 2010.
5. **Zhou, J.**, Ye, G. and van Breugel, K., Characterization of pore structure in cement-based materials using pressurization-depressurization cycling mercury intrusion porosimetry (PDC-MIP), *Cement and Concrete Research* 40(7) 1120-1128, 2010.
6. **Zhou, J.**, Qian, S., Guadalupe Sierra Beltran, M.G.M., Ye, G., van Breugel, K. and Li, V.C., Development of Engineered Cementitious Composites with limestone powder and blast furnace slag, *Materials and Structures* 43(6) 803-814, 2010.
7. Qian, S., **Zhou, J.**, de Rooij, M.R., Schlangen, E., Ye, G. and van Breugel, K., Self-healing behavior of strain hardening cementitious composites incorporating local waste materials, *Cement and Concrete Composites* 31(9) 613-621, 2009.
8. Koleva, D.A., van Breugel, K., Ye., G., **Zhou, J.**, Chamululu, G. and Koenders, E.A.B., Porosity and permeability of mortar specimens incorporating peo113-bPS218 micelles, *ACI Materials Journal*, SP267-09, 101-110, 2009.
9. **Zhou, J.**, Ye, G. and van Breugel, K., Early-age heat evolution and pore structure of Portland cement blended with blast furnace slag, fly ash or limestone powder, *Key Engineering Materials* 405-406 242-246, 2009.
10. **Zhou, J.**, Ye, G., Schlangen, E. and van Breugel, K., Modelling of stresses and strains in bonded concrete overlays subjected to differential volume changes, *Theoretical and Applied Fracture Mechanics* 49 (2) 199-205, 2008.

Conference papers

1. **Zhou, J.**, Ye, G. and van Breugel, K., Durability and service life of concrete repairs in the presence of cracks, in Proceedings of *the 2nd International Symposium on Service Life Design for Infrastructure*, 2010, Delft, the Netherlands, pp. 1121-1129.
2. **Zhou, J.**, Ye, G. and van Breugel, K., Cement hydration and bond Strength in concrete

repairs influence by water exchange between repair material and concrete substrate, in Proceedings of *ISCC2010*, 2010, Jinan, China.

3. **Zhou, J.**, Qian, S., Ye, G., van Breugel, K. and Li, V.C., Engineered cementitious composites with low volume of cement, in Proceedings of *the FramCos07*, 2010, Jeju, Korea, pp. 1551-1556.

4. Qian, S., Li, V.C. and **Zhou, J.**, Relating tensile properties with flexural properties in SHCC, in Proceedings of *the FramCos07*, 2010, Jeju, Korea, pp. 1612-1616.

5. **Zhou, J.**, Qian, S., Ye, G., van Breugel, K. and Li, V.C., Processing sequence in the production of engineered cementitious composites, in Proceedings of *the ConMat09*, 2009, Nagoya, Japan, pp. 333-338.

6. **Zhou, J.**, Ye, G. and van Breugel, K., New mercury porosimetry method for the measurement of pore size distribution in cement-based materials, in Proceedings of *the 2nd International RILEM Workshop on Concrete Durability and Service Life Planning*, 2009, Haifa, Israel, pp. 490-497.

7. **Zhou, J.**, Li, M., Ye, G., Schlangen, E., van Breugel, K. and Li, V.C., Modelling the performance of ECC repair systems under differential volume changes, in Proceedings of *the 2nd Conference on Concrete Repair, Rehabilitation and Retrofitting*, 2008, Cape Town, South Africa, pp. 1005-1009.

8. Qian, S., **Zhou, J.**, Liu, H., de Rooij, M.R., Schlangen H.E.J.G., Gard, W.F. and Kuilen, J.W., Self-healing cementitious composite under bending loads, in *Proceedings of the 2nd International Conference on Self-Healing Materials*, Chicago, USA, 2009, pp. 1-4.

9. Schlangen, H.E.J.G., Qian, Z., Sierra-Beltran, M.G. and **Zhou, J.**, Simulation of fracture in fiber cement based materials with a micro-mechanical lattice model, in *Proceedings of the 12th International Conference on Fracture*, Ottawa, Canada, 2009, pp. 1-10.

10. **Zhou, J.**, Ye, G., Schlangen, E. and van Breugel, K., Measurement of advancing and receding contact angles between mercury and cement-based materials, in *Proceedings of the 1st Conference on Microstructure Related Durability of Cementitious Composites*, 2008, Nanjing, China, pp. 1399-1403.

11. Koleva, D.A., Ye, G., **Zhou, J.**, Petrov, P. and van Breugel, K., Material properties of mortar specimens at early stage of hydration in the presence of polymeric nano-aggregates, in *Proceedings of the 1st Conference on Microstructure Related Durability of Cementitious Composites*, 13-15 Oct 2008, Nanjing, China, pp. 161-168.

12. **Zhou, J.**, Qian, S., Guadalupe Sierra Beltran, M.G.M., Ye, G. and van Breugel, K., Engineered cementitious composites with Blast furnace slag and limestone powder, in *Proceedings of the Workshop on the 50-year Teaching and Research Anniversary of Prof. Sun Wei*, 2008, Nanjing, China.

13. **Zhou, J.**, Ye, G., Schlangen, E. and van Breugel, K., Numerical study on predicting the performance of repair materials under differential volume changes, in *Proceedings of the International RILEM Symposium on Concrete Modelling*, 26-28 May 2008, Delft, the Netherlands, pp. 699-707.

14. **Zhou, J.**, Ye, G., Schlangen, E. and van Breugel, K., Modeling of stresses and strains in bonded concrete overlays subjected to differential shrinkage, in *Proceedings of the International Conference of MesoMechanics 2008*, 28 Jan.-1 Feb. 2008, Cairo, Egypt.

15. **Zhou, J.**, Ye, G., Schlangen, E. and van Breugel, K., Modified mercury porosimetry for the measurement of the pore size distribution in cement-based materials, in *Proceedings of the 1st International Conference on Recent Advances in Concrete Technology*, 19-21 Sep. 2007, Washington DC, USA, pp. 169-174.

16. **Zhou, J.**, Ye, G., Schlangen, E. and van Breugel, K., Simplied model for stresses and strains in Bonded concrete overlays, in *Proceedings of the Conference on Cracking in Engineering Structures*, 22-247 July 2007, Dalian, China, pp. 131-138.

17. **Zhou, J.**, Ye, G. and van Breugel, K., Experimental studies on the development of water permeability of Portland cement paste blended with blast furnace slag, in *Proceedings of the 12th International Congress on Cement Chemistry*, 8-13 July 2007, Montreal, Canada.

18. **Zhou, J.**, Ye, G., Schlangen, E. and van Breugel, K., Selection of materials for concrete patch repair, in *Proceedings of the Symposium on Serviceability of Underground Structures*, 19-20 Oct. 2006, Shanghai, China, pp. 195-201.

19. **Zhou, J.**, Ye, G. and van Breugel, K., Hydration process and pore structure of Portland cement paste blended with blast furnace slag, in *Proceedings of the 6th Symposium on Cement and Concrete*, 19-22 Sep. 2006, Xi'an, China, pp. 417-424.

20. **Zhou, J.**, Ye, G. and van Breugel, K., Hydration of Portland cement blended with blast furnace slag at early stage, in *Proceedings of the RILEM Symposium on Advances in Concrete through Science and Engineering*, 11-13 Sep. 2006, Quebec, Canada.

21. Ye, G., **Zhou, J.**, van Breugel, K. and De Schutter, G., Characterization of the hydration of Portland cement blended with blast furnace slag base don SEM image analysis, in *Proceedings of the RILEM Symposium on Concrete Durability and Service Life Planning*, 2006, Israel.

22. **Zhou, J.**, Ye, G., Schlangen, E. and van Breugel, K., Autogenous deformation of Portland cement paste blended with blast furnace slag measured by mini-TSTM, in *Proceedings of the RILEM Symposium on Volume Changes of Hardening Concrete: Testing and Mitigation*, 13-19 August 2006, Lyngby, Denmark, pp. 367-374.

Curriculum Vitae

Name: Jian Zhou
Date of Birth: June 1st, 1982
Place of Birth: Qihe, Shandong Province, China
Email: Jian820601@hotmail.com

May 2006 – Jan. 2010	PhD student in Structural Engineering, Faculty of Civil Engineering and Geosciences, Delft University of Technology, Delft, the Netherlands
Aug. 2007 – Nov. 2007	Visiting scholar, Department of Civil and Environmental Engineering, University of Michigan, Ann Arbor, USA.
Sep. 2004 – Apr. 2006	MSc student in Structural Engineering, Faculty of Civil Engineering and Geosciences, Delft University of Technology, Delft, the Netherlands.
Sep. 2000 – July 2004	Bachelor student in Civil Engineering, School of Civil Engineering, Shandong University, Jinan, China